University of Minnesota
St. Anthony Falls Hydraulic Laboratory
Mississippi River at 3rd Ave. S.E.

Project Report No. 254

FINAL TECHNICAL REPORT

RESEARCH PROGRAM IN HYDROACOUSTICS

Principal Investigators

Roger E. A. Arndt

Hiroshi Higuchi

Mostafa Kaveh

Robert Lambert

Robert Plunkett

Visiting Associate Professors:

Toshiaki Ikohagi

Vijay Arakeri

Prepared for

OFFICE OF NAVAL RESEARCH
Arlington, Virginia

Contract No. N00014-83-K-0145

ERRATA FOR

FINAL TECHNICAL REPORT

RESEARCH PROGRAM IN HYDROACOUSTICS

p. 25, line 2: instead of "monogram", should read "monograph".

p. 26, Eq. 5: instead of "]e ", should read " $]e^{-\tilde{\omega}}$ ".

p.24, Fig. V2.7: instead of "Experimental plot of the location of the convective peaks versus the normalized frequency $\tilde{\omega}$ for the bouyant body facility. The solid line is a fit of Eqs. 5 and 7 for the parameters given in the legend." should read "Comparison of the phase-speed prediction, Eq. 4, with experimental data of Blake."

p.28, Fig. V2.8: Instead of "Comparison of the phase-speed prediction, Eq. 4, with experimental data of Blake." should read "Experimental plot of the location of the convective peaks versus the normalized frequency $\tilde{\omega}$ for the bouyant body facility. The solid line is a fit of Eqs. 5 and 7 for the parameters given in the legend."

TABLE OF CONTENTS

I. EXECUTIVE SUMMARY

This program is concerned with two major problems in hydroacoustics; namely the nature of the low wavenumber characteristics of turbulent boundary layer pressure fluctuations including their relationship with structural vibration, and cavitation noise from tip vortices. There are four major tasks:

a) Development of signal analysis techniques that permit accurate estimates of the low wavenumber portion of the wavenumber-frequency pressure spectrum.

b) Measurements of the pressure spectrum and comparison of experiment with a theoretical wave guide model.

c) Determination of the structural response to wall layer pressure fluctuations and the influence of plate vibration on the structure of turbulence within the boundary layer.

d) Measurement of the spectral characteristics and source distribution of cavitation noise in tip vortices in steady and non-steady flow.

Both computer simulation and physical measurements are involved. All experimental work is in water, utilizing hydrodynamic research facilities at the St. Anthony Falls Hydraulic Laboratory.

The theoretical and algorithmic aspects of our research on the estimation of the frequency-wavenumber spectra of turbulent boundary layers (TBL) proceeded as follows. First, a statistical model of the cross-spectral density matrices (CSDM) of TBL random fields, as proposed by Chase and Corcos were developed. These models explicitly included dependence on the array geometry, measurement of time and signal-to-noise ratios at each sensor element, and formed the backbone of the simulations that were carried out to assess the performance of various estimators. Next, the most promising "modern" spectral estimation techniques were evaluated for suitability of representing the TBL spectral models. Finally, new spectral estimation techniques were developed that were aimed at high-fidelity, rather than high-resolution spectral estimation of the type of spectra expected from the TBL random fields. Where possible, theoretical analyses of the performance of the estimators were made. In all cases, extensive simulations were carried out to evaluate both the spectral fidelity and variability of the estimators.

Capon's Maximum Likelihood (ML) proved to be the most stable known modern spectral estimation technique for the estimation of the TBL wavenumber spectra. As a means of increasing the effective aperture of an array, with fixed number of sensors, nonuniform array alternatives were

investigated in conjunction with the MLM estimator. It was found that array geometries, such as Minimum-Redundancy, increase resolution in the case of multiple plane waves, but do not offer higher fidelity in estimating smooth spectra. This was attributed to the increase in the average level of the array sidelobes when a narrower mainlobe is generated by the extended array aperture. Certain limitations of this method were identified. To counter these deficiencies, a new method, denoted the Covariance Constrained MLM (CCMLM) was developed to alleviate this shortcoming and in the process improve the fidelity of the MLM. The CCMLM uses the MLM in an iterative fashion to generate an estimate of the spectrum that is asymptotically (large number of iterations) matched to the measured CSDM. A practical, stable iterative algorithm was designed and the performance of the method was evaluated both theoretically and through extensive numerical simulations. The CCMLM, which includes the MLM as a special case, proved to be the best technique that we evaluated or developed for the estimation of spectra such as those suggested by Corcos and Chase.

Research on boundary layer pressure fluctuations proceeded on two fronts: theoretical development of a wave guide model and experimental verification of the model using a buoyant body facility. The experimental work utilized the results of our research on spectral estimation. The experimental work verified the wave guide model, and in particular predicted dispersion characteristics of the pressure signal.

The major purpose of the experimentation with a flexible plate in a water tunnel was to investigate the validity of the assumptions which underlie the weighted integral approach now used to calculate the vibration response of water loaded plates subjected to turbulent boundary layer excitation. The most important assumption is that the plate vibration has so little effect on the turbulent boundary layer that the power spectral density (spectrum) of the pressure field on the wall is affected only to a negligible extent. The second major assumption is that the plate response is linear so that the superposition can be used. Measurement of both the temporal and spatial characteristics of the pressure field adjacent to a rigid wall, as well as the vibratory response of a flexible plate to the same boundary layer excitation, has been completed. Work is continuing on calculating the vibration cross spectra using dimensionless pressure spectra and the measured plate response functions. When completed, the results will be compared with the measured vibration cross spectra.

The tip vortex research consisted of three parts: a) measurement of cavitation inception and fully developed cavitation characteristics, b) measurement of the resulting noise intensity spectral characteristics, and noise source distribution within the cavitating vortex and c) LDV measurement of the velocity field, construction of a semi-empirical vortex model and estimation of the pressure within the vortex core.

The research program included the most exhaustive examination of cavitation inception in tip vortex available in the literature. A very subtle interrelationship between viscous effects and gas content effects has been identified as well as the surprising observation that cavitation inception often occurs only after significant levels of tension have been sustained. This infers that cavitation inception testing may be facility dependent. Unfortunately, there is not enough data available from

different facilities to verify or deny this possibility. The important practical finding is that the inception process at prototype Reynolds numbers can be quite different from the inception process at Reynolds numbers typically encountered in water tunnel testing of model propellers.

Several different types of noise signatures were noted, which were related to different types of cavitation inception. As expected, the levels of tip vortex cavitation noise are substantially lower than surface cavitation when it occurs. It is important to note that the cavitation indices for vortex cavitation are substantially higher. In many cases expansion of a cylindrical cavity was a significant noise mechanism.

A hydrophone array was utilized to identify the noise source location. In spite of limitations on spatial resolution and repeatability, the results of this study clearly indicate that cavitation noise sources are concentrated in the vortex rollup region less than one chord length from the tip of the hydrofoil.

The noise intensity associated with fully developed tip vortex cavitation is substantially lower than inception noise, or surface cavitation noise, when it occurs. At high angle of attack and under special circumstances, a very strong, low pitch tone occurs. The frequency of the tone varied with cavity core radius and free stream velocity, discounting the thought that this might be a flow induced vibration of the hydrofoil itself. Although no conclusive statement could be made from the present set of data, it was speculated that the oscillation of the twisted ribbon type cavity is responsible for this tone.

Although these tests were carried out in a highly reverberant water tunnel, experiments and computer simulations demonstrated that the shape of the measured spectra was unaffected by reverberation.

This project was a joint effort of five principal investigators from three different departments. All the experimental work was carried out at the St. Anthony Falls Hydraulic Laboratory. In addition to the five faculty, two visiting professors, and several visiting scholars were involved. The project supported partially, or totally, four Ph.D. dissertations and four M.S. theses. In addition, several undergraduates carried out special research projects.

IV. PUBLICATIONS AND PRESENTATIONS

Ph. D. Dissertations

Dean F. Long - "Noise Radiation and Coherent Structure in Turbulent Jets: Viscous and Compressibility Effects, Dec. 1985.

Reza Taghavi - "Cavitation Inception in Axisymmetric Turbulent Jets," May 1985.

G. H. Wakefield - "High Fidelity Estimation of Continuous Spectra," Dept. of Electrical Engineering, 1985.

N. Narayan - "Turbulent Boundary Layer Pressure Fluctuations Induced Vibrations in a Thin Elastic Plate," 1987.

M.S. Theses

Scott Forbes - "Acoustic Measurement of Cavitation in a Water Tunnel," Plan B, 1984.

Carlos Quadrelli - "An Experimental Investigation of Vortex Roll-Up for an Elliptically-Loaded Wing," April, 1985.

Michael Rogers - "Experimental Investigations of Tip Vortex Cavitation and Associated Noise," in press.

M. Wurtz - "Measurement of the Wave Number Frequency Spectra of the Wall Pressure Fluctuations in the Turbulent Boundary Layer of Water," 1987.

Professional Papers

1. "Pressure Spectra in Turbulent Free Shear Flows," W. George, P. Beuther, and R.E.A. Arndt, Journal of Fluid Mechanics, October 1984.

2. "Comparative Examination of Tip Vortex and Surface Cavitation Noise," H. Higuchi, S. Forbes, and R.E.A. Arndt, Journal of Acoustical Society of America, Supplement 1, Vol. 76, Oct. 1984, pp. 532 (108th meeting, Minneapolis, Minn.) abstract only.

3. "Comparative Examination of Tip Vortex and Surface Cavitation Noise," H. Higuchi and R.E.A. Arndt, Bulletin of American Physical Society, Vol. 29, No. 9, Nov. 1984 (37th Annual Meeting of the Division of Fluid Dynamics, Providence, RI), abstract only.

4. "Pressure Fluctuations Surrounding a Turbulent Jet; III: Characteristic Event," R.E.A. Arndt and D. Long, Bulletin of American Physical Society, Vol. 29, No. 9, p. 1536, Nov. 1984, abstract only.

5. "Vaporous and Gaseous Cavitation in Shear Flows," R.E.A. Arndt and R. Taghavi, Bulletin of American Physical Society, Vol. 29, No. 9, p. 1564, Nov. 1984, abstract only.

6. "Pressure Cross Spectra in Turbulent Boundary Layers in Water," N. Narayan and R. Plunkett, TR-AEM-85-1-RP, Department of Aerospace Engineering and Mechanics, University of Minnesota, Feb. 1985.

7. "Controlled Suppression or Amplification of Turbulent Jet Noise," R.E.A. Arndt, D. Long, and H. Kim, AIAA Jour., May 1985.

8. "Reverberation Effects on Cavitation Noise," H. Higuchi and R.E.A. Arndt, in Cavitation and Multiphase Flow Forum-1985, 20th Anniv. Issue, edited by J. W. Hoyt and O. Furuya, RED-Volume 23, ASME, New York, June 1985, pp. 21-24.

9. "Sound Source Location in Cavitating Tip Vortices," H. Higuchi, R. Taghavi, and R.E.A. Arndt, in Cavitation and Multiphase Flow Forum-1985, 20th Anniv. Issue, edited by J. W. Hoyt and O. Furuya, FED-Vol. 23, ASME, New York, June 1985, pp. 65-67.

10. "Tip Vortex Cavitation," R.E.A. Arndt and H. Higuchi, in Cavitation and Multiphase Flow Forum-1985, 20th Anniv. Issue, edited by J. W. Hoyt and O. Furuya, FED-Vol. 23, ASME, New York, June 1985, pp. 61-64.

11. "Cavitation in Various Types of Shear Flow," R.E.A. Arndt and R. Taghavi, in ASME International Symp. on Cavitation in Hydraulic Structures and Turbomachinery, edited by R.E.A. Arndt and D. Webb, Albuquerque, New Mexico, June 1985.

12. "Flow Around a Circular Cylinder in the First Subregion of the Critical Range," H. Higuchi, H. J. Kim, and C. Farell, AIAA Paper 85-1715, in Proc., AIAA 18th Fluid Dynamics, Phasmadynamics and Lasers Conference, July 1985, Cincinnati, Ohio.

13. "A Miniature Directional Surface-Fence Gage," H. Higuchi, AIAA Jour., Vol. 23, No. 6, Aug. 1985.

14. "The Orthogonal Decomposition of Pressure Fluctuations Surrounding a Turbulent Jet," R.E.A. Arndt and D. Long, Turbulent Shear Flow Conference, Aug. 1985.

15. "Recent Research on Turbulent Flow Noise Mechanisms," R.E.A. Arndt and D. Long, Shock and Vibration Digest, Oct. 1985.

16. "Plate Vibration Caused by a Turbulent Boundary Layer," N. Narayan and R. Plunkett, to appear in ASME special volume, ASME Winter Annual Meeting, Nov. 1985.

17. "Frequency-Wavenumber Spectral Estimation of the Wall-Pressure Field Beneath a Turbulent Boundary Layer," G. Wakefield and M. Kaveh, in

Trans. of 1985 ASME Winter Annual Meeting, Miami, Fla., Nov. 1985 (to appear).

18. "Frequency-Wavenumber Spectral Estimation of Non-Planar Random Fields," G. Wakefield and M. Kaveh, in Proceedings, IEEE International Conference on Acoustics, Speech, and Signal Processing, ICASSP '85, Tampa, Florida.

19. "The Covariance-Constrained Maximum Likelihood Method," G. Wakefield and M. Kaveh, in Proceedings, EUSIPCO '86.

Special Publications

Cavitation in Hydraulic Structures and Turbomachinery, American Society of Mechanical Engineers Special Publication, June 1985, (edited by Roger Arndt and Don Webb).

International Symposium on Cavitation and Multiphase Flow Noise, American Society of Mechanical Engineers, Special Publication, edited by Roger Arndt, M. L. Billet, and W. K. Blake, Dec. 1986.

Proceedings

1. "Comparative Examination of Tip Vortex and Surface Cavitation Noise," Roger E.A. Arndt, H. Higuchi, and S. Forbes, Jour. of Acoustical Society of America, Vol. 76, Suppl. #1, Oct. 1984.

2. "Comparative Examination of Tip Vortex and Surface Cavitation Noise," Roger E.A. Arndt and H. Higuchi, Bulletin of the American Physical Society, Vol. 29, No. 9, Nov. 1984.

3. "Sound Source Location in Cavitating Tip Vortices," R.E.A. Arndt, H. Higuchi, and R. Taghavi, Cavitation and Multiphase Flow Forum, American Society of Mechanical Engineers, June 1985.

4. "Reverberation Effects on Cavitation Noise," R.E.A. Arndt and H. Higuchi, Cavitation and Multiphase Flow Forum, American Society of Mechanical Engineers, June 1985.

5. "Cavitation Inception in Trailing Vortex from a Hydrofoil," R.E.A. Arndt, H. Higuchi, and S. Jiang, 13th IAHR Symposium, Section on Hydraulic Machinery, Equipment, and Cavitation, 1986.

6. "Assessment and Mitigation of Cavitation Pitting in Hydraulic Turbines," R.E.A. Arndt, A. Ferreira, P. R. Rodrigue, J. P. Sinclair, and R. P. Voigt, 13th IAHR Symposium, Section on Hydraulic Machinery, Equipment and Cavitation, 1986.

7. "Tip Vortex Cavitation," R.E.A. Arndt, H. Higuchi, and T. Ikohagi, International Symposium on Propeller and Cavitation, Wuxi, China, April 1986.

8. "Further Studies of Tip Vortex Cavitation," R.E.A. Arndt and H. Higuchi, 1986 Cavitation and Multiphase Flow Forum, Fluids Engineering Division, ASME, Atlanta, Georgia, May 1986.

9. "Characteristics of Tip Vortex Cavitation Noise," R.E.A. Arndt, H. Higuchi, and M. Rogers, ASME International Symposium on Cavitation Noise, Anaheim, California, Dec. 1986.

Progress Reports

"Research Program in Hydroacoustics - Progress Reports" submitted to Office of Naval Research
- March 1 through October 15, 1983
- October 15, 1985 through January 15, 1984
- January 15 through April 15, 1984
- April 15 through October 15, 1984
- October 16, 1984 through April 15, 1985

Presentations

- Acoustical Society of America, Minneapolis, Minnesota, April, 1984.

  "Hydroacoustic Research at the University of Minnesota," by R. Arndt, invited lecture.

- Hydraulic Engineering Research Institute (ICH), Bucharest, Romania, July, 1984.

  "Cavitation Research at the St. Anthony Falls Hydraulic Laboratory,", by R. Arndt.

- 5th ASCE-EMD Specialty Conference, Laramie, Wyoming, August 1984.

  "Cavitation Research and its Relevance in the Practice of Hydraulic Engineering," invited lecture by R. Arndt.

- American Society of Civil Engineers Hydraulics Division Specialty Conference, Coeur d'Alene, Idaho, August, 1984

  "Cavitation in Various Types of Shear Flow," by R. Arndt.

- University of Illinois, Hydrosystems Graduate Seminar Series, Urbana, Illinois, Oct. 1984.

  "Cavitating Jets and Related Topics," by R.E.A. Arndt, Invited Speaker.

- Central Water and Power Research Station, Puna, India, Jan. 1985

  Series of lectures on cavitation, by R. Arndt.

- Acoustical Society of American, Minneapolis, Minnesota, Oct. 1984

  "Measured Wall Pressure Cross Spectra Due to a Turbulent Boundary Layer," by N. Narayan and R. Plunkett.

  "Measurements of Low-Wavenumber Spectra of Wall Turbulence in a Buoyant Body Facility," by D. Long, M. Wurtz, and R. Lambert,

  "Spectral Estimation of the Low-Wavenumber Region of a Turbulent Boundary Layer: Maximum Likelihood Method," by G. Wakefield and M. Kaveh.

  "Comparative Examination of Tip Vortex and Surface Cavitation Noise," by H. Higuchi, S. Forbes, and R.E.A. Arndt.

- 37th Meeting of Division of Fluid Dynamics, American Physical Society, Providence, Rhode Island, November 1984.

  "Estimation of the Low-Wavenumber Region of a Turbulent Boundary Layer Using the Maximum Likelihood Method," by G. Wakefield and M. Kaveh.

  "Comparative Examination of Tip Vortex and Surface Cavitation Noise," by H. Higuchi and R.E.A. Arndt.

  "Measured Wall Pressure Cross Spectra Due to a Turbulent Boundary Layer," by N. Narayan and R. Plunkett.

  "Low Wave Number Spectra of Wall Pressure on a Buoyant Underwater Body," by R. Lambert, D. Long, and M. Wurtz.

- IEEE International Conference on Acoustics, Speech, and Signal Processing, ICASSP 85.

  "Frequency-Wavenumber Spectral Estimation of Non-Planar Random Fields," by G. Wakefield and M. Kaveh.

- St. Anthony Falls Hydraulic Laboratory Seminar Series.

  "Cavitation in Vortical Motion," by R. Arndt, Nov. 1984.

  "The Hydroacoustic Program at St. Anthony Falls Hydraulic Laboratory, by R. Arndt, March 1984.

- 24th AIAA Aerospace Sciences Meeting, Reno, Nevada, Jan. 1985.

  "An Experimental Investigation of Vortex Roll-Up for an Elliptically-Loaded Wing," by H. Higuchi, J. C. Quadrelli, and C. Farell, AIAA Paper 86-0562.

- Henkel Corporation Seminar, Minneapolis, Minnesota, May, 1985.

  "Cavitation Research at the St. Anthony Falls Hydraulic Laboratory, by Roger E.A. Arndt.

- Joint ASCE/ASME Mechanics Conference, Albuquerque, New Mexico, June 1985.

  "Reverberation Effects on Cavitation Noise," by H. Higuchi.

  "Sound Source Location in Cavitating Tip Vortices," by H. Higuchi.

  "Tip Vortex Cavitation," by R.E.A. Arndt.

  "Cavitation in Various Types of Shear Flow," by R.E.A. Arndt.

  "Utility Survey of Cavitation Erosion in Hydraulic Turbines," by Roger E.A. Arndt.

- Megatrends in Hydraulic Research for the Future, Fort Collins, Colorado, July 1985.

  "Cavitation Research: Synopsis and Perspective," invited lecture by R. Arndt.

- 21st IAHR Congress, Hydraulic Structures Seminar, Melbourne, Australia, Aug. 1985.

  "Cavitation in Hydraulic Structures," by R. Arndt.

- International Symposium on Propeller and Cavitation, Wuxi, China, April 1986.

  "Tip Vortex Cavitation," by R. Arndt.

- Institute of High Speed Mechanics, Sendai, Japan, April, 1986.

  "Cavitation Research at St. Anthony Falls Hydraulic Laboratory," invited lecture to faculty and students, by R. Arndt.

- American Society of Mechanical Engineers Cavitation and Multiphase Flows in Fluid Machinery, Atlanta, Georgia, May 1986.

  "Special Comments on a Recent Symposium on Cavitation held in China," by R. Arndt.

- NSF Romanian-U.S. Workshop in Hydraulic Engineering Research, Bucharest, Romania, July 1986.

  "Cavitation Research in Hydraulic Engineering," by R. Arndt.

- 12th American Hydraulics Congress of the IAHR Short Course, Sao Paulo, Brazil, Aug. 1986.

  "Cavitation," by R. Arndt

- American Physical Society, Columbus, Ohio, Nov. 1986.

  "Viscous Effects on Tip Vortex Roll-Up and Cavitation," by R. Arndt.

List of Honors, Awards

Robert Lambert received the first John C. Johnson Memorial Education Award from the Institute of Noise Control Engineering (INCE) "for excellence in teaching of acoustics and noise control engineering," Dec. 1984.

V. SYNOPSES OF RESEARCH PROJECT

1. Theoretical and Algorithmic Aspects of Frequency-Wavenumber Spectral Estimation of Turbulent Boundary Layers

M. Kaveh, Principal Investigator

The theoretical and algorithmic aspects of our research on the estimation of frequency-wavenumber spectra of turbulent boundary layers (TBL) proceeded as follows. First a statistical model of the cross-spectral density matrices (CSDM) of TBL random fields, as proposed by Chase and Corcos were developed. These models explicitly included dependence on the array geometry, measurement time and signal-to-noise ratios at each sensor element and formed the backbone of the simulations that were carried out to assess the performances of various estimators. Next, the most promising "modern" spectral estimation techniques were evaluated for suitability of representing the TBL spectral models. Finally, new spectral estimation techniques were developed that were aimed at high-fidelity, rather than high-resolution spectral estimation of the type of spectra expected from the TBL random fields. Where possible, theoretical analyses of the performance of the estimators were made. In all cases, extensive simulations were carried out to evaluate both the spectral fidelity and variability of the estimators.

The results are summarized below. Details of the methods and their performance can be found in the attached published papers and the Ph.D. dissertation by G. Wakefield.

1. Traditional approaches for the estimation of the TBL wavenumber spectra are based on the principle of beamforming by an array of sensors. Unfortunately, the relatively small array aperture of an experimental array does not allow for sufficient selectivity and resolution to eliminate leakage of power from the convective and sonic regions of spectra into the low-wavenumber region, whose characteristics are of primary interest. Our estimation results based on the beamformer were used as the baseline for evaluating the performance of other methods.

2. The maximum Entropy Method is perhaps the most widely used technique for high resolution spectral estimation. The performance of this method has usually been evaluated in the peak regions of peaky spectra. MEM was applied to the TBL models with mixed results. For sufficiently high signal-to-noise ratios, the fidelity of the estimates were found to be quite good. Statistical performance analyses, however, showed the MEM spectral variance in the low-wavenumber regions to be too large, rendering this method unreliable for this application.

3. Capon's Maximum Likelihood (ML) proved to be the most stable known modern spectral estimation technique for the estimation of the TBL wavenumber spectra. This technique produced spectral estimates that were more

biased, in the low wavenumber regions, than estimates generated by the MEM. The MLM estimator variance, however, was substantially lower than that of the MEM. Furthermore the MLM possesses a constrained spatial filtering interpretation that is intuitively pleasing and devoid of the imposition of a parametric model on the spectra.

4. As a means of increasing the effective aperture of an array, with fixed number of sensors, nonuniform array alternatives were investigated in conjunction with the MLM estimator. It was found that, whereas array geometries such as Minimum-Redundancy increase resolution in the case of multiple plane waves, they do not offer higher fidelity in estimating smooth spectra such as those of the TBL's. This was attributed to the increase in the average level of the array sidelobes when a narrower mainlobe is generated by the extended array aperture.

5. The MLM was extended to operate on a subspace of the eigenstructure of the CSDM. The subspace was chosen to include the CSDM eigenvectors whose Fourier transforms primarily contribute to the low wavenumber region. This implied the elimination of the eigenvectors corresponding to several of the largest eigenvalues that mainly form the convective specral peak. This technique improved the fidelity of the MLM in the low wavenumber regions. Determination of the significant eigenvalues for an unknown spectral model, however, proved to be a definite shortcoming of this technique.

6. One feature of the MLM is that, unlike the MEM and the beamformer, the inverse Fourier transform of the estimated spectrum does not match the CSDM from which the MLM spectrum was computed. A new method, denoting the Covariance Constrained MLM (CCMLM), was developed to alleviate this shortcoming and in the process to improve the fidelity of the MLM. The CCMLM uses the MLM in an iterative fashion to generate an estimate of the spectrum that is asymptotically (large number of iterations) matched to the measured CSDM. A practical, stable iterative algorithm was designed and the performance of the method was evaluated both theoretically and through extensive numerical simulations. The CCMLM, which includes the MLM as a special case, proved to be the best technique that we evaluated or developed for the estimation of spectra such as those suggested by Corcos and Chase.

2. Wavenumber/Frequency Spectral Estimation of Wall Pressure Fluctuations

R. Lambert, Principal Investigator

Measurements

The wall pressure fluctuations due to turbulence have been measured over the useful range of frequencies from approximately 45 Hz to 400 Hz and wavenumbers ranging from 0 to 400 m^{-1}. The measurements were obtained using a 10 sensor uniform spaced linear array with a sensor spacing D = 0.0158 M center to center and aperture of 0.14 meters. The data obtained has been normalized to dimensionless quantities using the following flow profile parameters: V_∞ = 8.55 M/s; δ = 0.025 M; δ^* = 0.125 δ = 0.00313 M.

The data in Figure V2.1 through V2.4 are wavenumber estimates at various selected frequencies. Figure V2.1 shows the relative performance of the three spectral estimation techniques. The traditional Blackman-Tukey method (BT); the Maximum Likelihood Method (MLM); and the Covariance Constrained MLM (CCMLM). The BT estimate is dominated by a large main lobe and side lobe leakage from the acoustic peak located at $k = \pm \omega/c$ where c is the speed of sound in water. In Figure V2.1 the BT estimate cannot resolve the convective peak because of side lobe leakage. (The MLM estimate on the other hand shows a significant reduction in leakage from the acoustic peak clearly resolves the convective peak.) The CCMLM estimate further improves the fidelity in the low wavenumber regions, by approximately 12dB at this frequency. At higher frequencies, however, the CCMLM improvements over the MLM estimates become less pronounced. This results because the MLM is "doing a good job" with regards to matching the inverse Fourier transform of the estimate to the original Cross Spectral Density Matrix (CSDM).

A caution in using the CCMLM is that as the estimate approaches its error reduction limit, anomalous nulls (or very small spectral levels) start to show up in the measured spectrum (see Figure V2.3). It is also worth mentioning that although the MLM estimator is an upper bound of the true spectrum by design, the CCMLM is not, and it is possible for the estimate to be significantly below the true spectrum in a given region when nulling occurs.

The wavenumber spectra have been assumed to be predominantly one sided and the estimate is periodic about $k_s = \pi/D = 0.0158\ m^{-1}$. This assumption gives approximately a doubling in the range of wavenumber that can be utilized for a given sensor spacing. Figure V2.4 shows the CCMLM estimate (which in this case is the MLM estimate) just prior to the convective peak aliasing into the acoustic peak.

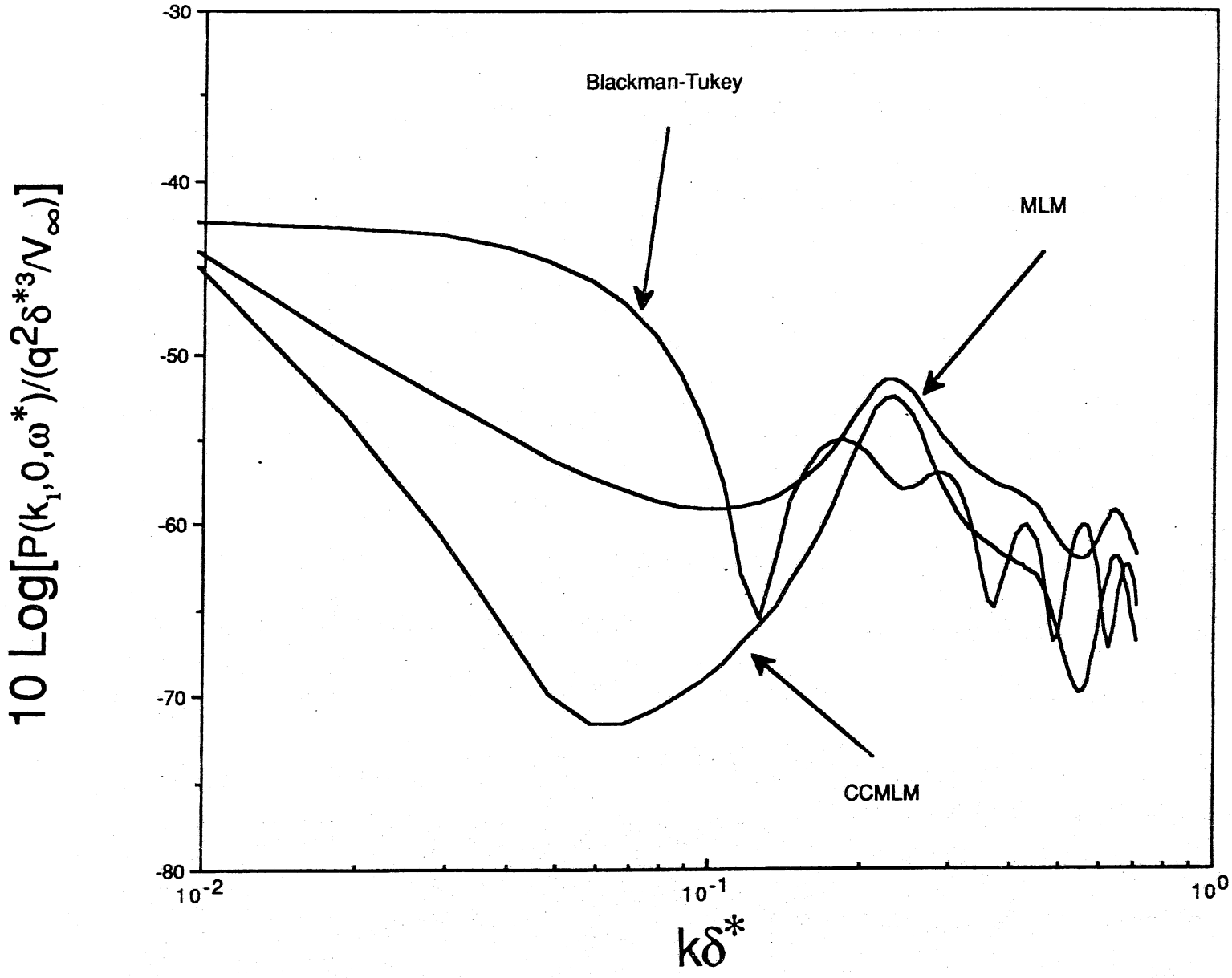

Figure V2.1. Comparison of the wavenumber-frequency spectra from the BT, MLM, and CCMLM estimators at $\omega^* = 0.19$, f = 84.5 hz.

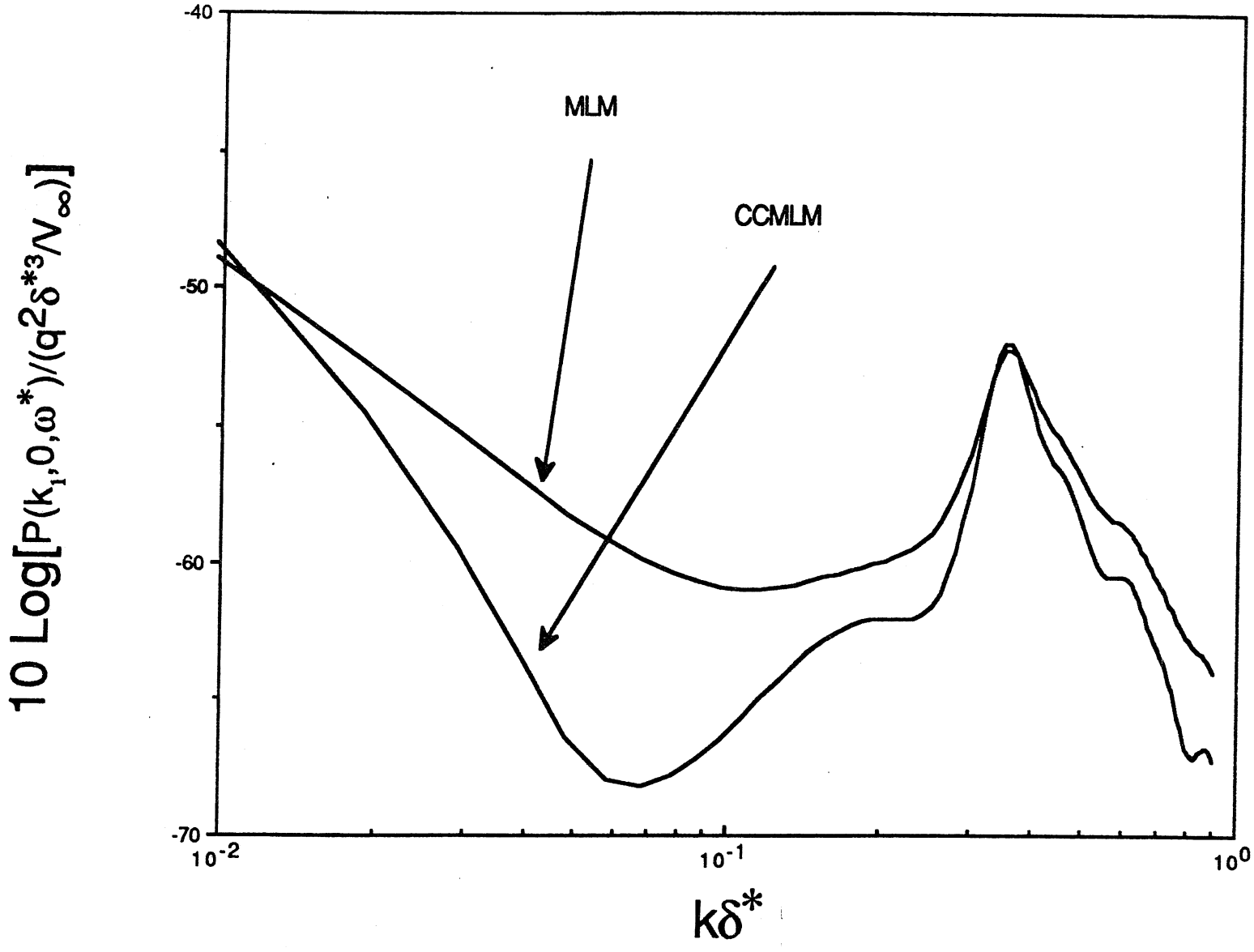

Figure V2.2. MLM and CCMLM spectral estimate at ω^* = 0.32, f = 140 hz.

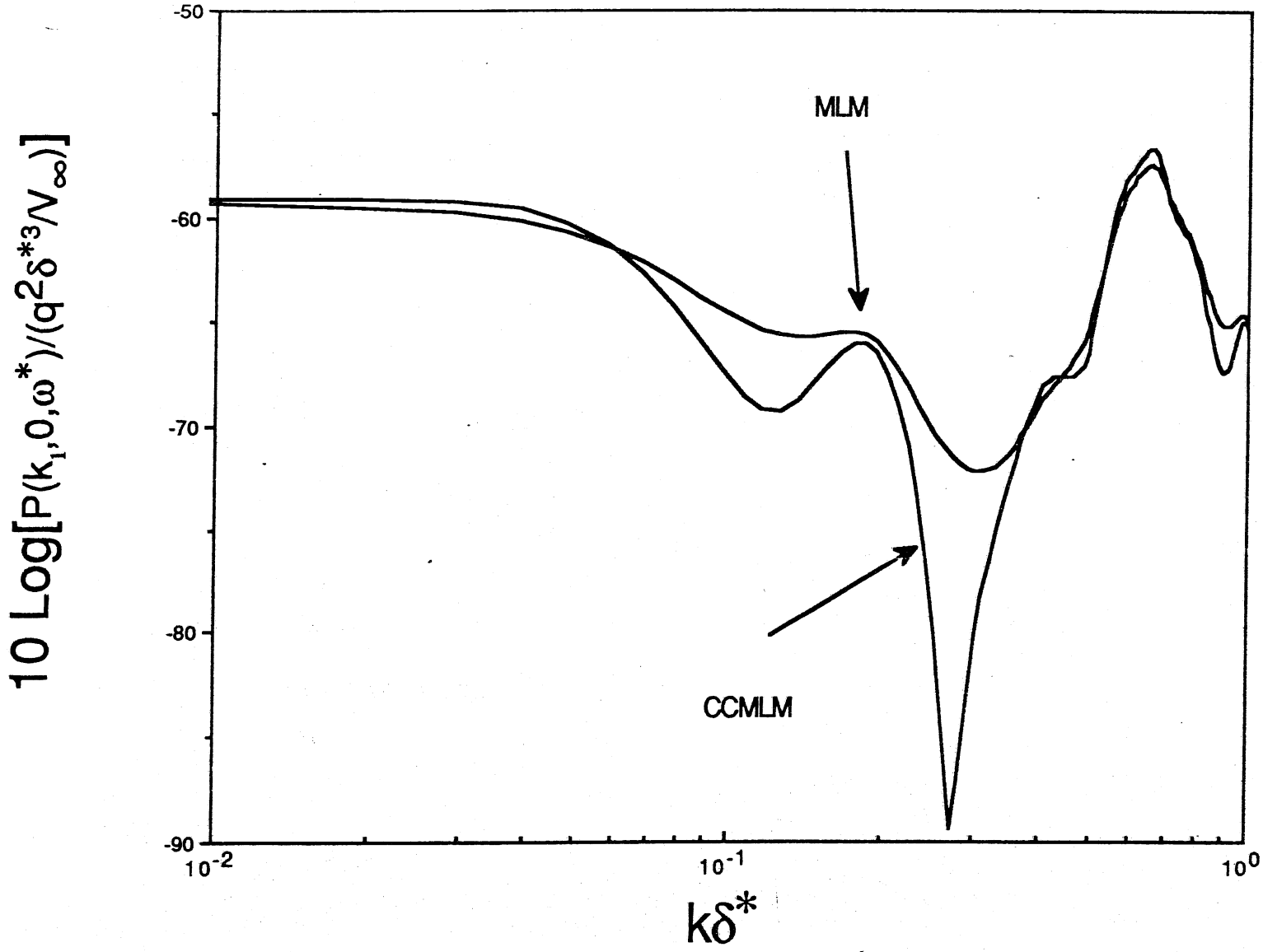

Figure V2.3. MLM and a nulling CCMLM estimate at ω^* = 0.58, f = 253 hz.

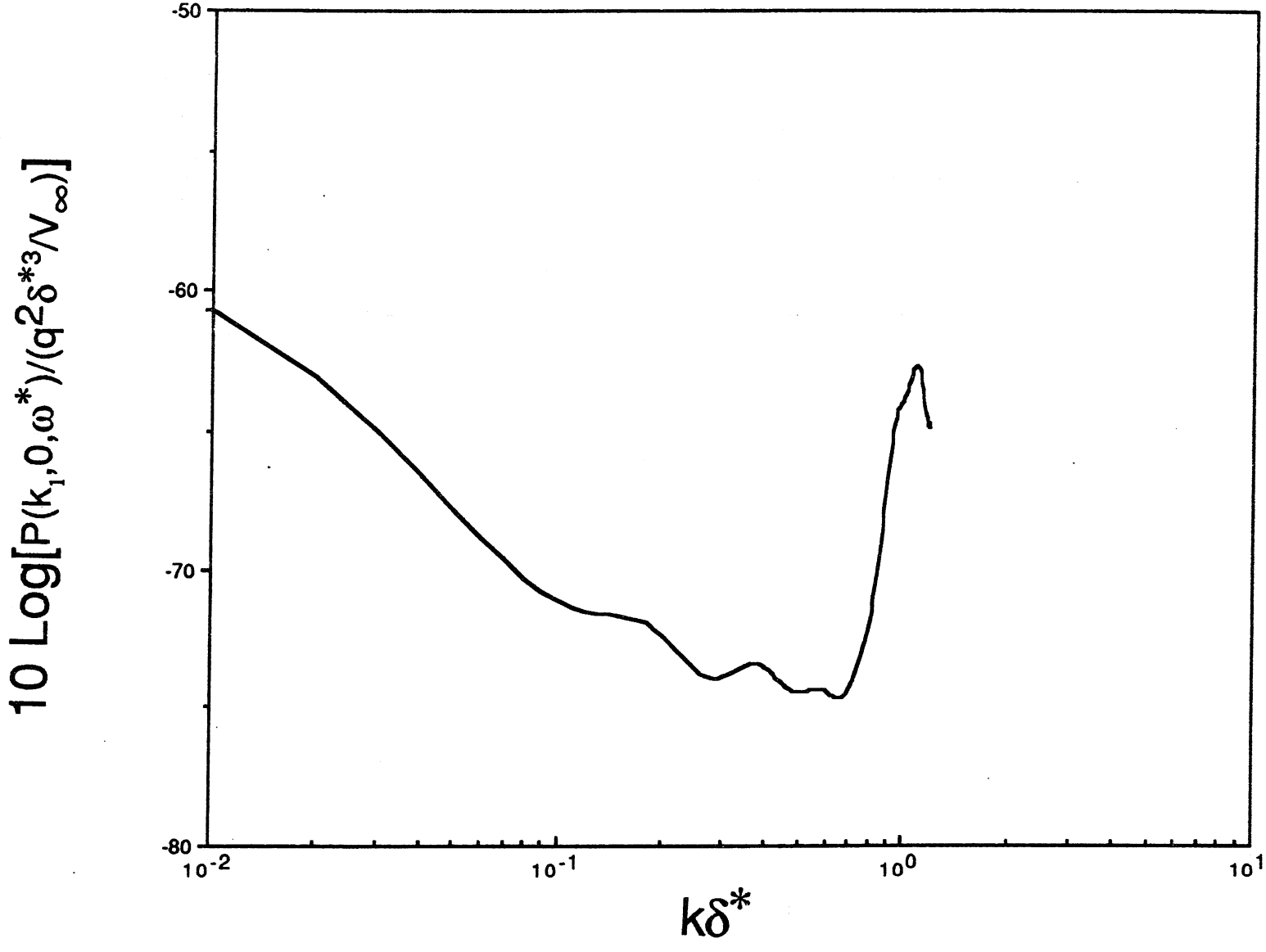

Figure V2.4. CCMLM estimate (which has converged to the MLM estimate) $\omega^* = 0.93$, f = 403 Hz.

The buoyant body facility, although lacking pump or turbine noise, was plagued with acoustic noise probably generated from the wake and amplified by the highly reverberant cylindrical structure of the buoyant body facility. Figure V2.5 shows the normalized auto power spectrum averaged over all sensors. The spectrum is dominated by acoustic energy below approximately $\omega^* = 0.3$. This can be verified by the phase spectrum of the first lag $\psi(\omega)$ shown in Figure V2.6. Note that the highly spatially correlated acoustic energy causes the phase to be nearly equal to zero below $\omega^* = 0.3$. The averaging effect of finite transducer size ($d^* = 3.0$) start coming into effect at frequencies greater than approximately $\omega^* = 1.0$, see Fig. V2.5. Although the data in V2.5 and V2.6 might be disappointing, there is no doubt that acoustic noise dominated the experimental results. However, it should be noted that the wavenumber estimates employing CCMLM distinguishes acoustic energy and turbulent energy to a certain extent. The limitation appears to be side lobe leakage. This is mentioned so that the data on the location of the convective peaks employed in Part B should not be discounted because of acoustic contamination, although the absolute levels of the peaks may have been affected somewhat because of the normalization and calibration techniques used.

Convective Waveguide Model-Wavenumber and Velocity Predictions

An effort was made early on in this research program to study and be cognizant of any possible wavenumber/frequency dispersion effects that could possibly be observed from spectral experiments in the buoyant body facility. It had been observed earlier that phase convective velocity measurements in wind tunnels did follow a characteristic in frequency that was dispersive. In fact, in both wind and water tunnels the phase velocity appeared to vanish at zero frequency, peak at some low frequency, and then level off at high frequencies at some fixed percentage of the mid-stream fluid velocity, usually between 0.6 and 0.8. If the peaks in the wavenumber/frequency spectrum, which lie on the convective ridge, could be observed with some fidelity, then any dispersive effects in the buoyant body facility also could be validated.

Narayan and Plunkett observed from phase measurements in a water tunnel that the convective phase velocity did appear to peak at low frequencies and then level off at higher frequencies at about 0.6 of the free stream velocity (see Fig. 21 in TR-AEM-85-1-RP dated 14 February 1985). A similar observation in a wind tunnel had been made by Blake, and his data taken at values of $\tilde{\omega} = \omega\delta^*/V_\infty \leq 0.50$ exhibited a peak and a definite trend towards zero (see Journal of Fluid Mechanics, 44, 1970, pp. 637-660). Blake's data are reproduced in Fig. V2.7, attached.

In order to help understand these and related phenomena, a set of nine internal memoranda were prepared, of which the last five (V thru IX) are appended to this report (Appendix B). The first four tracts were concerned with measurement techniques and data reduction methods, including such topics as frequency corrections for finite transducer size.

Tract V titled "Estimate of the Low Frequency Power Spectrum of Wall Pressure Fluctuations" details some of the basic ideas in what is herein referred to as a convective waveguide model. It starts with a review of

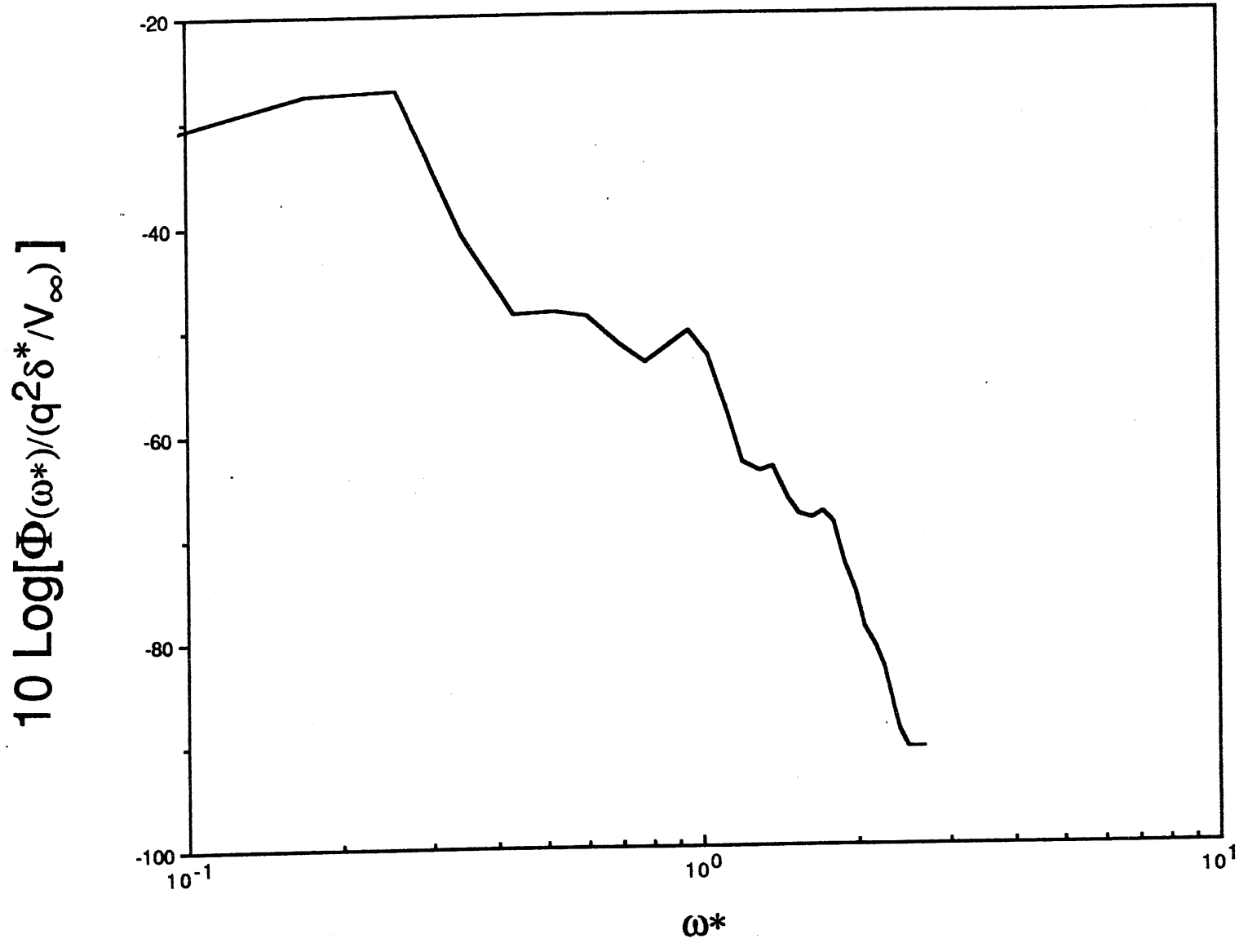

Figure V2.5. Normalized power spectrum showing acoustic contamination below $\omega^* = 0.3$ and finite transducer averaging effects above $\omega^* = 1.0$.

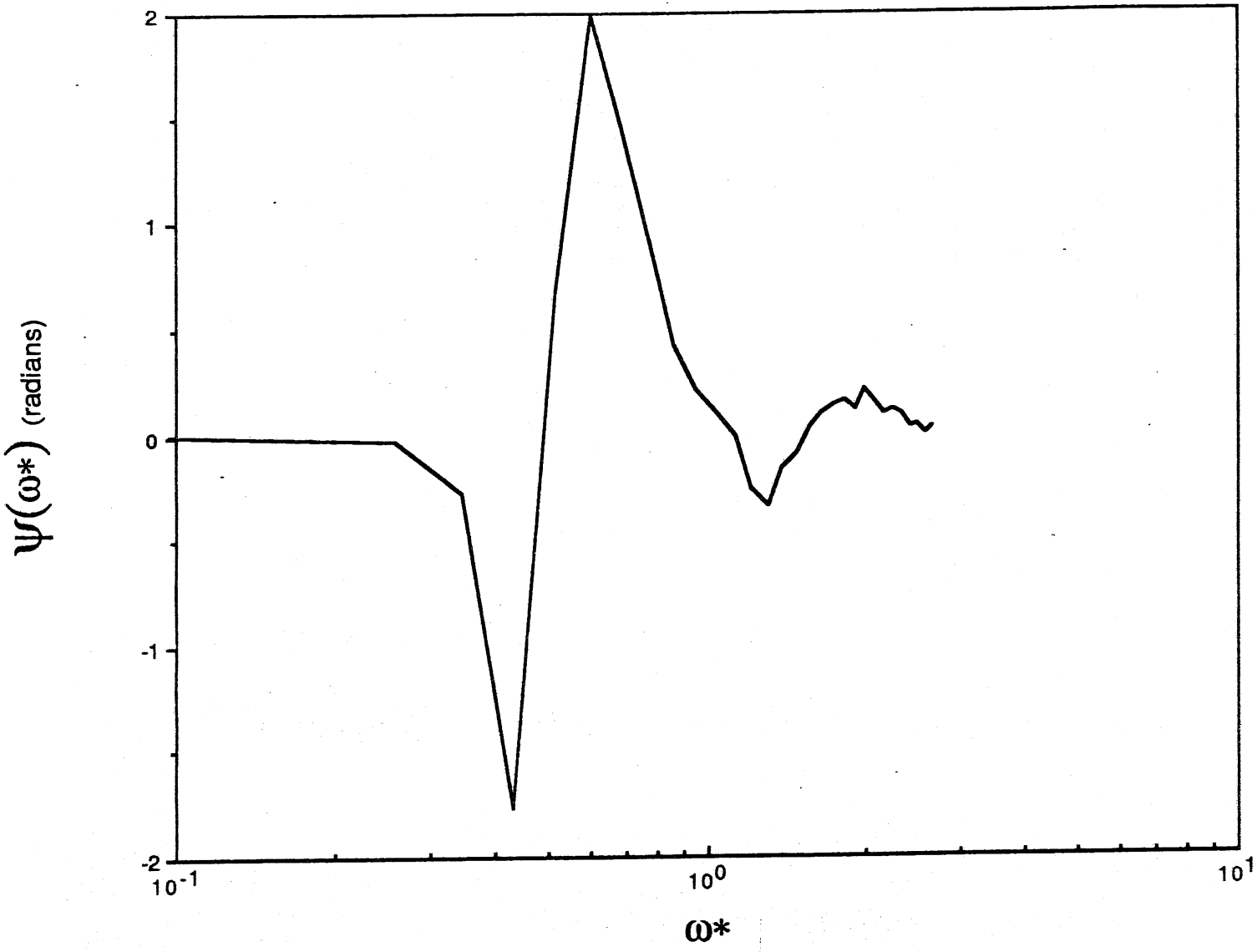

Figure V2.6. Phase spectrum $\psi(\omega^*)$ of the cross spectrum for the first sensor lag. D = 0.16 M, D^* = 5.06, d = 0.095 M, d^* = 3.0.

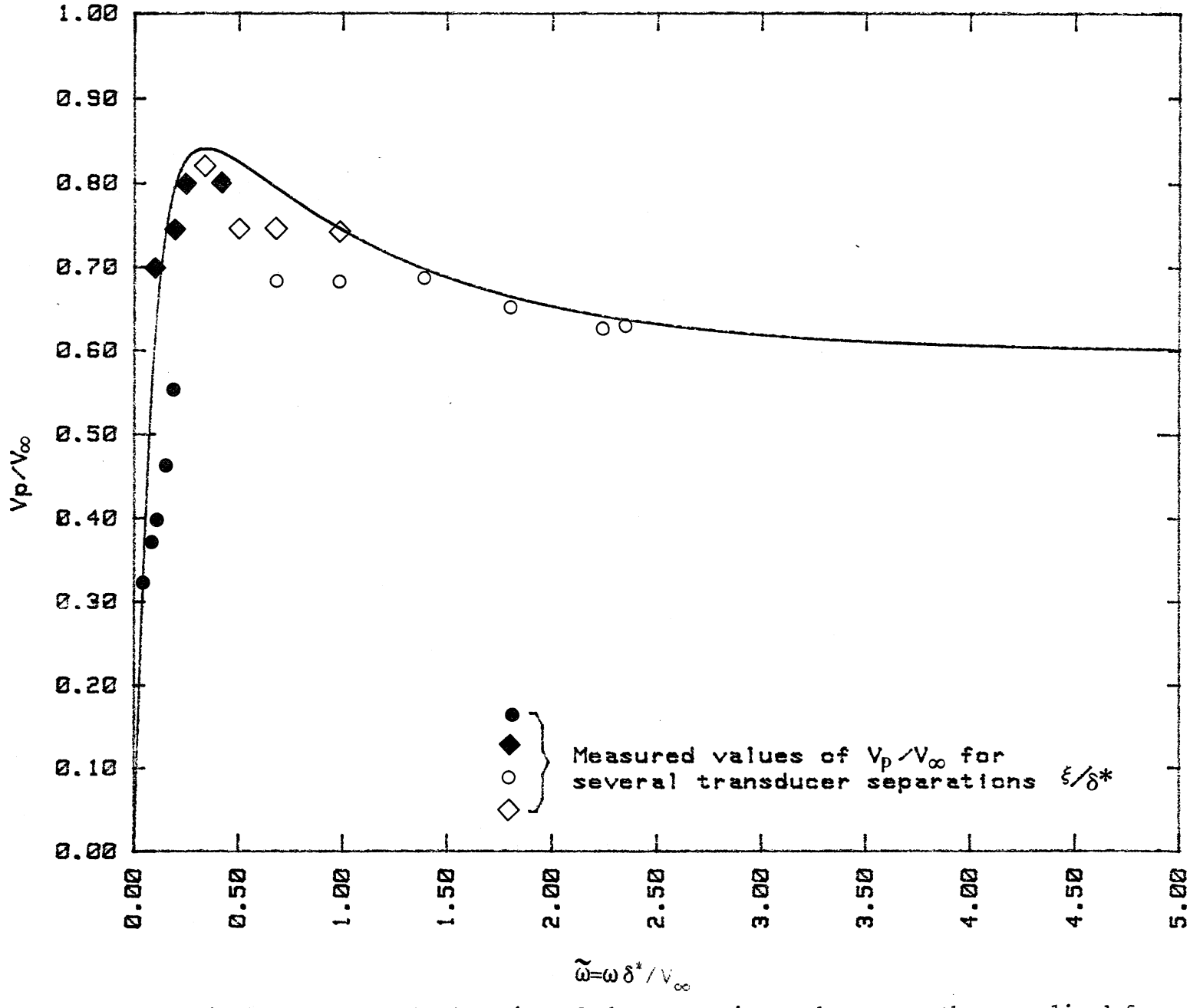

Figure V2.7. Experimental plot of the location of the convective peaks versus the normalized frequency $\tilde{\omega}$ for the buoyant body facility. The solid line is a fit of Eqs. 5 and 7 for the parameters given in the legend.

some ideas embodied in the Kolmogoroff Theory of Turbulence as interpreted and explained by G. K. Batchelor in his monogram. The waveguide model was developed on the hypothesis that in an experiment of finite dimensions (such as in a water tunnel or buoyant body facility) the wavenumber spectrum would actually cut-off below some finite value of wavenumber, k_o, greater than zero. This was based on the intuitive idea that eddies above a certain size (or below a certain wavenumber) were too large to be convected by an incompressible fluid. Since water has some compressibility, however small, there probably would not be a sharp cut-off or cut-on as the case may be, but rather the phenomena would occur gradually as the observed frequency is reduced.

As outlined in tract V, this development led to a rather simple relationship between frequency ω and wavenumber k of the form

$$\omega^2 = V_c^2 (k^2 - k_o^2) \qquad k \geq k_o \tag{1}$$

where V_c is called an eddy convection velocity and the cut-on wavenumber

$$k_o = \frac{\omega_o}{V_c} = \frac{1}{\Delta} \tag{2}$$

where $2\pi\Delta$ is the perimeter of the largest eddy in the guide. In the absence of better information it was decided to set $\Delta = \delta$ where δ is a boundary layer thickness defined in the usual way. The parameter V_c still is interpreted as an eddy convection velocity but not a phase velocity and hence is unobservable directly from phase measurements (except perhaps at very high frequencies).

However, the observed phase velocity

$$V_p \equiv \frac{\omega}{k} = \frac{V_c}{\sqrt{1 + \frac{\omega_o^2}{\omega^2}}} \tag{3}$$

is well-defined.

In terms of normalized variables, Eq. 3 can be rewritten as

$$\frac{V_p}{V_\infty} = \left(\frac{V_c}{V_\infty}\right) \frac{\tilde{\omega}}{\left[\tilde{\omega}^2 + \left(\frac{\delta^*}{\delta}\right)^2 \left(\frac{V_c}{V_\infty}\right)^2\right]^{1/2}} = \begin{cases} \left(\frac{V_c}{V_\infty}\right), & \tilde{\omega} \to \infty \\ 0, & \tilde{\omega} \to 0 \end{cases} \tag{4}$$

a form that requires knowledge of how V_c/V_∞ varies with frequency and a numerical value for δ^*/δ where δ^* is the displacement boundary layer thickness and where $\tilde{\omega} = \omega\delta^*/V_\infty$. If V_c/V_∞ = constant, then Eq. 4 predicts that V_p/V_∞ will increase from zero and gradually approach the value $V_p = V_c$ as $\tilde{\omega}$ is increased. However, Blake's data and the data of Narayan and Plunkett reveal a peak in the V_p/V_∞ characteristic at some low value of $\tilde{\omega}$ which requires a V_c/V_∞ also to vary with $\tilde{\omega}$. By trial it was determined that a choice for V_c/V_∞ of the form

$$\frac{V_c}{V_\infty} \simeq \left(\frac{V_p}{V_\infty}\right)_\infty + \left[1 - \left(\frac{V_p}{V_\infty}\right)_\infty\right] e^{} = \begin{cases} \left(\frac{V_p}{V_\infty}\right), \tilde{\omega} \to \infty \\ 1 \ , \tilde{\omega} \to 0 \end{cases} \tag{5}$$

would provide a satisfactory fit of the V_p/V_∞ characteristic, Eq. 4, to observed phase velocity data. Here $(V_p/V_\infty)_\infty$ = constant is the asymptotic value of V_p/V_∞ observed at high frequencies. Figure V2.7 shows a fit of Blake's data for the choice $(V_p/V_\infty)_\infty = 0.60$. Note Eqs. 4 and 5 also predict a peak in V_p/V_∞ of about 0.83 at $\tilde{\omega} \simeq 0.30$ is almost in exact agreement with Blake's measurements. This was the first indication that the convective waveguide model could be validated.

The data of Narayan and Plunkett also reveal a similar peak of about the same value at certain measurement distances. However, they did not normalize their frequency scale so a direct comparison was not made.

Further properties of the convective waveguide model were then developed and of special note is a suggested experiment in Appendix B of tract VIII. As noted there, the convective waveguide model predicted that the longitudinal wavenumber/frequency power spectrum $P(k_1, 0, \omega)$ would exhibit a peak at the wavenumber value k_p given by

$$k_p = \sqrt{\left(\frac{\omega}{V_c}\right)^2 + \frac{1}{\delta^2}\left(\frac{V_\infty}{V_c}\right)^2} \tag{6}$$

or in terms of normalized variables

$$k_p \delta = \left(\frac{V_\infty}{V_c}\right)\sqrt{1 + \left(\frac{\delta}{\delta^*}\right)^2 \tilde{\omega}^2} = \begin{matrix} \left(\frac{\omega}{V_c}\right)\delta, \tilde{\omega} \to \infty \\ 1 \ , \tilde{\omega} \to 0 \end{matrix} \tag{7}$$

Note Eq. 7 predicts that $k_p \to 1/\delta$ as $\tilde{\omega} \to 0$ and $k_p \to \omega/V_c$ as $\tilde{\omega} \to \infty$ by employing Eq. 5. Thus, the convective waveguide model exhibits a form of frequency dispersion not found in other theoretical formulations.

The suggested experiment was to isolate the peaks in the $P(k_1, 0, \omega)$ spectrum characteristic as accurately as possible and then plot k_p versus ω in order to see if the resulting dispersion characteristic did indeed

follow Eq. 7 and cutoff as predicted. It was felt that information about the location of peaks in the convective ridge of the longitudinal wavenumber/frequency spectrum would be the best information about the model that could be obtained even before the experiments were conducted. It was also felt that other critical information about the $P(k_1, 0, \omega)$ characteristic would be masked by acoustic background noise.

The suggested experiment was performed in the buoyant body facility and the peaks plotted as a function of frequency, see Fig. V2.8. It was decided to use a nominal value of $\delta^*/\delta = 0.125$ in the absence of experimental data on the actual boundary layer profile. The data of Fig. V2.8 approach a cutoff wavenumber $k_o = 40\ m^{-1}$ as ω tends to zero via empirical fits of either Eq. 6 or Eq. 7. This result then yields a value of $\delta = 0.025$ cm for the boundary layer flow over the buoyant body in the region where the spectral measurements were made. This value is about 2.5 times the thickness expected on the basis of discussions heretofore.

The high frequency data in Fig. V2.8 also reveals a value of $V_c/V_\infty = 0.80$ using a measured value of $V_\infty = 8.55$ m/s for the speed of the buoyant body.

A predicted dispersion diagram plotting ω versus κ is shown in Fig. V2.9. Two curves are plotted for comparison purposes, one showing a plot of $\omega = V_c k$ based on Eq. 5 (dotted line) and the other showing ω versus k based on Eqs. 1 and 7 revealing a sharp cut-on at $k = k_o$. The characteristics are based on empirical data for the buoyant body.

Finally, a predicted V_p/V_∞ characteristic based on this empirical information for the buoyant body is plotted in Fig. V2.10. There exists a predicted peak of about 0.9 that occurs at $\tilde{\omega} = 0.30$ which is in fair agreement with the work of others. Note, however, the predicted high frequency asymptote $(V_p/V_\infty)_\infty = 0.80$ which is somewhat higher than usually observed in wind tunnels and in the water tunnel data of Narayan and Plunkett.

Various other theoretical predictions based on a convective waveguide model were made in tracts V-IX. Of note are predictions of power spectrum in tract V and an estimate of the low wavenumber/frequency spectrum in tract VI. All of the numerical work in tracts V-IX was based on empirical information obtained from wind tunnel data. The various characteristics would have to be recomputed in order to make comparisons with either water tunnel or buoyant body spectrum measurements especially in view of the thicker boundary layer. Values of δ and δ^* influence most of the numerical predictions.

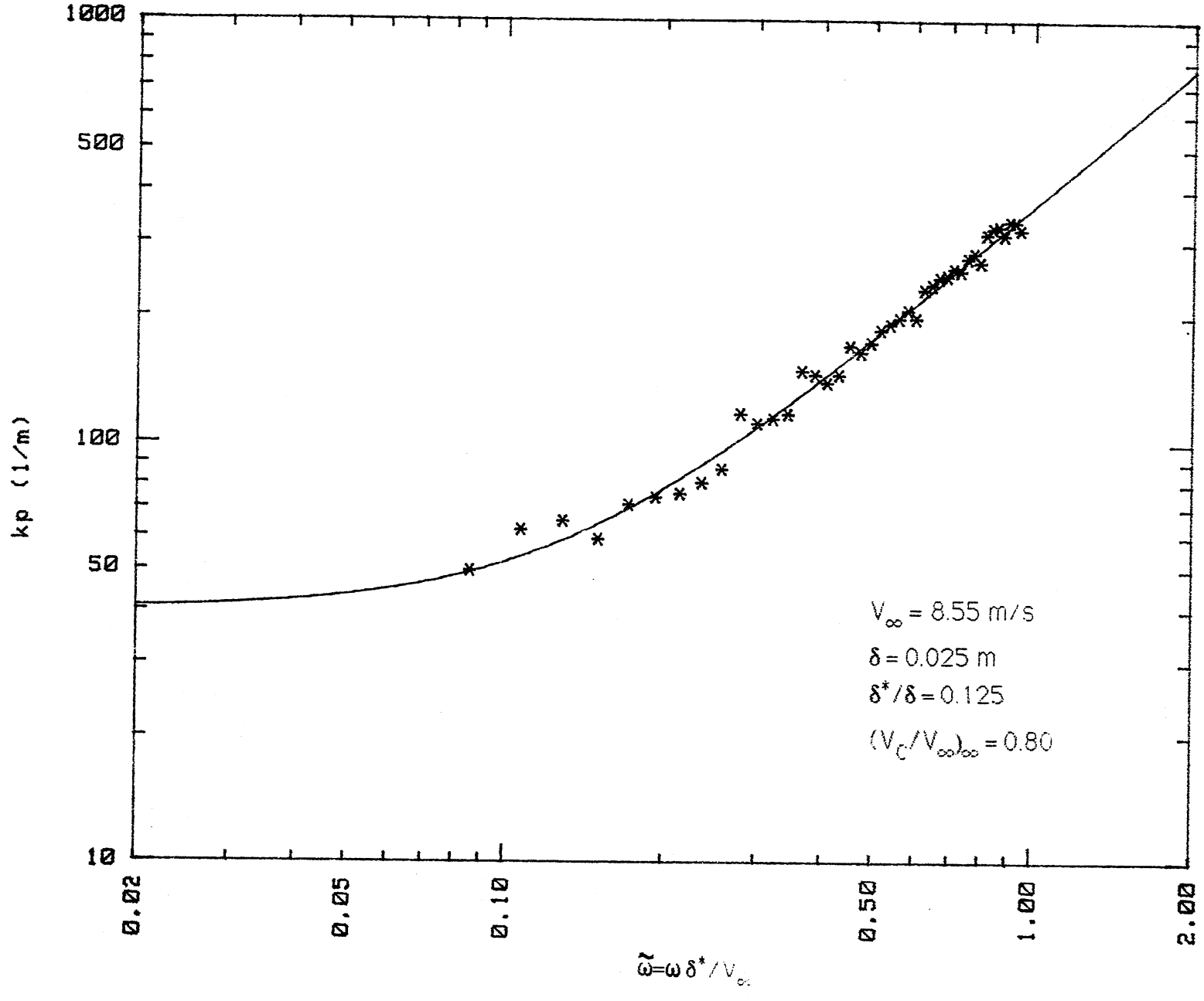

Figure V2.8. Comparison of the phase-speed prediction, Eq. 4, with experimental data of Blake.

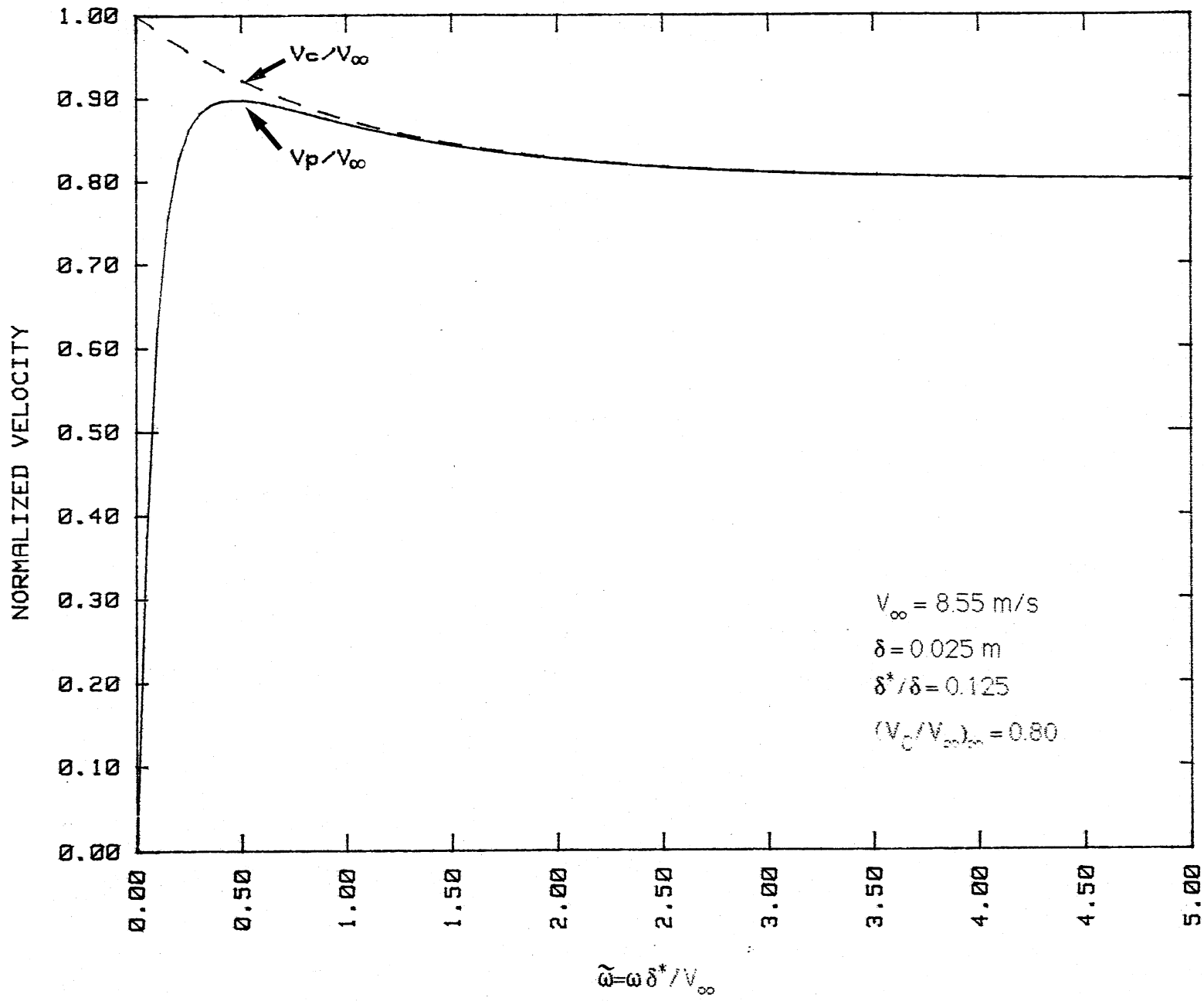

Figure V2.9. Predicted phase speed characteristic for the buoyant body based on Eqs. 4 and 5 employing parameters given in the legend.

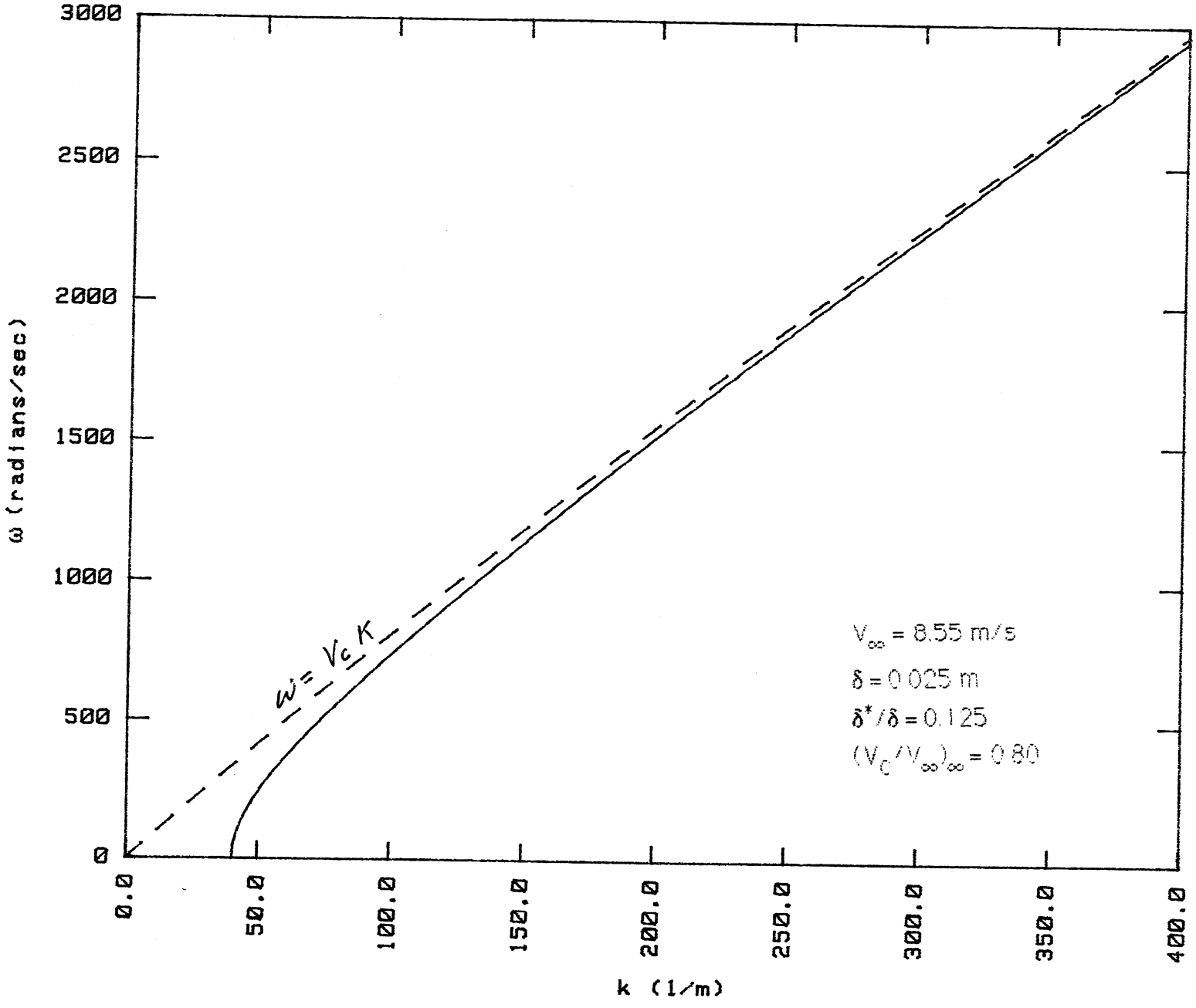

Figure V2.10. Predicted wave dispersion characteristics shown by solid line based on Eq. 1 for the buoyant body and the equation $\omega = V_c k$ based on Eq. 5 as shown by the dotted line. Note the dotted line is not a straight line.

3. Structural Response to Pressure Fluctuation

R. Plunkett, Principal Investigator

Introduction

The major purpose of this project was to investigate the validity of the assumptions which underlie the weighted integral approach which is now used to calculate the vibration response of water loaded plates subjected to turbulent boundary layer excitation. The most important assumption is that the plate vibration has so little effect on the turbulent boundary layer that the power spectral density (spectrum) of the pressure field on the wall is affected only to a negligible extent. The second major assumption is that the plate response is linear so that a superposition can be used.

These two assumptions are sufficient to establish the integral equation for the cross spectrum of the vibration response of the plate (Lin, 1967).

$$S_{vv}(x_1,x_2;\omega) = \int_A \int_A H^*(x_1,\rho_2;\omega)H(x_2,\rho_2;\omega)\Gamma(\rho_1,\rho_2;\omega)dA(\rho_1)dA(\rho_2) \quad (12)$$

where $\Gamma(\rho_1,\rho_2;\omega)$ is the cross spectrum of the normal pressure exerted by the boundary layer on the non-vibrating plate.

$H(x,\rho;\omega)$ is the response of the plate of x due to a unit sinusoidal force at ρ .

and $S_{vv}(x_1,x_2;\omega)$ is the cross spectrum of the response.

Tack and Lambert (1962) have demonstrated that this approach accurately predicts the vibration level for a narrow beam in air exposed to a turbulent boundary layer in a wind tunnel. Most of the papers in the open literature are concerned with ways of approximating H and Γ so as to make the integration relatively simple (Powell, 1958; Chandirimani, 1977). Our primary objective was to compare the measured response spectrum of a flat plate with that predicted from the measured cross spectra of the pressure field and the measured response functions of the plate. In this way, for at least one case, we will be able to determine what the controlling variables are and what accuracy is necessary in the two cross functions to obtain acceptable accuracy for the vibration level.

Work on this project has been reported in previous progress reports (Arndt, 1985). Up to November 1, 1985, the pressure cross spectrum was

measured and preliminary results were obtained for the vibration autospectrum. Since then, vibration cross spectra have been measured for the vibrating plate, the pressure cross spectrum has been measured upstream and downstream of the vibrating plate, and the boundary layer velocity profile has been measured. All of this work is now being written for a thesis in partial fulfillment of a Ph.D. for N. Narayan. The work remaining to be done is the actual calculation of the predicted PSD for the vibration, its comparison with the measured values, and the preparation of the thesis in its final form. When that is finished, the major results will be embodied in papers to be submitted to serial journals in the open literature.

Experimental Techniques

All of the measurements were made in the 7.5 inch square low noise water tunnel of the St. Anthony Falls Hydraulic Laboratory. Pressure spectrum measurements were first made on the surface of the thick plexiglass ceiling of the tunnel. The measured vibration levels in this wall were so low that the voltage induced in the pressure transducers by the vibration contributed less than 1% (- 40 dB) to the measured pressure levels. The pressure transducers were held in rotatable holders so that the cross spectra could be measured for a grid of pairs of points covering 180 mm axial separation and 50 mm transverse. The results were reported in an ASME symposium volume (Narayan and Plunkett, 1985).

The roof of the tunnel was then modified to take a stainless steel plate 200 mm long by 40 mm wide and 1.2 mm thick. The plate was backed by a chamber filled with air and pressurized to the static pressure of the tunnel. Five accelerometers were mounted on the back of the plate to measure the vibration cross spectra on the centerline for axial separations. Pressure transducers were mounted just upstream and just downstream of the vibrating plate to determine if the plate vibration affected the pressure cross spectra. Measurements were made at flow velocities of 7, 9, 12, and 15 m/sec.

The dynamic response functions from 50 to 2000 Hz were measured for the plate mounted in the ceiling separator in air, in a static water tank, and in the water tunnel by exciting each of the five accelerometer mounting points sinusoidally through a mechanical vibration impedance head. The mode shapes and natural frequencies were deduced from the response functions. The first five mode shapes had no longitudinal nodes and from zero to four transverse nodes. The water loaded frequencies ranged from about 460 Hz to 1500 Hz which agreed reasonably well with the predicted values when the edge fixities were suitably adjusted. The entrained water mass loading had about one third the effect of the accelerometer mass so that there was not much difference between the air and water loaded frequencies. The amplification factor at resonance (a measure of damping) was about 10 to 20 for the air loaded system and about 3 to 5 for the installation in the water tunnel.

Results

The velocity profile in the boundary layer was measured with a dynamic pressure probe which had a rectangular opening 0.2 mm high by 4 mm thick and a ground down lip thickness of 0.02 mm. The probe was traversed from just touching the wall to 39 mm away. A plot of the measured points at a free stream velocity of 3.8 m/sec is shown in Figure V3.1 along with the predicted profile based on the 1/7th power law.

There was negligible difference (usually less than 1 dB) for the auto and cross spectra measured just upstream and just downstream of the vibrating plate. The plate vibration level was about 0.01 of the boundary layer thickness.

The general characteristics of the plate vibration acceleration response autospectrum (Fig. V3.2) is a rather smooth curve falling about 20 dB from 100 Hz to 2500 Hz with two peaks at 750 Hz (3rd mode) and 1500 Hz (5th mode). The peaks rise about 10 dB above the general trend. Subject to verification in detail, the general response seems to be caused by the reverberant acoustic field and the two peaks are caused by the convected turbulent field.

The transverse cross correlation pressure field among the three pressure pickups in each of three positions (two upstream and one downstream) showed a much greater correlation length with the fixed pickups than had been measured before with the transducers in the rotatable holders. With no axial separation the correlation length for $y^* = \omega y/U_c$ was about 0.6 for the measurements made with the rotatable holders. It is about 2 for the fixed transducers. These new results make it possible to fit the dimensionless cross spectrum with a function of the form:

$$\Gamma(x,y,;\omega) = \Gamma_1(0,0;\omega)\Gamma_2(x^*,0)\Gamma_3(0,y^*)$$

where $\Gamma_2 = \exp(-\alpha x^{*2})$ and $\Gamma_3 = \exp(-\beta y^{*2})$

$\alpha = 0.0070$; $\beta = 0.183$;

and $x^* = \omega x/U_c$, $y^* = \omega y/U_c$.

Corcos (1964) had suggested a similar expression with $|x^*|$ and $|y^*|$ instead of the quadratic terms. The difference is most pronounced for small values of x^* and y^* ; a careful examination of our short distance data does not show the linear falloff that would be necessary for the absolute value formulation. His formulation has the added disadvantage of being difficult to deal with analytically. While it would be possible to improve the fit slightly by having some interaction between the axial (x^*) and transverse (y^*) dimensionless coordinates, the results are within the margin of experimental error. This is in contrast to the conclusions drawn in the earlier report (Narayan and Plunkett, 1985) where a substantial interaction was found because of the very short transverse correlation length at zero axial distance. We do not yet have a reasonable explanation for this discrepancy but assume it is caused by the slight steps on the edges of the rotating holders.

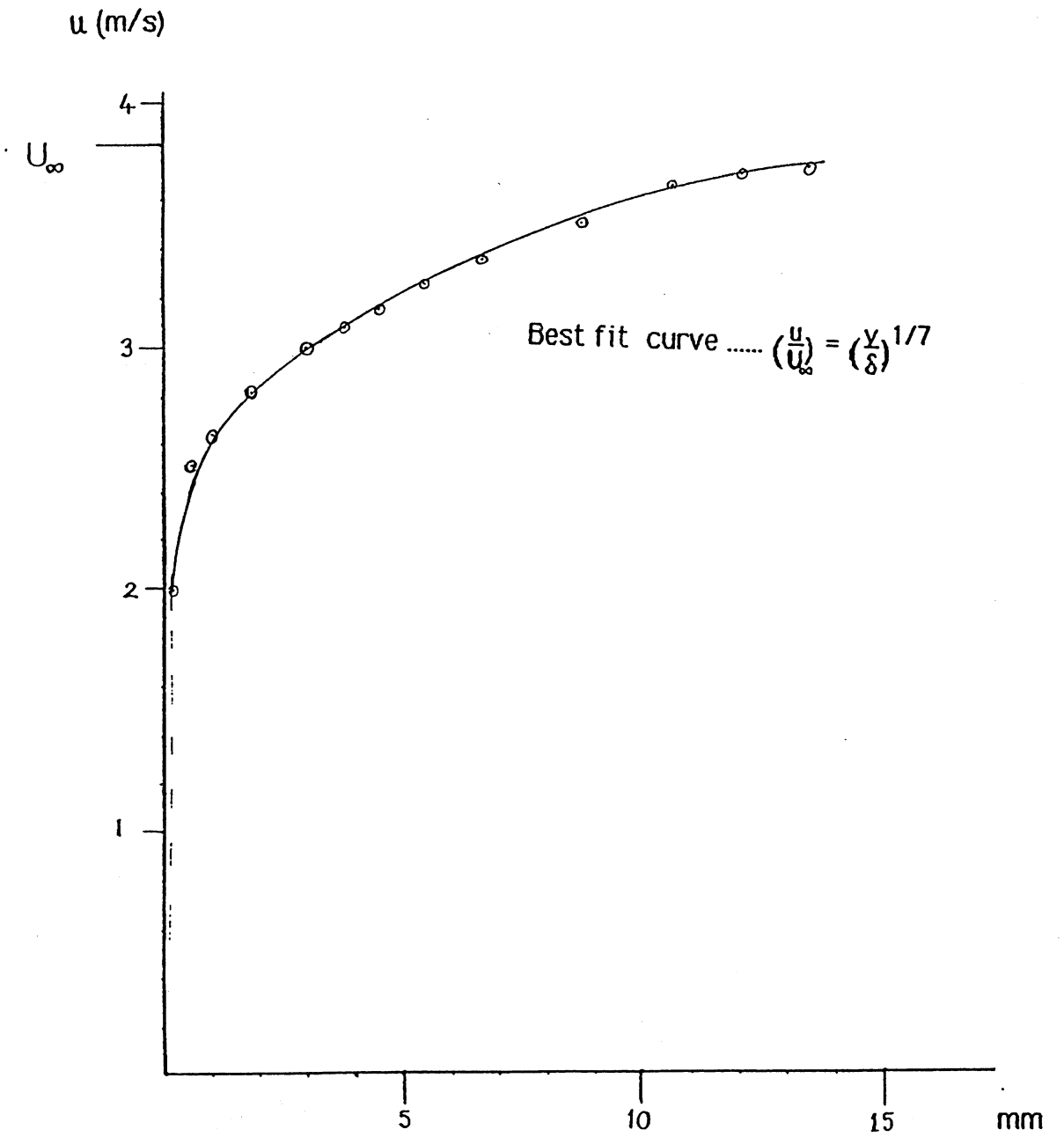

Figure V3.1. Boundary layer velocity profile (u vs. y). Free stream velocity = 3.8 m/s.

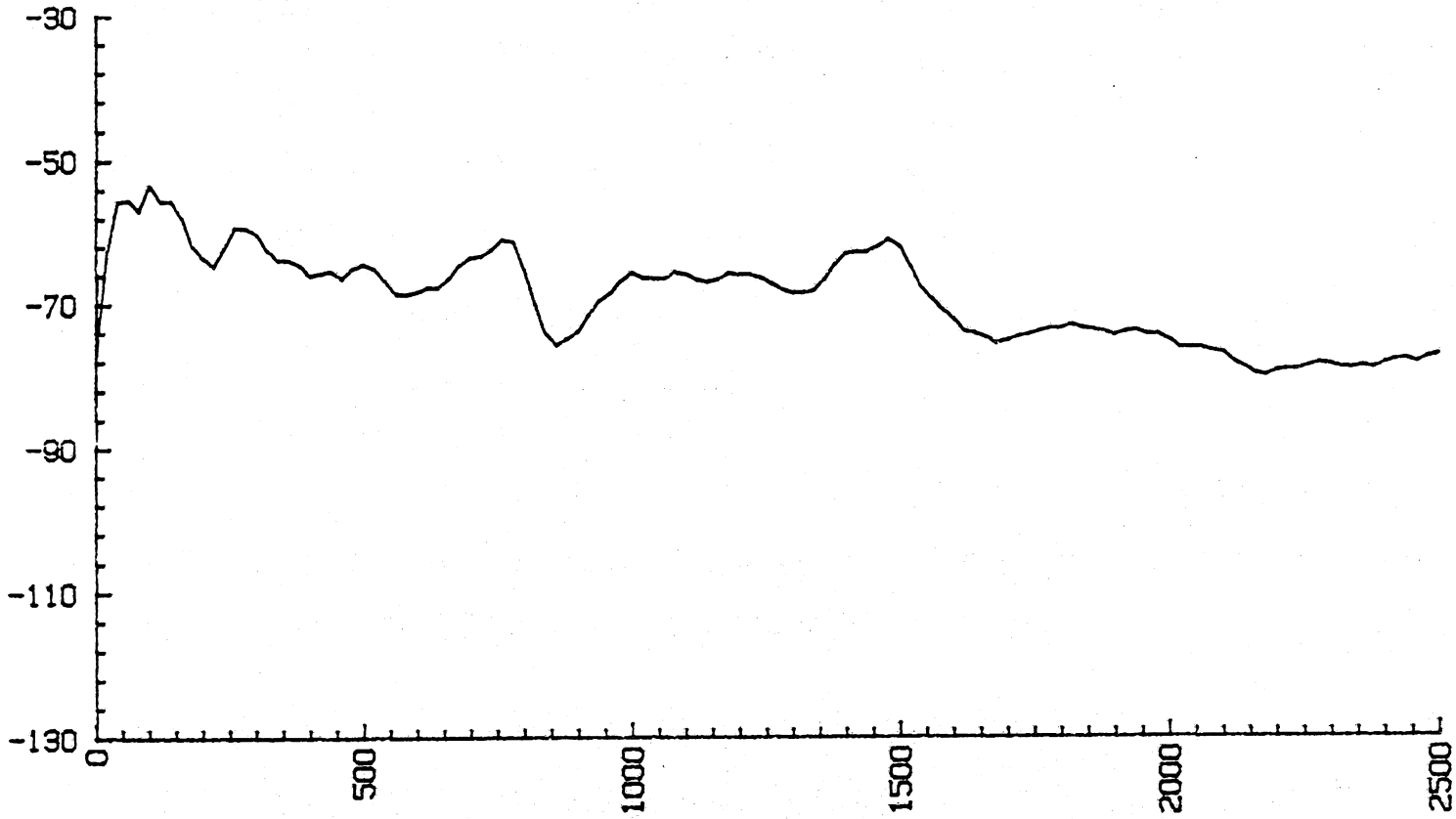

Figure V3.2. Plate vibration response autospectrum.

Current Status

All of the experimental work has been completed. All of the auto and cross spectra for both pressure and acceleration have been reduced. The predicted vibration cross spectra are being calculated from the dimensionless pressure spectra and the measured plate response functions. When this is completed, the results will be compared with the measured vibration cross spectra.

The thesis is being written at the same time. When that is completed, the results will be put into the form of published papers in the open literature.

References

Arndt, R.E.A., "End-of-the-Fiscal-Year Letter for FY 1985," Contract No. N00014-83-K-0145, November 1, 1985.

Chandirimani, K. L., "Vibration Response of Fluid Loaded Structures to Low Speed Flow Noise," JASA, 61, 1977, pp. 1460-1470.

Corcos, G. M., "The Structure of the Turbulent Pressure Field in Boundary Layer Flows," Jour. Fluid Mechanics, 18, 3, 1964, pp. 353-378.

Lin, Y. K., Probabalistic Theory of Structural Dynamics, McGraw-Hill, 1967, equation 7-14.

Narayan, N. and R. Plunkett, "Pressure Cross Spectra in Turbulent Boundary Layers in Water," in Shear Flow-Structure Interaction Phenomena, A. Akey and M. Reischman eds., NCA, Vol. 1, ASME, 1985, pp. 97-103.

Powell, A., "Response of Structures to Random Pressures," Chap. 8, Random Vibration, S. H. Crandall, ed., MIT Press, 1958.

Tack, D. H. and R. F. Lambert, "Response of Bars and Plates to Boundary-Layer Turbulence," Jour. Aerospace Science, 29, 3 March 1962, pp. 311-322.

4. Tip Vortex Cavitation and Noise

Roger E.A. Arndt & H. Higuchi Principal Investigator

Introduction

The tip vortex research program was broken down into three basic components: a) measurement of cavitation inception and fully developed cavitation characteristics, b) measurement of noise due to cavitation, and c) LDV measurement of the velocity field, construction of a semi-empirical model of a trailing vortex and estimation of the pressure within the core. Four different facilities were used in the experimental program. Cavitation and noise were studied in a low noise recirculating water tunnel, velocity measurements were made in a second water tunnel, dye studies were carried out in a flume, and oil film studies were carried out in a wind tunnel. The objectives of the study were: to determine the vortex roll-up process and the minimum pressure in the vortex, to relate the measured minimum pressure to cavitation observations and, finally, to determine the amplitude and spectral characteristics of the noise signal and relate it to the fluid mechanical aspects of tip vortices.

Experimental Procedures

Cavitation inception and noise were studied in a high speed water tunnel having a test section with a 190 mm square cross section, 1250 mm in length. The experimental set up is shown schematically in Fig. V4.1. The top wall of the test section was adjusted to produce zero axial pressure gradient.

Hydrofoils having an elliptic planform and an aspect ratio of 3.0 were the test bodies. Two different cross sections were studied. The bulk of the investigation utilized a hydrofoil with a NACA 66_2-415 cross section. This shape was selected to produce tip vortex cavitation in the absence of surface cavitation. A second hydrofoil having a 66-012 cross section was utilized to study surface cavitation in the absence of tip vortex cavitation. A comparison of the cavitation characteristics of the two hydrofoils is shown in Figure V4.2.

The acoustic signature was monitored by four Brüel & Kjaer (B & K) model 8103 hydrophones (nominal sensitivity -211dB re 1 V/Pa) positioned in a stagnant water chamber separated from the test section by an almost acoustically transparent wall. The positioning of the hydrophones is also shown in Fig. V4.1. The signals from the individual hydrophones were simultaneously digitized at 2 MHz per channel by a Nicolet model 4094 four-channel digital oscilloscope with a disk drive. The data were stored on disks and were analyzed in an on-lin HP9836A micro computer. The digital oscilloscope was set to capture the single noise events corresponding to either cavitation inception or continuous cavitation noise. An HP digital wave form analysis program which includes a standard fast Fourier transform

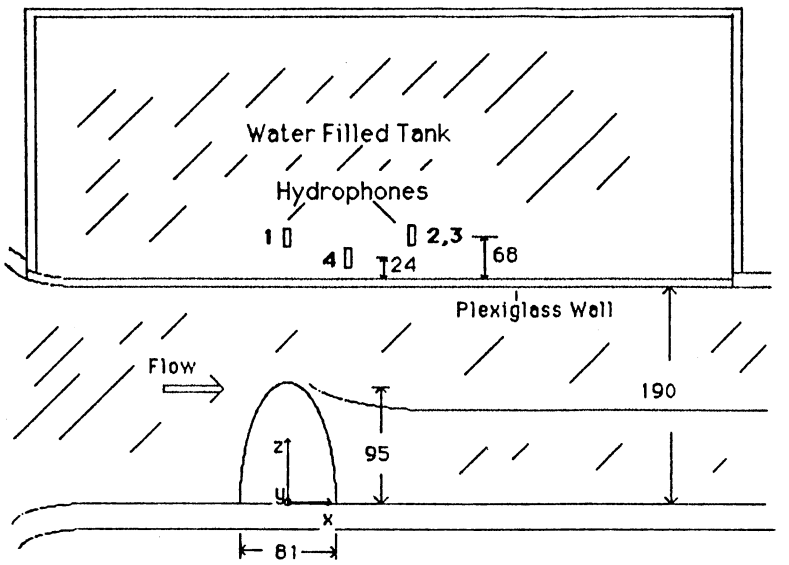

Side View

(All Dimensions are in mm)

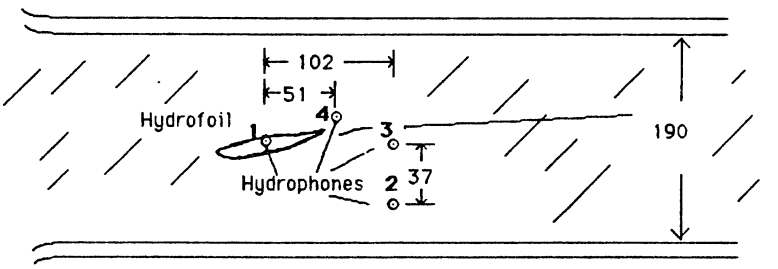

Top View

Figure V4.1. Experimental set up.

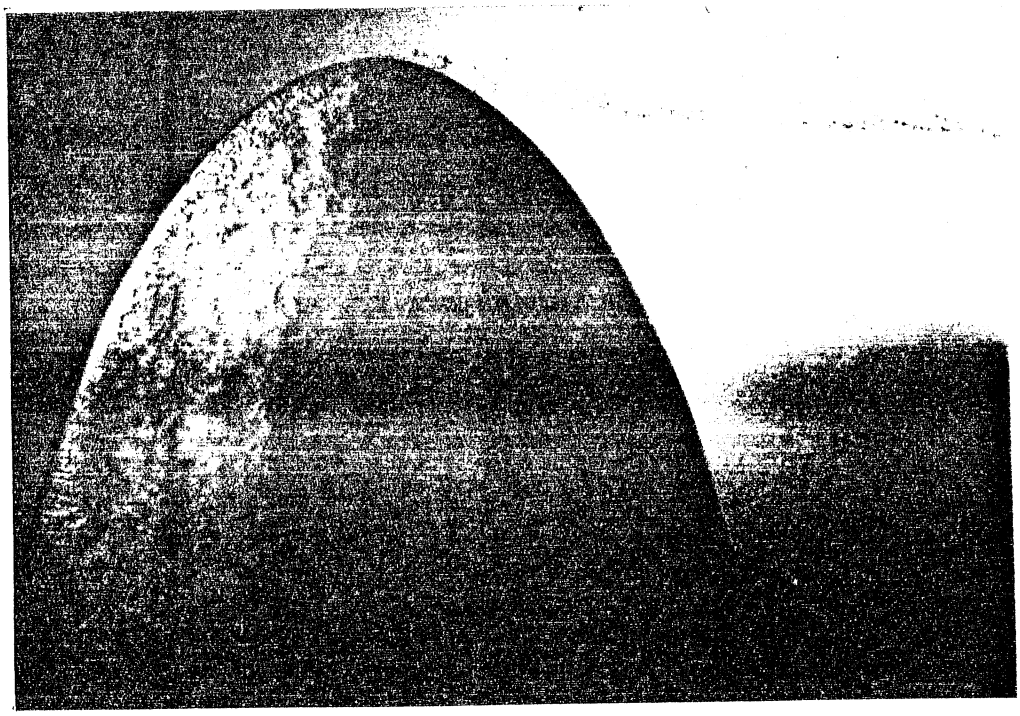

Figure V4.2a. Surface cavitation on a symmetric hydrofoil.

Figure V4.2b. Tip vortex cavitation without surface cavitation on a cambered hydrofoil.

routine and a Levingson autoregressive technique was used with minor modifications.

Cavitation inception was detected both visually and acoustically. The inception was marked by a distinct burst of noise in the flow field. By pre-triggering the A/D converter with the hydrophone signal itself, individual traces of instantaneous pressure time traces at four different locations could be recorded. By measuring the time delay of arrival among the four hydrophones, the sound location can be estimated by a triangulation method. Time delays among the initial pulses on the traces were measured with a cursor on the digital oscilloscope to an accuracy of 0.5 micro second. A cross-correlation technique applied to the pressure traces of the initial regions produced the same time delay as that obtained directly from the traces. Given three time delays among four hydrophones as inputs, implicit simultaneous equations for the three coordinates of the sound source were solved iteratively.

The pressure traces indicate that a significant amount of reverberation is present. By limiting the source location analysis to the direct signals from single events prior to the reflection from the tunnel walls, the effects of reverberation can be treated. The present method of sound source identification, unfortunately, is not applicable to the noise signal from more developed cavitation.

The four hydrophones were placed so the separation from each other was maximized with the constraint that direct radiation from the noise sources arrives at each hydrophone in advance of the arrival of any reflected pulses.

Acoustic data collection was concurrent with video observation. Thus, various types of noise signals could be correlated with different types of cavitation phenomena.

A very wide set of test cases were studied, as shown in Fig. V4.3. This was necessary in order to sort out the very complex interrelationships between viscous effects, dissolved gas content and free gas content (small bubbles or nuclei).

Velocity measurements were made in water using laser Doppler velocimetry. Because of the very small core radius at the higher Reynolds number tested, the optics had to be modified to improve the spatial resolution. The bulk of these studies were made in a second recirculating water tunnel, having the same size test section, but specially modified with optical quality glass walls.

Extensive flow visualization was also carried out in both air and water. Surface oil-flow visualizations were conducted in air to study the behavior of the foil boundary layer. These visualizations were carried out in a low speed open-return wind tunnel with a 43.2 cm by 30.5 cm test section, and free stream velocities which could be varied from 18 m/s to 70 m/s. Two Reynolds numbers were tested: $Re_c = 5.3 \times 10^5$ and 27×10^5, based on the root chord (129.4 mm). A mixture of a light mineral oil and titanium dioxide was used as a flow tracer.

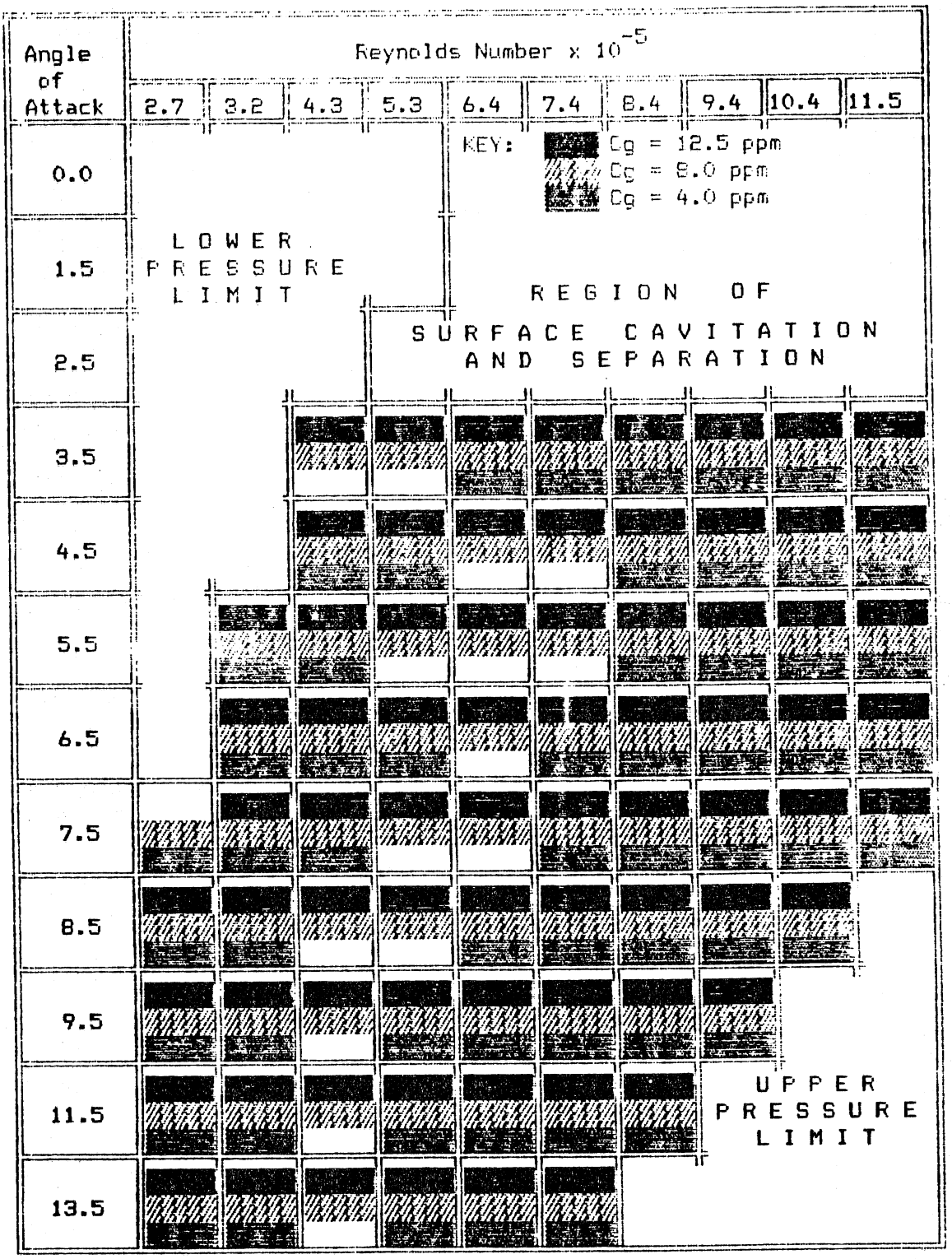

Figure V4.3. Summary chart of experimental case studies.

The experiments in water were carried out in a 30.5 cm-wide water channel. The dye visualizations were conducted using multiple dye injection holes on the foil and observing the streakline development downstream.

Cavitation Studies

The variation of inception index with angle of attack for various Reynolds numbers is shown in Fig. V4.4 for a gas content value of 4 ppm. The angle of attack dependency was found to be consistent with other investigators. With respect to the Reynolds number dependence, this figure indicates two distinct zones, one at low angle of attack and another at high angle of attack. The Reynolds number effect is seen to be more prominent at high angle of attack. This point is more clearly shown in Fig. V4.5 where the inception data are presented as a function of Reynolds number for fixed values of angle of attack with the same gas content. The figure shows that for angles of attack less than 7.5 degrees, very little variation of σ_i with Reynolds number is observed, while for higher angles of attack, the effect of the Reynolds number is more prominent. The slope of the lines appears to increase monotonically with increasing angle of attack. It may be pointed out here that details of the flow visualization study showed various viscous flow regimes at different angles of attack, in particular, separated flow existed slightly downstream of the mid-chord portion at low angles of attack. However, at higher angles of attack, separation with reattachment shifted to the leading edge resulting in complex flow patterns. The latter studies were limited to Reynolds number of 5.7×10^5, but similar effects are likely to exist at higher Reynolds number at least up to 1 million. It is very likely that these observations on viscous effects are very relevant to the observed dependency of σ_i values on Reynolds number and angle of attack.

Next, additional data similar to those presented in Fig. V4.4 are shown in Figs. V4.6 and V4.7 at Cg values of 8 ppm and 12.5 ppm, respectively. The results for 8 ppm appear very similar to those for 4 ppm; however, there is a distinct difference in the trend at Cg = 12.5 ppm. The observed strong Reynolds number dependence at higher angle of attack for 4 and 8 ppm are greatly reduced at 12.5 ppm. It is speculated that this may be related to the nuclei supply conditions which are influenced by many factors, some of these being facility dependent and others associated with viscous flow characteristics of the foil itself. However, the present results bring out the complex interactions between various physical factors which influence the inception process. Some of these questions, to the author's best knowledge, have not been addressed before. In order to further clarify the gas content effect, a gas content index was defined as follows.

$$G = Cg\beta/(0.5\rho U^2)$$

where β is Henry's constant. Figure V4.8 presents a set of results using this index rather than the absolute value of gas content in ppm. Firstly, the figure shows that the equilibrium theory for correcting gas content effect is not valid since the slopes do not remain constant, which would be required for the equilibrium theory. The slope apparently increases with

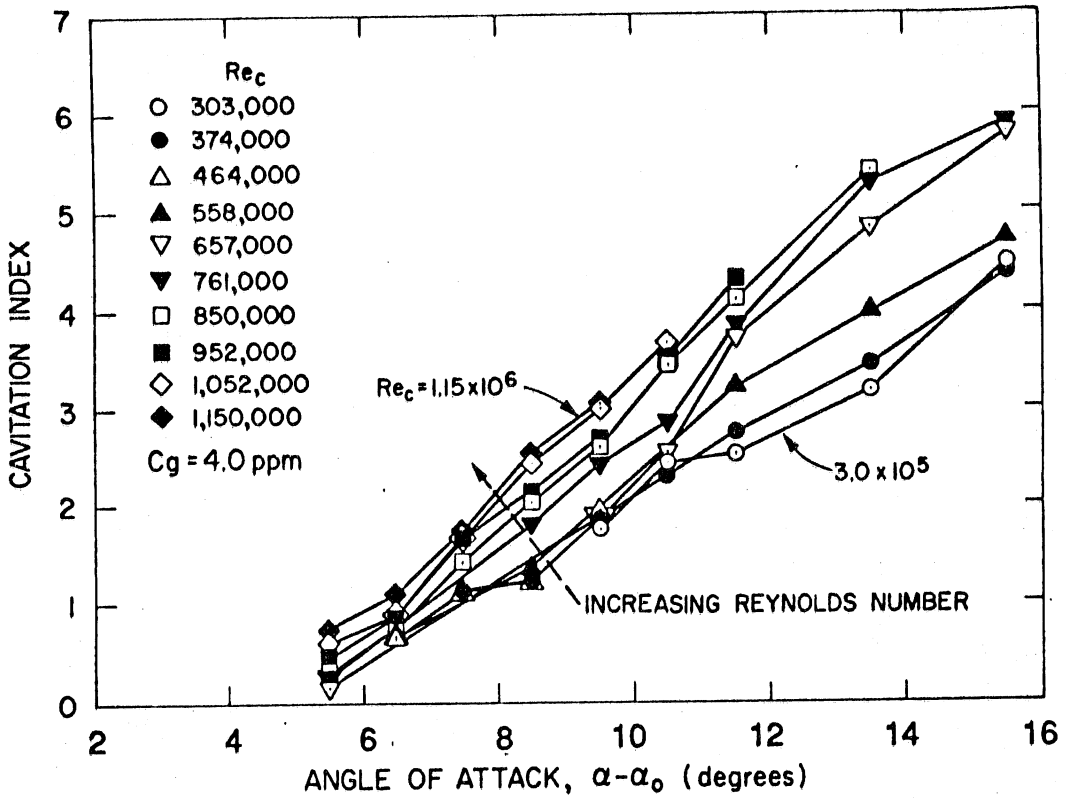

Figure V4.4. Cavitation inception index as a function of angle of attack gas content 4 ppm.

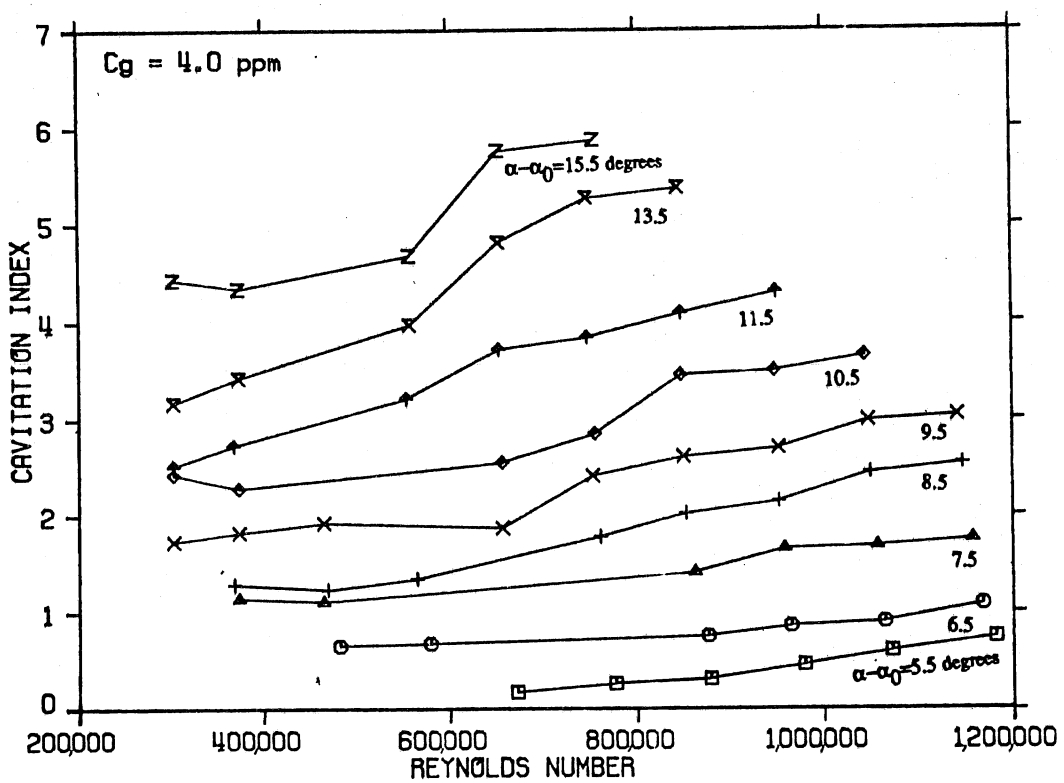

Figure V4.5. Cavitation inception index as a function of Reynolds number.

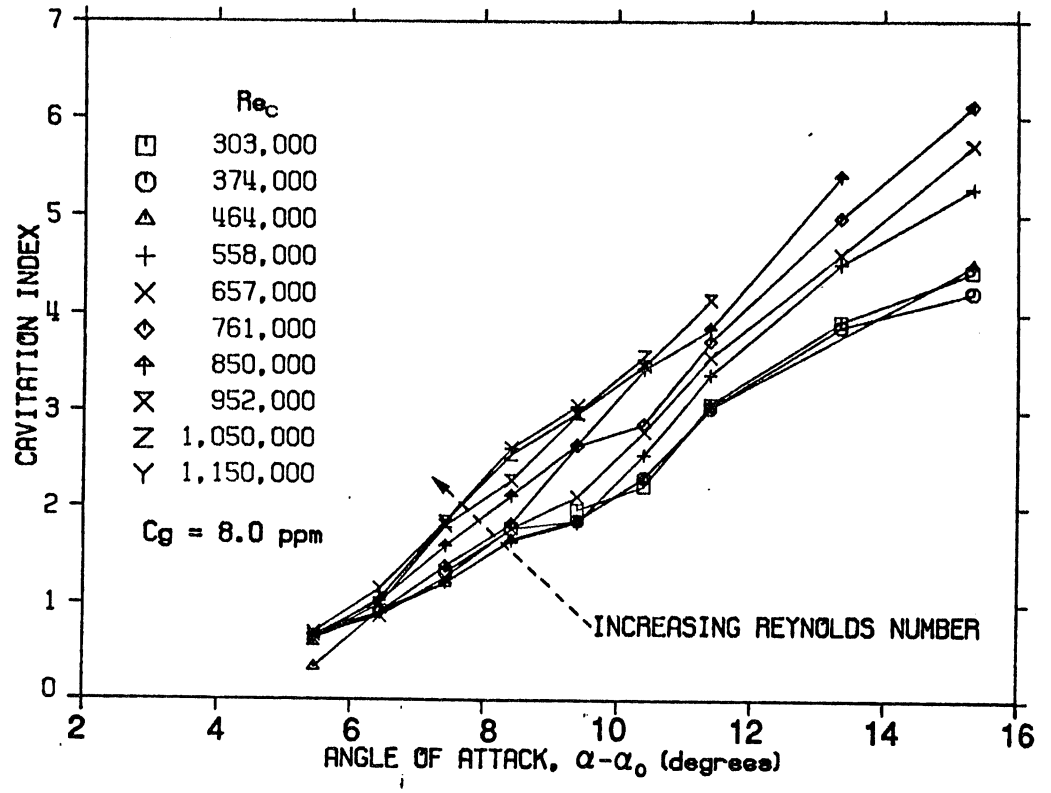

Figure V4.6. Cavitation inception index as a function of angle of attack gas content 8 ppm.

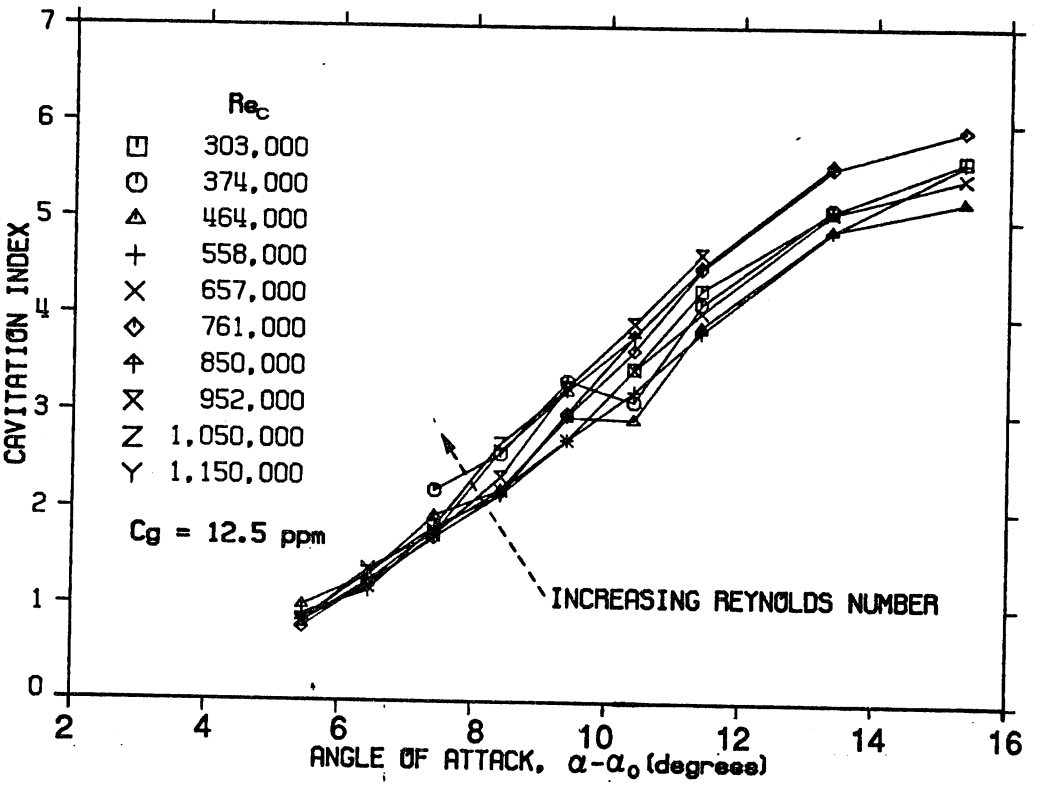

Figure V4.7. Cavitation inception index as a function of attack gas content 12.5 ppm.

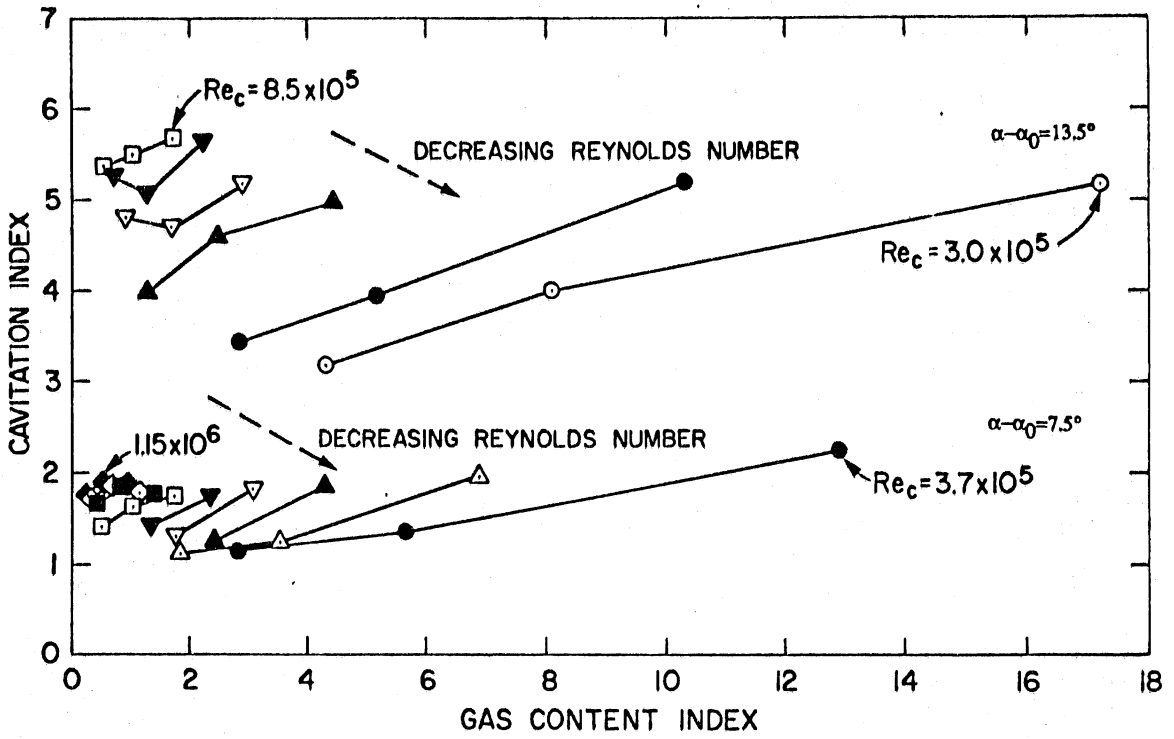

Figure V4.8. Cavitation inception index as a function of gas content index.

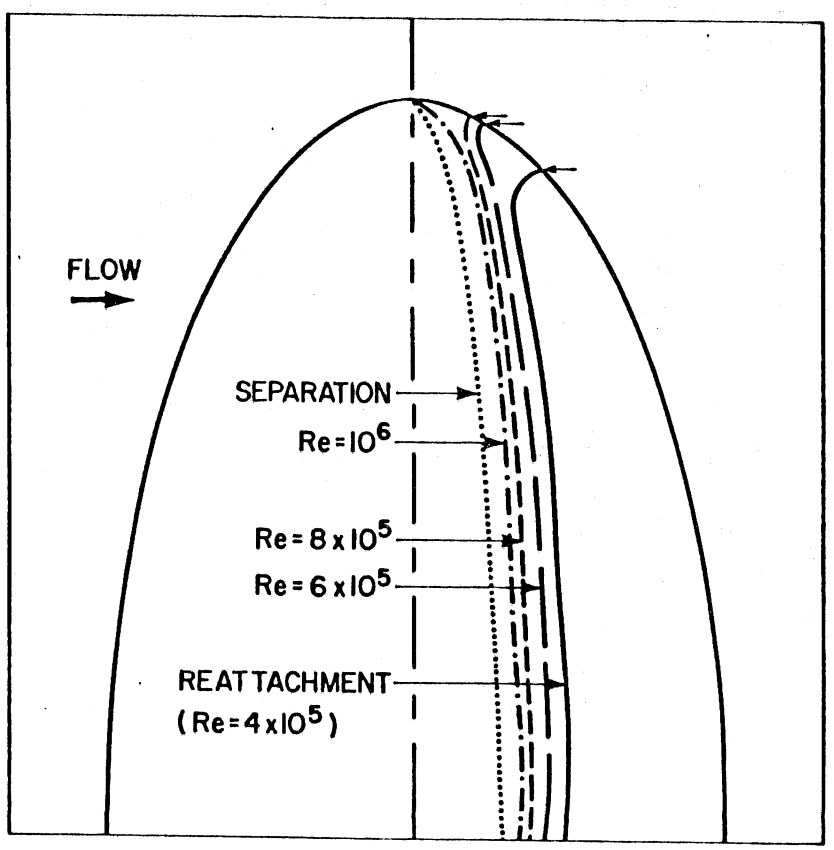

Figure V4.9. A schematic of the predicted viscous flow pattern on the suction side at $\alpha-\alpha_o = 5.5^o$.

increasing Reynolds number, which in this case was varied by increasing velocity. This is curious since the residence time decreases with increasing velocity which would have indicated the reverse trend. Any further conclusion should be based only on the observations carried out with changing of Reynolds number by altering the size of the foil.

It is well known that the nuclei characteristics of the facility can be altered by subjecting the tunnel water to various initial pressures prior to inception testing. The effect of this procedure was examined in Fig. V4.9. It is clear that there is a cut-off pressure below which the inception index is strongly influenced by pre-pressurization history. In other cases, very similar results were observed, though the cut-off pressure was found to be dependent on angles of attack and Reynolds numbers. It was concluded from this study that the trend of the dependence of σ_i on other parameters was consistent irrespective of the test procedure used for inception observations. However, the absolute values of σ_i were found to be dependent on this procedure as is evident from Fig. V4.9.

A detailed analysis of the effects of nuclei supply was made and recently reported (Arakeri et al., 1986). Nuclei can be supplied to the tip vortex from the free stream or from "body" nuclei. These are nuclei that are generated within separated, transitional or turbulent boundary layer regions on the hydrofoil itself (Katz, 1984). It was found that the conditions for the supply of body nuclei are strongly dependent on the viscous flow characteristics of the body. Boundary layer computations were made on both the suction and pressure side of the particular hydrofoil under consideration. The theoretical pressure distribution at a given angle of attack was computed using the method described in Abbott and Von Doenhoff (1959). These do not include any three-dimensional effects which are likely to be important in the tip region. Next, the boundary layer growth calculations were made using the Thwaites method, and the separation bubble, if existing, was decided to be either short or long based on the results of Gaster (1967). One set of computed results on the suction side at an angle of attack of $\alpha-\alpha_o = 5.5°$ is shown in Fig. V4.10. A laminar separation bubble is predicted as indicated. Since on an elliptic planform the local Reynolds number decreases sharply towards the tip, a long separation bubble is predicted near the region. The point of changeover from short to long separation bubble shifts towards the tip as Reynolds number is increased, indicated by a small arrow mark. Only at a Reynolds number of 10^6, a short separation bubble is predicted to exist almost all the way to the tip. Approximate stability estimates were also made to predict the transition location within the attached boundary layer. Separation is predicted just downstream of this at about 63 percent chord. Using the maximum spatial amplification factor, it was predicted that laminar separation would prevail up to a Reynolds number of 2×10^6.

On this foil, separation is also predicted on the pressure side at the angles of attack of present interest. In addition, the location of separation and pressure coefficient at separation were not found to be a strong function of angle of attack as indicated below for the suction side.

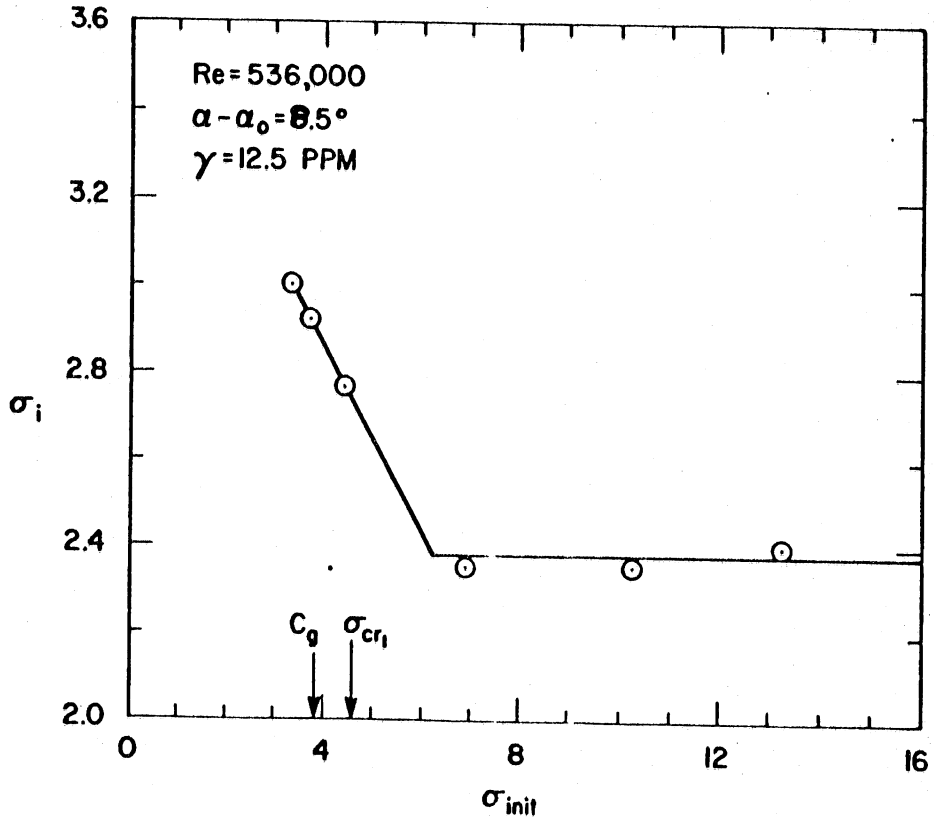

Figure V4.10. Dependence of σ_i on the initial cavitation number at the start of the inception tank.

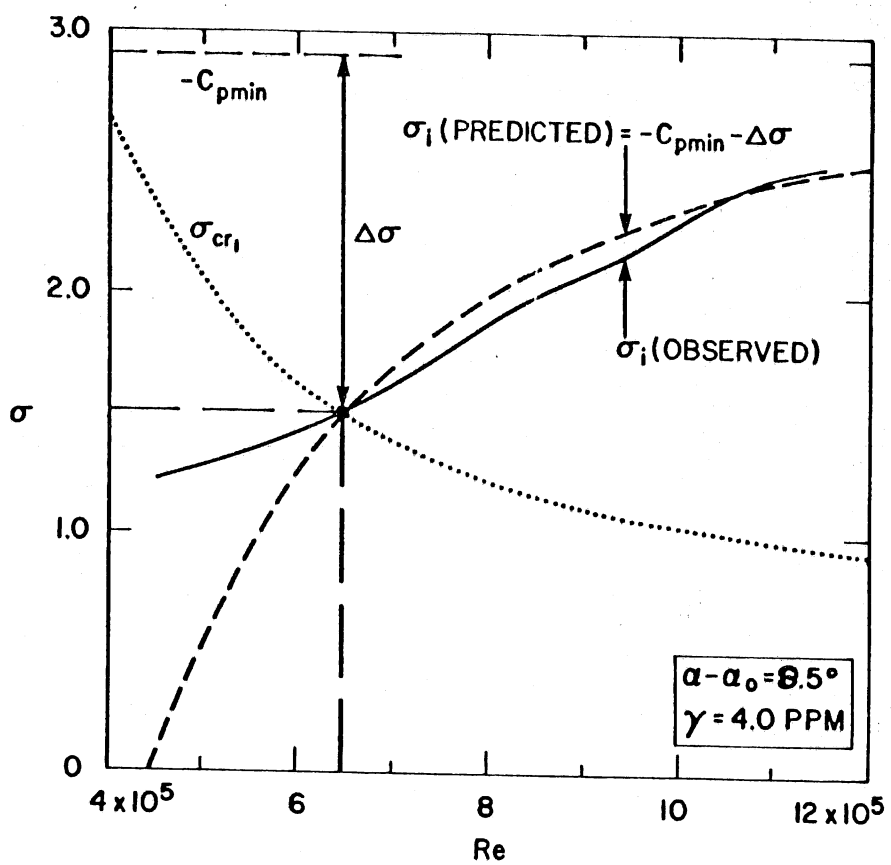

Figure V4.11. Conditions used for estimating dominant nuclei size and predicted behavior of σ_i • γ = 4 ppm.

TABLE 1. Suction Side Separation Properties			
$\alpha-\alpha_0$	4.2°	5.5°	7.5°
$(x/c)_x$	0.628	0.634	0.634
$-Cp_s$	0.66	0.70	0.74

Assuming that separated regions become sources of nuclei when the flow locally becomes saturated with gas, the critical values of σ for this to occur on the suction side or the pressure side can be calculated as σ_{cr1} and σ_{cr2}. σ_{cr3} will be used to denote supersaturation in the test section. Close examination of the inception data shows certain interesting general trends when compared with the behavior of critical σ's for nuclei supply. One of the clear trends is that if $\sigma > \sigma_{cr_1}$, then σ_i is a strong function of Re with σ_i increasing with an increase in Re. The second trend which is also apparent is that in the Reynolds number range for which $\sigma_{cr_3} \leq \sigma_i \leq \sigma_{cr_2}$, σ_i is almost independent of Re and finally we note that if $\sigma_i < \sigma_{cr_3}$, then σ_i increases with a decrease in Re. It is not obvious here that this trend is due to gaseous cavitation normally observed since we do not know the precise magnitude of $-Cp_{min}$. Using these ideas, along with an estimation of dominant nuclei size, as discussed in Arakeri et al. (1986), the salient features of the cavitation inception process can be predicted. An example is shown in Fig. V4.11. In this case, $R_o = 6.3 \times 10^{-6}$ (1.9 μm) and $-Cp_{min} = 3$ values were used. For Re > 6.4×10^5, the observed σ_i dependence with Re can be explained solely on the basis of tension effects. For this Reynolds number range also, there is no obvious source of nuclei based on static pressure considerations, and hence the assumption that R_o remains constant may be a valid one.

For Re < 6.4×10^5, the observed σ_i follows a different trend from the predicted one. In this region, at inception, the extent of supersaturation being proportional to $\sigma_{cr_1} - \sigma_i$ increases with decrease in Re or velocity. Thus we may not expect R_o to remain constant here but to increase roughly in proportion to $(\sigma_{cr_1} - \sigma_i) \sim 1/1/2\ \rho U^2$. In the same Reynolds number range $\Delta\sigma$ required for inception increases like $1/2\rho U^2$ and the two effects may cancel giving a constant σ_i value. This is roughly in agreement with the observations.

In summary, there is definite evidence that the observed complex behavior of σ_i for tip vortex cavitation inception with Reynolds number (actually velocity since body size was not varied), angle of attack and dissolved gas content are related to the critical conditions for nuclei supply. It is necessary to examine the latter for both the free stream and separated regions that may exist on the foil. In the regions of Reynolds numbers (velocities) where there is no obvious source for nuclei supply, the σ_i value is a strong function of Reynolds number and is almost independent of the dissolved gas content value. From the measured σ_i values, it

was possible to estimate the dominant nuclei size responsible for inception and these are found to be surprisingly small being of the order of 2 μm. Thus, some of the Reynolds number dependence on σ_i can be ascribed to the tension effects. It appears that in dealing with inception characteristics of flows with high $-Cp_{min}$ values, it is necessary to carefully examine the nuclei supply conditions. For flows with lower $-Cp_{min}$ values like axisymmetric bodies, the nuclei supply conditions may not be as critical. The above conclusions are valid for inception conditions.

Vortex Trajector as Visualized by Cavitation

The tip vortex roll-up process and the vortex trajectory are of practical importance as evidenced by a substantial number of recent numerical and experimental studies. In the present investigation, cavitation provided an excellent method for visualizing the mechanism of vortex roll-up.

Stroboscopic lighting with a 5 micro second duration was used. First the velocity of the incoming flow was set, and the static pressure of the test section was gradually lowered. Cavitation first occurs in the low pressure core region, and the inception of tip vortex cavitation is observed to be the intermittent appearance of a continuous cavity starting within one or two cord lengths from the tip of the foil. As the pressure is further decreased, a developed tip vortex cavity formed. While the cavity core radius is small, the flow field about the cavity can be considered to be representative of the single phase flow. Numerous photographs of the tip vortex cavity were taken at different angles of attack, Reynolds number, and gas content. These photographs were analyzed and the curvature and the spanwise position of the cavity were studied. The vortex trajectory up to 5.8 chord lengths was measured and at 4 chord lengths, the spanwise position reaches within 2% of the theoretical asymptotic position for an elliptically loaded wing ($y/s = 0.785$). The trajectory agrees well with the experimental data of Spreiter and Sachs (1951) for a larger aspect ratio (AR=5) than the present foil. Figure V4.12 summarizes the data in the vicinity of the foil taken at various test conditions. Lack of correlation with gas content is as expected, but it is to be noted that the general behavior of the trajectory is almost independent of the Reynolds number and the angle of attack. Spreiter and Sachs (1951) applied Kaden's theory in the near field to estimate the rate at which the vortex trajectory approaches its asymptotic value. According to this analysis, the downstream distance at which the vortex trajectory crosses the asymptotic value is expected to be inversely proportional to the lift coefficient, however, the variation among the present experimental data was found to be significantly smaller than predicted. For comparison, the vortex trajectory was also calculated using the Betz' (1933) roll-up model and Moore's (1974) numerical solution. The computed approach of the trajectory to the asymptote lagged experimental data considerably, and the agreement was poorer than Kaden's model. Naturally, these classical models are too simplistic since the flow over the wing or the three-dimensional roll-up process is not taken into account. Recently, Krasny (1987) carried out a computation of vortex sheet roll-up using a large scale discrete vortex method. The results for an elliptically loaded wing agreed with the Kaden's analysis in the near field, and also agreed fairly well with the experiment on the asymptotic vortex position. However, the transformation

Tip Vortex Trajectories

	Picture No.	Cav Index	Core Rad (mm)	Ang of Attack (Deg)	Reynolds Number (*10^-5)	Gas Content (ppm)
———	323-157	1.306	0.79	8.5	10.4	12.6
———	323-158	1.007	1.41	8.5	10.4	12.6
———	323-159	0.896	1.81	8.5	10.4	12.6
———	323-160T	0.859	1.93	8.5	10.4	12.6
———	323-161	0.655	2.60	8.5	10.4	12.6
- - - - - - -	323-177	0.714	0.80	7.5	5.3	4.0
- - - - - - -	323-178	0.586	1.10	7.5	5.3	4.0
- - - - - - -	323-179	0.529	1.42	7.5	5.3	4.0
- - - - - - -	323-181	1.153	0.83	9.5	5.3	4.5
- - - - - - -	323-182T	0.582	2.22	9.5	5.3	4.5
- - - - -	323-192	1.539	0.39	8.5	10.4	4.5
- - - - -	323-193	1.465	0.50	8.5	10.4	4.5

	Picture No.	Cav Index	Core Rad (mm)	Ang of Attack (Deg)	Reynolds Number (*10^-5)	Gas Content (ppm)
- - - - -	323-194	1.280	0.56	8.5	10.4	4.5
- - - - -	323-195	0.984	0.86	8.5	10.4	4.5
- - - - -	323-196	0.680	1.71	8.5	10.4	4.5
———	323-197T	0.614	2.07	8.5	10.4	4.5
———	323-218	3.19	0.70	15.5	6.5	7.0
———	323-221	2.76	0.66	13.5	6.5	7.0
———	323-223	2.05	0.85	11.5	6.5	7.0
———	323-225	1.44	0.94	10.5	6.5	7.0
— — — ·	323-213	2.42	0.56	9.5	6.5	7.0
— — — ·	323-227	0.92	0.84	8.5	6.5	7.0
— — — ·	323-229	0.26	1.05	6.5	6.5	7.0
— — — ·	323-231	0.40	0.95	5.5	6.5	7.0

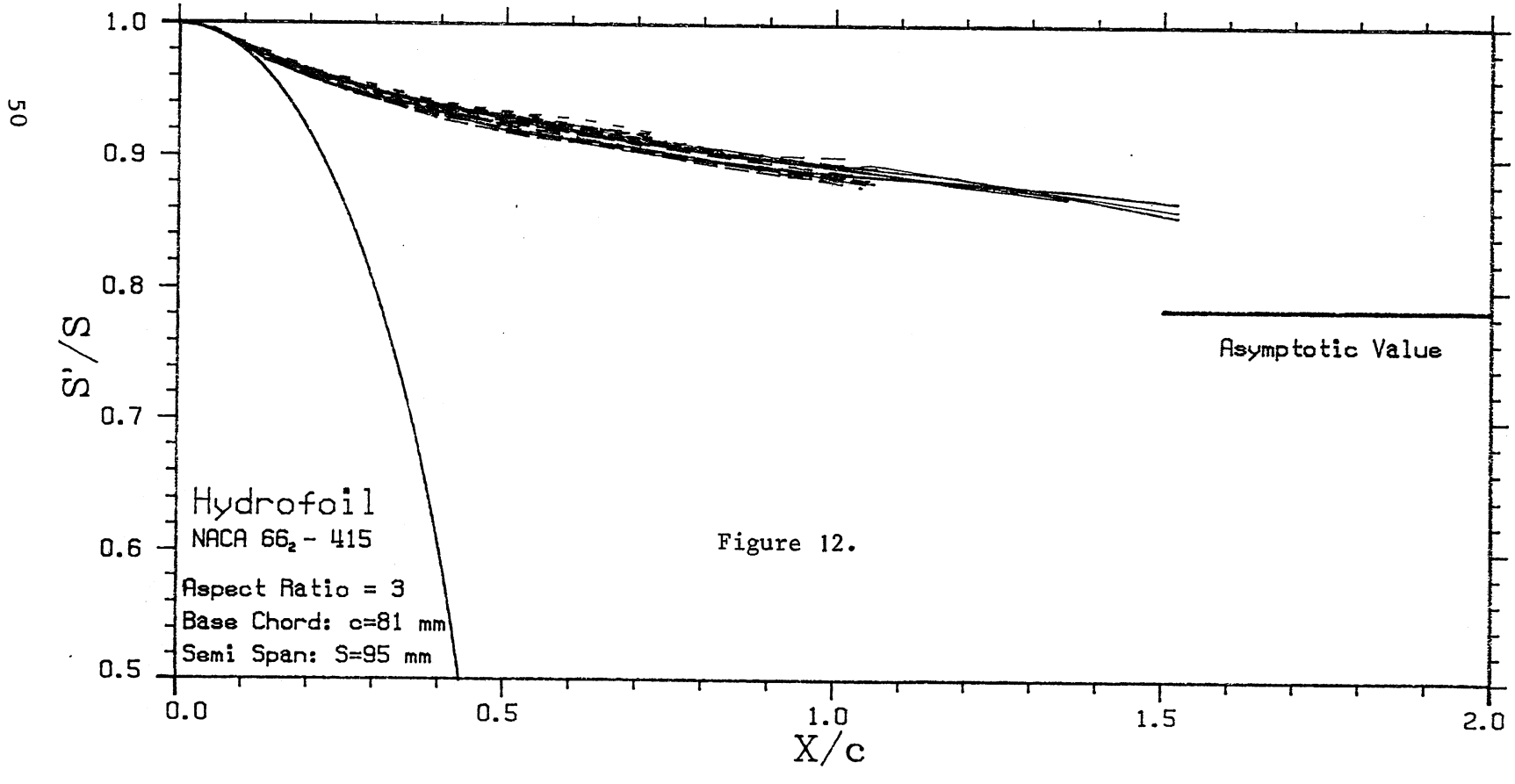

Figure 12.

from the Trefftz plane to the physical plane is linearly related to the wing circulation, and the result becomes more sensitive to the angle of attack than experimentally observed. Numerical simulation with the full Navier-Stokes equations of the vortex roll-up from a rectangular wing has been reported by Srinivasan et al. (1986), but no numerical data exist on the low aspect ratio elliptic wing.

The Structure of Trailing Vortices

In order to relate the observed cavitation characteristics to the minimum pressure within the tip vortex, a semi-empirical model of the near wake structure was developed. This model was based on LDV measurements made in a water tunnel and a flume.

The structure of vortices trailing from wings of finite span has been treated extensively by previous investigators. The impetus for this previous work was aircraft safety. The results of this research do not provide sufficient information for the tip vortex cavitation problem (McCormick, 1962; Platzer and Souders, 1979). The minimum pressure in the vortex is not of much interest in aerodynamics, since the aircraft hazard problem is concerned with the structure of the far wake and not the near wake where cavitation inception occurs. In much of the previous work on vortex cavitation, the data are analyzed on the basis of an assumed Rankine vortex model (Billet and Holl, 1979; Latorre et al., 1984). The core radius in these studies was assumed to scale with the boundary layer thickness on the pressure side of the hydrofoil. Recently, it has been pointed out that there are inconsistencies in this approach (Arndt et al., 1985).

In order to deal with the trailing vortex analytically, many inviscid techniques (Bilanin and Donaldson, 1975) have been developed. These models have been expanded to include laminar and turbulent diffusion effects (Lamb, 1945; Moore and Saffman, 1973; Phillips, 1981; Squire, 1965). However, none of the available theoretical models are successful in accurately describing the near wake characteristics of a trailing vortex. It was found, for example, that the functional dependence of core radius on both Reynolds number and the angle of attack, which has been confirmed by the recent LDV measurements (Orloff, 1974; Quadrelli, 1985), is not predicted in any of the existing analyses. Moreover, the predicted core pressure diverges near the tip.

The evolution of a trailing vortex with downstream distance, x, may be broken down into four basic regions as illustrated in Fig. V4.13. In the fully rolled-up region, the roll-up process is complete and observed self-similar characteristics are consistent with the previously mentioned analytical work. In the initial roll-up region of interest, more complicated near wake characteristics are evident. For example, the vortex circulation Γ_ℓ is not necessarily equal to the mid-span circulation Γ_o. In addition, the tangential velocity profiles are asymmetric. The asymmetry of the flow is difficult to address and has been ignored in this simple analysis. An important feature of the model is the consideration of turbulent diffusion in the core region. The modelled "inner" and "outer" core regions are similar in structure to Squire's (1965) turbulent vortex. With the

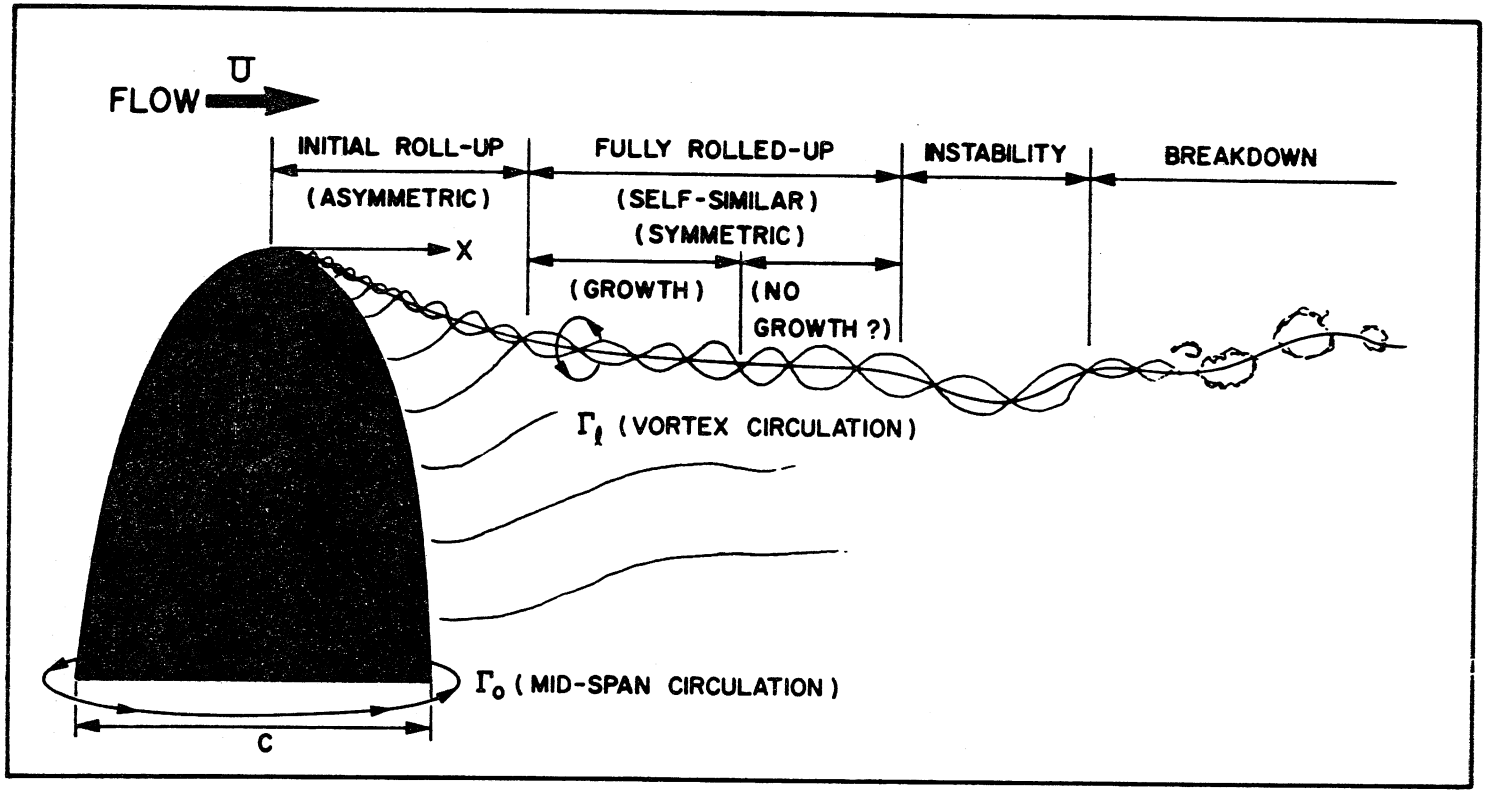

Figure V4.13. Evolution of trailing vortex.

modelled velocity field, the pressure drop in the vortex core can be estimated by integrating the momentum equation for an axisymmetric swirling flow

$$\frac{\partial p}{\partial r} = \rho v_\theta^2 / r$$

The model depends heavily on measured velocity data. In addition to the measurements reported in Quadrelli (1985), extensive water tunnel measurements were made at a Reynolds number of 5.6×10^5. A comparison of the model and measurements is shown in Figures V4.14 and V4.15. Details are found in Ikohagi et al. (1986). Figure V4.14 compares the measured circulation as a function of distance from the centerline of the vortex. The agreement with the model is much better on the suction side of the vortex (as shown) than on the pressure side. In fact, an axisymmetric model is only a fair approximation to the measured velocity data as shown in Figs. V4.15a and V4.15b.

Comparisons of tangential velocity are made for various α and x/C_o to examine the validity of the proposed semi-empirical modelling. Although there is some asymmetry of the velocity profiles, with higher velocities noted on the suction side of foil, fair agreement is obtained except for the case $\alpha = 15°$. The data also indicate that the core radius increases with increasing α. This suggests that the incipient cavitation number for a tip vortex scales with a smaller power of α than α^2. The axial gradient of pressure is almost zero within a few chord lengths downstream after a sharp pressure drop near the tip. The semi-empirical approach used here circumvents the problem of pressure divergence near the tip, found in existing theoretical models.

Although the near wake characteristics are quite different from the far wake characteristics, and the near wake can be adequately modelled semi-empirically, the issue of what physical mechanisms are involved still remains to be solved. A much more sophisticated analytic approach is necessary to adequately describe the near wake region of a trailing vortex, at least for the purpose of further elucidating the cavitation problem.

Cavitation Noise

Different types of cavitation phenomena were observed and recorded on still photos and on video tapes. Reynolds number (free stream velocity), angle of attack, dissolved gas content and the test section pressure were varied.

Surface cavitation on the symmetric hydrofoil was as expected. The first appearance of cavitation was along the leading edge. The appearance of the cavitation was in qualitative agreement with the assumption that the hydrofoil was elliptically loaded, though a more careful study indicated three-dimensional behavior of the foil boundary layer with separation.

The inception of tip vortex cavitation occurred either as an unsteady appearance of a single bubble within one or two chord lengths from the tip

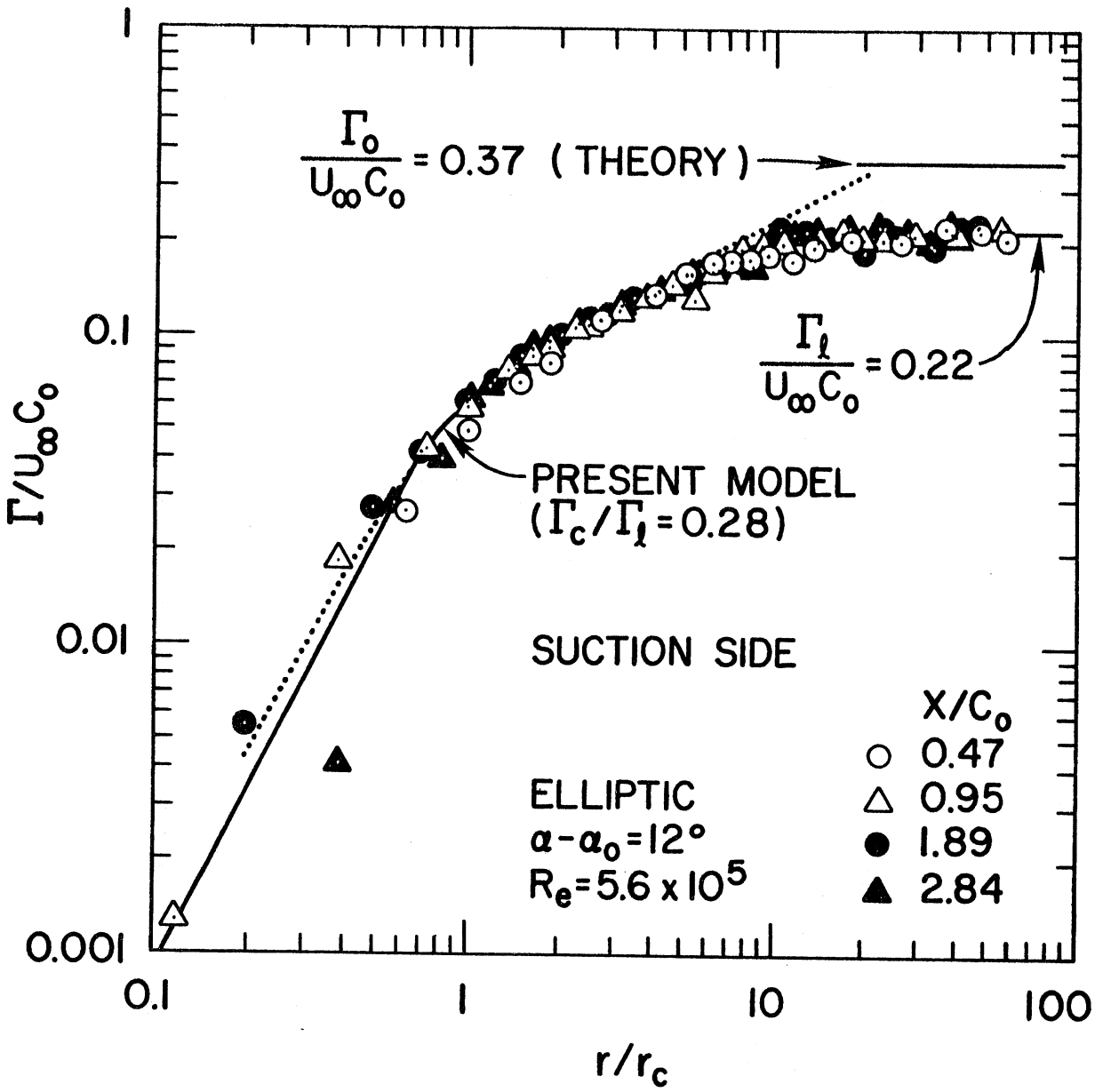

Figure V4.14. Measured circulation as a function of distance from the centerline of the vortex.

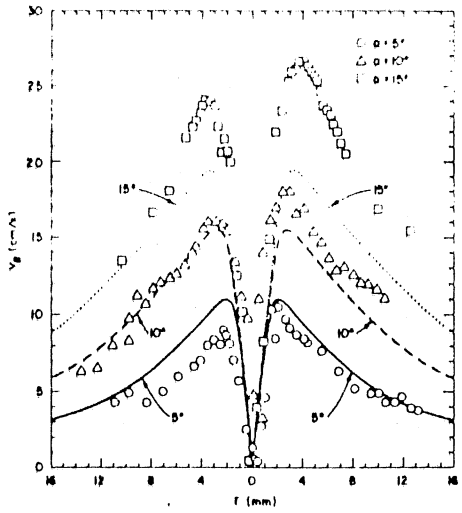

(a)

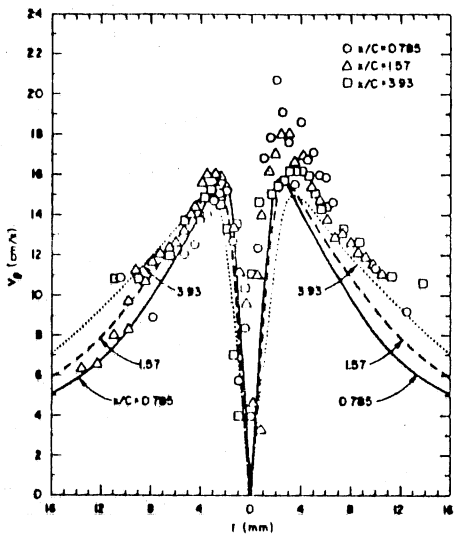

(b)

Figure V4.15. Comparison of tangential velocity profiles (a) x/C_o = 1.57 and (b) $\alpha = 10^o$.

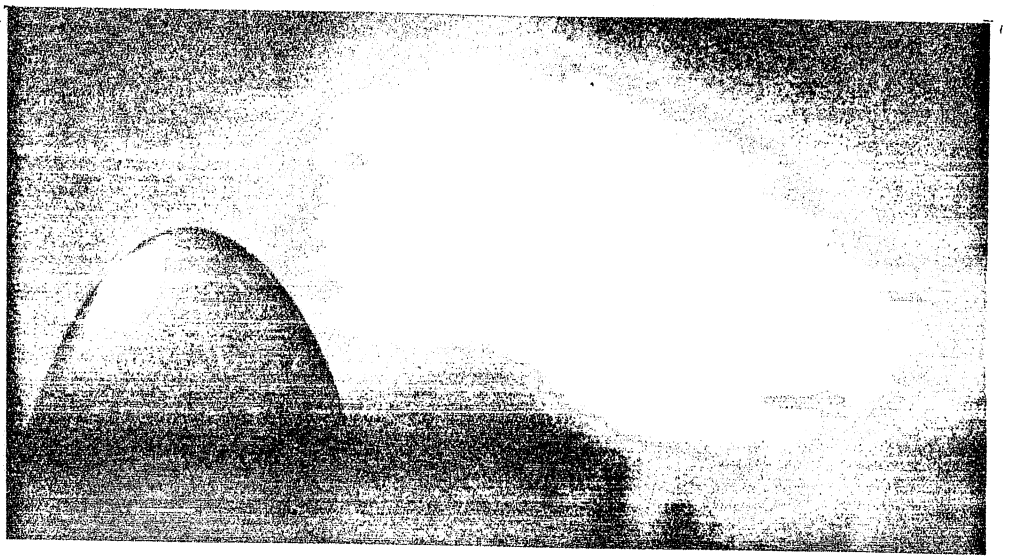

(a)

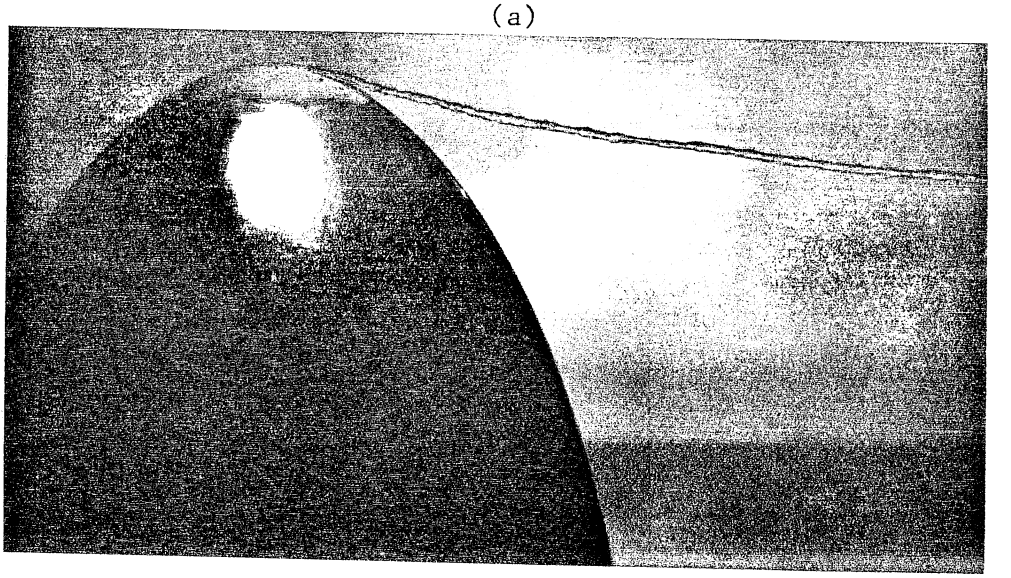

(b)

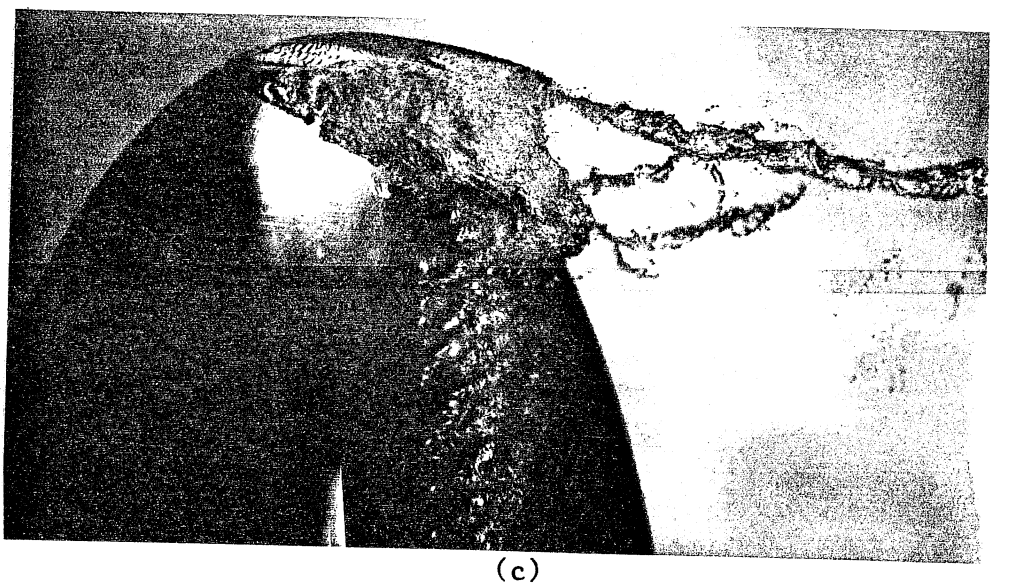

(c)

Figure V4.16. Various types of tip vortex cavitation.
(a) Inception (σ=1.4, $\alpha-\alpha 0$=2.4^{o}, Re=6.1x10^{5})
(b) Continuous tip vortex cavity (σ=1.15, $\alpha-\alpha 0$=9.5^{o}, Re=5.3x10^{5})
(c) Tip vortex cavitation with surface cavitation (σ=0.43, $\alpha-\alpha 0$=11.5^{o}, Re=5.3x10^{5}).

or as a continuous cavity suddenly appearing from about the same position and attaching itself to the tip. Typical cavitation phenomena with the cambered foil are shown in Fig. V4.16. In particular, Figs. V4.16b and V4.16c were taken with a strobe with a 5 micro second duration. Figure V4.16a is an example of intermittent cavitation inception where a single bubble is captured on the film in the vortex roll-up region. In other cases, video tapes showed that the inception occurred as a continuous cavity travelling upstream and attaching itself at the foil tip. An example of this type of a developed tip vortex cavitation is shown in Fig. V4.16b. In either case of inception, distinct sound pulses are radiated. As the test section pressure is further decreased, the cavity extends over the entire tip region, and subsequently the vortex develops a twisted ribbon shape. The noise level decreases with the appearance of fully developed cavitation until a cavity starts to cover a portion of the foil tip with further lowering of the cavitation index. As the pressure is further decreased, surface cavitation develops. As shown in Fig. V4.16c, cavitation is observed in the region where trailing edge boundary layer separation was predicted and observed in oil film visualization studies.

Three types of pressure traces were noted during tip vortex cavitation in inception. Typical inception data shown in Fig. V4.17a have a sharp pressure peak at the onset followed by a series of rebounds due to bubble oscillation and tunnel reverberation. Similar sharp pulses were observed either when the intermittent short cavitation bubble becomes visible at one or two chord lengths downstream in the tip vortex, or when a continuous cavity appears at a similar axial position and rapidly moves upstream and attaches itself to the foil tip. In other cases, very regular low frequency oscillations occurred (see Fig. V4.17b). These low frequency oscillations were observed at different gas contents, Reynolds numbers and angles of attack. The frequency of oscillation varied from 2.5 KHz to 6 KHz depending on various test conditions. In many cases, particularly at low angles of attack, cavitation inception had the appearance of elongated bubbles, presumably the result of discrete portions of the vortex core intermittently cavitating as shown in Fig. V4.16a. Although the natural frequency of such elongated bubbles is unknown, the observed noise frequency range is comparable to the natural frequencies of spherical bubbles of equivalent size. One problem with this hypothesis as a cause of the noise is that this type of noise was observed over a wide range of gas content. Unfortunately there is no discernible relationship between frequency and gas content. Further analysis of a cylindrical cavity is needed to more accurately describe the source of the low frequency noise. The third type of noise source occurs when the gas content is low, or when the cavitation index is lowered rather rapidly. Under such circumstances a steady cavity core often appears suddenly. Figure V4.17 corresponds to such a case, which displays a negative transient pressure due to this cavity formation.

Once continuous tip vortex cavitation occurs, the noise level decreases markedly, as shown in Fig. V4.17c. As the pressure is further decreased, the cavity core radius increases and the foil tip starts to cavitate. The sound level significantly increases with the onset of a surface cavity.

Within a very narrow band of cavitation number and at a surface cavity angle of attack ($\approx 10\pm2°$), a discrete tone is generated in the frequency

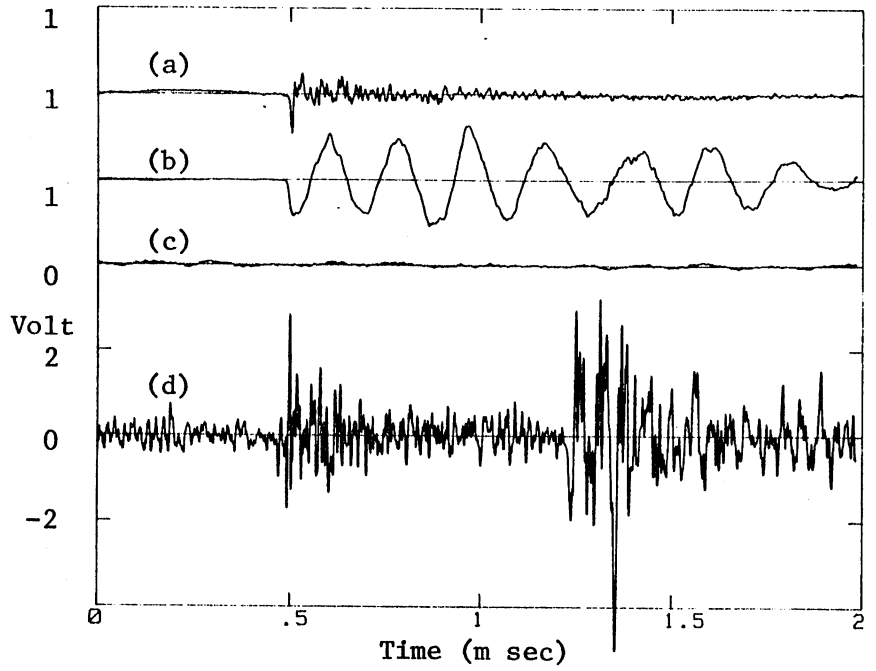

Figure V4.17. Time traces of tip vortex cavitation (=12.5 ppm)
(a) Inception (σ=2.76, $\alpha-\alpha 0$=13.5°, Re=6.1x10^5)
(b) Inception (σ=3.97, $\alpha-\alpha 0$=12.5°, Re=9.5x10^5)
(c) Continuous tip vortex cavity
(σ=3.29, $\alpha-\alpha 0$=15.5°, Re=9.1x10^5)
(d) Tip vortex cavitation with surface cavitation
(σ=0.52, $\alpha-\alpha 0$=9.5°, Re=7.5x10^5)

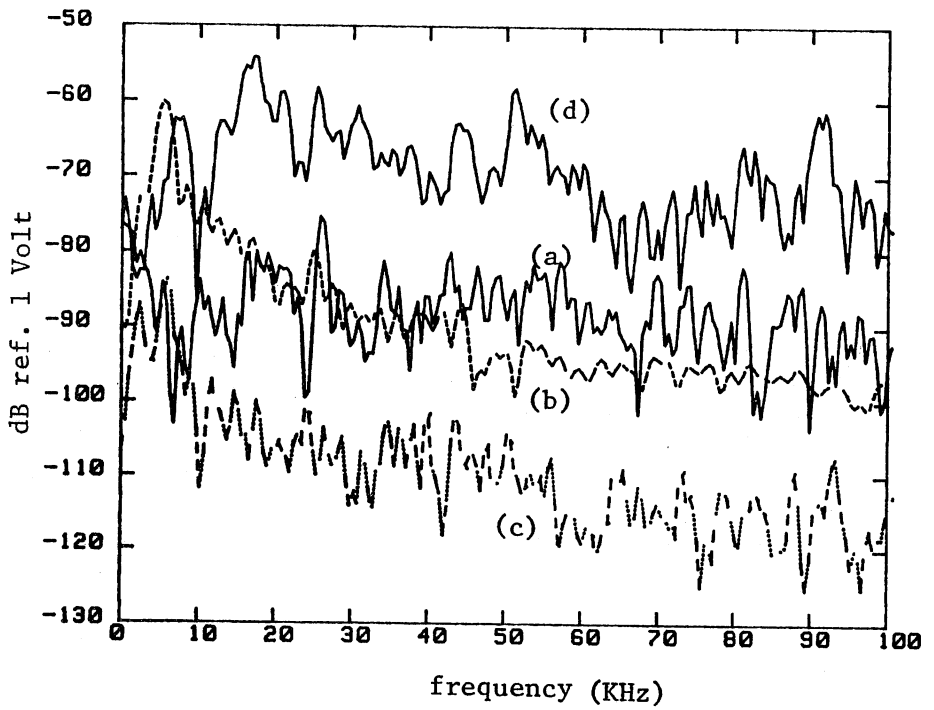

Figure V4.18. Power spectral density
(a & b) Inceptions
(c) Continuous tip vortex cavity
(d) Tip vortex cavitation with surface cavitation

(same as in Fig. V4.17)

range 340-900 Hz. Holding free stream velocity constant, it is observed that the frequency of the tone varies continuously within a certain range of cavitation number, a higher pitch corresponding to higher cavitation number and smaller cavity core radius. Limited data indicate that the frequency varies almost linearly with velocity at constant cavitation number. This phenomenon is apparently associated with cavitation on the suction side of the tip and the braided structure of the vortex cavity. Under strobscopic illumination, it is observed that the tip cavity pulsates and the braided structure rotates in synchronism with the emitted tone. At first it was conjectured that the phenomenon was due to a flow induced vibration of the foil since the resonance frequency of the foil was determined to be about 400 Hz. The fact that the tonal frequency varied continuously with free stream velocity and cavitation number, discounts this theory. The actual mechanism for noise generation in this regime remains to be investigated.

As the cavitation index is further lowered, surface cavitation appears in the vicinity of the region where a laminar separation and a turbulent reattachement occurs. This region has been observed to be in agreement with theoretical prediction and the flow visualization studies. The noise level increases, mainly in the high frequency range, as shown in Fig. V4.17d. No marked effect of different gas content (between 4.5 ppm and 12.5 ppm) was observed.

The effect of tunnel reverberation was studied for the cases of surface cavitation inception as reported by Higuchi and Arndt (1985a). By ensemble averaging the cavitation inception data, a wave form of a single bubble collapse in the free field was obtained. A simple acoustic model of the reverberant water channel was utilized to quantify the reverberation in a computer simulation. The power spectrum of a simulated single bubble collapse was compared to the power spectrum of a simulated pulse with reverberations and the Fourier transform of the measured pressure trace. It was found that the effects of reverberation on the measured spectrum was only on the relative magnitude. The general shape of the spectrum remained unchanged and was in general agreement with Fitzpatrick and Strasberg's (1956) theoretical spectrum for a single bubble.

Arakeri and Iyer (1986b) conducted a study of the noise due to bubble induced by nuclei seeding by an electrolysis technique. They found that the spectrum of the noise from multiple cavitation collapses retains the shape of the single bubble spectrum. The amplitude scales with the rate of cavitation events. They also noted that the mutual interaction among bubbles is negligible. This is consistent with our present computer simulation of the single bubble collapse accompanied by reflected waves. The important point is that cavitation noise can be studied in a highly reverberant water tunnel.

Acoustic spectra of tip vortex cavitation at different stages of development are present in Fig. V4.18. As mentioned earlier, two types of acoustic signals were noted during tip vortex cavitation inception. The power spectrum corresponding to an inception with a sharp sound pulse (Fig. V4.17a) exhibited a gradual decrease of spectrum level at high frequency. Unlike the spectra for surface cavitation inception, no high frequency spectral peak is noted. The power spectrum shown in Fig. V4.18b

corresponds to inception when there is a low frequency regular oscillation (Fig. V4.17b). A dominant peak is evident at low frequency, and the spectrum drops off rather rapidly. The noise level decreases abruptly as steady tip vortex cavitation develops to form a well defined cavity core trailing from the tip of the foil (e.g. Fig. V4.16b). Figure V4.18 shows the corresponding spectrum. Within a narrow range of the cavitation number where the ribbon type cavity appears, the distinct tone is generated with a sharp spectral peak at 340-900 Hz. The pitch decreases and then the noise level decreases again at lower cavitation numbers. The noise level increases dramatically, especially in the higher frequency bends when surface cavitation appears, as shown in Fig. V4.18d. The power spectrum of the combined tip vortex and surface cavitation is very similar to the spectrum of continuous surface cavitation alone on the symmetric foil. Thus it can be assumed that, when it occurs, surface cavitation is the dominant noise source.

The present inception data under various conditions were examined for their source locations and the results are tabulated in Rogers' thesis (1987). Substantial scatter in the resulting positions (as much as 30 mm under the similar conditions) were observed. Due to the small vertical separation between the hydrophone No. 4 and the other hydrophones, the numerical convergence of the vertical coordinate was often poor. In these cases the vertical position of the visualized vortex was given as alternative input. The latter was the method reported earlier when only three hydrophones were available (Higuchi et al., 1985b). In spite of the scatter in the data, the present results clearly showed that the noise sources are concentrated very close to the hydrofoil tip. They were either within a couple of chord lengths downstream from the tip corresponding to the vortex roll-up region, or in the immediate neighborhood of the foil tip corresponding to the upstream end of the continuous cavity. These observations were in good agreement with the visual observation recorded on video tape.

The findings of this investigation are summarized below:

Several different types of cavitation inception noise signatures were noted. Cavitation inception was observed to be either the sudden appearance of a continuous cavity or the intermittent appearance of an elongated bubble extending axially over a relatively small portion of the tip vortex. The transient noise signal due to the former type of inception consisting initially of a negative pressure pulse implies that sudden expansion of a cylindrical cavity was important in the noise generation process. In the latter case, either high frequency, intermittent pulses, or a relatively low frequency damped oscillation was observed in the noise signature. It was not possible to relate the occurrence of either type of signal with Reynolds number or gas content, nor was it possible to relate the noise signals to gas bubble oscillation (pseudo cavitation) or to the growth and collapse of true vapor cavities.

A hydrophone array was utilized to identify the noise source location. In spite of limitations on spatial resolution and repeatability, the results of this study clearly indicate that cavitation noise sources are concentrated in the vortex rollup region, less than one chord length from the tip of the hydrofoil.

The noise intensity associated with fully developed tip vortex cavitation is substantially lower than inception noise, or surface cavitation noise, when it occurs. At high angle of attack, and under special circumstances, a very strong, low pitch tone occurs. The frequency of the tone varied with cavity core radius and free stream velocity, discounting the thought that this might be a flow induced vibration of the hydrofoil itself. Although no conclusive statement could be made from the present set of data, it was speculated that the oscillation of the twisted ribbon-type cavity is responsible for this tone.

If surface cavitation occurs, it is the dominant noise source, overwhelming any type of vortex cavitation noise. Surface cavitation in the absence of tip vortex cavitation was examined with a hydrofoil having a symmetric foil section. Well defined noise pulses were observed, which correspond to individual bubble implosions on the hydrofoil surface. The noise sources were concentrated in a narrow region on the foil.

Although these tests were carried out in a highly reverberant water tunnel, experiments and computer simulations demonstrated that the shape of the measured spectra was unaffected.

References

Abbott, I. H. and Von Doenhoff, A. E., Theory of Wind Sections, Dover Publication, 1959, pp. 75-79.

Arakeri, V. H. and Iyer, R. N., "A New Technique in Cavitation Noise Research," in Proceedings of International Symposium on Cavitation, Vol. I," edited by H. Murai, Sendai, Japan, 1986, pp. 299-304.

Arakeri, V. H., Higuchi, H., and Arndt, R.E.A., "Analysis of Recent Tip Vortex Cavitation Inception Data," Proc. of 21st American Towing Tank Conference, Washington, D. C., 1986.

Arndt, R.E.A., Higuchi, H. and Quadrelli, C. J., "Tip Vortex Cavitation," Proc., ASME Cavitation and Multiphase Flow Forum, 1985, pp. 61-64.

Betz, A., "Behavior of Vortex Systems," NACA TM-713, June 1933, translated from ZAMM BD XII No. 3, June 1932.

Bilanin, A. J. and Donaldson, C. duP., "Estimation of Velocities and Roll-Up in Aircraft Vortex Wakes," Journal of Aircraft, Vol. 12, No. 7, 1975, pp. 578-585.

Billet, M. L. and Holl, J. W., "Scale Effect in Various Types of Limited Cavitation," Proc., International Symposium on Cavitation Inception, ASCE, 1979, pp. 11-23.

Fitzpatrick, H. M. and Strasberg, M., "Hydrodynamic Sources of Sound," 1st Symposium on Naval Hydrodynamics, F. S. Sherman (ed.) Publication 515, National Academy of Sciences, Washington, D. C., 1956, pp. 241-280.

Gaster, M., "The Structure and Behavior of Laminar Separation Bubbles," NPL Aero Report 1181 (revised), National Physical Laboratory, Great Britain, 1967.

Higuchi, H. and Arndt, R.E.A., "Reverberation Effects on Cavitation Noise," in Cavitation and Multiphase Flow Forum-1985, 20th Anniversary Issue, edited by J. W. Hoyt and O. Furuya, FED-Vol. 23, ASME, N. Y., 1985a, pp. 21-24.

Higuchi, H., Taghavi, R., and Arndt, R.E.A., "Sound Source Location in Cavitating Tip Vortices," in Cavitation and Multiphase Flow Forum-1985, 20th Anniversary Issue, edited by J. W. Hoyt and O. Furuya, FED-Vol. 23, ASME, N. Y., 1985b, pp. 65-67.

Ikohagi, H., Higuchi, H. and Arndt, R.E.A., "The Structure of Trailing Vortices," ASCE, Advancements in Aerodynamics, Fluid Mechanics, and Hydraulics, Minneapolis, Minnesota, May 1986.

Katz, J., "Cavitation Phenomena Within Regions of Flow Separation," Journal of Fluid Mechanics, Vol. 140, 1984, pp. 397-436.

Krasny, R., "Computation of Vortex Sheet Roll-up in the Treftz Plane," to be printed in Journal of Fluid Mechanics, 1987.

Lamb, H., Hydrodynamics, 6th edition, Dover Press, New York, 1945, pp. 591-592.

Latorre, R., Ligneul, P. and Bovis, A., "Analysis of Tip Vortex Cavitation Inception from Elliptical Planform Hydrofoils with Roll-Up and Acoustic Consideration," Proc., International Symposium on Cavitation Inception, ASME, 1984, pp. 169-175.

McCormick, B. W., Jr., "On Cavitation Produced by a Vortex Tailing from a Lifting Surface," Journal of Basic Engineering, Transaction of ASME, 1962, pp. 369-379.

Moore, D. W. and Saffman, P. G., "Axial Flow in Laminar Trailing Vortices," Proceedings of Royal Society, London, A333, 1973, pp. 491-508.

Orloff, K. L., "Trailing Vortex Wind-Tunnel Diagnostics with a Laser Velocimeter," Journal of Aircraft, Vol. 11, No. 8, 1974, pp. 477-482.

Phillips, W.R.C., "The Turbulent Trailing Vortex During Roll-Up," Journal of Fluid Mechanics, Vol. 105, 1981, pp. 451-467.

Platzer, G. P. and Souders, W. G., "Tip Vortex Cavitation Delay with Application to Marine Lifting Surfaces--Literature Survey," DTNSRDC Report 79/051, David W. Taylor Naval Ship and Development Center, 1979.

Quadrelli, C. J., "An Experimental Investigation of Vortex Roll-Up for an Elliptically Loaded Wing," M.S. Thesis, University of Minnesota, Minneapolis, MN, 1985.

Rogers, M., "Experiments in Tip Vortex Cavitation and Associated Noise," M.S. Thesis, University of Minnesota, 1987.

Spreiter, J. R. and Sachs, A. H., "The Rolling Up of the Trailing Vortex Sheet and Its Effect on the Downwash Behind Wings," Jour. Aerospace Sciences, Jan. 1951.

Squire, H.B., "The Growth of a Vortex in Turbulent Flow," The Aeronautical Quarterly, Vol. 16, 1965, pp. 302-306.

Srinivasan et al., "Numerical Simulation of Tip Vortices of Wings in Subsonic and Transonic Flows," AIAA Paper 86-1095, May 1986.

APPENDIX A

SELECTED PUBLICATIONS ON

SPECTRAL ESTIMATION

The Covariance-Constrained Maximum Likelihood Method

Gregory H. Wakefield and M. Kaveh

Department of Electrical Engineering and Computer Science
University of Michigan
Ann Arbor, Michigan USA 48109
and
Department of Electrical Engineering
University of Minnesota
Minneapolis, Minnesota USA 55455

The Covariance-Constrained Maximum Likelihood Method (CCMLM) defines a class of power spectrum estimators which adjust Capon's Maximum Likelihood Method to best fit the observed covariance of the random process. In this paper, a particular form of the CCMLM is introduced, several of its properties are discussed, and examples of its application are provided.

1. Introduction

In recent years, there has been renewed interest in spectrum estimation based on non-parametric procedures such as Capon's Maximum Likelihood Method (MLM) or the Blackman-Tukey (BT) method. This interest stems, in part, from the observation that the performance of parametric procedures may be highly sensitive to errors in the assumed model [1]. Since MLM and BT spectra are not formulated with respect to a parametric representation of the spectrum, these procedures have proven to be more robust to modelling errors than parametric methods. However, the loss in resolution, or fidelity, that is associated with these methods has remained one of their primary disadvantages. Significant research effort, therefore, has been put into the development of procedures for improving the performance of these non-parametric spectrum estimators.

Improvements have been achieved through "post-estimator" procedures in which the original estimated spectrum is modified to satisfy additional constraints. These constraints are most often stated with respect to the observed data or their statistics. Most research has focussed on the BT spectrum [2,3]. With respect to the MLM, D'Assumpcao [4] has proposed an "inverse-fit" procedure that transforms the MLM spectrum into one with a covariance matrix R' such that $R'R^{-1} \approx I$, where R is the observed covariance matrix.

In the following, we propose a new method for modifying the MLM spectrum. The Covariance-Constrained MLM (CCMLM) modifies the MLM spectrum to minimize the difference between the observed covariance matrix and that of the spectrum estimate. The paper is divided into three sections. In the first section, the basic approach of the CCMLM is presented and the unity-gain iterative solution to the covariance-matching problem is proposed. The second section considers briefly issues of convergence of the unity-gain procedure. Finally, the third section compares the performance of the unity-gain CCMLM with that of MLM for several simulated observation sequences.

2. Derivation of the CCMLM

2.1. Definitions

Let $P(\omega)$ be the original spectrum with covariance matrix R of dimension NxN. We shall refer to $P_1(\omega)$ as the MLM spectrum that is obtained from R. Let the covariance matrix of $P_1(\omega)$ be R_1 and the error covariance matrix E_1 be defined as

$$E_1 = R_1 - R \tag{1}$$

Since the MLM spectrum does not match the observed autocorrelation sequence, E_1 will be nonzero and is, in fact, guaranteed to be positive definite since $P_1(\omega) > P(\omega)$ [5]. Thus, E_1 is a valid covariance matrix and corresponds to the error spectrum $E(\omega)$ defined as:

$$E(\omega) = P_1(\omega) - P(\omega) \tag{2}$$

2.2. Transformation of $P_{MLM}(\omega)$

We are interested in transforming $P_1(\omega)$ (i.e., $P_{MLM}(\omega)$) into $P'(\omega)$ such that $R' - R = 0$. The obvious transformation is to choose

$$P'(\omega) = P_1(\omega) - E(\omega) \tag{3}$$

which, of course, cannot be achieved since we observe the *truncated* error covariance matrix E_1. Therefore, it is necessary to estimate $E(\omega)$ from E_1 and use $E_1(\omega)$, the estimated error spectrum, to modify the MLM spectrum.

The CCMLM solves the problem of estimating the error spectrum by using the MLM. Thus

$$E_1(\omega) = \frac{1}{\underline{e}^h(\omega)E_1^{-1}\underline{e}(\omega)} \tag{4}$$

where $\underline{e}(\omega)$ is the vector of Fourier coefficients. The original spectrum is then updated by computing the difference

$$P_2(\omega) = P_1(\omega) - E_1(\omega) \tag{5}$$

Since the covariance matrix for $E_1(\omega)$ is not necessarily equal to E_1,

$$R_2 \neq R \tag{6}$$

and a new, non-zero error matrix results:

$$E_2 = R_2 - R \tag{7}$$

The results above suggest the following three-step procedure for iteratively updating the CCMLM spectrum. On the i-th stage, we are given $P_i(\omega)$ from which we

1. construct the error covariance matrix

$$E_i = R_i - R \tag{8}$$

2. compute the MLM spectrum for the matrix E_i

$$E_i(\omega) = \frac{1}{\underline{v}^h(\omega) E_i^{-1} \underline{v}(\omega)} \tag{9}$$

3. update the current CCMLM spectrum

$$P_{i+1}(\omega) = P_i(\omega) - E_i(\omega) \tag{10}$$

The procedure is terminated when E_i is sufficiently close to the zero matrix.

Although other spectrum estimation methods could be used to estimate the error spectrum at each step, the MLM is chosen for several reasons. Firstly, the MLM is often used in those cases for which parametric methods are judged inappropriate because of their poor approximation or statistical properties. Therefore, having failed to estimate accurately the original spectrum, it is not clear that a parametric model should estimate the error spectrum with any greater fidelity. Secondly, among nonparametric methods, the MLM is better than BT since it gives an unbiased minimum-power estimate at each frequency. Finally, the upper-bound [5] and local properties [6] of the MLM suggest that poor fits to the error spectrum over certain regions of the spectrum will be confined primarily to neighborhoods around those regions.

The upper-bound property of the MLM, however, may also cause problems for the iterative procedure. Let us consider the equation for the first update:

$$P_2(\omega) = P_1(\omega) - E_1(\omega) \tag{11}$$

Since $E_1(\omega) \geq E(\omega)$, $P_2(\omega)$ may become negative in regions of the spectrum where the difference between $E_1(\omega)$ and $E(\omega)$ are large relative to $P_1(\omega)$. In such cases, $P_2(\omega)$ is no longer a valid power spectrum and the updated error matrix E_2 is not necessarily a covariance matrix. Since the MLM is defined for covariance matrices, the non-positive matrix E_2 presents a problem at the next stage of the iteration. One way to correct this problem is to introduce weights in the update formulas for $P_i(\omega)$ and E_i so that (i) the spectrum is always non-negative and (ii) the error matrix is always positive definite.

2.3. Unity-gain procedure

There are several methods for incorporating the positivity constraints into the update equations. In the following, we propose a suboptimal solution to this problem in which weights are selected independently at each stage of the iteration so that the unity-gain constraint of the original MLM spectrum is preserved. Under these simplifying assumptions, it has been shown that the update equations depend on a single scalar, β_i, which must be selected to satisfy the positivity constraints [6]. Therefore, the update equations for the unity-gain CCMLM are:

$$P_{i+1}(\omega) = P_i(\omega) - \beta_i E_i(\omega) \tag{12}$$

and

$$E_{i+1} = E_i - \beta_i D_i \tag{13}$$

where the matrix D_i is the covariance matrix for the estimated error spectrum at the i-th stage, $E_i(\omega)$. The sequence is initialized by

$$P_1(\omega) = \frac{1}{\underline{v}^h(\omega) R^{-1} \underline{v}(\omega)} \tag{14}$$

and

$$E_1 = R_1 - R \tag{15}$$

The β_i's are chosen at each stage such that $P_i(\omega) \geq 0$ and E_{i+1} is positive definite. In the examples that follow, β_i was selected by an iterative search procedure.

3. Convergence Properties.

Several comments with respect to the convergence of the unity-gain procedure are necessary before proceeding with examples of the CCMLM.

Tr E_i^2. It can be shown that there will always exist a non-zero β_i at each stage of the iteration that satisfies the positive-definiteness constraint. For such a β-sequence, the trace of the square of the updated sequence. Furthermore, this result can be used to show that the updated error spectrum is stable, in the sense that is does not become unbounded as the number of iterations becomes large. In proving these assertions, however, it is clear that the unity-gain CCMLM will not, in general, converge to a solution for which the error covariance matrix goes to zero. Therefore, the unity-gain CCMLM reduces the disparity between the observed and computed covariance matrices, but does not necessarily converge to an exact match.

Stopping criteria. Stopping criteria have been studied with respect to E_i and an alternative, $E_{n,i}$, which is formed by taking the difference of the two covariance matrices after each is normalized with respect to variance along the main diagonal. Our results indicate that the trace of $E_{n,i}^2$, is a better measure of performance. For many test cases, this alternative measure of performance exhibits a local minimum which corresponds to the best fitting estimate in the spectral domain. This result is consistent with the observation that further reductions in Tr E_i^2 reflect adjustments in the overall displacement of the estimated spectrum, rather than refinements in its shape. Therefore, we suggest that a stopping criterion based on this normalized error covariance matrix is preferable to one based on the non-normalized form.

Sensitivity to the β-sequence. Based on simulations, the unity-gain CCMLM does not appear to be sensitive to the choice of β-sequence; different β-sequences appear to converge to the same spectrum. The choice of β-sequence appears to determine only the rate of convergence.

4. Examples

Figures 1-4 compare the CCMLM and MLM methods for several test cases. The first two figures show results from a simulation based on a proposed model of the wall-pressure spectrum beneath a turbulent boundary layer using a linear array of sensors. The remaining figures show results from simulations based on ARMA spectra.

4.1. Wall-pressure Wavenumber Spectrum

Considerable interest exists among fluid-dynamicists with respect to the wavenumber spectrum of the wall-pressure field beneath a turbulent boundary layer. Measurements have obtained accurate estimates of this spectrum only in the neighborhood of the convective ridge which appears as a broad peak in the wavenumber domain. There is, however, considerable controversy over the nature of the wavenumber spectrum at very low wavenumbers. The dashed line in Figures 1 and 2 represent one such model of this wavenumber spectrum in which the spectrum is approximately 50 dB below the convective peak at wavenumbers of interest [7].

The nonhomogeneous nature of the turbulent boundary layer restricts the aperture of the sensor array which is used to measure the wall pressure along the boundary. Thus, this wavenumber spectrum estimation problem is similar to that found in other array signal processing problems such as bearing estimation in which the number of sensors is typically limited. However, the performance criterion differs from that most often assumed in these other applications since the estimation problem is focused primarily on the general shape of the spectrum, rather than on the resolution of spectral peaks. We are, therefore, interested in a high-fidelity rather than high-resolution procedure.

When high-resolution techniques are applied to this problem, it is found that they perform poorly in the regions of the noise floor and, therefore, are not appropriate [8]. Both the MLM and the CCMLM, on the other hand, exhibit considerably better fidelity. The results of 4 simulations based on 12 sensors and 25 snapshots are shown by the solid curves for the MLM (Figure 1) and the CCMLM (Figure 2). In general, the bias of the CCMLM in the low wavenumber region of the spectrum is reduced by more than 10 dB from that exhibited by the MLM. This decrease in bias is offset somewhat by an increase in the variance of the estimate, although the effects in this simulation are not great.

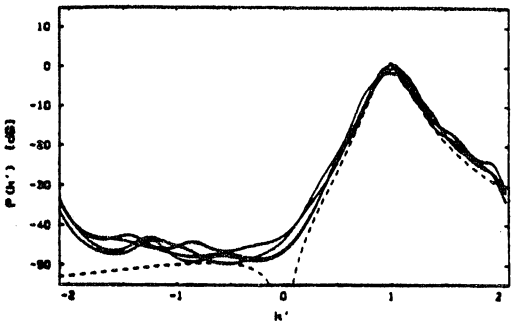

Figure 1

Simulations of the MLM (solid lines) for the Chase model of the wall-pressure wavenumber spectrum (dashed line) beneath a turbulent boundary layer. Simulations are based on 25 snapshots of a 12-sensor, uniform linear array. Wavenumber is normalized with respect to the convective peak.

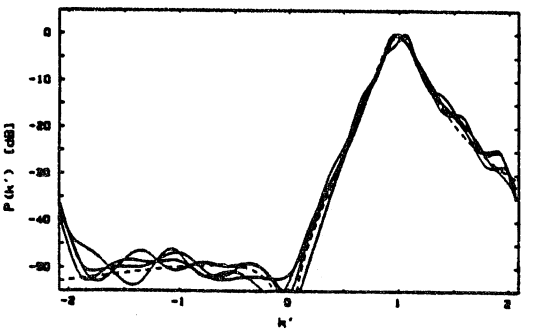

Figure 2

CCMLM results for the same conditions in Figure One.

4.2. ARMA spectrum estimation.

One of the interesting properties of the CCMLM is that it is a pole/zero form of estimator. This raises the possibility that the CCMLM may be useful in estimating ARMA spectra. The examples shown in Figures 3 and 4 are based on 25 simulations of the MLM and CCMLM. The dashed line represents the actual ARMA(2,2) spectrum (see [9] for details on the spectra). Each simulation was based on 40 samples of the ARMA process and estimates of the first 12 terms in the autocorrelation sequence. The estimated mean and variability (within 1 standard deviation of the mean) of the CCMLM spectra are shown by the solid and dotted lines, respectively.

The results support the assumption that the CCMLM is a useful procedure for estimating ARMA spectra. Several trends in the data are worth noting, however. Although the fidelity of the CCMLM is superior to that of MLM, the variance of the estimator is also larger. When compared with that for other ARMA methods, however, this variance is not unreasonable. Secondly, the CCMLM, unlike other ARMA methods, does not involve an explicit computation of model order. An initial order is, of course, implicit in the choice of dimension for the covariance matrix. This selection trades bias against variance and requires further study.

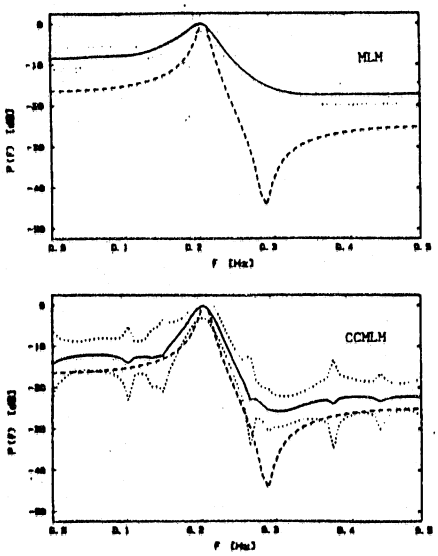

Figure 3

MLM (top) and CCMLM (bottom) estimates for ARMA(2,2) time series (dashed line) based on 40 samples and estimates of the first 12 autocorrelation lags. The solid line in each panel shows the estimated mean and the dotted lines represent a range of 1 standard deviation about the mean.

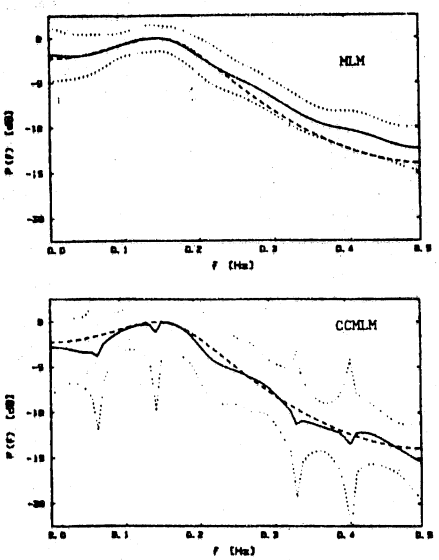

Figure 4

MLM (top) and CCMLM (bottom) for a different ARMA(2,2) time series. Conventions are the same as in Figure Three.

5. Conclusions

The CCMLM is a general procedure which modifies the MLM spectrum to obtain an estimate that is more consistent with the observed covariance matrix. An iterative suboptimal implementation of this procedure reduces the differences between the observed and computed covariance matrices, but does not guarantee that this difference goes to zero. Nevertheless, the fidelity of the unity-gain CCMLM is superior to that of the MLM and other parametric procedures when evaluated for spectra which are not dominated by multiple, narrowly spaced peaks.

Acknowledgments This work was supported by a Selective Research Opportunity in Hydroacoustics by the Office of Naval Research.

References

1. Tong, P. S. and Rees, F. L., "TBL Flow Noise Measurements Using a Maximum Entropy Method," Binary Systems Inc., ONR Contract No. N00014-72-C-0318, April, 1979.

2. Konvalinka, I. S., "Iterative nonparametric spectrum estimation," IEEE Transactions on Acoustics, Speech and Signal Processing, vol. ASSP-32, (1984), 59-59.

3. Steinhardt, A. O., Goodrich, R. K., and Roberts, R., "Spectral estimation via minimum energy correlation extension," IEEE Transactions on Acoustics, Speech and Signal Processing, vol. ASSP-33, (1985), 1509-1515.

4. d'Assumpcao, H. A., "Some new signal processors for arrays of sensors," IEEE Transactions on Information Theory, vol. IT-26, (1980), 441-430.

5. Marzetta, T. L., "A new interpretation for Capon's maximum likelihood method of frequency-wavenumber spectral estimation," IEEE Transactions on Acoustics, Speech, and Signal Processing, vol. ASSP-31, (1983), 445-449.

6. Wakefield, Gregory H., High-fidelity Estimation of Continuous Spectra, Ph.D. dissertation, Department of Electrical Engineering, University of Minnesota, Minneapolis, MN, 1985.

7. Chase, D. M., "Modeling the wavevector-frequency spectrum of turbulent boundary layer wall pressure," Journal of Sound and Vibration, v. 70, (1980), 29-67.

8. Wakefield, G. H. and Kaveh, M., "Frequency-wavenumber spectral estimation of non-planar random fields," Proceedings of ICASSP-85, Tampa, Florida (1985), 808-811.

9. Kaveh, M. and Bruzzone, S. B., "A Comparative overview of ARMA spectral estimation," Proceedings of the 1st ASSP Workshop on Spectra Estimation, Hamilton, Ont., Canada (1981).

ASME, Shear Flow-Structure
Interaction Phenomena Proc.,
A. Akay and M. Reischman eds., 1985

FREQUENCY-WAVENUMBER SPECTRAL ESTIMATION OF THE WALL-PRESSURE FIELD BENEATH A TURBULENT BOUNDARY LAYER

G. H. Wakefield and M. Kaveh
Department of Electrical Engineering
University of Minnesota
Minneapolis, Minnesota

ABSTRACT

We have investigated the application of two non-linear data-adaptive techniques to the problem of estimating the frequency-wavenumber spectrum of the pressure field beneath a Turbulent Boundary Layer. Although the Maximum Likelihood Method (MLM) exhibits greater bias at wavenumbers below the convective ridge, Monte Carlo simulations demonstrate that its variance at each wavenumber is smaller than that of the Maximum Entropy Method and is, therefore, preferred in cases of limited numbers of sensors and snapshots of data. Subspace extension of the MLM is shown to improve its performance at low-wavenumbers.

INTRODUCTION

The problem of estimating the frequency-wavenumber (ω-$\underline{k}$) spectrum of a random field is a topic of great interest in the physical sciences. While a "large-sample" theory for this estimation problem exists, in practice many of the assumptions essential to the theory are violated. Frequently, a random field is stationary and homogeneous only over relatively small spatial separations and temporal delays. According to the definition, a ω-$\underline{k}$ spectrum for such a field does not exist. Nevertheless, it is often useful to characterize the local properties of the field by a ω-$\underline{k}$ spectrum. In this case, one could apply an estimation procedure that assumes long data records and many spatial samples to a problem with very few temporal and spatial samples and hope that the results will be satisfactory. Unfortunately, they rarely are.

The problem of limited temporal and spatial records has generated a number of alternative spectral estimators. Much of the original work in this area was in time-series analysis but has been extended, over the last twenty years, to the analysis of time/space series, particularly with respect to the bearing estimation problem in radar and sonar.

This paper is as much an effort to promote cross-fertilization of ideas among investigators in fluid mechanics and spectral estimation as it is an investigation and extension of spectral estimation techniques to wall-pressure spectra. After reviewing definitions and issues concerned with sampling, we present a brief tutorial on issues and methods of importance in spectral estimation theory. We avoid a review of all known spectral estimators and instead focus attention on three estimators that have dominated research for many years. Thus, this section is not intended as a survey of the available techniques but rather as an introduction to the general problem of spectral estimation based on limited samples of a random field. We then discuss an extension of the Maximum Likelihood Method and investigate its application for estimating wall-pressure ω-$\underline{k}$ spectra.

DEFINITIONS

The autocorrelation function (acf) of a random field is defined as:

$$\phi(t_1,t_2,\underline{x}_1,\underline{x}_2) = E[\, p^*(t_1,\underline{x}_1)\, p(t_2,\underline{x}_2)\,] \qquad (1)$$

where $p(t,\underline{x})$ is the pressure of the field at position $\underline{x}$ and at time t, superscript "*" denotes complex conjugation and $E[.]$ is the statistical expectation operator.

For a stationary, homogeneous random field, the acf is invariant with respect to temporal lag and spatial separation and can be written as:

$$\phi(\tau,\underline{\xi}) = E[\, p^*(t,\underline{x})\, p(t+\tau,\underline{x}+\underline{\xi})\,] \qquad (2)$$

The frequency-wavenumber (ω-$\underline{k}$) spectrum of a stationary, homogeneous random field is the Fourier transform of the field's acf with respect to temporal lag and spatial separation:

$$P(\omega,\underline{k}) = \int\int \phi(\tau,\underline{\xi})\, e^{-j(\omega\tau-\underline{k}^t\underline{\xi})}\, d\tau d\underline{\xi} \qquad (3)$$

where "t" denotes the transpose of the vector.

Although the acf and ω-$\underline{k}$ spectrum specify completely the second-order statistics of a stationary, homogeneous random field, one or the other is often

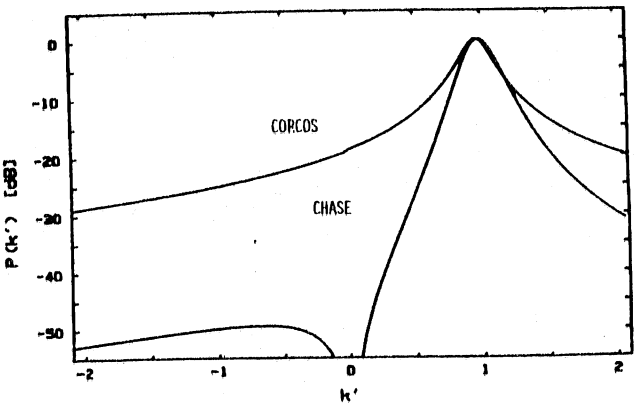

Fig. 1. Theoretical wavenumber spectra for two models (Corcos and Chase) of the wall pressure beneath a TBL are shown. The abscissa is plotted in units of k normalized by the ratio of radian frequency to convective velocity. The ordinate is plotted in dB relative to the maximum value of each individual spectrum.

more appropriate when it is necessary to characterize particular properties of the field. For example, the acf is useful in determining the temporal lags and spatial separations over which events in the field tend to be highly correlated. The ω-$\underline{k}$ spectrum characterizes directly the average distribution of power in the field across frequency and wavenumber. The latter characterization is important in the physical description of the pressure field induced by a Turbulent Boundary Layer (TBL) along the wall boundary.

MODELS OF THE WALL PRESSURE SPECTRUM

For many years, fluid dynamicists have been interested in the frequency-wavenumber characteristics of fluctuations in wall pressure that are induced by the Turbulent Boundary Layer. This interest has led to several models of the wall pressure spectrum, e.g., Corcos (1), Chase (2), and Ffocz-Williams (3).

There tends to be general agreement among theoreticians as to the properties of the wall pressure ω-$\underline{k}$ spectrum at wavenumbers corresponding to convection of turbulent pressures. At a given frequency, the wavenumber spectrum in the direction of flow is a smooth, continuous function of wavenumber which reaches a maximum at the so-called convective peak. The location of this peak is, to a first approximation, proportional to the ratio of frequency ω and convective velocity u_c. The greatest disagreement among theoreticians concerns properties of the wavenumber spectrum below the convective peak. This disagreement centers around two issues: the general roll-off in spectrum level with k and the presence of spatially narrowband components at very low wavenumbers.

An example of the differences in spectral roll-off is shown in Figure One where the Chase and Corcos models[1] of the wavenumber spectrum are compared for a normalized frequency ω^* of 0.3 ($\omega^* = \omega\delta^*/u_i$, where u_i = 10 m/s, is the free-stream velocity and $\delta^* = 0.00125$ m is the boundary layer displacement thickness).

MEASUREMENT OF THE WALL PRESSURE FIELD

Measurement of the wall pressure field is, of course, necessary as a first step towards estimating the ω-$\underline{k}$ spectrum. Various approaches have been suggested for obtaining such measurements. The approach taken in this paper measures the wall pressure field by an array of pressure transducers that are mounted flush along the surface of the wall. We consider only the one dimensional ω-k spectrum estimation problem; therefore, the geometry of the sensor array is restricted to the line and a uniform separation d between sensors is assumed. Nevertheless, the techniques developed for the one-dimensional linear uniform array can be extended directly to the estimation problem for the two-dimensional ω-$\underline{k}$ spectrum based on a rectangular uniform array.

To avoid aliasing, the wall pressure field must be sampled at frequencies and wavenumbers greater than twice the highest corresponding frequency and wavenumbers of the field. When the spectrum is not bandlimited, pre-filtering is necessary to restrict the bandwidth and thereby minimize the effects of aliasing. In the time domain, such pre-filtering is accomplished by lowpass filtering the sensor output prior to time sampling. Pre-filtering in the spatial domain is much more difficult since one cannot manipulate the field prior to sampling at the array. Therefore, the recovery of the wavenumber spectrum at a given frequency is limited directly by $\underline{d}$, the separation between the centers of adjacent sensors; components at wavenumbers above the Nyquist wavenumber[2] k_N will be aliased into the sampled spectrum.

The models of the wall pressure ω-k spectrum suggest that for each frequency the wavenumber spectrum has a bandpass characteristic and, except for the Corcos model, is predominantly one-sided. The sampling wavenumber for one-sided bandpass processes can be reduced by a factor of two since components from k_N to $2k_N$ are aliased into the zero region of the original spectrum. If we assume a one-sided spectrum and furthermore assume that the spectrum is highly attenuated above the convective peak, then the maximum frequency for which the ω-k spectrum can be recovered after spatial sampling is:

$$f_{max} = (u_c)/d \qquad (4)$$

where the convective peak is located at $k = \omega/u_c$.

The effect of finite sensor size is to lowpass filter the random field in the wavenumber domain. If the face of the sensor is assumed to be circular with

1. For the Chase model, the proportionality constants were: convective velocity/free-stream velocity = 0.8, friction velocity/convective velocity = 0.056, and boundary layer displacement/boundary layer displacement thickness = 8.0. The model parameters are from (2) and were obtained originally by fitting the model to Bull's data (4): $\mu = 0.176$, $a_t = 0.766$, $b_m = 0.756$, $b_t = 0.378$, and $r_t = 0.389$. The parameter β of the Corcos model was set to 0.11.

2. The Nyquist wavenumber k_N is defined as $k_N = 1/2\ k_s$ where $k_s = 2\pi/d$ is the sampling wavenumber (also known as either the grating lobe wavenumber or the aliasing lobe wavenumber).

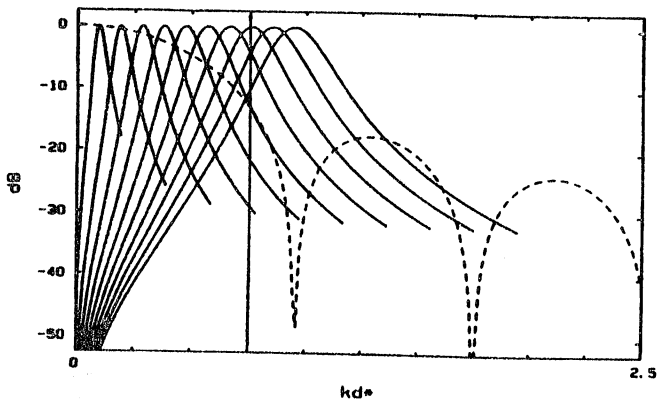

Fig. 2. Chase spectra are shown by the solid lines for various frequencies (100 to 1000 Hz in 100 Hz steps) and the spatial response of an ideal transducer (radius = 0.005m) is shown by the dashed line. The solid vertical line denotes the highest wavenumber sampling frequency that can be obtained in theory (d = 2 x radius); in practice, the sampling wavenumber will be significantly lower due to physical constraints in sensor placement.

radius r and uniformly sensitive, then the wavenumber response characteristic of the sensor can be written:

$$|H(\bar{k})|^2 = \frac{4J_1^2(\bar{k}r)}{(\bar{k}r)^2} \qquad (5)$$

where $\bar{k} = (k_1^2 + k_2^2)^{(1/2)}$ and $J_1(.)$ is a first order Bessel function.

The width of the main lobe of this lowpass filter is inversely proportional to the diameter of the sensor. Therefore, greater lowpass filtering of the wavenumber spectrum is achieved only by increasing the size of the sensor. Such an increase in size, however, increases the lower limit of the sensor spacing and therefore decreases f_{max}. Since the lower bound on d is the diameter of the sensor, finite sensor size cannot act as a "pre-filter" to attenuate the convective region of the spectrum. This is demonstrated in Figure 2 where the wavenumber response of the ideal circular sensor of radius 0.005 m is shown along with a family of wavenumber spectra generated by the Chase model with frequency as the parameter. Wavenumber is normalized to the boundary layer displacement thickness, δ^* = 0.00125 m. The maximum unaliased wavenumber of inversely proportional to the spacing of the sensors, which spacing can be as small as the sensor diameter 0.01 m; this maximum wavenumber is indicated in non-dimensional coordinates by the solid vertical line in Figure 2. Finite sensor size helps, to some extent, by further attenuating components in the wavenumber spectrum that are well above the convective region of the spectrum but it cannot prevent severe aliasing if spectra are estimated at frequencies above $f_{max} = u_c/d$.

ESTIMATION OF THE FREQUENCY-WAVENUMBER SPECTRUM

The preceding section on measurement formulated the absolute limits for the recovery of a continuous random field from its samples in time and space. These limits also restrict any estimate of the ω-k spectrum to the unaliased region of the spectrum. Besides these sampling limits, the fact that the field is measured over a finite period of time by a finite aperture array implies that even within this unaliased region of the spectrum, errorless recovery is impossible; statistical errors in the estimator and restricted samples of the acf limit the performance of any procedure.

The spectral estimation problem is posed with respect to limitations in the measurements: given a finite sample at discrete points in time and space of a random field, we are interested in processing the data to provide the "best" estimate of the ω-k spectrum.

Statistical estimators $g(\underline{x})$ are functions that operate on data $\underline{x}$ to estimate some characteristic or parameter $(\underline{\theta})$ of the data. Since the data are random, each $g(\underline{x})$ will have a probability distribution function (pdf) that depends directly on the stochastic representation of the data. Statistical estimators have many properties by which they are judged to be good. The bias $b_g(\underline{\theta})$ and variance $var_g(\underline{\theta})$ of an estimator ($\underline{\theta} = g(\underline{x})$) are the first and second central moments of pdf, i.e.,

$$b_g(\underline{\theta}) = E[\, g(\underline{\theta}) - \theta \,] \qquad (6)$$

$$var_g(\underline{\theta}) = E[\, (g(\underline{\theta}) - \underline{\theta})^2 \,] \qquad (7)$$

There are numerous ways to estimate a given characteristic of the data. In general, bias and variance are criteria that are used to determine which estimator, from a given set, is best. In the ideal case, the best estimator is unbiased and exhibits the least variance among those estimators in the set; in practice, this is not always true. Optimum estimation techniques, such as maximum likelihood estimation, are often useful in deriving a "best" estimator for a given problem. For this reason, the development of spectrum estimation theory has been based on "empirical" research in the sense that the theory consists of numerous forms of estimators each of which performs well for a given class of problems but none of which is necessarily optimum among the class of all possible estimators.

This section reviews three general forms of spectral estimator that have been proposed in the literature and discusses the performance of each with respect to bias and variance for the Corcos and Chase models of the wall pressure ω-k spectrum. We consider the problem of bias and variance separately. Initially, the effects of truncating the acf on the deterministic component of the estimator bias are studied by computing the estimated spectrum based on exact values of the truncated acf. Later, we consider bias and variance in greater detail by use of Monte Carlo simulation.

Without loss of generality, each estimator is introduced by considering the estimation of the power spectrum of a stochastic process: the results are the same for the wavenumber spectrum of a stochastic spatial field.

Let $r(\tau)$, be the autocorrelation function of the stochastic process, and let $r(\tau_i)$ be its sampled version. In practice, $r(\tau_i)$ must be estimated from the sampled process by some appropriate technique. Let $r(\tau_i)$ denote such an estimate. Finally, assume that $P(\omega)$, the power spectrum, is a lowpass process and that the sampling frequency is sufficiently high to prevent aliasing.

Fourier Transform of the Truncated acf: Blackman-Tukey and Periodogram methods

The Blackman-Tukey method estimates $P(\omega)$ by performing a discrete Fourier transform (DFT) on a windowed version of length L of the estimated acf:

$$P_{BT}(\omega) = \mathrm{DFT}[\, w(\tau_i)\, \hat{r}(\tau_i)\,] \qquad (8)$$

One computational disadvantage of the Blackman-Tukey method is that the sample acf must be estimated first from the data. The periodogram is an alternative procedure that estimates the power spectrum directly from the data $x(\tau_i)$ by segmenting the data into S sections of length N, performing a DFT on each section, and averaging over section transforms. The estimate of the power spectrum is taken as the average of the squared magnitude of the transforms. Thus:

$$P_p(\omega) = (1/S) \sum | \mathrm{DFT}[\, \underline{x}_s(\tau_i)\,] |^2 \qquad (9)$$

The Blackman-Tukey and periodogram methods yield different estimated spectra but, on the average, the periodogram method is the same as the Blackman-Tukey method with a Bartlett (triangular) window applied to the first N-1 lags.

Bias. The effect of truncating the acf at lag L on estimator bias can be studied by substituting the exact expression of $r(\tau_i)$ and computing the $P_{BT}(\omega)$. For an arbitrary window, the $P_{BT}(\omega)$ can be re-written in the frequency domain as the convolution of the true spectrum with the window function:

$$P_{BT}(\omega) = W(\omega) * P(\omega) \qquad (10)$$

where "*" denotes the convolution operator. Thus, the resulting spectral estimate is smoothed due to smearing of adjacent components in the spectrum by the main lobe and to leakage of more distant components through the sidelobes of $W(\omega)$. Bias can be reduced to arbitrarily small values but only by taking more samples of the acf.

Capon's Maximum Likelihood Method.

The general form of the averaged periodogram is:

$$P_p(\omega) = (1/S) \sum | \underline{w}^h(\omega) \underline{x}_s |^2 \qquad (11)$$

where superscript "h" denotes the conjugate transpose, and, for the specific case of the periodogram, $\underline{w}(\omega) = \underline{e}(\omega)$, the discrete Fourier operator:

$$\underline{e}(\omega) = (\, 1,\, e^{j\omega\tau_s},\, \ldots,\, e^{j\omega(N-1)\tau_s}\,)^t \qquad (12)$$

and $\underline{x}_s$ is the data x_i written in vector form:

$$\underline{x}_s = (\, x_s,\, x_{s+1},\, \ldots,\, x_{s+N}\,)^t \qquad (13)$$

Taking the expectation of both sides of Eq. (11) yields:

$$P_p(\omega) = \underline{e}^h(\omega)\, R\, \underline{e}(\omega) \qquad (14)$$

which is a quadratic form involving the covariance matrix R of the random vector $\underline{x}$:

$$R = E[\, \underline{x}\, \underline{x}^h\,] \qquad (15)$$

In the periodogram method, $\underline{w}(\omega)$ has the same form regardless of the particular ω. In Capon's formulation, $\underline{w}(\omega)$ is chosen for each frequency to minimize the expected estimate of the power subject to the constraint that the spectral component at ω is passed with unity gain:

$$\min E[\, |\underline{w}^h(\omega)\underline{x}|^2\,] \quad \text{with} \quad \underline{w}^h(\omega)\underline{e}(\omega) = 1 \qquad (16)$$

This minimization problem can be solved using Lagrange multipliers to yield:

$$\underline{w}(\omega) = \frac{R^{-1}\underline{e}(\omega)}{\underline{e}^h(\omega)R^{-1}\underline{e}(\omega)} \qquad (17)$$

and

$$P_{MLM}(\omega) = \frac{1}{\underline{e}^h(\omega)R^{-1}\underline{e}(\omega)} \qquad (18)$$

Capon's method has also been termed the Maximum Likelihood Method (MLM) although it is not the maximum likelihood estimate of power spectral density. Nevertheless, the term MLM continues to be used when referring to Capon's method and we, too, shall adhere to this (misleading) convention.

Bias. Truncating the acf in the Fourier-based methods is equivalent, for the deterministic case, to convolving the power spectrum with that of the lag window. The effects of truncation on the MLM spectrum are more difficult to characterize since the "window" changes as a function of frequency and depends on the covariance matrix R. In general, bias can only be evaluated by comparing the MLM spectrum with examples from the particular class of spectra that are under consideration.

Maximum Entropy Method

Given the sample acf, $r(\tau_i)$, truncated after lag L, an infinite number of $P(\omega)$ exist that have $r(\tau_i)$ as the first L+1 terms in their acf sequence (5). The Maximum Entropy Method selects that $P(\omega)$ from this infinite set which has the maximum entropy. This optimization problem can be written as:

$$\max \int \ln \hat{P}(\omega)\, d\omega \qquad (19)$$

such that $\hat{P}(\omega)$ satisfies

$$r(\tau_i) = \int \hat{P}(\omega)\, e^{j\tau_i\omega}\, d\omega, \quad i = 0, L \qquad (20)$$

For the one-dimensional case with uniformly spaced samples, the MEM solution reduces to another form of spectral estimator, the all-pole or autoregressive (AR) estimator, in which the wavenumber spectrum is approximated by an all-pole spectrum. Thus,

$$P_{MEM}(\omega) = \frac{\sigma_\varepsilon^2}{|\, 1 - \underline{a}^t\underline{e}(\omega)|^2} \qquad (21)$$

where the coefficient vector $\underline{a}$ is determined from the covariance matrix R (6):

$$\underline{a} = R^{-1}\underline{r} \qquad (22)$$

with

$$\underline{r} = (r(\tau_1), r(\tau_2), \ldots, r(\tau_L))^t \qquad (23)$$

Bias. By maximizing the entropy, the MEM solution forces the least amount of "structure" onto the correlation-matching $P(\omega)$. In the case of one-dimensional uniform sampling, this solution implies that an all-pole model of order L is the most entropic choice. It is not clear how bias and entropy are related. If, in fact, the spectrum is all-pole of order L, then the MEM solution is exact and there is no bias. When the spectrum is unknown and few assumptions can be made a priori as to the appropriateness of an all-pole model of given order, the question of bias remains unanswered. Considerable attention has been paid to this issue and it remains an active area of research.

Nonlinear Data-adaptive procedures.

Both MLM and AR are examples of data-adaptive procedures in which the weighting vector ($\underline{w}$) or the AR coefficient vector ($\underline{a}$) depend nonlinearly on the sample covariance R. This contrasts with the linear dependence of the two Fourier methods on R.

Interest in nonlinear data-adaptive procedures developed quickly when it was shown in the mid-1960's that such methods are better able to resolve closely spaced peaks in the spectrum than Fourier methods for equal numbers of lags and high signal-to-noise ratio. The term "high-resolution" has often been applied to estimators such as AR and MLM with reference to their superior resolution of spectra that consist of several line components in a white background noise. The study of spectral estimation has since been dominated by the problem of resolving peaks in the spectrum under conditions of very few noisy samples of the acf. Therefore, many of the high-resolution spectral estimators that have been developed over the past decade should be more appropriately labeled parameter estimators since the measure of performance reflects the accuracy with which the estimator locates the spectral peaks.

In general, the spectrum predicted by any of the models of the wall-pressure field is not dominated by narrowband peaks nor does the interest lie particularly in measuring the spectrum within the region of the broad convective peak. Instead, the research focus is on estimating accurately the wavenumber spectrum over a broad range of k. Thus, the estimator must exhibit minimum bias or high fidelity over a targetted region of the spectrum rather than resolve peaks that are located throughout the spectrum. Since both MLM and AR modeling are nonlinear data-adaptive procedures that have been designed for resolution (parameter estimation) rather than spectral fidelity (spectral estimation), it is not clear whether resolution for line spectra extends to fidelity for broad, smooth spectra.

Spectral estimation: temporal component of the ω-k spectrum.

The ω-k spectrum can be estimated in one step by applying a multidimensional version of one of the three methods discussed above, or, alternatively, in two steps by first estimating the cross-spectral density (CSD) as a function of frequency where

$$\Gamma(\omega,\xi) = \int \phi(\tau,\xi)\, e^{-j\omega\tau}\, d\tau \qquad (24)$$

and then estimating the wavenumber spectrum from the CSD using

$$P(\omega,k) = \int \Gamma(\omega,\xi)\, e^{jk\xi}\, d\xi \qquad (25)$$

Because of its computational efficiency and well-developed theory of bias and variance, the Fourier approach is generally preferred when there is sufficient data available for processing. In the case of TBL studies, the amount of data sampled over time is limited primarily by the availability of storage space and by the time span of the experiment. The number of spatial samples, however, is usually very restricted both because of the difficulties associated with calibrating and maintaining large arrays and because of the relatively small range over which the pressure field can be assumed to be homogeneous. Therefore, a two-stage approach to the estimation problem is appropriate in which the frequency component is estimated from DFTs of the sampled time series of each of the sensors.

Spectral estimation: spatial component of the ω-k spectrum.

Assume that the pressure field is sensed by an N-element linear uniform array. Let $\underline{x}_s(j\omega)$ be the s-th snapshot of the linear array at frequency ω, i.e., $\underline{x}_s(j\omega)$ is a complex N-dimensional vector with components $x_{s,i}(j\omega)$ equal to i-th sensor output that is evaluated at complex frequency $j\omega$ over the s-th time segment of the data. As noted above, $x_{s,i}(j\omega)$ can be obtained by performing a DFT on the time-segmented data. The sample cross-spectral density matrix (CSDM) at frequency ω, $R(\omega)$, is formed by summing across the outer product of the snapshots:

$$R(\omega) = (1/S) \sum \underline{x}_s(j\omega)\, \underline{x}_s^h(j\omega) \qquad (26)$$

For notational convenience, the dependence of R and $\underline{x}_s$ on ω is assumed implicitly, so the argument ω is dropped.

A periodogram estimate of the wavenumber spectrum is equivalent to appropriately steering the beam of the array for a desired wavenumber k and taking the squared magnitude of the steered array output as the estimate of the wavenumber spectrum:

$$P_p(k) = \underline{e}^h(k)\, R\, \underline{e}(k) \qquad (27)$$

where $\underline{e}(k)$ is the discrete Fourier operator with respect to the spatially sampled data.

Recall that the primary concern with the Fourier approach is the potential bias that can exist due to smearing of the true spectrum by the main lobe of the lag window and leakage of the spectrum through the side lobes. For a small number of sensors, the degrees of freedom available for designing a suitable lag window are restricted so that an array response with sufficient selectivity at the k of interest and nulls away from that k is difficult, if not impossible, to design for arbitrary spectra and for all k.

Spatial analogs for AR and for MLM follow directly from the temporal results by denoting the output of the spatial sensors at a given ω as the data and substituting the sampled CSD and CSDM for $\underline{r}(\tau_i)$ and the covariance matrix R, respectively.

The performance of the periodogram is compared with MLM and AR modeling in the two panels of Figure 3

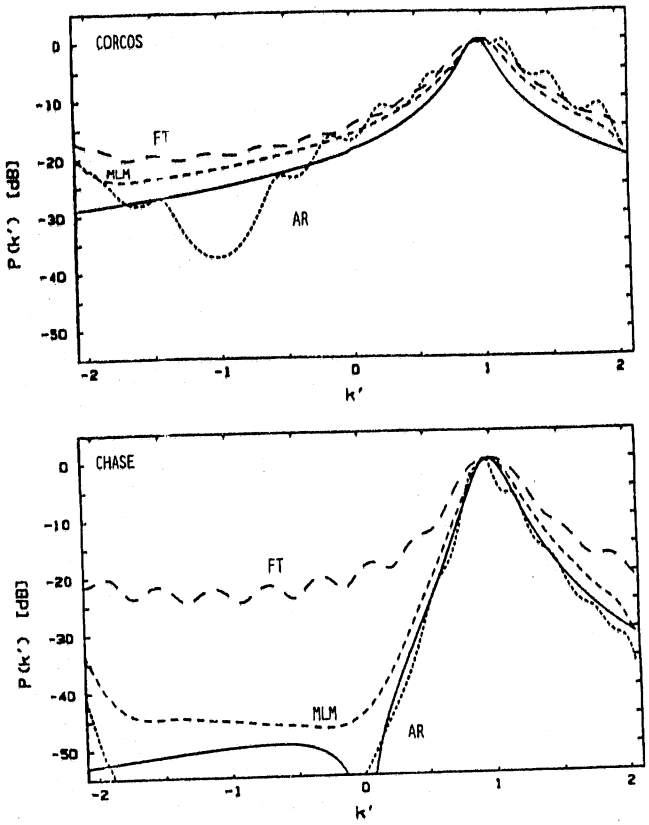

Fig. 3. The performance of three spectral estimators, Fourier transformation (FT), Maximum Likelihood Method (MLM), and Auto-Regressive Modeling (AR) are compared for the Corcos and Chase models of the wall-pressure wavenumber spectrum. The computed spectra are based on exact values of the CSDM for a 12-sensor linear uniform array.

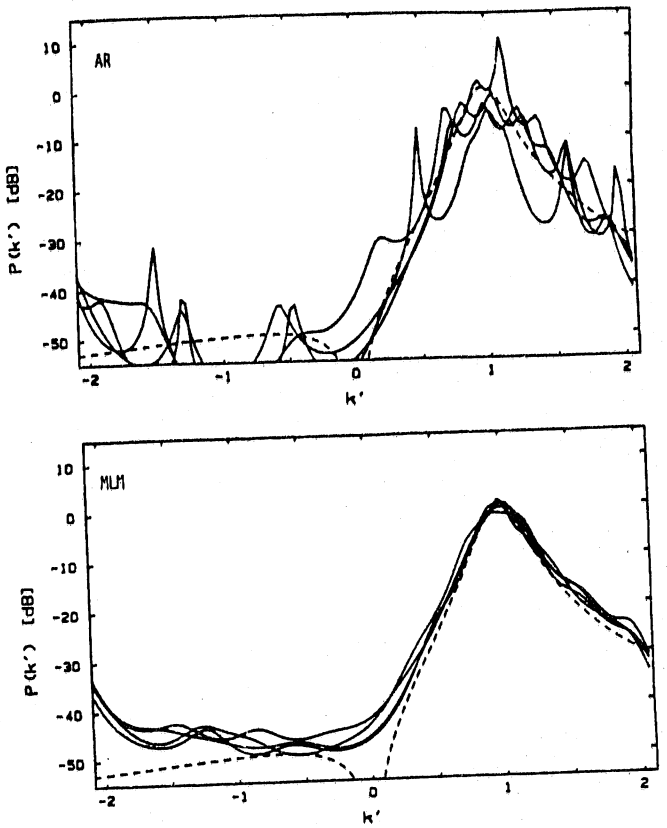

Fig. 4. The performance of two spectral estimators, MLM and AR, are compared when the CSDM is estimated from 25 snapshots of the 12-sensor linear uniform array. The Chase spectrum is shown by the dashed lines and the four simulations for each estimator are shown by the solid lines.

for the Chase and Corcos models (dotted lines) of the wall pressure wavenumber spectrum. For comparison purposes, the methods are evaluated based on a linear uniform array of 12 sensors[3]. The results are based on the exact CSDM for each model. Each result is referenced with respect to its peak.

The performance of the periodogram is reasonably accurate for the Corcos model but is considerably biased for the Chase model. Therefore, the Corcos model is sufficiently broad and smooth that convolving it with the wavenumber spectrum of the lag window, e.g., the beampattern of the 12-sensor array, has little effect on the final estimate. On the other hand, the periodogram is unable to follow the spectral roll-off of the Chase model due primarily to the effects of sidelobe leakage. The differences between the two computed spectra are very slight. If the effects of statistical error in estimating the CSDM are included, the distributions of the estimator for the two spectra overlap considerably. Therefore, the periodogram (beamforming) method is inadequate as an estimate of the wavenumber spectrum, particularly in the very low wavenumber regime.

The AR model and the MLM follow the general trend of the two models quite well. When referenced to the peak level, MLM provides an upper bound on the underlying spectrum in both cases. AR, on the other hand, exhibits less bias, on the average, particularly for the Chase model, but also introduces rippling in both of the computed spectra. This rippling reflects the poor fit between these spectra and ones generated by all-pole models of order 11. The two methods differ considerably with respect to bias in the very low wavenumber region of the spectrum. MLM shows more than 10 dB of bias for wavenumbers that are less than 1 decade below the convective peak. AR, on the other hand, exhibits little bias over this region.

Variance of the estimates. It is difficult, in general, to obtain a closed-form expression for the variance of the AR spectral estimate for the small-sample case. Therefore, Monte Carlo simulations were performed to study the sensitivity of AR and of MLM to statistical errors in the estimate of the CSDM, R, from the data. Instead of simulating the data vector x under ($j\omega$) directly, R was simulated using a complex Wishart distribution (7). Figure 4 compares the results of four simulations with the actual spectrum when R is estimated from 25 snapshots of the data. As

3. As the final goal of the estimation design is to process data from the SAFHL (Saint Anthony Falls Hydraulics Laboratory) test facility at the University of Minnesota, all methods were evaluated within the limits of the number of sensors available for the experiment.

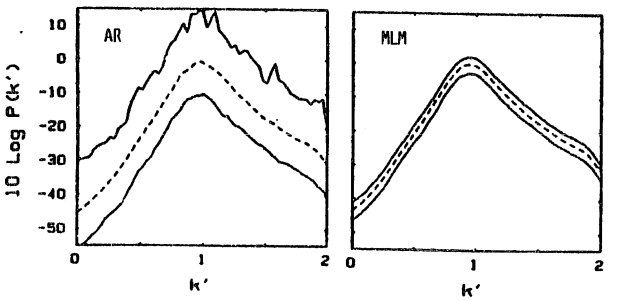

Fig. 5. 95% confidence intervals based on 200 simulations of the AR and MLM estimators are shown by the solid lines and the mean is shown by the dashed line. Monte Carlo simulations were based on 25 snapshots from a 12-sensor linear uniform array.

can be seen, the effects of statistical error on the performance of AR are substantially greater than those on MLM. Figure 5 shows 95% confidence intervals that are based on 200 simulations which support these conclusions.

Evaluation of the three methods

The effect of truncating the cross-spectrum on the bias can be reduced, for each estimator, only by increasing the total number of sensors. Since this value is determined by the constraints of the experiment, a periodogram (beamforming) approach cannot recover the underlying spectrum with sufficient fidelity in the low-wavenumber region. The truncation effects are less severe for both MLM and AR; MLM overestimates the underlying spectrum whereas AR exhibits fidelity which is superior to that of MLM, particularly at low wavenumbers for the Chase spectrum, but introduces false "peaks" or "ripples" throughout the computed spectrum. Nonetheless, AR is considerably more sensitive to statistical errors than MLM. Thus, the superior fidelity of AR can be realized, in practice, only by increasing substantially the number of snapshots used to estimate the CSDM. MLM, on the other hand, is less sensitive to these effects but is also more biased than AR in the region of interest.

In addition to statistical error, the performance of each method can be degraded by mismatches in phase and amplitude across the sensors and by errors in sensor placement. Studies of these effects have shown that AR is also more sensitive than MLM to these errors in the design of the linear array (8, 9).

SUBSPACE EXTENSION OF CAPON'S METHOD: ss-MLM

The relatively stable behavior of MLM suggests that it is a useful estimate of the upper bound of the true wall-pressure wavenumber spectrum at a given ω. In the following, we develop a new method whereby the performance of MLM can be improved over a targeted region of the spectrum.

Consider the eigen-decomposition of the CSDM R:

$$R = \sum \lambda_i \, \underline{z}_i \, \underline{z}_i^h \qquad (28)$$

where λ_i and $\underline{z}_i$ are the i-th eigenvalue and eigenvector of R, respectively. Substituting this expression

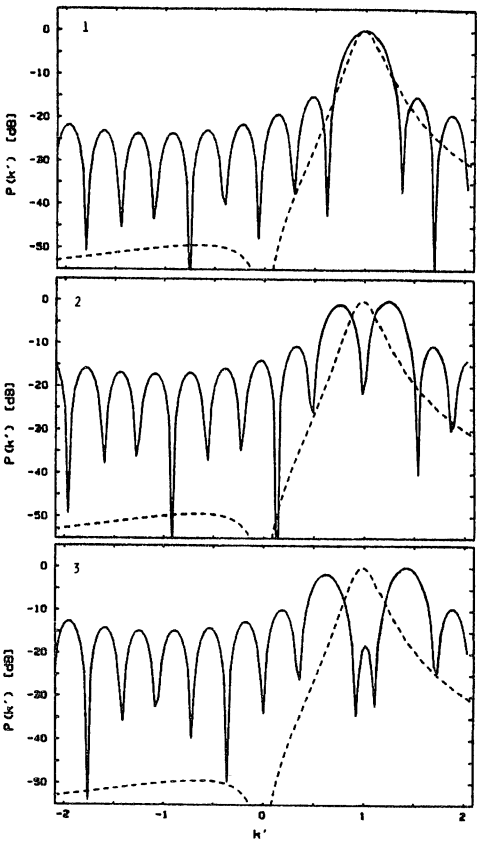

Fig. 6. Eigenbeams for the Chase model (dashed line) based on a 12-sensor linear uniform array are shown by the solid lines for the first three largest eigenvalues.

into Eq. (18),

$$P_{MLM}(k) = \frac{1}{\underline{e}^h(k)\left(\sum 1/\lambda_i \, \underline{z}_i \, \underline{z}_i^h \right)\underline{e}(k)} \qquad (29)$$

we find

$$P_{MLM}(k) = \frac{1}{\sum 1/\lambda_i \, | \, Z_i(k) \, |^2} \qquad (30)$$

where $Z_i(k) = \underline{z}^h \, \underline{e}(k)$. Thus, the MLM estimate at each k is inversely proportional to the weighted sum of the power in each Fourier transformed eigenvector at that k.

Let us consider the spectral properties of the eigenvectors of the Chase CSDM. In Figure 6, the eigenbeams, e.g., $| Z_i(k) |^2$, of the eigenvectors that correspond to the three largest eigenvalues of the Chase spectrum are shown. These eigenbeams vary with eigenvalue dominance. The main lobe of the largest eigenvector (the eigenvector with the largest eigenvalue) is centered on the convective peak of the spectrum. For the second and third eigenvectors, the mainlobe splits in two and a slight null is introduced.

at the convective peak. For smaller eigenvectors (not shown in the Figure) a single mainlobe structure reappears first at low wavenumbers and finally in the negative wavenumber region of the spectrum. Along with this migration in the location of the mainlobe, the null in the eigenbeam becomes stronger and broader at the lower eigenvalues and is localized in the neighborhood of the convective peak.

Reduction of Bias: Subspace Analysis

As argued above, the performance of the MLM over a specific region of the wavenumber spectrum is determined by the relative dominance of the weighted powers of the eigenvectors in that region. Thus, an improvement in the fidelity may be achieved by performing the MLM on an appropriate subspace of R, rather than on the full space.

To determine an such appropriate subspace, the performance of the MLM over all possible subspaces of R must be determined for the targetted region of the spectrum. Given a suitable choice of error metric d(.,.), the problem becomes:

$$\min \; d(\hat{p}(k), p(k)) \qquad (31)$$

where the minimization is performed over all possible subspaces R_s of R and p(k) is termed the design spectrum. The subspace estimate takes the form:

$$P_{ss\text{-}MLM}(k) = \frac{1}{\sum 1/\lambda_j \mid z_j(k) \mid^2} \qquad (32)$$

where the summation extends over the indices of the chosen subspace R_s.

The search procedure for the optimal subspace is over all possible combinations of the CSDM eigenspaces and thus can become computationally intensive even for a moderate number of sensors. An alternative search procedure is used for designing the subspaces for the Chase and Corcos spectra. This procedure searches through an embedded set of subspaces by removing, at each stage, the eigenspace of the largest eigenvalue of the subspace and selecting as the "optimal" subspace that which minimizes the mean-square error between the estimate and the design spectrum over wavenumbers between 0 and the convective peak.

Figure 7 shows results from four Monte Carlo simulations in which the MLM was performed on the subspace spanned by the 10 smallest eigenvectors of the estimated CSDM. The procedure reduces the bias from 10 to 4 dB within one decade below the convective peak. Furthermore, the procedure is not overly sensitive to statistical error as was the case for AR. Similar results were obtained for the Corcos model. For this spectrum, however, the minimizing subspace was spanned by the 11 smallest eigenvectors.

Further Refinement

The subspace technique can be further refined by including fractional weighting of the eigenspaces. Under such an approach, each eigenspace is assigned a value between 0 and 1 rather than the binary value 0 or 1. The advantage of fractional weighting is that a better fit to the design spectrum over the targetted region can be achieved. This refinement of the procedure is far more sensitive to statistical errors.

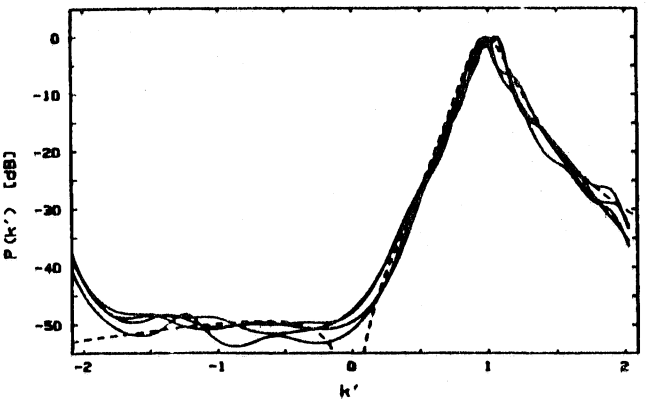

Fig. 7. The performance of the MLM using the subspace of the CSDM spanned by the 10 smallest eigenvectors, i.e., the eigenvectors corresponding to the 10 smallest eigenvalues, is compared with the Chase spectrum. Each solid line denotes the simulated performance of a 12-sensor linear uniform array using 25 snapshots of the data.

Since the weighting scheme depends on the exact eigenvalues, statistical errors in the estimated eigenvalues are equivalent to "de-tuning" the refinement procedure. Therefore, the success of fractional weighting depends to a large extent on the sensitivity of the spectral error metric to perturbations in the weights which, in turn, is a function of the design spectrum.

CONCLUSIONS

Estimation of the frequency-wavenumber spectrum of a random field is a difficult problem when relatively little data is available. Sources of error in the estimated spectrum include truncation of the acf and statistical errors in estimates of the acf. Nonlinear spectral estimators exist and are known to perform well for certain classes of frequency-wavenumber spectra under a resolution criterion. These estimators, however, are not necessarily the best choice for all classes of spectra. In particular, the class of smooth, broad spectra that are thought to be characteristic of the wall-pressure fluctuations beneath a Turbulent Boundary Layer are estimated with greater fidelity by the Maximum Likelihood Method rather than by Auto-Regressive modeling, i.e., the Maximum Entropy Method for the case of a linear uniform array. Further improvement in the fidelity of the estimate can be realized by performing the Maximum Likelihood Method on an appropriately selected subspace of the cross-spectral density matrix R.

ACKNOWLEDGEMENTS

The authors wish to thank the anonymous reviewer for the careful review and useful suggestions. This work was supported by a Selected Research Opportunity in Hydroacoustics from the Office of Naval Research.

REFERENCES

1. Corcos, G. M., "Resolution of Pressure in Turbulence," J. Acoust. Soc. Am., vol. 35, no. 2, pp. 192-199, Feb. 1963.

2. Chase, D. M., "Modeling the Wavevector-Frequency Spectrum of Turbulent Boundary Layer Wall Pressure," J. Sound Vib, vol. 70, no. 1, pp. 29-67, 1980.

3. Ffowcs Williams, J. E., "Boundary-Layer Pressures and Corcos Model: A Development to Incorporate Low-Wavenumber Constraints," J. Fluid Mech., vol. 125, pp. 9-25, Dec. 1982.

4. Bull, M. K., "Wall pressure fluctuations associated with subsonic turbulent flow," J. of Fluid Mech., v. 28, pp, 719-754, 1967.

5. Pisarenko, V. F., "The Retrieval of Harmonics from a Covariance Function," Gephys. J. R. Astr. Soc., vol. 33, pp. 347-366, 1973.

6. Lacoss, R. T., "Data Adaptive Spectra Analysis Methods," Geophysics, vol. 36, pp. 661-675, Aug. 1971.

7. Capon, J. and Goodman, N. R., "Probability Distributions for Estimators of the Frequency-Wavenumber Spectrum," Porc. IEEE, vol. 58, pp. 1785-1786, 1970.

8. Tong, P. S. and Rees, F. L., "TBL Wavenumber Spectral Measurement Using Maximum Likelihood Methods," Binary Systems Inc., ONR Contract No. N00014-72-C-0318, April 1979.

9. Tong, P. S. and Rees, F. L., "TBL Flow Noise Measurement Using A Maximum Entropy Method," Binary Systems Inc., ONR Contract No. N00014-72-C-0318, April 1979.

FREQUENCY-WAVENUMBER SPECTRAL ESTIMATION OF NON-PLANAR RANDOM FIELDS

Gregory H. Wakefield and M. Kaveh

Department of Electrical Engineering
University of Minnesota
Minneapolis, MN 55455

ABSTRACT

Spectral estimation for a class of smooth, broad spectra generated by the Turbulent Boundary Layer is discussed in terms of spectral fidelity and sensitivity to statistical error. When the number of sensors is limited, which is often the case in array problems, MLM-based estimators exhibit better performance than all-pole models. These performance differences underscore the fact that for certain classes of spectra high-resolution and high-fidelity are competing criteria.

INTRODUCTION

The past twenty years have witnessed a growth in the number of spectral estimators used in array processing, particularly in the area of source-angle estimation. Although this problem and its time-series equivalent, the estimation of frequencies of sinusoids, have often been approached within the context of spectral estimation, both are more appropriately characterized as parameter-estimation problems for which source-wavenumber (or frequency) serves as the unknown parameter. New estimators of source angle are often evaluated on the extent to which the spectrum is resolved into peaks that correspond to the correct bearing of each of the sources. In the more general case of spectral, as opposed to parameter, estimation, the 'typical' spectrum may not be dominated by strong peaks so that estimators which exhibit high-resolution may exhibit worse performance than others because of poorer fidelity in regions away from the spectral peaks. Our work focuses on the problem of spectral estimation as opposed to parameter estimation, and is motivated specifically by a measurement problem in fluid dynamics.

WAVENUMBER SPECTRUM OF THE TBL

For well over a century, turbulence has been a dominant focus of research in fluid dynamics, both from a theoretical as well as measurement standpoint. Due to its stochastic nature, most efforts have been directed to characterizing the first and second-order statistics of the turbulent field. Models based largely on theory predict a broad, unimodal wavenumber spectrum in the direction of streamwise flow for wall pressure beneath a turbulent boundary layer (TBL). For wavenumbers near the convective peak, the models are consistent with physical measurement, but for low wavenumbers, where reliable data is almost nonexistent, these models differ significantly with respect to level and smoothness of the spectrum. Although the spectrum level at low wavenumbers is believed to be small, e.g., 30-50 dB below that of the convective peak, accurate estimates are essential to an understanding of turbulence and its effect on the structural stability of non-rigid boundaries. Thus, an estimator that performs well primarily in the peak region of the TBL spectrum is not satisfactory; only one that performs uniformly well over a (possibly) large dynamic range will adequately solve the TBL measurement problem.

The measurement problem is all the more difficult because, in this case, estimation of the spectrum cannot be translated into a parameter-estimation problem. The theoretical models are primarily qualitative descriptions of the true wavenumber spectrum and thus could bias estimates based on inaccurate parametric forms. In addition, the speculative nature of the models prevents their use as vehicles for hypothesis-testing formulations of the spectral-estimation problem. At best, the models can serve as test cases for evaluating the performance of a given estimator; at worst, they can lead to erroneous conclusions about an estimator's performance over a more general class of TBL spectra.

Several other aspects of the TBL measurement problem increase the difficulty of determining an appropriate spectral estimator. As is often the case in array processing, physical factors prevent the use of large arrays so that the class of possible estimators is restricted to those that perform well based on very few samples of the cross-spectrum. Finally, the uncertainty with respect to spectral smoothness in the low-wavenumber region

CH2118-8/85/0000-0808 $1.00 © 1985 IEEE

Subspace Analysis

Source-bearing estimators based on the projection of the SCM onto the signal subspace have proven to yield excellent performance in many signal/noise environments. The success of these estimators depends, to a large extent, on the eigenvalues of the SCM; only when these break down into two distinct sets can the covariance space be decomposed accurately into signal and noise subspaces. The SCM for the Chase model, however, has no such clear-cut distinction between different portions of the eigenspace; the eigenvalues are distributed almost uniformly in dB over a 50 dB range. Nevertheless, a subspace formulation of the MLM can improve performance over a restricted region of the spectrum.

The amplitude spectra of the SCM eigenvectors reveals that each eigenvector is dominant over a relatively restricted portion of the wavenumber spectrum. Thus, one method of improving performance at low wavenumbers is to project the SCM onto the space spanned by those eigenvectors with beam patterns having main lobes away from the convective peak. Since the spectral density is greatest in the vicinity of the convective peak, this projection is equivalent to projecting the SCM onto the s smallest eigenvectors. Let $\underline{z}_i$ denote the i-th eigenvector, ranked in order of descending eigenvalues (λ_i). Then the MLM based on the subspace spanned by the s smallest eigenvectors can be written as:

$$P(k) = \{ \underline{e}^h(k) \, [\Sigma_1^s (1/\lambda_i) \underline{z}_i \underline{z}_i^h] \, \underline{e}(k) \}^{-1}$$

where $\underline{e}(k)$ is the direction vector for wavenumber k. This formulation, in effect, throws out what would be considered the "signal space" in the bearing-estimation problem and estimates the spectrum from the "noise space".

The simulations shown in Fig. 4 are the result of projecting the SCM onto the subspace spanned by the 8 smallest eigenvectors for a 12-sensor array based on the Chase spectrum. These results show that projecting the SCM onto the appropriate subspace improves the performance of the MLM over particular portions of the wavenumber spectrum. The demonstrated success of this "crude" subspace version of the MLM suggests the use of more general weighting schemes of the eigenspace to optimize performance over restricted regions of the wavenumber spectrum.

CONCLUSIONS

The MLM is superior to AR for TBL spectra with respect to spectral fidelity, smoothness, and statistical stability. An added advantage of MLM over other classes of estimators, particularly when little is known about the true spectrum, is that it always forms an upper bound of the true spectrum [7]. Nevertheless, the optimality of the MLM or of its subspace version has certainly not been demonstrated. Our efforts on the TBL measurement problem continue to be dominated by a search for estimators which are robust statistically and are not overly sensitive to modeling errors.

The primary purpose of this paper was to draw attention to the growing need for spectral estimators designed for wavenumber spectra that are typically smooth rather than peaked. This problem is particularly acute in the array case where the number of spatial samples is very small. The design of such estimators must be considered with some care. When spectral peaks are not desired, estimators such as low-order AR may introduce inappropriate peaks in the spectrum and lead to false conclusions about the true spectrum. Frequently, the processes underlying the random field are poorly understood, as is the case in turbulent boundary layer research. These cases pose, perhaps, the most difficult problem in spectral estimation in as much as the estimator must be designed around a broad class of possible spectra; performance for one or two exemplars of such a class may not be indicative of that for the entire class.

ACKNOWLEDGEMENTS

This work was supported by a Selected Research Opportunity in Hydroacoustics from the Office of Naval Research.

REFERENCES

[1] R. T. Lacoss, "Data Adaptive Spectral Analysis Methods," *Geophysics*, vol. 36, pp. 661-675, Aug. 1971.

[2] D. M. Chase, "Modeling the Wavector-frequency Spectrum of Turbulent Boundary Layer Wall Pressure," *J. Sound Vib.*, vol. 70, no. 1, pp. 29-67, 1980.

[3] G. M. Corcos, "Resolution of Pressure in Turbulence," *J. Acoust. Soc. Am.*, vol. 35, no. 2, pp.192-199, Feb. 1963.

[4] J. Capon and N. R. Goodman, "Probability Distributions for Estimators of the Frequency-wavenumber Spectrum," *Proc. IEEE*, vol. 58, pp. 1785-1786, 1970.

[5] A. B. Baggeroer, "Confidence Intervals for Regression (MEM) Spectral Estimates," *IEEE Trans. Inform. Theory*, vol. IT-22, pp. 534-545, Sept. 1976.

[6] A. Moffet, "Minimum-Redundancy Linear Arrays," *IEEE Trans. Ant. and Prop.*, vol. AP-16, no. 2, March 1968.

[7] T. L. Marzetta and S. W. Lang, "Power Spectral Density Bounds," *IEEE Trans. Inform. Theory*, vol. IT-30, no. 1, pp. 117-122, Jan. 1984.

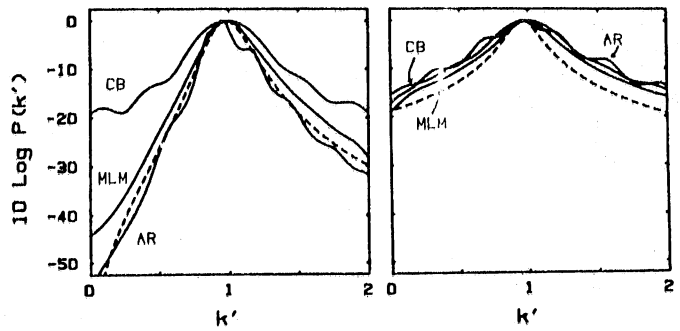

Fig. 1. CB, MLM, and AR estimates of the TBL wavenumber spectrum are shown for two theoretical models of the spectrum: Chase (left) and Corcos (right).

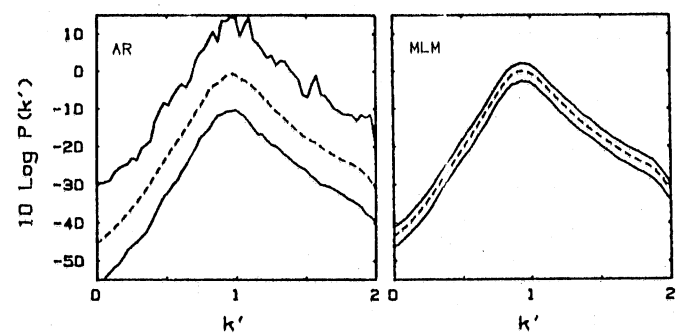

Fig. 2. 95% confidence intervals based on Monte Carlo simulations are shown for AR (left) and for MLM (right). The simulations were based on 24 snapshots from a 12-sensor array and used the Chase model of the TBL spectrum. The solid line denotes the average spectra.

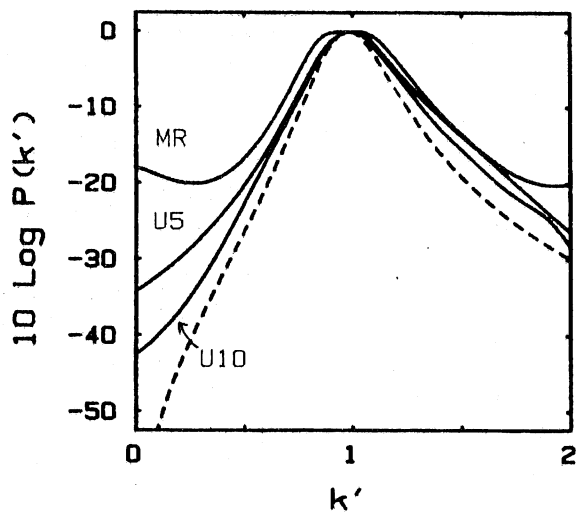

Fig. 3. Performance of the MLM (solid) is compared with the Chase spectrum (dotted) for minimum redundancy (MR), sensor-equivalent uniform (U5), and aperture-equivalent uniform (U10) arrays. All spectra are based on the exact SCM.

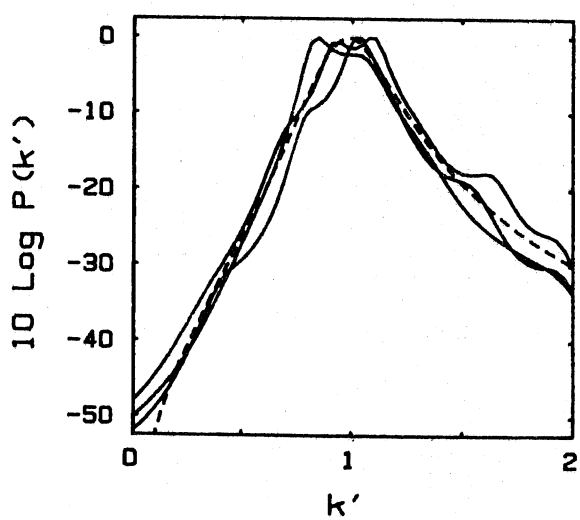

Fig. 4. Three simulations (solid) of a subspace formulation of the MLM are shown for the Chase model (dotted) of the TBL spectrum.

penalizes estimators that introduce distortion in the form of peaks or ripples in the spectrum.

EVALUATION OF THREE SPECTRAL ESTIMATORS

In an attempt to isolate properties that are essential to the TBL measurement problem, the performance of three, well-known estimators [1] was studied. Evaluations of conventional beamforming (CB) with a triangular taper, Auto-Regressive Modeling (AR) and the Maximum Likelihood Method (MLM) were based on spectral fidelity and sensitivity to statistical error using the Chase [2] and Corcos [3] models of the TBL spectrum. These models were chosen for their extremes in dynamic range and therefore provide a means to assess performance across the class of spectra that vary in rolloff below the convective peak.

Spectral fidelity

The spectral fidelity of the estimators can be determined by comparing the computed (solid lines) against the theoretical (dotted lines) spectra in the two panels of Fig. 1. For purposes of illustration, all spectra are based on the exact spatial covariance matrix (SCM) at a given frequency for a twelve-sensor, linear uniform array.

The poor fidelity of CB at low wavenumbers is not surprising given the leakage of power from the convective region which is expected from a twelve-sensor beamformer; it is clear from the slight differences between the two computed spectra that energy near the spectral peak dominates the CB spectrum at all wavenumbers.

Compared with the CB results, MLM and AR provide much better fits to the theoretical spectra. The superior dynamic range of AR, however, is also accompanied by spectral rippling and thus compromises any smoothness criterion. To achieve accurate, smooth fits to such TBL spectra, the order of the AR model must be increased well beyond the number of sensor elements; lower order models produce even greater distortion in the form of rippling.

Statistical error

The comparisons in the previous subsection were based on the exact values of the SCM. To determine the effects of statistical error, the performance of each estimator was studied by modeling the snapshot-averaged estimate of the SCM as a complex-Wishart random matrix and performing Monte Carlo simulations. Results for the Chase spectrum are reported and are based on 24 snapshots from a 12-sensor, linear uniform array.

Fig. 2 shows 95% confidence intervals (solid lines) along with the average estimator performance based on a 12x12 SCM for AR (left panel) and for MLM (right panel). The results are consistent with known statistical properties of the estimators [4,5]; the confidence intervals for AR are substantially greater than those for MLM. This greater sensitivity of AR to statistical error is often compensated by its higher resolution in those cases where the spectrum is dominated by narrowband peaks [5]. The present results indicate that AR loses its advantage over the statistically more stable MLM for smooth spectra such as the TBL spectrum.

EXTENSIONS OF THE MLM

The good spectral fidelity and relative insensitivity to statistical error exhibited by the MLM for TBL spectra is encouraging and raises the possibility that better performance may be achieved through extensions of the MLM. We report on two attempts at improving the performance of the MLM, particularly in the low-wavenumber region.

Non-uniform array geometries

Non-uniform array geometries have produced improved source-bearing estimates by increasing the array aperture for a fixed number of sensors. A non-uniform formulation of the MLM based on a Minimum Redundancy array [6] of five sensors produced, somewhat unexpectedly, a degradation in performance from that achieved by a uniform array of five sensors for the Chase and Corcos spectra. These results are shown in Fig. 3 for the Chase spectrum along with the computed MLM spectrum for a 10 sensor, linear array that has the same aperture as the MR, five sensor array.

The apparent discrepancy between source-bearing and the TBL results can be accounted for by differences in the beampatterns of the MR and uniform arrays. Although MLM does not depend directly on the array beampattern, as is the case for conventional beamforming, it nevertheless molds the optimum steering vector out of the array beampattern. Examination of the beampatterns for the two arrays reveals narrower mainlobe and higher sidelobe levels in the MR array than for the uniform array which would enhance the ability of the MR array to suppress components near the target wavenumber but reduce its ability to suppress components far away. This underscores the fact that resolution and spectral fidelity may be competing criteria, depending on the nature of the underlying spectrum.

APPENDIX B

INTERNAL MEMORANDA ON A WAVE GUIDE MODEL OF BOUNDARY LAYER PRESSURE FLUCTUATIONS

V. Estimate of the Low Frequency Power Spectrum of Wall Pressure Fluctuations

by

Robert F. Lambert
Institute of Technology
University of Minnesota

Introduction

Up to the present most descriptions of wall pressure fluctuations in wind tunnels, water tunnels, and the like have been based on two point space-time correlation measurements. Regardless of experimental techniques whatever facts we know about these fluctuations, say power spectra, must be gleaned from experimental observation. The best information to date which comes from wind tunnel data employing flush mounted pressure sensitive transducers of various sizes lies in a restricted normalized frequency range

$$0.02 \lesssim \frac{\omega \delta^*}{V_\infty} = \tilde{\omega} \lesssim 10 \qquad (1)$$

where V_∞ is the free stream velocity of the fluid and δ^* is the displacement boundary layer thickness. Power spectra measurements at lower frequencies have been contaminated by acoustic noise which can dominate the wall pressures and hence are not deemed valid.

Nevertheless, we would like reasonable estimates of the wall pressure power spectra due to turbulence at lower frequencies, i.e. $\tilde{\omega} < 0.02$ in order to design experiments, predict the performance of new electronic instrumentation designed to make pressure measurements in low noise facilities, and make other acoustic power predictions.

The work here presented describes one approach to that low frequency estimate. It is a semi-empirical approach based on experimental information

about the space-time correlations and power spectrum-gathered at higher frequencies together with an estimate of the low frequency characteristics in the spectrum obtained by viewing the turbulent boundary layer as a sort of convective waveguide of finite width. It is called a "convective waveguide model". This information in turn can be used to estimate a half-power bandwidth and center frequency for the spectrum. In order to estimate the spectral level at and below the low frequency cut-on for boundary layers of finite thickness a wave number translation is hypothesized. The model also is useful in estimating the wavenumber/frequency pressure spectrum at low frequencies and low wavenumbers at low mach numbers.

Background

In order to make the extension to lower frequencies a normalized space-time correlation function $R_n(\xi,\eta,\tau)$ and a normalized power spectrum $\Phi_n(\omega)$ will be utilized. They are related by the expression

$$\Phi_n(\omega) = \int_{-\infty}^{\infty} R_n(0,0,\tau)e^{i\omega\tau}d\tau \qquad (2)$$

where τ is a time delay and ξ and η are longitudinal and lateral spatial separation variables, respectively.

Although many phenomenological models of R_n have been proposed to represent experimental observations none, even the most elaborate ones, have been entirely successful. Since no reliable low frequency data now exist only a very simple model for $\Phi_n(\omega)$ will be here proposed. Later, a more elaborate model can be developed if the data warrant.

Accordingly, the trial function for R_n will be

$$R_\eta^*(\xi,\eta,\tau) = \exp\left[-\frac{|\xi|}{V_c\Theta}\right]e[-\kappa_2|\eta|]\exp[\kappa_1|\xi-V_c\tau|] \qquad (3)$$

which yields a low pass power spectrum that is deemed valid at high frequencies only. Here V_c is a mean convection speed and Θ is a mean eddy lifetime.

Before proceeding a few remarks about the above functional form for R_η are in order. When the above function is compared with various experimental observations several points can be made. First, when $R_\eta(o,\eta,o)$ versus η/δ^* is fit to most wind tunnel data the parameter $\kappa_2 \simeq 2/\delta^*$. Second when $R_\eta(\xi,o,\xi/Vc)$ is fit to longitudinal data one finds that

$$\Theta\ V_\infty/\delta^* \simeq 18$$

and

$$V_c/V_\infty \simeq 0.8 \qquad (4)$$

at least for ξ/δ^* sufficiently large, i.e. $\xi > 0.8V_\infty\Theta$. Further, most data exhibit sharp peaks in $R_\eta(\xi,o,\xi/Vc)$ for close observation points only and the curves become broader as ξ increases. Also, Vc is not strictly constant but varies from $0.58V_\infty$ for very close observation points and gradually approaches $0.80V_\infty$ as ξ is increased. However, when one fits power spectra data to measured values a "best fit" usually obtains for $Vc \simeq 0.8V_\infty$. Eq. 3 on the other hand exhibits sharp peaks in $R_\eta(\xi,o,\xi/Vc)$ for all ξ. Finally, there are discrepancies in absolute pressure levels of roughly 2 to 3 dB due to finite transducer size effects at higher frequencies which is deemed not so serious as discrepancies in convective velocity predictions. The ratio of the rms surface pressure $\langle p2(x,y,t)\rangle^{1/2}$ to the dynamic velocity head $1/2\ \rho_o V_\infty^2$, where ρ_o is the mean fluid density, is a constant whose value can be determined.

To introduce the convective waveguide model I refer to the Kolmogoroff theory of turbulence which asserts that energy for sustenance of the fluctuating

part of the flow is given directly to a group of eddies (here called energy-bearing eddies) in a rather definite range of sizes through inertial transfer from the mean flow. A very complete discussion of this process can be found in Batchelor[1] and the theoretical and experimental results here utilized are taken from chapters 6 and 7 of his book.

On the other hand, energy is removed from the turbulent flow at the same rate by viscous dissipation which is strongest for eddies whose scale is much smaller than the scale size L_e of a typical energy bearing eddy. The range of eddy sized $L < L_e$ is called the universal equilibrium range because the motions of these eddies is uniquely determined on a statistical basis by only two parameters, the energy per unit mass E_e supplied by the fluctuating flow and the kinetic viscosity ν of the fluid.

It is possible to relate the sustaining energy supplied to the energy bearing eddies to a peripheral velocity V_e and a scale length L_e via the relation

$$E_e = \frac{V_e^3}{L_e} \tag{5}$$

Then this theory predict a time scale for the energy bearing eddies of roughly

$$\Theta_e \simeq \frac{L_e}{V_e} \simeq \frac{\delta^*}{V_e} . \tag{6}$$

In order for Eqs. 5 and 6 to be valid, it is required that the inertial forces predominate over the viscous forces, hence the Reynolds number

$$R_e = \frac{V_e L_e}{\nu} >> 1 \tag{7}$$

for a universal equilibrium range to exist. The mean value of the rms fluctuating velocity V_e is approximately $0.05\ V_\infty$.

These numbers yield

$$\Theta e = \frac{\delta^*}{.05V_\infty} = 20\,\frac{\delta^*}{V_\infty} \tag{8}$$

which is in close agreement with the result of Eq. 4 and which in turn were based on the correlation function of Eq. 3. Hence, we readily interpret the parameter θ in Eq. 3 as a "mean eddy lifetime". The parameter κ_1 in Fig. 3 that best fit most experimentalist data in wind tunnels is $\kappa_1 \simeq 1/\delta^*$ and hence κ_1 is interpreted as an "inverse mean eddy size".

By taking the Fourier transform of the normalized trial temporal correlation functions

$$R_n^*(0,0\tau) = \exp[-\kappa_1 V_c|\tau|] \tag{9}$$

the normalized power spectrum becomes

$$\frac{1}{2}\,\omega_h \Phi n^*(\tilde{\omega}) = \frac{1}{(\frac{V_\infty}{V_c})^2 \tilde{\omega}^2 + 1} \tag{10}$$

where $\omega_h = V_c/\delta^*$ is interpreted on the upper cut-off frequency of the power spectrum and numerically is in excellant agreement with high frequency spectral data. The normalized frequency $\tilde{\omega}$ is given by Eq. 1.

However, at the low end of the power spectrum there is much more uncertainty and ambiguity. By viewing the turbulent boundary layer as a convective wave guide we will set the scale of the largest energy bearing eddies as $Lm \simeq \delta$ where δ is the boundary layer thickness. For smooth boundaries $\delta = 8\delta^*$ on the basis of the 7th power law velocity profile. If Le is the scale size of the eddy and V_e is the peripheral eddy velocity, then the time it takes for the eddy to cycle once is

$$T_e = \frac{\pi L_e}{V_e} = \pi\Theta_e \tag{11}$$

where from Eq. 4 we take $\Theta_e \simeq 18\delta^*/V_\infty$. Then for the largest energy bearing eddies their characteristic frequency will be

$$\omega_\ell = \frac{2\Pi}{T_\ell} = \frac{2}{\Theta_\ell} = \frac{2V_\infty}{18\delta^*} = 0.1111\frac{V_\infty}{\delta^*} \tag{12}$$

or

$$\tilde{\omega}_\ell = 0.1111. \tag{13}$$

Thus, we take ω_ℓ as the estimate of the lower frequency half-power point in the power spectrum for incompressible fluid flow.

As an aside it is interesting to observe several other matters. The scale of the energy bearing eddies now should be

$$\delta > L_e > \delta^*/8$$

while

$$V_{cmid} = 0.8V_\infty \simeq V(\frac{3}{2}\ \delta^*) \tag{14}$$

Thus, the center of mean energy bearing eddy is located an average distance 3/2 δ^* from a smooth wall. By the same token

$$V_{cmin} = 0.58V_\infty \simeq V(\frac{3}{16}\ \delta^*) \tag{15}$$

which is characteristic of the smallest eddies in the energy bearing range. Note, they are much closer to the wall.

We also speculate that any variation in V_c with spatial separation as observed by various investigators can be attributed to the more rapid decay of energy in the high frequency eddies. Since these are small eddies that lie close to the boundary they tend to lower the average drift velocity as observed at small separations. However, at greater separation distances say $\xi > 0.8V_\infty\Theta$ or $\xi/\delta^* > 14$ only the low frequency eddies retain any coherence from point to point. This observation also may account for any broadening of the peaks in the

space-time correlations at larger separations. Thus, we are aware of variations in the average drift velocity with sensor element spacing which could be a troublesome point when interpreting coherence data obtained from an array of sensors spaced a finite distance apart.

Low frequency estimate of $\Phi_n(\omega)$ based on the convective waveguide model.

The general shape of the normalized measured power spectrum for $\tilde{\omega}>0.02$ is shown in Fig. 1. We note that it peaks at some frequency ω_p and exhibits a high frequency cut-off (-3 dB point) at $\tilde{\omega}_h$. The drop-off date for $\tilde{\omega}>>\tilde{\omega}_h$ is -6 dB per octave. However, frequencies below $\tilde{\omega}_p$ the normalized spectra does not decrease rapidly with decreasing frequency but appears to approach a constant for $\tilde{\omega}<<\tilde{\omega}_p$ characteristic of some static pressure level associated with the fluid flow.

A number of attempts have been made by others to reproduce this spectrum theoretically at low frequencies but all require a large number of adjustable parameters. Moreover, these parameters are difficult to interpret physically and just as difficult to measure experimentally. A somewhat different approach will be presented next which seems to incorporate most of the salient features of $\Phi_n(\omega)$ and hopefully is accurate at low frequencies, well below $\tilde{\omega}_p$. Also, any parameters that control $\Phi_n(\omega)$ for $\tilde{\omega}<\tilde{\omega}_p$ should be readily measureable, preferably independent of spectral measurements.

The first task is to incorporate the estimate of $\tilde{\omega}_\ell$ Eq. 12 into the normalized power spectra. For this purpose the convective waveguide will be viewed as a bandpass filter and a typical low-pass to band-pass frequency transformation of Eq. 10 will be utilized. However, that transformation by itself will not be sufficient since the estimated spectra will drop off too rapdily below

$\tilde{\omega}_p$. In order to insure a proper low frequency asymptotic behavior, a cut-on in wave number at some low-frequency ω_o will be hypothesized for a turbulent boundary layer of finite depth. We could estimate $\tilde{\omega}_o \simeq \tilde{\omega}_\ell$ and this may well suffice. However, initally I would prefer to say that the cut-on occurs when the perimeter of the largest eddy permitted by the guide $2\pi\Delta$ equals the eddy wavelength V_c/f_o where $f_o = \omega_o/2\pi$. Here 2Δ is the physical width of the waveguide.

Thus, we have for the cut-on wavelength

$$\frac{V_c}{f_o} = 2\pi\Delta \qquad \text{a)}$$

yielding a cut-on wave number (16)

$$k_o = \frac{\omega_o}{V_c} = \frac{1}{\Delta} \; . \qquad \text{b)}$$

The convective waveguide now will be dispersive at low frequencies and the convective ridge obeys the relation

$$\omega^2 = k^2 V_c^2 - \omega_o^2 \qquad k > k_o \qquad \text{a)}$$

or (17)

$$k = \sqrt{\frac{\omega^2 + \omega_o^2}{V_c}} \qquad \text{b)}$$

Note for the sufficiently large ω, $k \to \frac{\omega}{V_c}$. However, as $\omega \to 0$, $k \to \frac{\omega_o}{V_c}$ and

$$\frac{V_\infty}{V_c}\tilde{\omega} \to \frac{\delta^*}{\Delta} = \mu \qquad (18)$$

Thus, the power spectrum must be modified to agree with Eq. 17 which requires that the normalized frequency $\tilde{\omega}$ be transformed to $\tilde{\omega}^2 + (\frac{\delta^*}{\Delta})^2 = \tilde{\omega}^2 + \mu^2$ where $o < \mu \leq 1$ since $0 < \delta^* \leq \Delta$.

Before proceeding with the frequency translation required by Eq. 17 let us

examine the phase velocity of spectral components defined as

$$V_p \equiv \frac{\omega}{k} = V_c/\sqrt{1 + \omega_o^2/\omega^2} \tag{19}$$

Clearly, V_p cannot exceed the convection speed of the fluid V_c but will approach V_c as $\omega \to \infty$. Note, $V_p \to 0$ as $\omega \to 0$ in this formulation. More about the behavior of V_p in a subsequent tract.

Further, the group velocity V_g defined as

$$V_g \equiv \frac{\partial \omega}{\partial k} \tag{20}$$

has characteristics that enable it to exceed V_c, and below a critical frequency can exceed the speed of sound c.

Before making the required frequency transformation a few definitions are required. First, we define a half-power bandwidth for the turbulent wall pressure spectrum as

$$\omega_b \equiv \omega_h - \omega_\ell \tag{21}$$

where $\omega_h = 0.8\ V_\infty/\delta^*$ and $\omega_\ell = 0.1111\ V_\infty/\delta^*$. Also we define a band center frequency

$$\omega_c \equiv \sqrt{\omega_\ell \omega_h} \tag{22}$$

When these parameters are normalized

$$\begin{aligned} \tilde{\omega}_b &= 0.689 \qquad \text{a)} \\ \text{and } \tilde{\omega}_c &= 0.298 \qquad \text{b)} \end{aligned} \tag{23}$$

Note, that the predicted spectrum actually will peak somewhat below $\tilde{\omega}_c$ due to the frequency translation.

Following standard procedures we now rewrite Eq. 10 in factored form

$$\frac{1}{2}\ \omega_h\ \overset{*}{\Phi}_n(\omega) = \frac{1}{\left[\frac{V_\infty}{V_c}\ (i\ \omega) + 1\right]\left[\frac{V_\infty}{V_c}\ (-i\ \omega) + 1\right]} \tag{24}$$

and then replace

$$\left(\frac{V_\infty}{V_c}\right)(i\,\tilde{\omega}) \text{ by } \frac{\tilde{\omega}_c^2 - (\tilde{\omega}^2 + \mu^2)}{i\sqrt{\tilde{\omega}^2 + \mu^2}\;\tilde{\omega}_b} \qquad \text{a)}$$

and (25)

$$\left(\frac{V_\infty}{V_c}\right)(-i\,\tilde{\omega}) \text{ by } \frac{\tilde{\omega}_c^2 - (\tilde{\omega}^2 + \mu^2)}{(-i\sqrt{\tilde{\omega}^2 + \mu^2}\,)\,\tilde{\omega}_b} \qquad \text{b)}$$

in order to obtain a normalized spectrum that reduces to Eq. 10 for $\tilde{\omega}^2 >> \mu^2$ and has the requisite low frequency behavior for $\tilde{\omega}^2 << \mu^2$.

The transformed spectrum now becomes

$$\frac{1}{2}\,\omega_h\,\Phi_n(\tilde{\omega},\mu) = \frac{\tilde{\omega}_b^2\,(\tilde{\omega}^2 + \mu^2)}{(\tilde{\omega}^2 + \mu^2)^2 + (\tilde{\omega}_b^2 - 2\tilde{\omega}_c^2)(\tilde{\omega}^2 + \mu^2) + \tilde{\omega}_c 4} \tag{26}$$

which exhibits the proper high and prescribed low freqency behavior. Note that

$$\frac{1}{2}\,\omega_h\,\Phi_n\,(\tilde{\omega}) \underset{\tilde{\omega}\,\to\,\infty}{\to} \frac{\tilde{\omega}_b^2}{\tilde{\omega}^2} \quad . \tag{27}$$

Thus at high frequencies, $\tilde{\omega}^2 >> \omega_h^2$, $\tilde{\omega}^2 >> \mu^2$, Eq. 27 predicts the -6 dB per doubling of frequency in agreement with most reliable wind tunnel data. The spectrum peaks at $\tilde{\omega}_p = \sqrt{\tilde{\omega}_c^2 - \mu^2}$ as required but will not exhibit a -3 dB point below $\tilde{\omega}_c$ unless μ^2 is sufficiently small.

At low frequencies $\tilde{\omega}^2 << \tilde{\omega}_c^2, \tilde{\omega}^2 << \mu^2$, Eq. 26 reduces to

$$\frac{1}{2}\,\omega_h\,\Phi_n^*\,(\mu) \underset{\tilde{\omega}\to\,0}{\to} \frac{1}{1 + \dfrac{\mu^2}{\tilde{\omega}_b^2}\left(1 - \dfrac{\tilde{\omega}_c^2\,2}{\mu^2}\right)} \tag{28}$$

which predicts a finite normalized level (less tha 0 dB) for finite values of μ. Note, the power spectrum will be flat for $\tilde{\omega}<\tilde{\omega}_c$ in the special case $\tilde{\omega}_c=\mu$.

It is convenient and plausible to approximate Δ by δ, the boundary layer thickness, on the basis of the convective waveguide theory applied to a wind

tunnel or water tunnel. If $\Delta = \delta$, then $\mu = \delta^*/\delta = 0.125$ for a 1/7 power shear velocity profile. Note, numerically that $\mu \simeq \tilde{\omega}_\ell$ which probably is not fortuitous.

Eq. 28 predicts at low frequencies that

$$10 \log_{10}[\omega_h \Phi_n(.125)] \simeq -2.4 \text{ dB} \tag{29}$$

in excellent agreement with reliable low frequency wind tunnel spectral data, see Fig. 1. Most wind tunnel data level off between -0.5 and -2.5 dB with about a ± 1/2 dB spread.

Note, as $\mu \to 0$, the value of the low frequency asymptote $\Phi_n^*(\mu)$ becomes progressively lower. For $\mu=0$

$$\frac{1}{2} \omega_h \Phi_n(\tilde{\omega}) \to \frac{\tilde{\omega} b^2}{\tilde{\omega}_c^4} \tilde{\omega}^2 \tag{30}$$

A plot of Eq. 30 also is shown in Fig. 1 for comparison purposes.

A few remarks about the experimental curves are in order. Normalized power spectrum measurements of M. K. Bull performed at Southhamptom in 1963 in a low noise wind tunnel are shown by the shaded area. This normalization was done by Dr. D. H. Tack in 1965 who also attempted to reproduce the spectrum theoretically using other techniques, namely a modification of Eq. 3 which agreed more closely with Bull's spatial correlation data. Bull's data still are regarded as among the best and most complete available for wind tunnels. His pressure sensors were miniature, 0.76 mm diameter lead-zirconate-titinate discs flush mounted on the wall. His experimental parameters were flow speeds from 100 to 164 m/s and displacement thickness between 1.5 and 4.4 mm. The individual measurement points are not shown, only the range of spread after normalization. The data do normalize exceedingly well in the range $\tilde{\omega} > 0.02$ as shown by the shaded area.

Also shown for other comparison purposes are low frequency wall pressure fluctuation spectra obtained from glider experiments. These data do exhibit rather wide scatter but level off at about 10 dB below their peak at low frequencies whereas Bull's data leveled off considerably higher. If the asymptote is taken to be -10 dB re maximum, then from Eq. 28 $\mu \simeq 0.042$ utilizing the same scaled values of $\tilde{\omega}_b$ and $\tilde{\omega}_c$, requiring a somewhat smaller boundary layer ratio for δ^*/Δ. Currently a search is being made to find good low frequency spectral data utilizing a range of boundary layer thickness ratios.

This formulation of the power spectrum does provide relatively simple quantitative relationships between the normalized power level and the boundary layer profile as measured by δ^*/δ, Eqs. 26 and 28. This relationship is worthwhile exploring in more detail since δ^* and δ can be measured independently of $\Phi(\omega)$. (See appendix).

However, what is especially appealing about this formulation is that fairly accurate values for both ω_b and ω_c are available from high frequency experimental data combined with a simple hypothesis about the scales of the energy bearing eddies.

Finally, a table of parametric values of δ^*, ω_h, ω_ℓ, and ω_c for the water tunnel facility at a number of flow speeds ranging from 3 to 18 m/s is attached. The estimates of $f_\ell = \frac{\omega_\ell}{2\pi}$ range from 30 to 217 Hz. Hopefully, these values are within the range of good spectral measurements in our facilities.

Table

V_∞-Fluid Velocity		δ^*	$V\infty/\delta^*$	ω_h	ω_ℓ	ω_c
f/s	m/s	m	s-1	r/s	r/s	r/s
10	3.05	.001828	1668	1334	185	497
20	6.10	.001737	3512	2810	312	936
30	9.15	.001645	5562	4450	617	1658
40	12.2	.001584	7702	6162	855	2295
50	15.3	.001524	10006	8005	1111	2982
60	18.3	.001493	12257	9806	1361	3653

Appendix

This appendix will consider several implications of the results and may suggest some additional experiments.

For example, if one assumes a $\frac{1}{n}$ power low for the shear flow near the wall then the parameter

$$\mu = \frac{\delta^*}{\delta} = \frac{1}{n+1} \qquad \text{A1}$$

which leads to the result that $\mu \to 0$ as $n \to \infty$. The value of μ has to do with the shape of the shear boundary layer flow profile which in turn is related to the compressibility of the flow, the geometry of the wall, the surface roughness, etc.

Also it can be shown that

$$\mu = \alpha \frac{V_\tau}{V_\infty} \qquad \text{A2}$$

where V_τ is a friction (shear stress) velocity and α is a constant that can be evaluated numerically under certain hydrodynamics assumptions and approximations.

For small values of μ the normalized power spectrum approaches the value

$$\frac{1}{2}\omega_h \Phi_{n(\mu)} \underset{\mu \to 0}{\to} \alpha^2 \left(\frac{V_\tau}{V_\infty}\right)^2 \left(\frac{1}{\tilde{\omega}_\ell} - \frac{1}{\tilde{\omega}_h}\right)^2 , \quad \tilde{\omega} << \mu^2 \qquad \text{A3}$$

revealing that V_τ becomes an important parameter in setting the low frequency power level. These predictions suggest that controlling μ via boundary layer shape could be an important experimental procedure.

In 1970 Aupperle and Lambert reported in a study supported by NASA that the surface roughness could alter the low frequency power level by as much as 10dB,

the rougher the surface the higher the level. We were able to normalize the effects of surface roughness on the power spectrum by employing the parameters α and V_τ. The changes in measured values of μ also were consistent with the changes in observed values of $\Phi_\eta(\tilde{\omega},\mu)$. However, another independent scale parameter is required to normalize the frequency scale properly for rough surfaces. This is the earliest study I know of where a deliberate attempt to roughen the surface was made to enhance the effect of wall pressure fluctuations at low frequencies. The signal to ambient acoustic noise ratios were of the order of + 25dB over most of the frequency range of interest. The studies were conducted down to 200 Hz.

As far as I can tell all of the predicted results in this tract are compatible with experiment and in no significant way conflict with theoretical power spectrum predictions by Blake (1984), Chase (1980) and perhaps Williams (1982). In the situation discussed by Williams one can see that $\Phi_\eta(\omega)\sim\omega^2$ at low frequencies i.e. $\tilde{\omega}^2<<\tilde{\omega}_p{}^2$ and $\tilde{\omega}^2<<\mu^2$, only in the limiting case $\mu \to 0$. The glider experiment seems to be as close to that situation as any experiment known to me. An evaluation of Williams work will be made later.

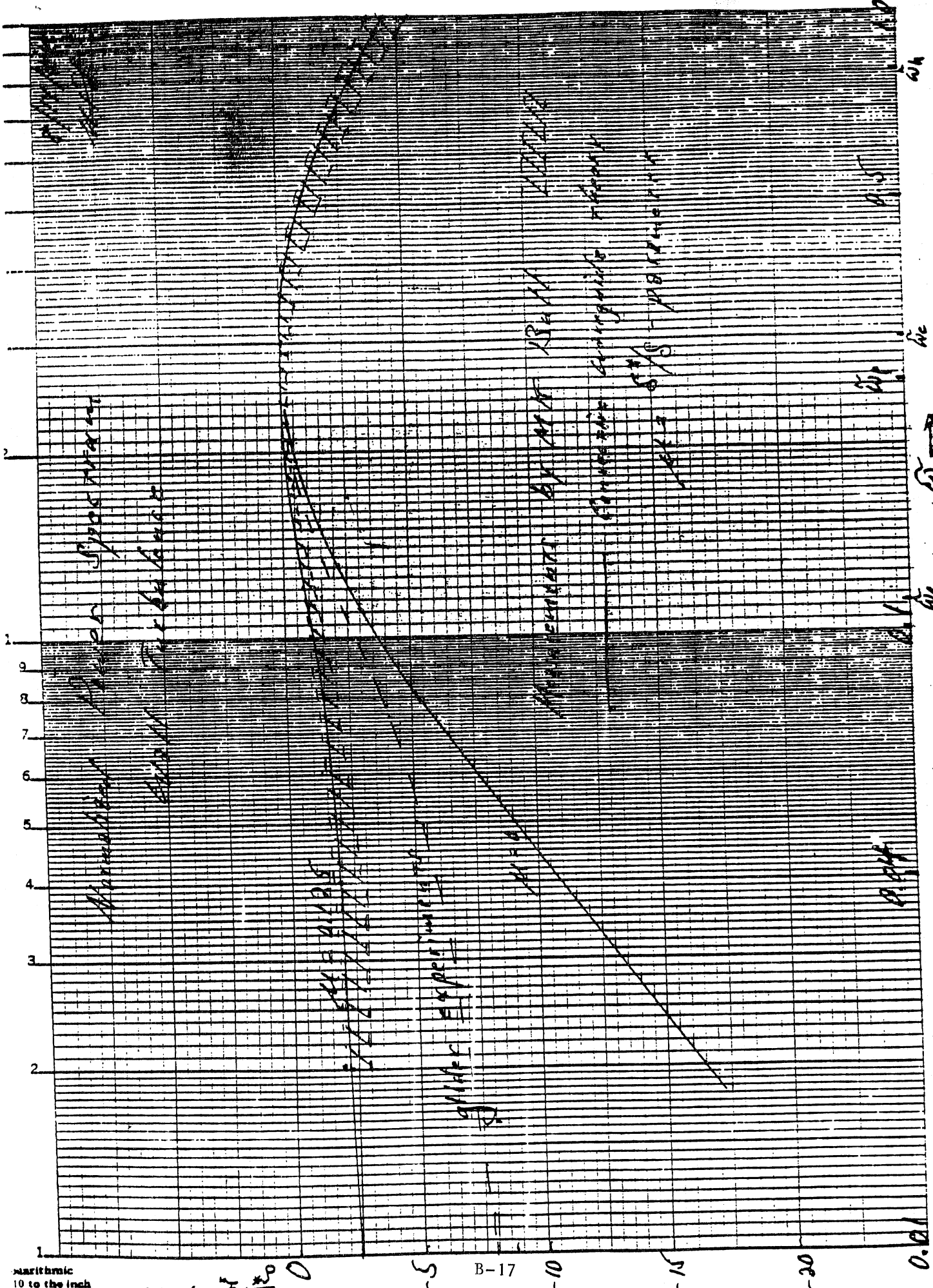

VI Estimate of the Low Wavenumber/frequency Spectrum of Wall Pressure Fluctuations

by

Robert F. Lambert

Introduction

Recently, in tract V, I proposed a new method for estimating the normalized power spectrum $\Phi_n(\omega)$ for wall turbulence that was consistent with experiment especially at low frequencies and had a fairly simple physical interpretation in terms of measureable parameters. The turbulent boundary layer was viewed as a convective waveguide that cuts-on at a frequency of about $\omega_o \simeq V_c/\delta$ above which the fluid motion could be regarded as incompressible. Here V_c is the convective fluid velocity and δ is the thickness of the boundary layer. Below a corresponding wavenumber the pressure fluctuations are governed by compressible wave motion, i.e. sound waves. The transition wave number was estimated to be $k_o = \omega_o/V_c \simeq 1/\delta$ at low convective mach numbers.

An analytical expression for a normalized power spectrum $\Phi_n(\tilde{\omega},\mu)$ was developed which yielded results consistent with most experiments and whose shape was controlled by three parameters, $\omega_h = V_c/\delta^* \simeq 0.8\ V_\infty/\delta^*$, $\omega_\ell \simeq V_\infty/9\delta^*$, and $\mu = \delta^*/\delta$. It predicted a low frequency asymptote that was dependent on these three parameters according to the relationship

$$1/2\omega_h\ \Phi_n(o,\mu) = \frac{1}{1+\frac{\mu^2}{\tilde{\omega}_b^2}\left(1-\frac{\tilde{\omega}_c^2}{\mu^2}\right)^2}$$

where ω_b and ω_c are related to ω_h and ω_ℓ. Here $\tilde{\omega} = \omega\delta^*/V_\infty$ is a dimensionless frequency variable. In the limit as $\mu \to o$, corresponding to perfectly incompressible flow, $\Phi_n(\tilde{\omega},o)$ approaches zero as $\tilde{\omega}^2$ as $\tilde{\omega}$ tends to zero. The general results seem

to be consistent with theoretical predictions by other workers except for a recent paper by Williams (1982). More on that matter later.

The purpose of this tract is to extend the convective waveguide scenario to predictions of the wavenumber/frequency spectrum $P(k_1,k_2,\omega)$ where k_1 and k_2 are longitudinal and lateral wavenumbers, respectively, and ω is the radian frequency in question. To do this from first principles is a long arduous task and rarely done, so it is expedient to make use of some of the results developed by Williams (1982) and then adapt them to a convective waveguide model. I deem William's general results to be valid only in the normalized frequency range $(\omega\delta/V_\infty)^2 >> 1$. This does not exclude the wavenumber region $k\simeq\omega/c$ so some of his results on compressible flow can be utilized directly. The emphasis will be on developing suitable analytical forms for the wavenumber/frequency spectrum valid for low longitudinal wavenumbers and low frequencies at low mach numbers.

Analysis

Briefly, Williams (1982) derived an expression for the wavenumber/frequency spectrum by a modification of the Corcos model so as to "account for compressibility of the fluid at low wavenumbers while retaining the apparently good agreement with experiment at high frequencies and at higher values of wavenumber where the spectrum is immune from the influence of compressibility". In that sense his contribution is valuable. Without going into any detail his predicted wavenumber/frequency spectrum has the general form

$$P(k_1,k_2,\omega) = \rho_o^2 V^3 \delta^3 G_o\left(\frac{\omega\rho}{V}\right) A_o\left[1+k_1\frac{V}{1\omega}\right] B_o\left(k_2\frac{V}{\omega}\right)$$

$$x\{a_o\left(\frac{Vk}{\omega}\right)^2 + a_1 M^2 + a_2 M^4 \ell n\left(\frac{R}{\delta}\right) u_\infty\left[\left(\frac{KV}{\omega}\right)^2 - M^2\right]\} \qquad a)$$

or (1)

$$P^*(k_1,k_2,\omega) = P_o(\overline{k},\omega) + P_1(\overline{k},\omega) + P_2(\overline{k},\omega) \qquad b)$$

consisting of three separate additive components. In his view the component P_o

is due exclusively to incompressible flow while P_1 and P_2 which are mach dependent, M=V/c, are contributions from compressible fluid flow. The parameter $G_o(\omega\delta/V)$ is the frequency spectrum due to an integrated fluctuating velocity source function that tends to a constant as $\frac{\omega\delta}{V}$ tends to zero. While I have no serious qualms about that particular result some of the details are not clear from his work. The functions $A_o[\ ]$ and $B_o[\ ]$ are longitudinal and lateral wavenumber dependent factors that "agree with experiment". The other parameters a_o, a_1, a_2, are scaling constants and R is a "large radius on a flat surface over which the turbulent field is homogeneous". The function $U_\infty[\ ]$ is a singularity function that arises from a spatial transform of the lossless wave equation and predict a singularity in $P_3(\overline{K},\omega)$ at $k=\omega/c$.

Williams proceeds to compute a power spectrum

$$\Phi(\omega) = \int_{-\infty}^{\infty}\int P(k_1,k_2,\omega)dk_1dk_2 \qquad (2)$$

which yields

$$\Phi(\omega) = \rho_o V^3\delta(\tfrac{\omega\delta}{V})^2 G_o(\tfrac{\delta\omega}{V})\{\alpha + \beta M^2 + \gamma M^4 \ell n(\tfrac{R}{\delta})\} \qquad a) \quad (3)$$

or

$$\Phi(\omega) = \Phi_o(\omega) + \Phi_1(\omega) + \Phi_2(\omega) \qquad b)$$

where α,β, and γ are constant of integration.

Williams results then reveal that all three terms in $\Phi(\omega)$ corresponding to both incompressible and compressible flow tend to zero as ω^2 as ω tends to zero. He also notes that the shape of the spectrum is independent of M, only its level is mach dependent. I do question the validity of these general results and there is no credible evidence to support his predictions at least for $\omega\delta/V_\infty \leq 1$. His predictions are at odds with power spectrum predictions by others and results predicted by myself in tract V. I do have reason to believe that $\Phi_1(\omega)$ and $\phi_2(\omega)$ do exhibit an ω^2 behavior at low frequencies but not for the reasons

stated by Williams. The leading term $\Phi_0(\omega)$ should not exhibit an ω^2 behavior unless $\delta^*/\delta=0$ according to the convective waveguide model of tract V.

However, I can bring the two formulations into comptability (to within a constant multiplier) by noting that the frequency parameter $\tilde{\omega}^2+\mu^2$ in tract V can be rewritten as

$$\tilde{\omega}^2 + \mu^2 = \left(\frac{\omega\delta^*}{V_\infty}\right)^2 + \left(\frac{\delta^*}{\delta}\right)^2 = \delta^{*2}\left(\frac{V_c}{V_\infty}\right)^2\left\{\left(\frac{\omega}{V_c}\right)^2\left[1+\left(\frac{V_\infty}{\omega\delta}\right)^2\right]\right\} \tag{4}$$

In this analysis I will call the frequency variable

$$\left(\frac{\omega}{V_c}\right)_* = \left(\frac{\omega}{V_c}\right)\sqrt{1+\left(\frac{V_\infty}{\omega\delta}\right)^2} = \begin{cases} \dfrac{V_\infty}{V_c\delta} \quad , \quad \left(\dfrac{V_\infty}{\omega\delta}\right)^2 >> 1 & \text{a)} \\ \dfrac{\omega}{V_c} \quad , \quad \left(\dfrac{V_\infty}{\omega\delta}\right)^2 << 1 & \text{b)} \end{cases} \tag{5}$$

and treat $\frac{V_c}{V_\infty}$ and δ^* as constant parameters.

If the inequality in Eq. 5b holds then my results agree with William's predictions but that condition does not hold at low frequencies which are of special interest.

Next, I will hypothesize the cross spectral density function $\Gamma_0(\xi,\eta,\omega)$ has the new similarity form

$$\Gamma^*_0(\xi,\eta,\omega) = \Phi^*(\omega)A\left[\left(\frac{\omega}{V_c}\right)_*\xi\right]B_0\left[\left(\frac{\omega}{V_c}\right)_*\eta\right]e^{i\left(\frac{\omega}{V_c}\right)_*\xi} \tag{6}$$

where $\Phi^*(\omega) = \Gamma^*_0(o,o,\omega)/A(o)B(o)$ is a known function and compatible with Eq. 24 in tract V.

We now can compute the new $P_0(k_1,k_2,\omega)$ in a purely formal way and the result can be expressed as

$$P_0^*(k_1,k_2,\omega) = \left(\frac{V_c}{\omega}\right)^2_*\Phi^*(\omega)\ A_0^*\left[1-\left(\frac{V_c}{\omega}\right)_*k_1\right]B_0^*\left[\left(\frac{V_c}{\omega}\right)_*k_2\right] \tag{7}$$

where

$$A^*(\tau_1) = \frac{1}{2\pi}\int_{-\infty}^{\infty} A(\beta)e^{-\tau 1\beta}d\beta \tag{a}$$

and (8)

$$B^*(\tau_2) = \frac{1}{2\pi}\int_{-\infty}^{\infty} B(\beta)e^{-\tau 2\beta}d\beta \quad . \qquad (b)$$

We now can follow Williams in detail and re-express Eq. 1a) in the form

$$P^*(k_1,k_2,\omega) = \rho_0 V^3\delta^3 G_0(\tfrac{\omega\delta}{V_\infty})A^*[\ ]B^*[\ ]$$

$$x\{a_0(\tfrac{V_c}{\omega})_*^2 k^2 + a_1 M_*^2 + a_2 M_*^4 \ell n(\tfrac{R}{\delta})u_\infty[(\tfrac{kV}{\omega})_*^2 - M_*^2]\} \qquad (9)$$

where the two mach dependent terms now are <u>frequency dependent</u> according to the relation

$$M_*^2 = \frac{\omega^2}{c^2}(\frac{V_c}{\omega})_*^2 = \frac{M^2}{1+(\frac{V_\infty}{\omega\delta})^2} = \begin{cases} (\frac{\omega}{c})^2\delta^2 & , \quad (\frac{V_\infty}{\omega\delta})^2 >> 1 \\ \frac{V_c^2}{c^2} & , \quad (\frac{V_\infty}{\omega\delta})^2 << 1 \end{cases} \qquad (10)$$

and $k^2 = k_1^2 + k_2^2$ in Eq. 9.

The location of the singularity at $k=\omega/c$ remains unchanged by this transformation, ie by utilizing Eq. 5. At this point we do not have functional forms for either A*[ ] and B*[ ] in Eq. 9 that "agree with experiment" so we can test only specific integrals in Eq. 9.

To complete the comparisons and highlight differences with William's results I will now recompute the $\Phi(\omega)$ and in particular the $\Phi_0(\omega)$ term.

Thus, by specific integrals $\Phi(\omega)$ now becomes

$$\Phi_0^*(\omega) = \rho_0^2 V^3\delta^3(\tfrac{\omega}{V_c})_*^2 G_0(\tfrac{\omega\delta}{V_\infty})\{\alpha + \beta M_*^2 + \gamma M_*^4 \ell n(\tfrac{R}{\delta})\} \qquad (a) \quad (11)$$

or

$$\Phi^*(\omega) = \Phi_0^*(\omega) + \Phi_1^*(\omega) + \Phi_2^*(\omega) \qquad (b)$$

where the integration constant

$$\alpha = a_0 \int\int_{-\infty}^{\infty} A^*[\quad]B^*[\quad]k^2(\tfrac{V_c}{\omega})_*^2 d^2[k(\tfrac{V_c}{\omega})_*]. \qquad (a) \quad (12)$$

$$\beta = a_1 \int_{-\infty}^{\infty} A^*[\quad]B^*[\quad]d^2[k(\frac{V_c}{\omega})_*]. \qquad (b)$$

and

$$\gamma = a_2\pi\, A^*[1 - M_*]B^*(o) \qquad (c)$$

The low frequency behavior of Eq. 11 now should be compared with the low frequency behavior predicted by Eq. 24 in tract V. The normalized spectrum corresponding to $\Phi_o{}^*(\omega)$ reduces to

$$\Phi_{o_n}{}^*(\omega) = \frac{\delta}{\delta^*}(\frac{\omega\delta}{V_{c^*}})^2(\frac{V_c}{V_\infty})^2 G_o(\frac{\omega\delta}{V_\infty}) = \begin{cases} \frac{\delta}{\delta^*} G_o(\frac{\omega\delta}{V_\infty}) \ , & (\frac{V_\infty}{\omega\delta})^2 >> 1 \\ \frac{\delta}{\delta^*} (\frac{V_c}{V_\infty})^2(\frac{\omega\delta}{V_c})^2 G_o(\frac{\omega\delta}{V_\infty}) \ , & (\frac{V_\infty}{\omega\delta})^2 << 1 \end{cases} \qquad (13)$$

The normalized spectrum now approaches a <u>constant</u> as ω tends to zero which is the desired result for the leading $\Phi_o{}^*(\omega)$ term and is now compatible with Eq. 24 in tract V. We could factor out the term $(\bar{\omega}^2+\mu^2)(\frac{V_\infty}{V_c})^2(\frac{\delta}{\delta^*})^2$ from Eq. 24 in tract V and identify the $G_o(\frac{\omega\delta}{V_\infty})$ factor more explicitly but that is not necessary to make our point.

However, we also can say that the leading term in Eq. 9

$$P_o{}^*(k_1,k_2,\omega) = a_o\rho_o{}^2V^3\delta^3 G_o(\frac{\omega\delta}{V_\infty})\ A^*[1-k_1(\frac{V_c}{\omega})_*]B^*[k_2(\frac{V_c}{\omega})_*](\frac{V_c}{\omega})_*{}^2k^2 \qquad (14)$$

could be used for an initial estimate of the low wavenumber spectrum at low mach numbers and low frequencies provided $a_o, a_1, A^*[\ ]$ and $B^*[\ ]$ can be determined from experiments. Certainly this will be the case for $k^2 >> \frac{a_1}{a_o}\omega^2/c^2$. A singularity can be expected at $k=M_*(\frac{\omega}{V_c})_* = \frac{M\omega}{V_c}$ but that point probably will fall outside the range of our experiments at low mach numbers.

There are some difficulties with making numerical estimates of $P^*(k_1,k_2,\omega)$ over a wide range of wavenumbers. For example, if we choose

$$A[(\frac{\omega}{V_c})_*\xi] = e^{-\alpha(\omega/V_c)_*|\xi|} \qquad (a)$$

and (15)

$$B[(\frac{\omega}{V_c})_* \eta] = e^{-\alpha_2(\frac{\omega}{V_{c*}})|\eta|} \qquad (b)$$

where α_1 and α_2 are empirical constants and proceed to calculate $A^*[\ ]$ and $B^*[\ ]$ from Eq. 8 then there are difficulties at high wavenumbers. The functions in Eq. 15 yield, for axial wavenumbers k_1 and lateral wave numbers $k_2 = 0$, the wavenumber/frequency spectrum (see Appendix A)

$$P_o^*(k_1,o,\omega) = a_o \frac{G(\omega)}{\pi^2} (\frac{\alpha_1}{\alpha_2}) \frac{K_1^2 (\frac{V_c}{\omega})^2_*}{[k_1 - (\frac{\omega}{V_c})_*]^2 + \alpha_1^2 (\frac{\omega}{V_c})^2_*} \qquad (a) \quad (16)$$

$$= a_o \frac{G(\omega)}{\pi^2} (\frac{\alpha_1}{\alpha_2}) \frac{k_1^2}{1+\alpha_1^2} \quad \text{for } k_1 << (\frac{\omega}{V_c})_* \qquad (b)$$

$$= a_o \frac{G(\omega)}{\pi^2} (\frac{\alpha_1}{\alpha_2}) (\frac{V_c}{\omega})^2_* \text{ for } k_1 >> (\frac{\omega}{V_c})_* \qquad (c)$$

where $G(\omega) = P_o V^3 \delta^3 G_o(\frac{\omega\delta}{V_\infty})$.

Note, Eq. 16c does not exhibit the proper high wavenumber behavior and this difficulty has been pointed out by Chase who also attempted to modify the Corcos forum to fit his theoretical results.[1] Eq. 16b, however, does appear to exhibit the proper low wavenumber behavior as observed by Chase and others.

On the other hand, if one selects

$$A[(\frac{\omega}{V_c})_* \xi] = [1+|\alpha_1 (\frac{\omega}{V_c})_* \xi|) e^{-\alpha_1 (\frac{\omega}{Vc})_* |\xi|} \qquad (a) \quad (17)$$

and

$$B[(\frac{\omega}{V_c})_* \eta] = e^{-\alpha_2 (\frac{\omega}{V_c})_* |\eta|} \qquad (b)$$

---

[1]The spectrum of Eq. 16a does peak at $k_1 = (\frac{\omega}{V_c})_*$ but the high wavenumber asymptote is only 14dB below the peak value for $\alpha_1 = 0.2$. It should be at least 20dB below the peak.

then for axial wavenumbers one obtains the spectrum

$$P_o^*(k_1,o,\omega) = \frac{2a_o G(\omega)}{\pi^2}\left(\frac{\alpha_1}{\alpha_2}\right) \frac{\alpha_1^2 k_1^2 \left(\frac{\omega}{V_c}\right)_*^2}{\left\{\left[k_1 - \left(\frac{\omega}{V_c}\right)_*\right]^2 + \alpha_1^2 \left(\frac{\omega}{V_c}\right)_*^2\right\}^2} \qquad (a)$$

$$= 2a_o \frac{G(\omega)}{\pi^2}\left(\frac{\alpha_1}{\alpha_2}\right) \frac{\alpha_1^2 k_1^2}{(1+\alpha_1^2)} \left(\frac{V_c}{\omega}\right)_*^2 \quad , \text{ for } k_1 << \left(\frac{\omega}{V_c}\right)_* \qquad (b) \quad (18)$$

$$= 2a_o \frac{G(\omega)}{\pi^2} \frac{\alpha_1^3}{\alpha_2} \frac{1}{k_1^2} \quad , \text{ for } k_1 >> \left(\frac{\omega}{V_c}\right)_* \qquad (c)$$

which has the proper wavenumber behavior at high wavenumbers but a somewhat different parametric dependence at low wavenumbers than predicted by Eq. 16b.

As of this date I have not made any numerical comparisons between the results of either Eq. 16 or Eq. 18 and Chase's predictions of $P(\overline{k},\omega)$ so will not comment further on that matter. I plan to do so in the near future.

However, several other comments regarding William's predictions of $\Phi(\omega)$ with respect to the compressible flow terms $\Phi_1(\omega)$ and $\Phi_2(\omega)$ can be made. In the $\Phi_1^*(\omega)$ contribution, the βM_*^2 factor now reveals an ω^2 dependence for $\left(\frac{\omega\delta}{V_\infty}\right) < 1$. This is easily seen from Eq. 10. For $\left(\frac{V_\infty}{\omega\delta}\right)^2 << 1$ the contribution reduces to Williams prediction. Hence, at low frequencies, $\left(\frac{V_\infty}{\omega\delta}\right)^2 >> 1$, the $\Phi_1(\omega)$ will be greatly diminished in comparison with $\Phi_o(\omega)$ and probably not of experimental significance especially at low mach numbers, i.e. $M^2 << 1$.

In the $\Phi_2^*(\omega)$ contribution the $\gamma M_*^4 \ell n\left(\frac{R}{\delta}\right)$ factor now reveals an ω^4 dependence for $\left(\frac{\omega\delta}{V_\infty}\right) < 1$. Hence $\Phi_2^*(\omega)$ should also yield an extremely small contribution to $\Phi^*(\omega)$ at all frequencies at low mach numbers for realistic values of R.

Conclusions

Thus, I conclude that the two terms in $\Phi^*(\omega)$ corresponding to $\Phi_1^*(\omega)$ and $\Phi_2^*(\omega)$ are not experimentally significant on the basis of a convective waveguide model at all frequencies at low mach numbers. This conclusion satisfies my intuition and agrees with all experimental results that I have seen to date. The $\Phi_{on}(\omega)$ term as predicted by Eq. 24 in tract V, therefore, should yield good agreement with experiment for all $\alpha > \beta_0$ and all frequencies $\tilde{\omega} > 0$ at low mach numbers. Eq. 14 is promising as an initial estimate of the low wavenumber/frequency spectrum of wall pressure flutuations at all frequencies at low mach numbers on the basis of the convective waveguide model. Synthesis of the proper functional forms for $A_0^*[\ ]$ and $B_0^*[\ ]$ still await experimental results. I intend to compare numerical predictions of $P^*(k_1,k_2,\omega)$ based on Eqs. 16 and 18, with predictions based on the Chase model for a range of parameters.

Appendix A

Some numerical comparisons of low wavenumber spectra

For this purpose we must represent the analytical form of both the longitudinal and lateral coherence functions A_0 and B_0. On the basis of experiment and Chases' work I have selected them in the convenient forms

$$A[(\frac{\omega}{V_c})_* \xi] = [1 + |\sigma_1(\frac{\omega}{V_c})_* \xi|]e^{-\alpha_1(\frac{\omega}{V_c})_* |\xi|} \quad \text{a)}$$

and (A-1)

$$B[(\frac{\omega}{V_c})_* \eta] = e^{-\alpha_2(\frac{\omega}{V_c})_* |\eta|} \quad \text{b)}$$

where the parameter

$$\sigma_1 = \frac{\alpha_1}{1+r} \quad , \quad r > 0 \qquad (A\text{-}2)$$

and r is a mixture coefficient. If the pressure fluctuations are dominated by the mean shear then $r << 1$ and $\sigma_1 \simeq \alpha_1$. Both α_1 and α_2 must found experimentally.

An expression for $P_0^*(k_1,k_2,\omega)$ now is found via Eqs. 8 and 14 to be

$$P_0^*(k_1,k_2,\omega) = \frac{a_0}{\pi^2} G(\omega)(k_1^2 + k_2^2)^{\alpha_2} \times \left[\frac{(\frac{\omega}{V_c})_*^2 \alpha_1^2 (\alpha_1 + \sigma_1) + [k_1 - (\frac{\omega}{V_c})_*]^2 (\alpha_1 - \sigma_1)}{\{[k_1 - (\frac{\omega}{V_c})_*]^2 + \alpha_1^2 (\frac{\omega}{V_c})_*^2\}^2 [k_2^2 + \alpha_2^2 (\frac{\omega}{V_c})_*^2]} \right] \qquad (A\text{-}3)$$

where

$$G(\omega) = \rho_o{}^2 V^3 \delta^3 G_o\left(\frac{\omega\delta}{V\infty}\right) \tag{A-4}$$

in William's notation.

For handy reference purposes the Corcos form is

$$P_c(k_1,k_2,\omega) = \frac{\Phi(\omega)}{\pi^2}\left(\frac{V_c}{\omega}\right)^2 \frac{\alpha_1\alpha_2}{\left[\left(\frac{k_1 V_c}{\omega}-1\right)^2+\alpha_1{}^2\right]\left[\left(\frac{k_2 V_c}{\omega}\right)^2+\alpha_2{}^2\right]} \tag{A-5}$$

which cannot be obtained directly from A-3.

Two special cases that may have some relevance in our experiments will be considered initially and compared with the Corcos prediction.

In the first case (case A)

$\sigma_1 = \alpha_1$ or $r = 0$.

Then the spectrum corresponding to $k_2 = 0$ takes the form

$$P_o{}^*(k_1,o,\omega) = \frac{2a_o}{\pi^2} G(\omega)\left(\frac{\alpha_1^3}{\alpha_2}\right) \frac{k_1{}^2\left(\frac{V_c}{\omega}\right)_*^4}{\left\{\left[k_1\left(\frac{V_c}{\omega}\right)_* - 1\right]^2 + \alpha_1{}^2\right\}^2} \tag{A-6}$$

At its peak $k_1 = \left(\frac{\omega}{V_c}\right)_*$ and

$$P_o{}^*\left[\left(\frac{\omega}{V_c}\right)_*,o,\omega\right] = \frac{2a_o}{\pi^2} G(\omega)\left(\frac{\left(\frac{V_c}{\omega}\right)^2}{\alpha_1\alpha_2}\right) \tag{A-7}$$

The ratio of Eq. A-6 to A-7 now can be simplified to read

$$\frac{P_{oA}{}^*(x)}{P_{oA}{}^*(1)} = \frac{\alpha_1{}^4 x^2}{\left[(x-1)^2+\alpha_1{}^2\right]^2} \tag{A-9}$$

where $x = k_1\left(\frac{V_c}{\omega}\right)_*$.

In the second case (case B)

$\sigma_1 = 0$ or $r \to \infty$

Then the normalized spectrum corresponding to $k_2 = 0$ becomes

$$\frac{P_{oB}^*(x)}{P_{oB}^*(1)} = \frac{\alpha_1^2 x^2}{(x-1)^2+\alpha_1^2} \qquad \text{(A-10)}$$

Finally, the Corcos spectrum (case C) yields

$$\frac{P_{oC}(x)}{P_{oC}(1)} = \frac{\alpha_1^2}{(x-1)^2+\alpha_1^2} \qquad \text{(A-11)}$$

Note, only one parameter α_1 is required to plot this ratio (in all cases) versus the dimensionless variable x. This makes the approach adopted here very appealing.

To plot these results I initially will choose $\alpha_1 = 0.20$, a nominal value based on wind tunnel experiments. In this case the Corcos spectrum levels off at about -14dB for $x \ll 1$. The three cases are plotted in the attached figure for $x < 1$. There are substantial differences in the three curves for all x below about 0.8. There will be some differences for $x > 1$ but that matter is not of immediate concern.

There are, of course, many other possibilities for choices of A and B. I deem it wise to wait until measured spectra are available and then base any further analytical work on those results. A numerical comparison with the Chase spectra will be the next endeavor.

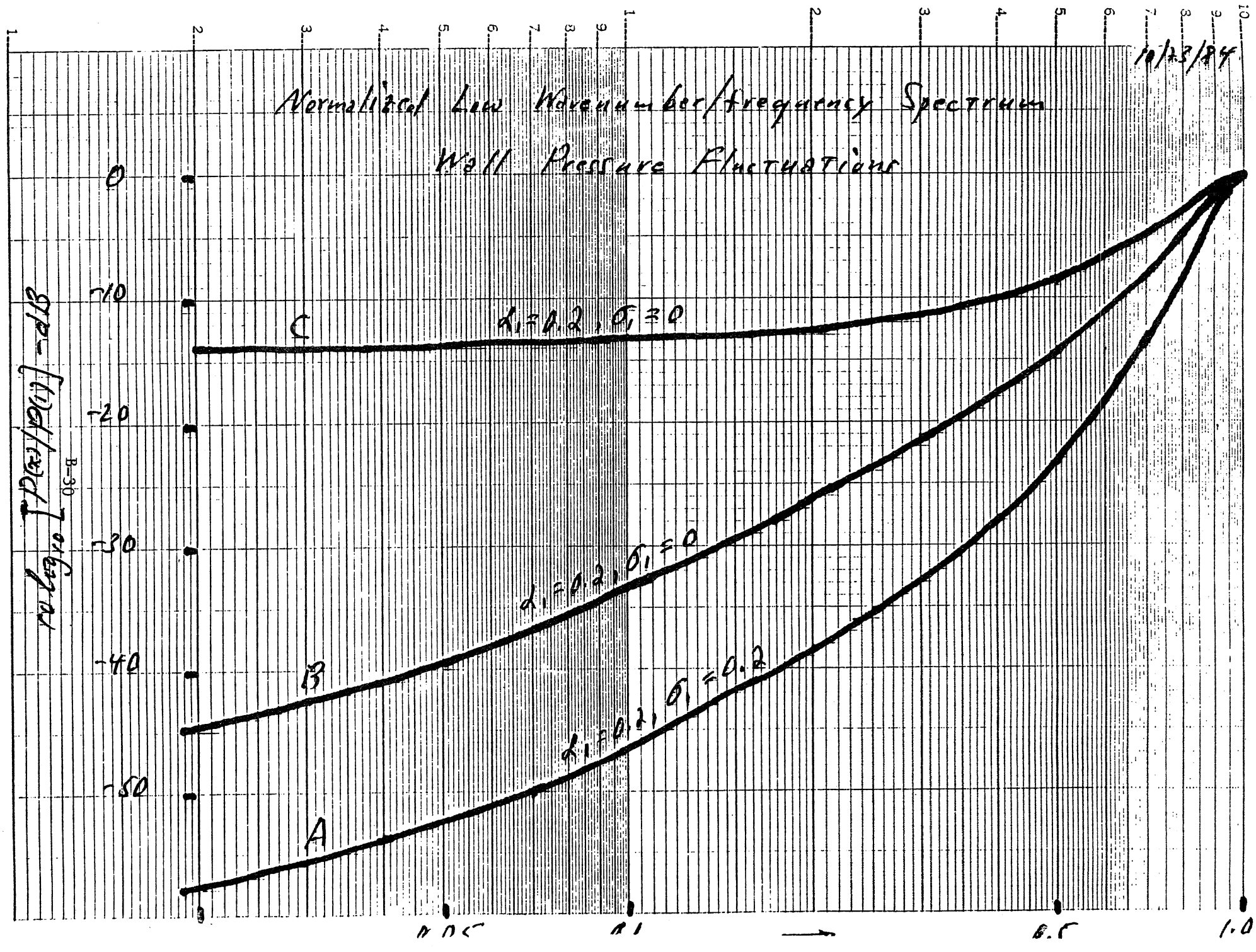
10/15/84
Normalized Low Wavenumber/Frequency Spectrum
Wall Pressure Fluctuations
0
-10
-20
-30
-40
-50
C
B
A
$\alpha_1 = 0.2, \sigma_1 = 0$
$\alpha_1 = 0.2, \sigma_1 = 0$
$\alpha_1 = 0.2, \sigma_1 = 0.2$
B=30
0.5
1.0

VII Spectral Properties of the Convective Waveguide Model of Wall Pressure Fluctuations

Robert F. Lambert

Introduction

The purpose of this tract is to make some numerical predictions of the wavenumber/frequency spectrum level employing the convective waveguide model and compare the results with the Chase model. Because of the dispersive properties of the waveguide model at low frequencies some significant differences are expected. In particular, I would like to compare the effects of frequency on the location of the convective peak which occurs at the longitudinal wavenumber ω/V_c in both the Chase model and other high frequency models. It turns out that at sufficiently high frequencies, i.e. $\omega^2/\omega_o^2 >> 1$, that all models agree where $\omega_o \simeq V_c/\delta$ in the convective waveguide model. All other frequencies will be considered as low frequencies.

Analysis

In order to make a fair comparison with the Chase model I have selected the logitudinal and lateral coherence functions to be of the special forms

$$A\left[\frac{\omega\xi}{V_c}, \frac{\xi}{\delta}\right] = \left[1 + |\sigma_1(\frac{\omega\xi}{V_c})_*|\right] e^{-\alpha_1|(\frac{\omega}{V_c})_*\xi|} \qquad a)$$

$$B\left[\frac{\omega\eta}{V_c}, \frac{\eta}{\delta}\right] = \left[1 + |\sigma_2(\frac{\omega\eta}{V_c})_*|\right] e^{-\alpha_2|(\frac{\omega}{V_c})_*\eta|} \qquad b) \qquad (1)$$

respectively, where the decay parameters $\alpha_1 > o$ and $\alpha_2 > o$ are treated as constants and must be found from experiments. From tract VI, $(\omega/V_c)_* = \sqrt{(\omega/V_c)^2 + \frac{1}{V_c^2}(\frac{V\infty}{\delta})^2} = \frac{\omega}{V_c}\sqrt{1 + \omega^2_o/\omega^2}$.

The parameters σ_1 and σ_2 are associated with α_1 and α_2 by the formulas

$$\sigma_1 = \alpha_1/(1+r) \qquad a)$$

$$\sigma_2 = \alpha_2(1-r)/(1+r) \qquad b) \qquad (2)$$

and

$$\frac{\sigma_2}{\sigma_1} = \frac{\alpha_2}{\alpha_1}(1-r) \qquad c)$$

where r is a mixture coefficient that appears to lie between 0 and 1. If $r << 1$ the pressure fluctuations are dominated by the mean shear.

In order to determine a self consistent set of numerical values for α_1, α_2 and r I employed the coherence data of M. K. Bull and attempted a good fit of Eqs. 1a and 1b to his data for several choices of ξ/δ and η/δ.

I was not able to obtain a "best" fit in any mathematical sense but did establish by trial that the choices $\alpha_1 = 0.2$, $\alpha_2 = 1.0$ and $r = 0.6$ provided an acceptable fit to Bull's data. The resulting ratio $\alpha_2/\alpha_1 = 5$ seems to be consistent with choices made by others including Chase who selected $\alpha_2/\alpha_1 = 7$. For this set of parameters the values of $A[0, \xi/\delta]$ and $B[0,\eta/\delta]$ are both less than unity for all values of ξ/δ and η/δ greater than zero. For the choices made both $A\left[\frac{\omega\xi}{V_c}, \frac{\xi}{\delta}\right]$ and $B\left[\frac{\omega\eta}{V_c}, \frac{\eta}{\delta}\right]$ peak at the origin.

It is interesting to note that the coherence functions in Eq. 1 may or may not exhibt a maximum value for $\frac{\omega\xi}{V_c}$ and $\omega\eta/V_c$ greater than zero depending on the relative values of the other parameters involved. For example, if $A\left[\frac{\omega\xi}{V_c}, \frac{\xi}{\delta}\right]$ is plotted versus $\frac{\omega\xi}{V_c}$ employing ξ/δ as a parameter it will exhibit a maximum for $|\omega\xi/V_c| > 0$, provided

$$\alpha_1 < \sigma_1 \qquad a)$$

and (3)

$$\left(\frac{1}{\alpha_1} - \frac{1}{\sigma_1}\right)^2 > \left(\frac{V_\infty}{V_c}\right)^2\left(\frac{\xi}{\delta}\right)^2 \qquad b)$$

For M. K. Bull's data that did not appear to be the case. Moreover, Eq. 2

requires that $\sigma_1 < \alpha_1$ for $r > o$.

From the definitions in tract VI we now have by direct integration of Eq. 1

$$A^*\left[\left(\frac{k_1 V_c}{\omega}\right)_* - 1\right] = \frac{1}{\pi}\left(\frac{V_c}{\omega}\right)_* \left[\frac{\alpha_1^2(\alpha_1+\sigma_1)+(\alpha_1-\sigma_1)\left[\left(\frac{k_1 V_c}{\omega}\right)_* - 1\right]^2}{\left\{\alpha_1^2 + \left[\left(\frac{V_c k_1}{\omega}\right)^* - 1\right]^2\right\}^2}\right] \quad a) \tag{4}$$

and

$$B^*\left[\left(\frac{k_2 V_c}{\omega}\right)_*\right] = \frac{1}{\pi}\left(\frac{V_c}{\omega}\right)_* \left[\frac{\alpha_2^2(\alpha_2+\sigma_2)+(\alpha_2-\sigma_2)\left(\frac{k_2 V_c}{\omega}\right)_*^2}{\left\{\alpha_2^2 + \left(\frac{V_c k_2}{\omega}\right)_*^2\right\}^2}\right] \quad b)$$

The above expressions are then incorporated into the leading term for the wavenumber/frequency spectrum (Eq. 9 of tract VI) namely

$$P_o(k_1, k_2, \omega) = a_o G(\omega) A^*\left[\quad\right] B^*\left[\quad\right]\left(\frac{V_c k}{\omega}\right)_*^2 \quad a)$$

where

$$G(\omega) = \rho_o V_c^3 \delta^3 G_o\left(\frac{\omega\delta}{V_\infty}\right) \quad b) \tag{5}$$

and

$$k^2 = k_1^2 + k_2^2 \quad c)$$

This formulation yields a power spectrum due to incompressible fluid flow of the form

$$\Phi_o(\omega) = \alpha\left(\frac{\omega}{V_c}\right)_*^2 G(\omega) \tag{6}$$

where α is a constant of integration and in the notation of tract V the spectrum parameter

$$G_o\left(\frac{\omega\delta}{V_\infty}\right) = \frac{1}{2}\left(\frac{V_\infty}{V_c}\right)^2\left(\frac{\delta^*}{\delta}\right)\frac{\tilde{\omega}_b^{\,2}}{\left(\frac{\delta^*}{\delta}\right)^4\left(\frac{\omega\delta}{V_\infty}\right)^4 + \left(\tilde{\omega}_b^{\,2}-2\tilde{\omega}_c^{\,2}\right)\left(\frac{\delta^*}{\delta}\right)^2\left(\frac{\omega\delta}{V_\infty}\right)^2+\tilde{\omega}_c^{\,4}} \tag{7}$$

where the parameters are related to the power spectrum center frequency ω_c and the power spectrum bandwidth ω_b via definitions in tract V.

By setting k_2 in Eq. 5 to zero the longitudinal wavenumber/frequency spectrum reduces to

$$P_o(k_1,\ o,\ \omega) = \frac{a_o\left(\frac{\omega}{V_c}\right)_*^{\,2}G(\omega)}{\pi^2}\left(\frac{k_1V_c}{\omega}\right)_*^{\,2}\left(\frac{\alpha_2+\sigma_2}{\alpha_2^{\,2}}\right) \times \left[\frac{\alpha_1^{\,2}(\alpha_1+\sigma_1) + (\alpha_1-\sigma_1)\left[\left(\frac{k_1V_c}{\omega}\right)_* -1\right]^2}{\left\{\alpha_1^{\,2}+\left[\left(\frac{V_ck_1}{\omega}\right)_* -1\right]^2\right\}^2}\right] \tag{8}$$

Note, a_o is an unknown paramter in this formulation and also both α_2 and σ_2 are involved in the prediction.

The peak occurs at $\left(\frac{V_ck_1}{\omega}\right)_* = 1$ which yields

$$P_o\left[\left(\frac{\omega}{V_c}\right)_*,\ o,\ \omega\right] = \frac{a_o\left(\frac{V_c}{\omega}\right)_*^{\,2}G(\omega)}{\pi^2}\frac{(\alpha_2+\sigma_2)(\alpha_1+\sigma_1)}{\alpha_1^{\,2}\alpha_2^{\,2}} \tag{9}$$

which could afford an evaluation of a_o if the other parameters are known from independent measurements.

Since at present we don't have values for all the parameters it is expedient and convenient for comparison purposes to normalize the spectrum with respect to its peak value, Eq. 9. After normalization the longitudinal wavenumber/frequency spectrum level takes the form

$$10 \log_{10}\left[\frac{P(x_*)}{P(1)}\right] = 10 \log_{10}\left[\frac{\alpha_1^4 + \alpha_1^2\left(\frac{\alpha_1-\sigma_1}{\alpha_1+\sigma_1}\right)(x_*-1)^2}{[\alpha_1^2 + (x_*-1)^2]^2}\right] x_*^2 \}\text{dB} \qquad (10)$$

where $x_* = (k_1 V_c/\omega)_* = \left(\frac{k_1 V_c}{\omega}\right)\frac{1}{\sqrt{1+\omega_o^2/\omega^2}}$.

Numerical Predictions

The above expression can be plotted either as a function of x_* (or $x = \frac{V_c}{\omega}$ if $\omega_{o/\omega}$ is taken as a parameter) for both positive and negative values of x_*. It will peak at $x_*=1$ and approaches a constant as $x_* \to \infty$. The value of this asymptote is important and is quite sensitive to the difference $\alpha_1-\sigma_1$. If $\alpha_1=\sigma_1$, i.e. r=o, then $P(x_*)\to 0$ as $x_* \to \infty$.

Typical plots of Eq. 10 for the parameters $\alpha_1=0.2$ and r=0.6 are shown in Figs. 1 and 2. Note, in particular that Eq. 10 levels off at about -20 dB for both $x_* >> 1$ and $x_* << 1$ for this choice of parameters.

The same general type of plot can be made for the lateral spectrum $P(0, k_2, \omega)$.

After normalization the lateral wavenumber/frequency spectrum level takes the form

$$10 \log_{10}\left[\frac{P(y)}{P(1)}\right] = 10 \log_{10}\left[\frac{\alpha_1^4 + \alpha_1^2\left(\frac{\alpha_1-\sigma_1}{\alpha_1+\sigma_1}\right)}{(\alpha_1^2+1)^2}\right] \times \left[\frac{\alpha_2^4 + \alpha_2^2\left(\frac{\alpha_2-\sigma_2}{\alpha_1+\sigma_1}\right)(y_*^2}{(\alpha_2^2 + y_*^2)^2}\right] y_*^2 \}\text{dB} \qquad (11)$$

where $y_* = \left(\frac{k_2 V_c}{\omega}\right)_*$.

Eq. 11 is symmetrical in y_* and a typical plot is shown in Fig. 3. Note again, the function tends to level off at about-20 dB for $y_* >> 1$. These results suggest that I have selected a self consistent set of parameters α_1, σ_1, α_2, σ_2 on the basis of Bull's measurements.

At this point I am satisfied that a meaningful comparison between the level predictions of Eq. 10 and Chases' predictions can be made. Chase also selected the parameters in his numerical work from Bull's data. Several comparisons are shown in the next set of figures. It should be obvious that for $\omega_o^2/\omega^2 << 1$, $(\frac{k_1 V_c}{\omega})_* \simeq \frac{k_1 V_c}{\omega}$ and the comparison is direct. On the other hand for $\frac{\omega_o}{\omega} \geq 1$ that will not be the case and effects of waveguide or other frequency dispersion should be evident.

A plot of the Chase spectrum is shown in Fig. 4 employing frequency as a parameter. In all of the comparisons δ=1cm, V_∞=10cm/s and $x=k_1 V_c/\omega$. In the Chase model all of the curves peak at x=1 independent of ω but there are some dispersive effects at frequencies below 500 Hz which are very evident. The normalized level increases with decreasing frequency quite significantly at low wavenumbers. Note, above 1000 Hz there is no significant change in level with increasing frequency at all wavenumbers for the parameters chosen.

Plots of Eq. 10 versus $x= \frac{k_1 V_c}{\omega}$ on the other hand, exhibit a significantly different behavior if frequency is employed as a parameter. This is quite evident in Fig. 5 where $\omega_o = V_c/\delta$=1000 and ω/ω_o is employed as the parameter. The function peaks at $k_1 = \frac{\omega}{V_c}$ at high frequencies, i.e. $\omega_o^2/\omega^2 << 1$, as expected but the peaks shift to higher values of k_1 as ω is decreased especially in the range $\omega \leq \omega_o$. Note, the predicted level decreases at low wavenumbers as frequency is decreased on this scale. Fig. 6 shows the same results but on a logarithmic

wavenumber scale which is easier to use at low wavenumbers for comparison purposes.

It also is informative to plot the Chase spectrum level versus $x_* = (k_1 V_c/\omega)_*$ for the parameter $\omega_0 = 1000$ and then employ frequency as a parameter. This characteristic is shown in Fig. 7. Note the shift in wavenumber peak is now downward as frequency is decreased and there exists a correspondingly greater increase in normalized level with decreasing frequency. This general result is to be expected and such trends should be observable experimentally.

The last two figures show the effects of varying α_1 about a nominal value of 0.2. In the results shown in Fig. 8 r=0.6 is fixed. Thus, one can see that experimental errors in finding α_1 and α_2 can be significant, the greater the decay rates the higher the predicted level at both low and high wavenumbers.

Fig. 9 shows the extreme case where r=o. Then $\sigma_1 = \alpha_1$ and the levels are greatly diminished at both low and high wavenumbers for the same choice of α_1. The corresponding wavenumber/frequency spectrum is very sharp. Hopefully, such trends also will be observable experimentally.

Figure Legend

I. Normalized longitudinal wavenumber/frequency spectrum level versus $x_*=(\frac{k_1 V_c}{\omega})_*$ for $x_* > o$ and $\sigma_1=0.20$, $r=0.6$. Convective waveguide model.

II. Normalized longitudinal wavenumber/frequency spectrum level versus x_* for $x_* < o$ and $\alpha_1=0.20$ and $r=0.6$. Convective waveguide model.

III. Normalized lateral wavenumber/frequency spectrum level versus $y_*=(\frac{k_2 V_c}{\omega})_*$ for $\alpha_1=0.20$, $\alpha=1.00$, and $r=0.6$. Convective waveguide model.

IV. Normalized longitudinal waveguide/frequency spectrum level versus $x=\frac{k_1 V_c}{\omega}$ employing frequency as a parameter for $\delta=1$cm. Chase model.

V. Normalized longitudinal wavenumber/frequency spectrum level versus $x=\frac{k_1 V_c}{\omega}$ employing ω/ω_0 as a parameter. Here $\omega_0=1000$r/s corresponding to $\delta=1$cm and $V\infty=10$ cm/s. Linear wavenumber scale. Note the predicted wavenumber shift due to waveguide dispersion.

VI. Same plot as figure V but x is shown on a logarithmic scale. Note predicted wavenumber shift due to waveguide dispersion.

VII. Chase spectrum when plotted versus $x_*=(\frac{k_1 V_c}{\omega})_*$. Note, the wavenumber shift due to dispersion.

VIII. Sensitivity calculation showing the effects of variations in α_1 in the longitudinal wavenumber/frequency spectrum. Here $r=0.6$ is held fixed.

IX. Sensitivity calculations showing the effect of lowering the mixing parameter r to zero.

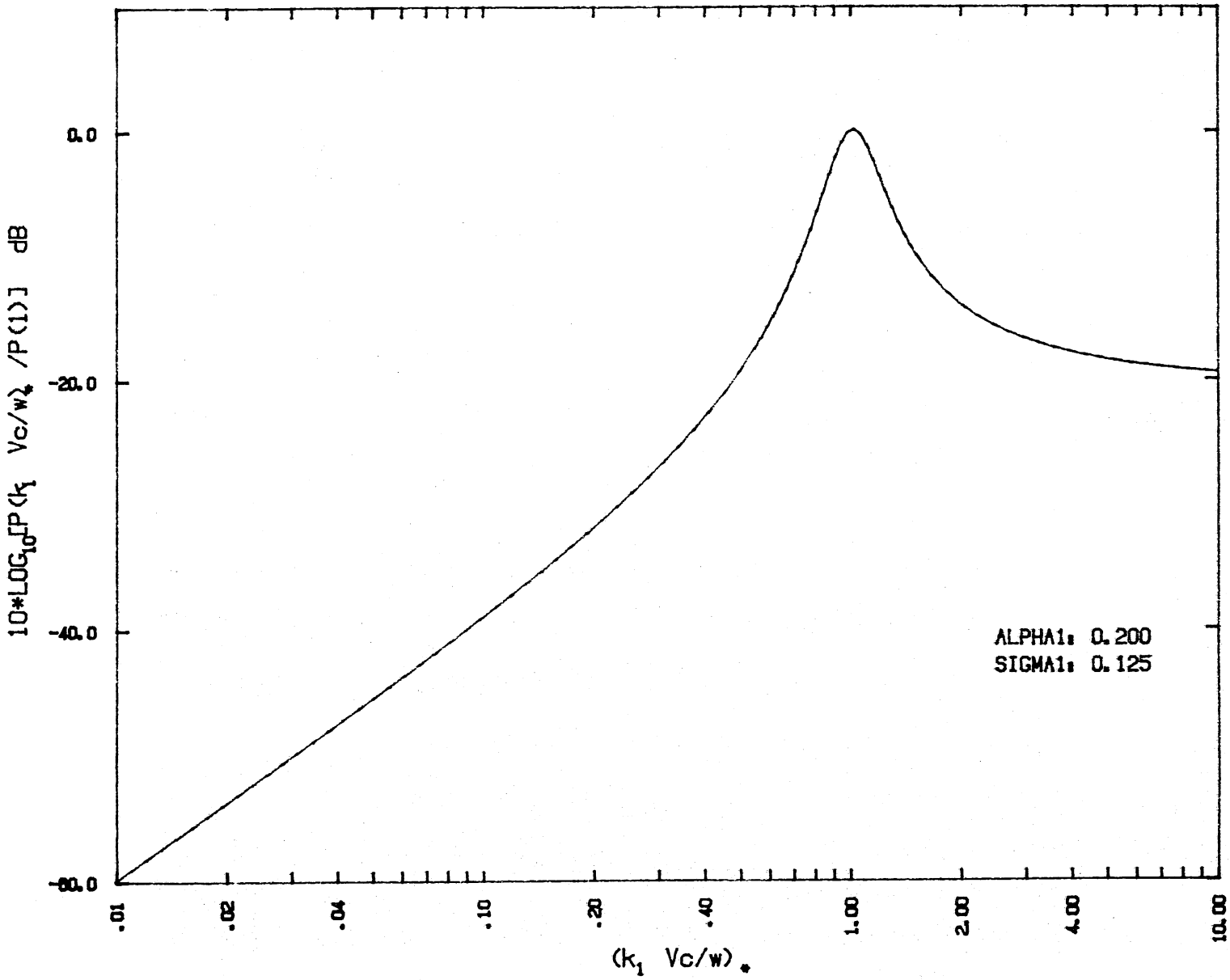
0.0
-20.0
-40.0
-60.0
10*LOG10[P(k1 Vc/w)* /P(1)] dB
.01
.02
.04
.10
.20
.40
1.00
2.00
4.00
10.00
(k1 Vc/w)*
ALPHA1: 0.200
SIGMA1: 0.125

Fig. 1

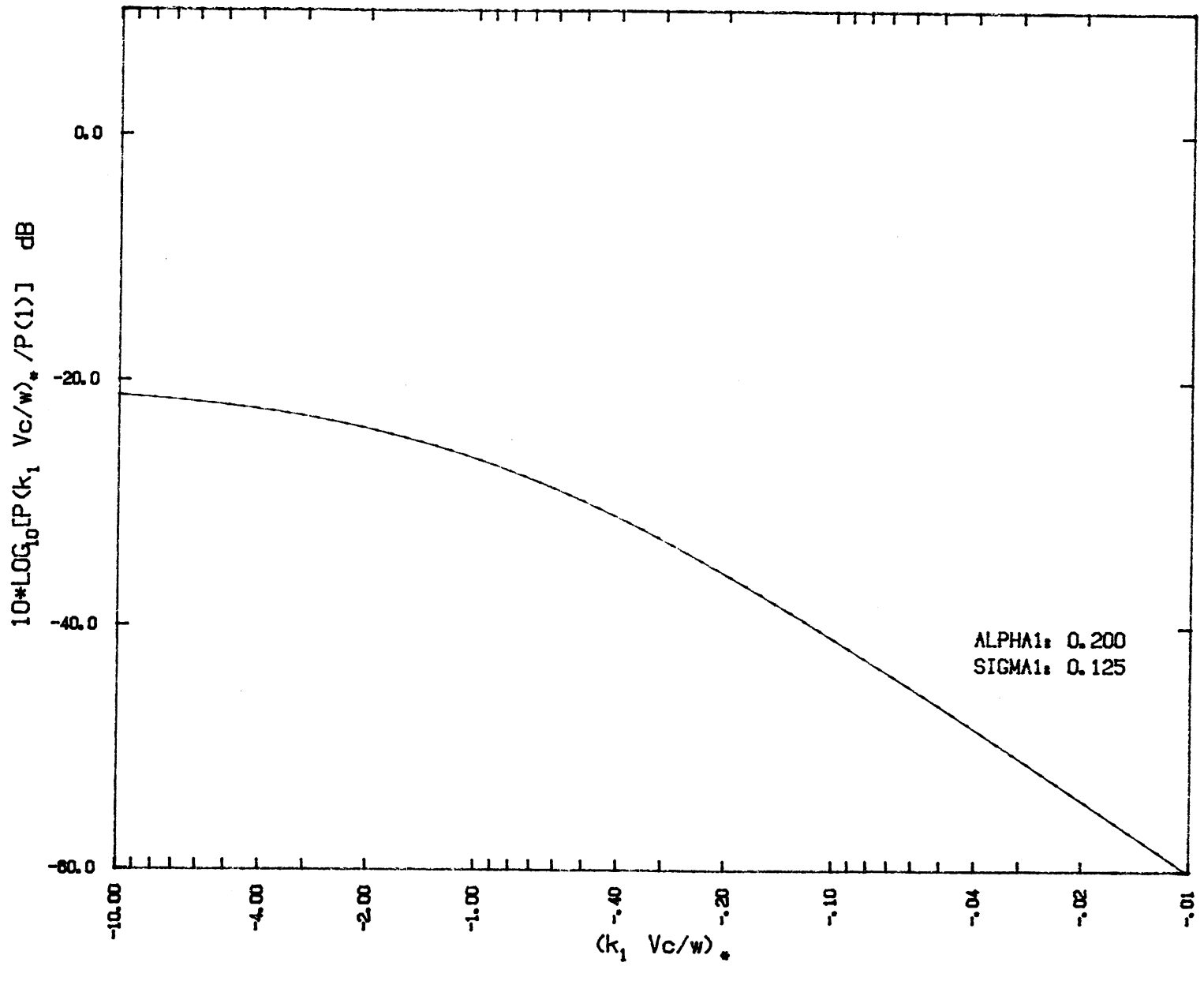
0.0
-20.0
-40.0
-60.0
10*LOG10[P(k1 Vc/w)* /P(1)] dB
-10.00
-4.00
-2.00
-1.00
-.40
-.20
-.10
-.04
-.02
-.01
(k1 Vc/w)*
ALPHA1: 0.200
SIGMA1: 0.125

Fig. 2

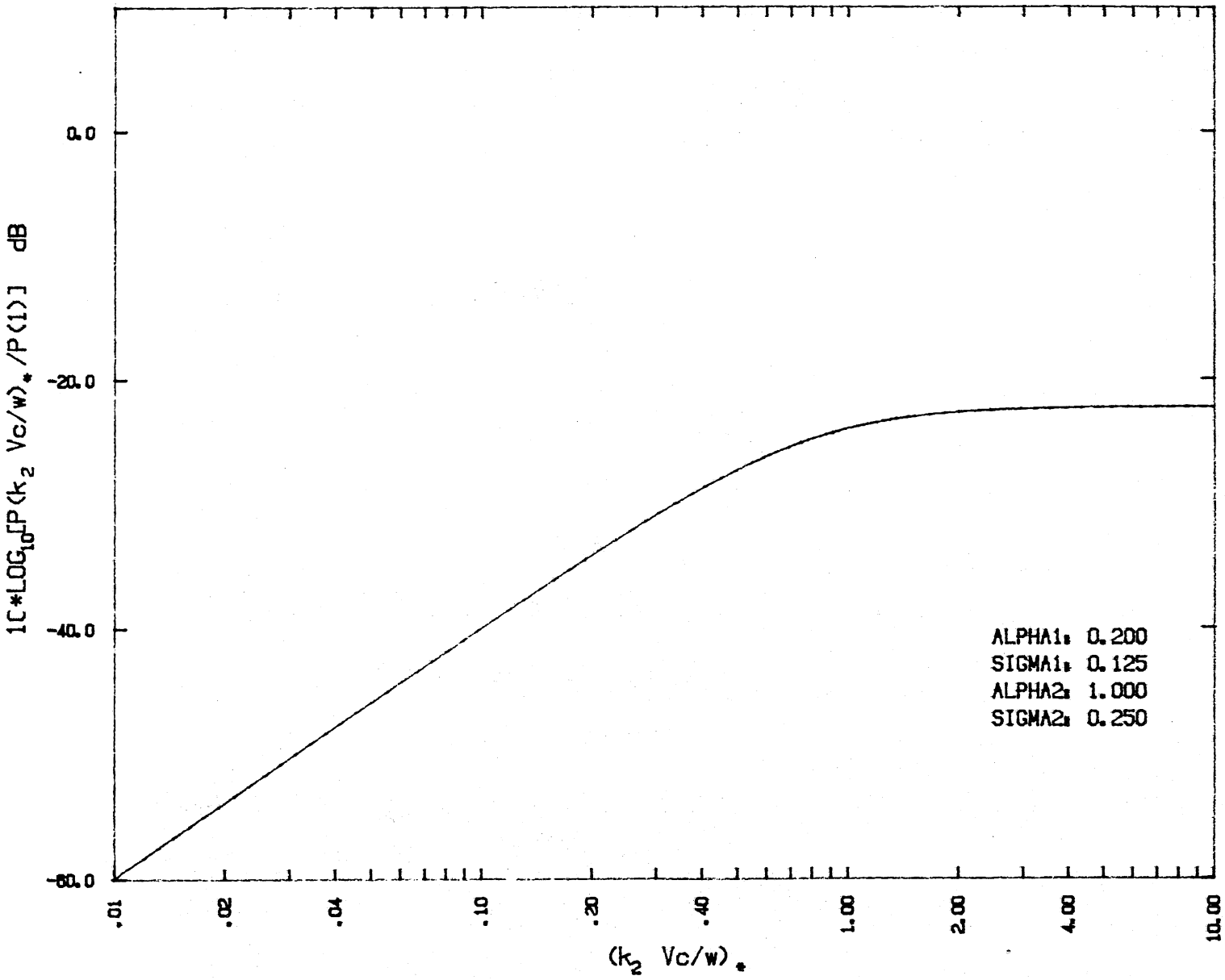
0.0
-20.0
-40.0
-60.0
10*LOG10[P(k2 Vc/w)* /P(1)] dB
.01
.02
.04
.10
.20
.40
1.00
2.00
4.00
10.00
(k2 Vc/w)*
ALPHA1: 0.200
SIGMA1: 0.125
ALPHA2: 1.000
SIGMA2: 0.250

Fig. 3

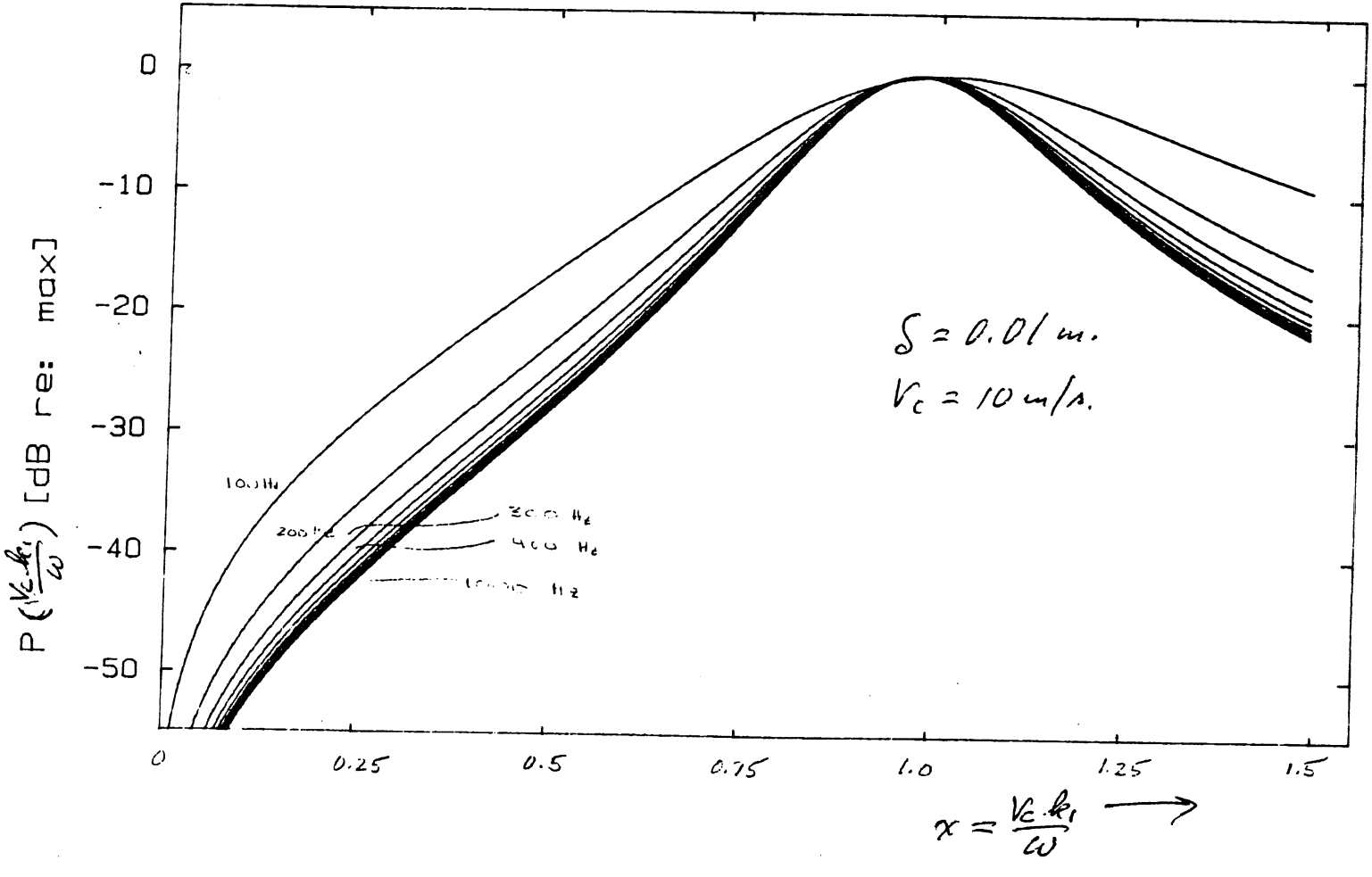
0
-10
-20
-30
-40
-50
P (Vc.k1/ω) [dB re: max]
0
0.25
0.5
0.75
1.0
1.25
1.5
x = Vc.k1/ω
δ = 0.01 m.
Vc = 10 m/s.
100 Hz
200 Hz
400 Hz

Fig. 4

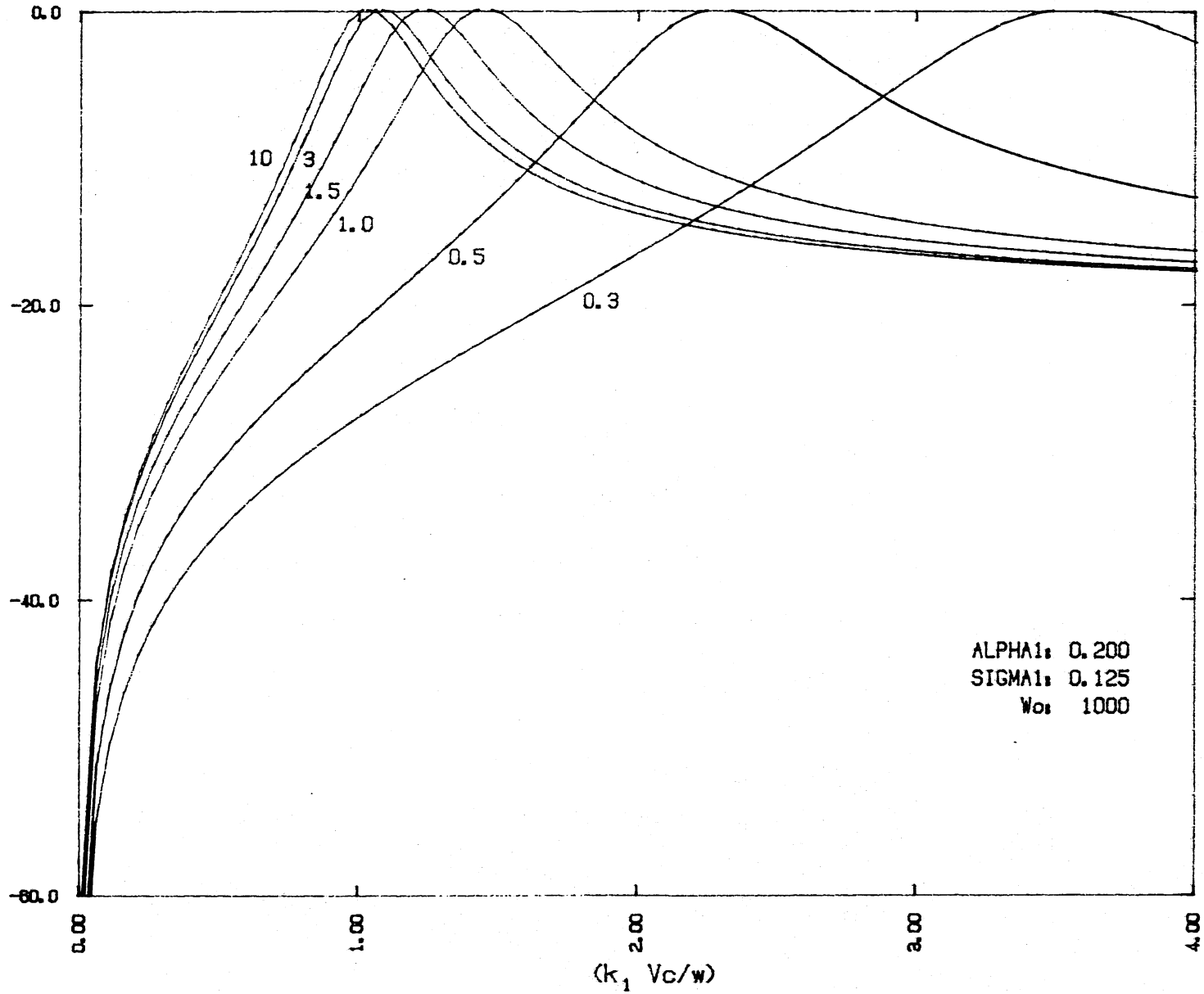
0.0
-20.0
-40.0
-60.0
10*LOG10[P(k1 Vc/w)/P(1)] dB
10
3
1.5
1.0
0.5
0.3
ALPHA1: 0.200
SIGMA1: 0.125
Wo: 1000
0.00
1.00
2.00
3.00
4.00
(k1 Vc/w)

FIG. 5

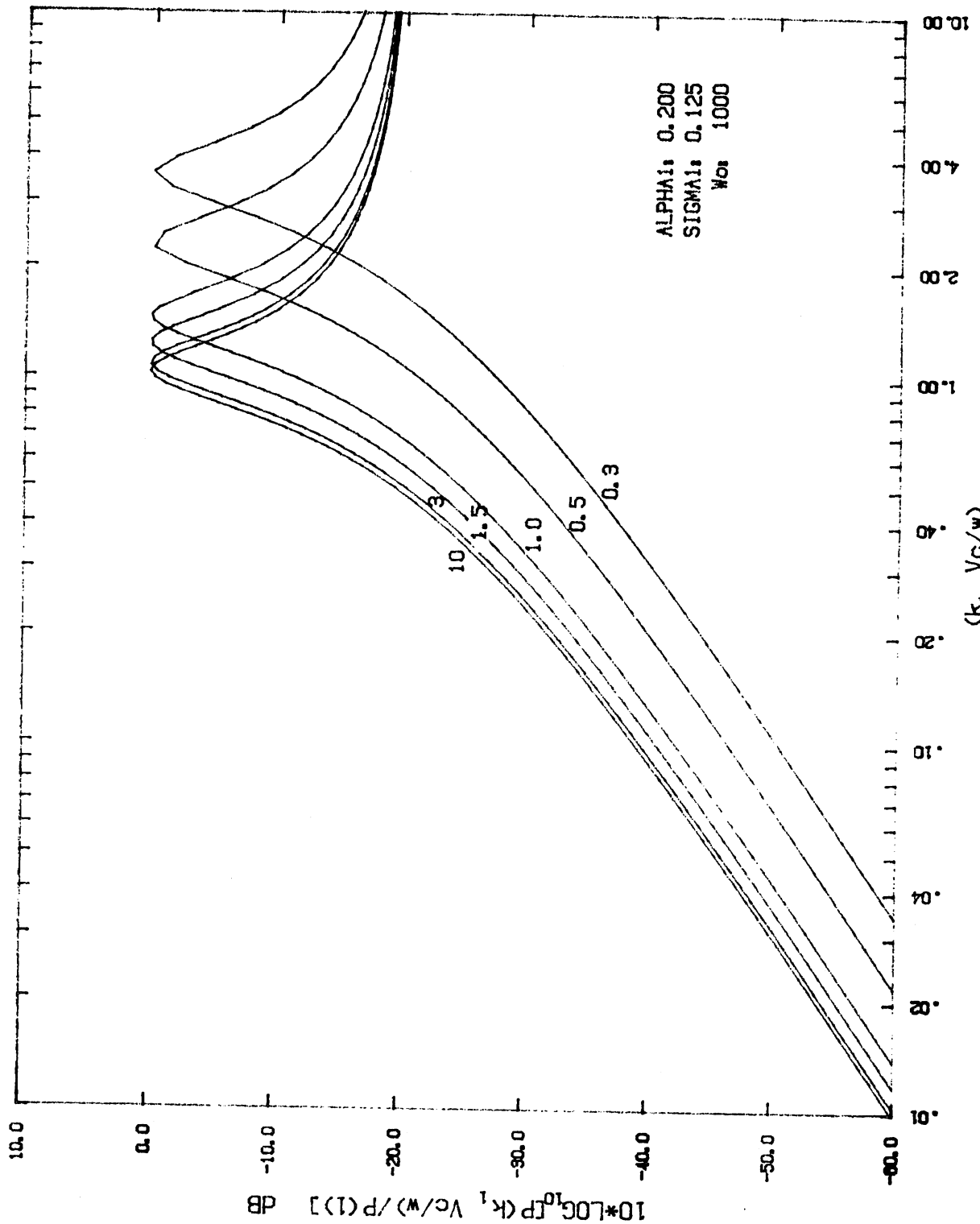
ALPHAi: 0.200
SIGMAi: 0.125
Wo: 1000
0.3
0.5
1.0
1.5
3
10
10.0
0.0
-10.0
-20.0
-30.0
-40.0
-50.0
-60.0
10*LOG10[P(k1 Vc/w)/P(1)] dB
.01
.02
.04
.08
.1
.2
.4
.8
1.0
2.0
4.0
8.0
10.0
(k1 Vc/w)

Fig. 6

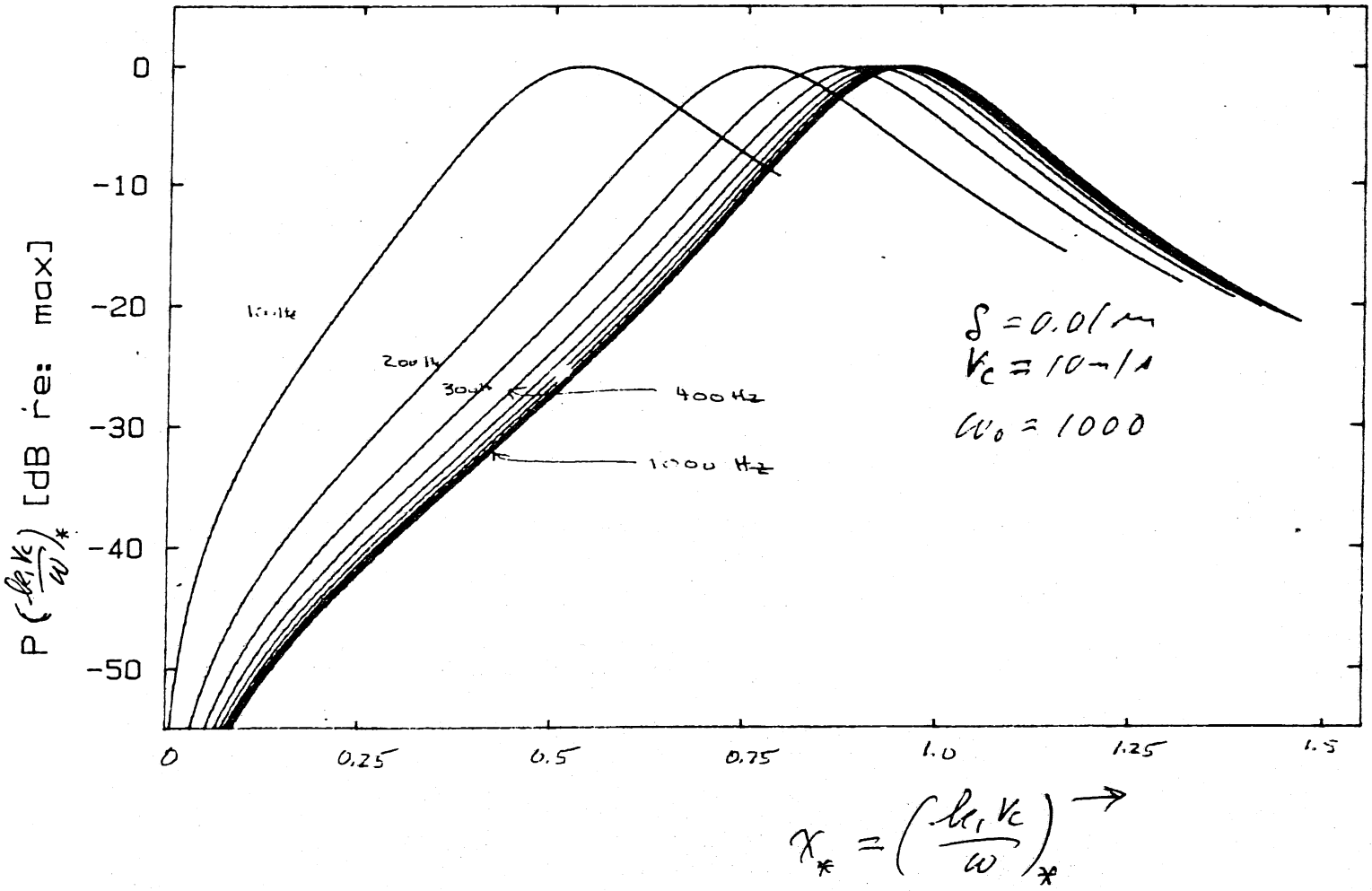
0
-10
-20
-30
-40
-50
0
0.25
0.5
0.75
1.0
1.25
1.5
P(-k1Vc/ω)* [dB re: max]
200 Hz
300 Hz
400 Hz
1000 Hz
δ = 0.01 m
Vc = 10-11
ω0 = 1000
χ* = (-k1Vc/ω)*

Fig. 7

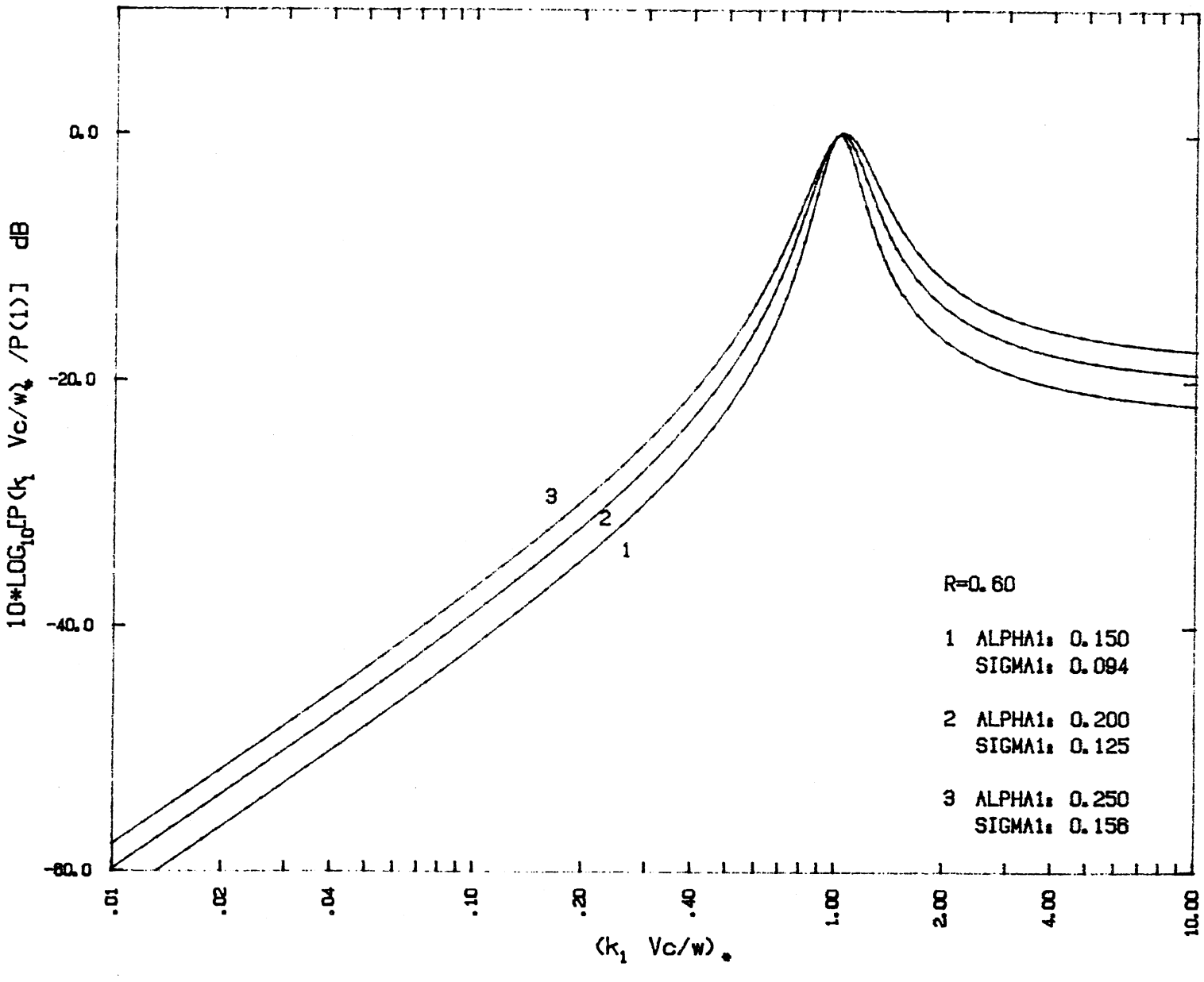
0.0
-20.0
-40.0
-60.0
10*LOG10[P(k1 Vc/w)* /P(1)] dB
.01
.02
.04
.10
.20
.40
1.00
2.00
4.00
10.00
(k1 Vc/w)*
3
2
1
R=0.60
1 ALPHA1: 0.150
SIGMA1: 0.094
2 ALPHA1: 0.200
SIGMA1: 0.125
3 ALPHA1: 0.250
SIGMA1: 0.156

Fig. 8

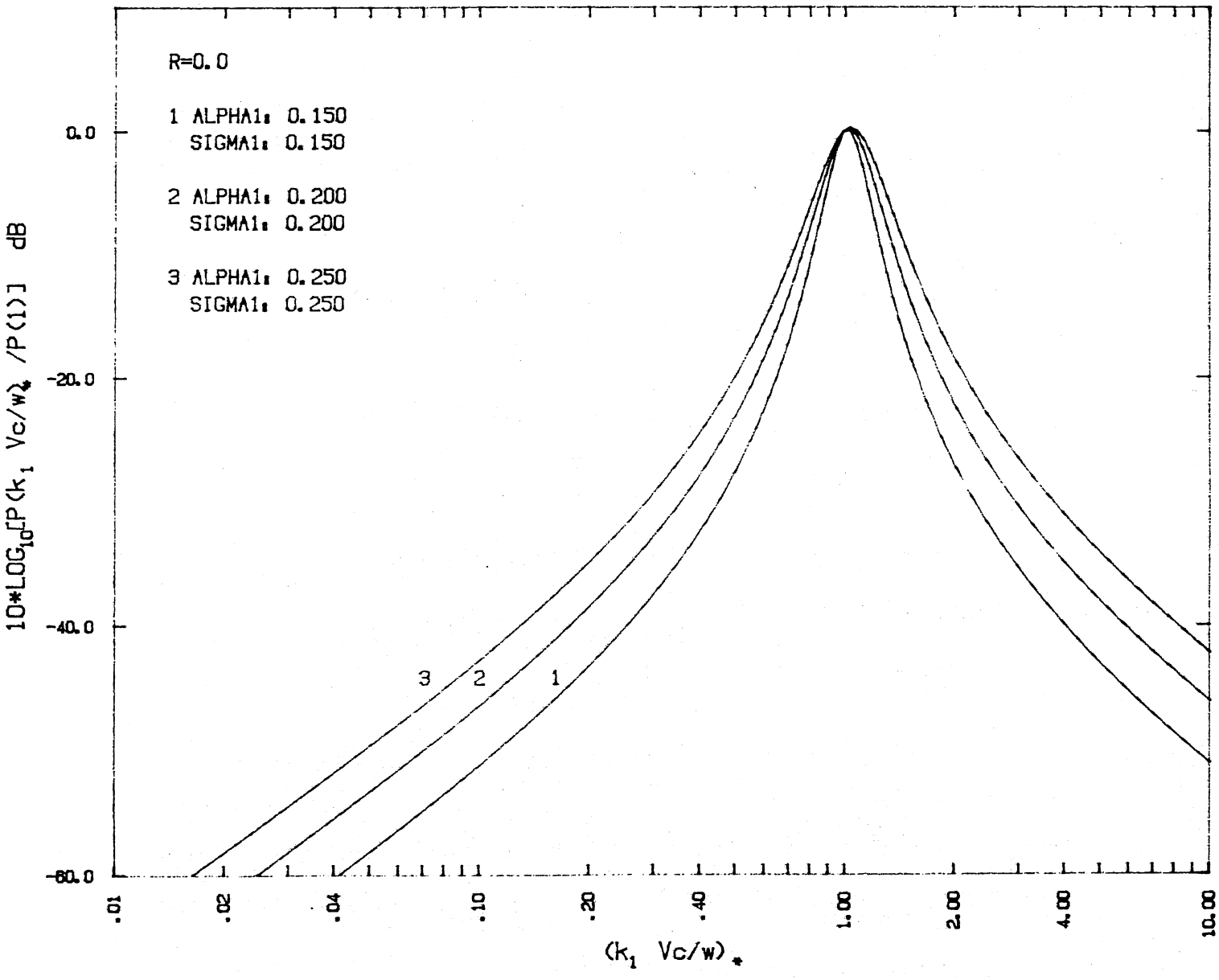
R=0.0
1 ALPHA1: 0.150
SIGMA1: 0.150
2 ALPHA1: 0.200
SIGMA1: 0.200
3 ALPHA1: 0.250
SIGMA1: 0.250
0.0
-20.0
-40.0
-60.0
10*LOG10[P(k1 Vc/w)* /P(1)] dB
3
2
1
.01
.02
.04
.10
.20
.40
1.00
2.00
4.00
10.00
(k1 Vc/w)*

Fig. 9

VIII. Properties of the Spatial Coherence Functions

Wall Pressure Fluctuations

by

Robert F. Lambert and Keith Alcock

Introduction

The purpose of this tract is to focus attention on the functional form and evaluation of numerical parameters for the longitudinal and lateral spatial coherence functions that were employed in tracts VI and VII to predict the spectral characteristics of wall pressure fluctuations in boundary layer flow. Also in Appendix B a new experiment is suggested. In tracts VI and VII we employed these functions in the special forms

$$A\left[\frac{\omega\xi}{V_c}, \frac{\xi}{\delta}\right] = \left[1+|\sigma_1(\frac{\omega\xi}{V_c})_*|\right]e^{-\alpha_1|(\frac{\omega\xi}{V_c})_*|} \quad \text{a)}$$

and (1)

$$B\left[\frac{\omega\eta}{V_c}, \frac{\eta}{\xi}\right] = \left[1+|\sigma_2(\frac{\omega\eta}{V_c})_*|\right]e^{-\alpha_2|(\frac{\omega\eta}{V_c})_*|} \quad \text{b)}$$

with explicit constraints between α_1 and σ_1 and between α_2 and σ_2.

From tract VI both

$$(\frac{\omega\xi}{V_c})_* = \sqrt{(\frac{\omega\xi}{V_c})^2+(\frac{V_\infty}{V_c})^2(\frac{\xi}{\delta})^2} \quad \text{a)}$$

and (2)

$$(\frac{\omega\eta}{V_c})_* = \sqrt{(\frac{\omega\eta}{V_c})^2+(\frac{V_\infty}{V_c})^2(\frac{\eta}{\delta})^2} \quad \text{b)}$$

involve a number of dimensionless parameters. It was discovered early on in coherence measurements in wind tunnels that all five parameters were important: namely, $\frac{\omega\xi}{V_c}$, $\frac{\omega\eta}{V_c}$, $\frac{V_\infty}{V_c}$, $\frac{\xi}{\delta}$ and $\frac{\eta}{\delta}$. The convective waveguide model is consistent with those observations and yields Eq. 2 directly from the dispersive properties

of the model. The problem is how to optimize subject to constraints the choice of α_1, σ_1, α_2, and σ_2. In particular, their values depend on the ratio $V\infty/Vc$ via Eq. 2. Initially, it was assumed that $\frac{V_c}{V_\infty} = 0.80$ a value characteristic of the main energy bearing eddies whereas, in actuality, the ratio is frequency (eddy size) dependent. At extremely low frequencies, (i.e., $\frac{\omega\delta^*}{V_\infty} < 0.2$,) it is usually assumed that $\frac{V_c}{V_\infty}$ approaches unity. At extremely high frequencies, i.e., $\frac{\omega\delta^*}{V_\infty} > 5$, the measured value is closer to 0.6. (See Appendix B).

A method for measuring Vc and determining values for both A and B was described in tract I., Eqs. 6 and 7.

In tract VII the fit of Eq. 1 to coherence measurements by M. K. Bull was reasonable but not entirely satisfactory, especially for small values of $\frac{\omega\xi}{V_c}$ and $\frac{\omega n}{V_c}$. It appeared that one could obtain a better fit of Bull's data if $V_c/V_\infty = 0.60$ (see tract V.) The observed drift velocity is smaller at small spatial separations, i.e., small values of ξ/δ and n/δ.

It was decided to relax the requirement that σ_1 and σ_2 be positive numbers and to reformulate the A and B functions as

$$A\left[\frac{\omega\xi}{V_c}, \frac{\xi}{\delta}\right] = \left[1+\sigma_1\left|\left(\frac{\omega\xi}{V_c}\right)_*\right|\right]e^{-\alpha_1\left|\left(\frac{\omega\xi}{V_c}\right)_*\right|} \qquad a) \tag{3}$$

and

$$B\left[\frac{\omega n}{V_c}, \frac{\xi}{\delta}\right] = \left[1+\sigma_2\left|\left(\frac{\omega n}{V_c}\right)_*\right|\right]e^{-\alpha_2\left|\left(\frac{\omega n}{V_c}\right)_*\right|} \qquad b)$$

and then to attempt a new fit for $\frac{V_c}{V_\infty} = 0.60$ utilizing the values of ξ/δ and μ/δ employed by Bull.

Numerical Predictions

The values of the four numerical parameters obtained by a numerical curve sitting algorithm are:

$$\alpha_1 = 0.166 \qquad \alpha_2 = 0.786$$

$$\sigma_1 = 0.074 \qquad \sigma_2 = -.0842$$

which yields a mixture coefficient $r = 1.24$.

Plots of A, Eq. 3a, versus $\omega\xi/V_c$ employing ratios of $\xi/\delta = 0$, 1.23, and 2.52 are shown in Fig. 1. The data of M. K. Bull for $\xi/\delta = 1.23$ and 2.52 are shown for comparison.

Plots of B, Eq. 3b, versus $\omega\eta/V_c$ employing $\eta/\delta = 0$, 0.103, and 0.627 are shown in Fig. 2. Bull's data points for the same ratio are shown for comparison.

The agreements now are more satisfactory for close spatial separations but not so good for values of $\omega\eta/V_c > 1$ as before. Again maximum values of both A and B occur at the origin. The peak value for $\xi/\delta = 0$ and $\eta/\delta = 0$ is unity.

Several characteristics of the predicted cross spectrum AxB, where

$$A\left[\frac{\omega\xi}{V_c}, \xi/\delta\right]B\left[\frac{\omega\eta}{V_c}, \frac{\eta}{\delta}\right] = \frac{1}{\Phi(\omega)e^{i\left(\frac{\omega\xi}{V_c}\right)*}} \int_{-\infty}^{\infty} R_p(\xi,\eta,\tau)e^{i\omega\tau}d\tau$$

are shown in Figs. 3, 4, 5 and 6 for several parametric choices of ξ/δ and η/δ. Note, the surfaces are similar (but not identical) in shape to cross spectrum measurements obtained in the water tunnel, save for differences in amplitude and spatial scales (See Fig. 9 in the April 1984 - October 1984 program progress report.)

In the last three figures (7, 8 and 9) are plots of normalized wavenumber/frequency spectra $P(k_1,0,\omega)$ versus $(k_1,V_c/\omega)^*$ for a range of both positive and negative k_1 and $P(0,k_2,a)$ versus $(k_2V_c/\omega)^*$ for a range of positive $(k_2V_c/\omega)^*$.

These curves are to be compared with those in Figs. 1, 2, and 3 of tract VII. As can be seen the two sets of predicted spectral characteristics are for all practial purposes the same. This is evident by noting that the dominant term in Eq. 10, tract VII, at both low and high wavenumbers is proporational to $\alpha_1^2(\frac{\alpha_1-\sigma_1}{\alpha_1+\sigma_1})$, a factor that did not change by more than half a decibel. The same result is obtained for Eq. 11 where the $\alpha_2^2(\frac{\alpha_2-\sigma_2}{\alpha_2+\sigma_2})$ term changed by at most 1 decibel. The conclusion is that any changes in the cross spectrum AxB would have to be quite drastic to change the $P(k_1,k_2,\omega)$ functions by 5 decibels or more at both low and high wavenumbers. Even the peak value given by Eq. 9, tract VII, did not change by more than 0.5 decibels in this example. It should be possible to improve the level predictions by assuming an appropriate frequency dependence for Vc/V_∞ and repeating the evaluation of α_1, σ_1, α_2 and σ_2. But that alone is not likely to change the spectral level of $P(k_1, k_2, \omega)$ by a significant amount. However, it will change the predicted location of the convective peak in $P(k_1, o, \omega)$ (see Appendix B).

Appendix A - Curve fitting procedures

In this application the problem is to convert two sets of data points (x_{11},y_{11}), $(x_{12},y_{12}),\cdots,(x_{1m},y_{1m})$ and $(x_{21},y_{21}),\cdots,(x_{2n},y_{2n})$ which are characterized by parameters $k = a_1,a_2$, respectively, into a specified function

$$f(x,k) = [1+\sigma\sqrt{x^2+k^2}\,]e^{-\alpha\sqrt{x^2+k^2}} \qquad \text{(A-1)}$$

with α and σ selected to best fit the data points. The approach used is a variation of the method of least squares by Gauss.

The first step is to construct, by hand, smooth curves through each set of data points. These curves can correct any data errors or deviations that do not appear to be representative of the entire data set.

The initial curves so contributed are then sampled at intermediate point into two new sets of data points $(x_{11}^*,y_{11}^*),\cdots,(x_{1m}^*,y_{1m}^*)$ and $(x_{21}^*,y_{21}^*),\cdots,(x_{2n}^*,y_{2n}^*)$ which then replace the initial sets. Such samples can be taken either evenly spaced or weighted (i.e., close together where an accurate fit is very important) and thereby provide discrete data to be entered into a computer routine and then compared to $f(x,k)$ for choices of α and σ.

The next step is to write a program that will generate values of α and σ and calculate $f(x,k)$ using the values $x_{11}^*,x_{12}^*,\cdots,x_{1n}^*$ and $x_{21}^*,x_{22}^*,\cdots,x_{2n}^*$ as generated above for domain values and $k = a_1,a_2$ for appropriate curves. The difference in the range values y_{11}^*, $y_{12}^*,\cdots,y_{1m}^*$ and $y_{21}^*,y_{22}^*,\cdots,y_{2n}^*$ and the values of $f(x,k)$ is a measure of the accuracy of the value of α and σ. For each α and σ all values of $f(x,k)$ are calculated for each domain value, subtracted from the range value (of the sampled point), squared, and summed. That is

$$VAR = \sum_{i=1}^{m}[f(x_{1i}^*,k_1)-y_{1i}^*]^2 + \sum_{i=1}^{n}[f(x_{2i}^*,k_2)-y_{2i}^*]^2 \qquad \text{(A-2)}$$

which is analogous to the variance or area between f(x,k) and the data points.

The problem now reduces to finding values of α and σ that minimize VAR. Best fit values, α_{bf} and σ_{bf}, are recorded and the function f(x,k) then is plotted for continuous x as a comparison. If the fit to the data point is not satisfactory the original curve can be re-sampled with greater weighting at the segment of greatest variance and the steps repeated. One could also conclude that the function f(x,k) is not appropriate for the data set, which does not appear to be the case.

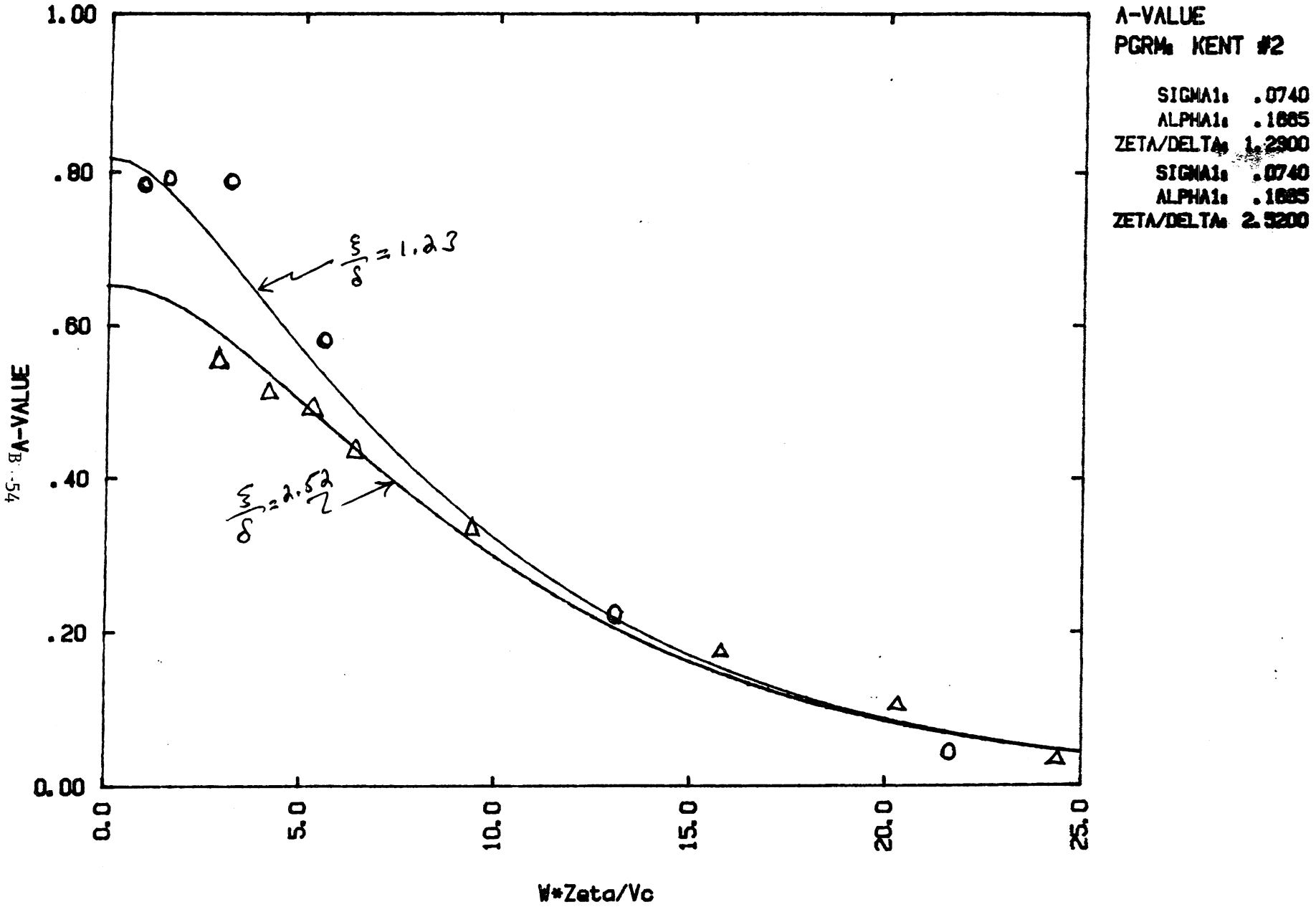
A-VALUE
PGRM: KENT #2
SIGMA1: .0740
ALPHA1: .1885
ZETA/DELTA: 1.2300
SIGMA1: .0740
ALPHA1: .1885
ZETA/DELTA: 2.5200
1.00
.80
.60
.40
.20
0.00
A-VALUE
0.0
5.0
10.0
15.0
20.0
25.0
W*Zeta/Vc
ξ/δ = 1.23
ξ/δ = 2.52

Fig. 1

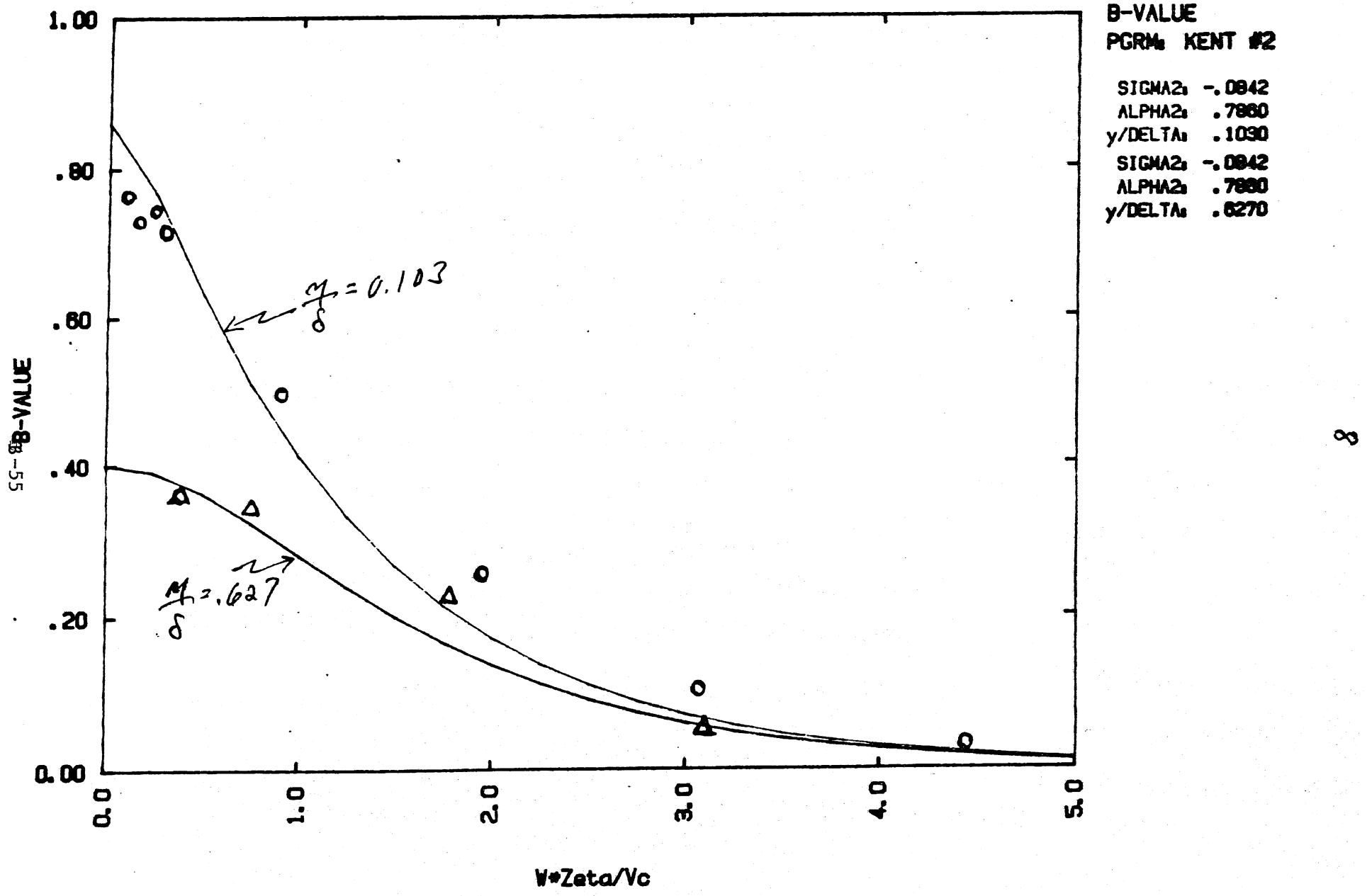
B-VALUE
PGRM: KENT #2
SIGMA2: -.0842
ALPHA2: .7860
y/DELTA: .1030
SIGMA2: -.0842
ALPHA2: .7860
y/DELTA: .6270
1.00
.80
.60
.40
.20
0.00
B-VALUE
0.0
1.0
2.0
3.0
4.0
5.0
W*Zeta/Vc
y/δ = 0.103
y/δ = .627

Fig. 2

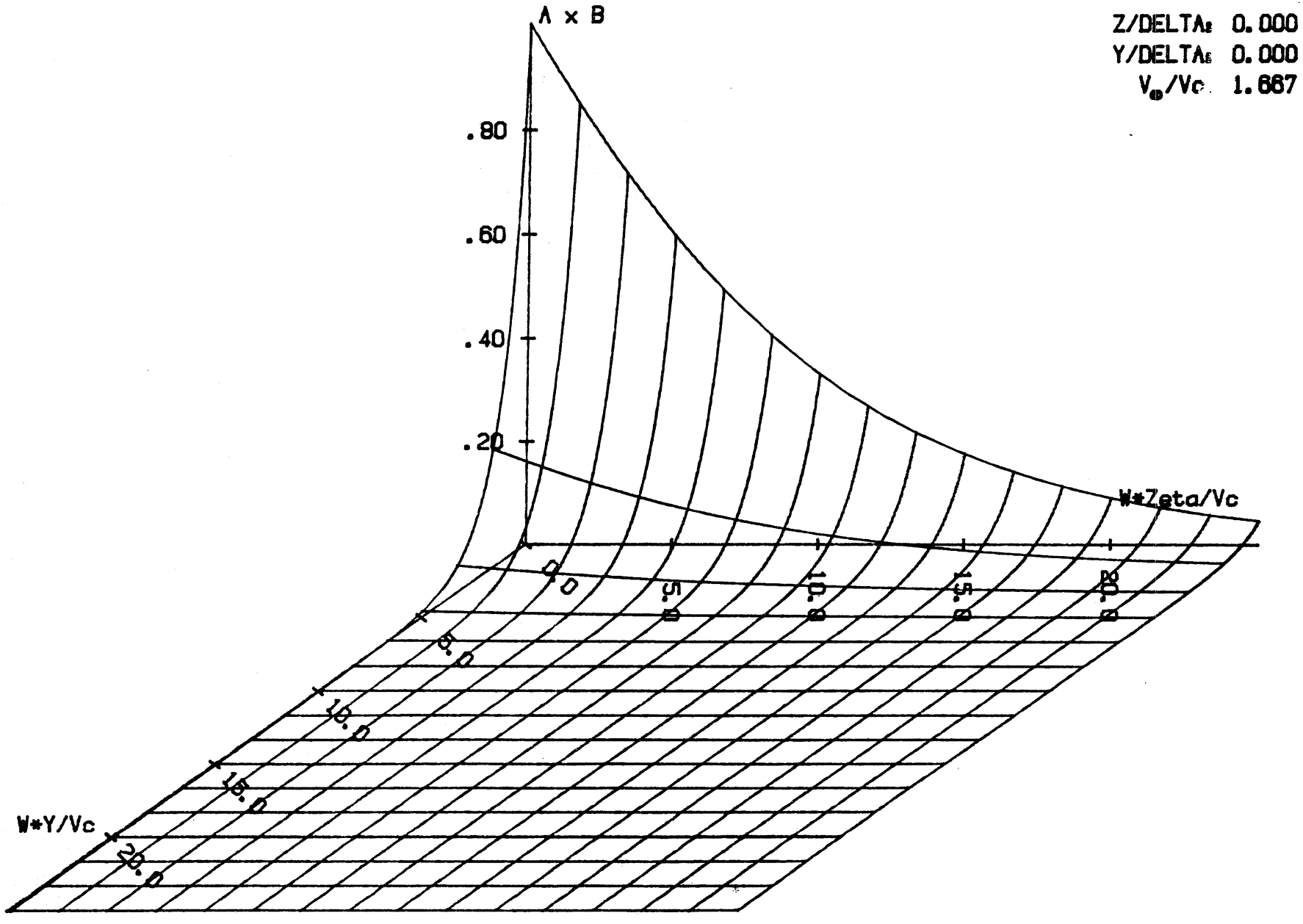
A x B
Z/DELTAε 0.000
Y/DELTAε 0.000
Vp/Vc 1.667
.80
.60
.40
.20
W*Zeta/Vc
0.0
5.0
10.0
15.0
20.0
W*Y/Vc
0.0
5.0
10.0
15.0
20.0

Fig. 3

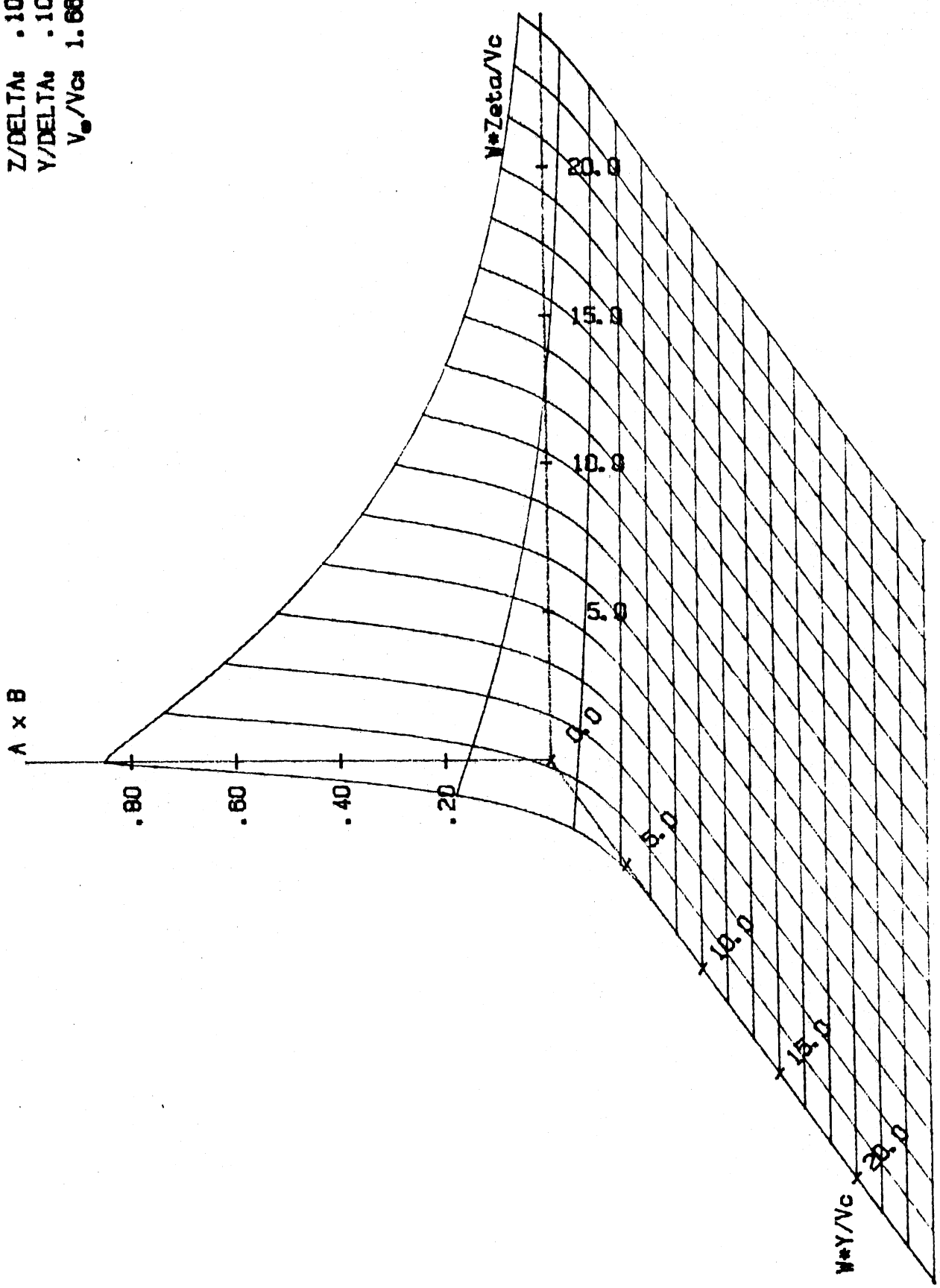
Z/DELTAs .100
Y/DELTAs .100
Vo/Vcs 1.667
A x B
.80
.60
.40
.20
W*Zeta/Vc
20.0
15.0
10.0
5.0
0.0
-5.0
-10.0
-15.0
-20.0
W*Y/Vc

Fig. 4

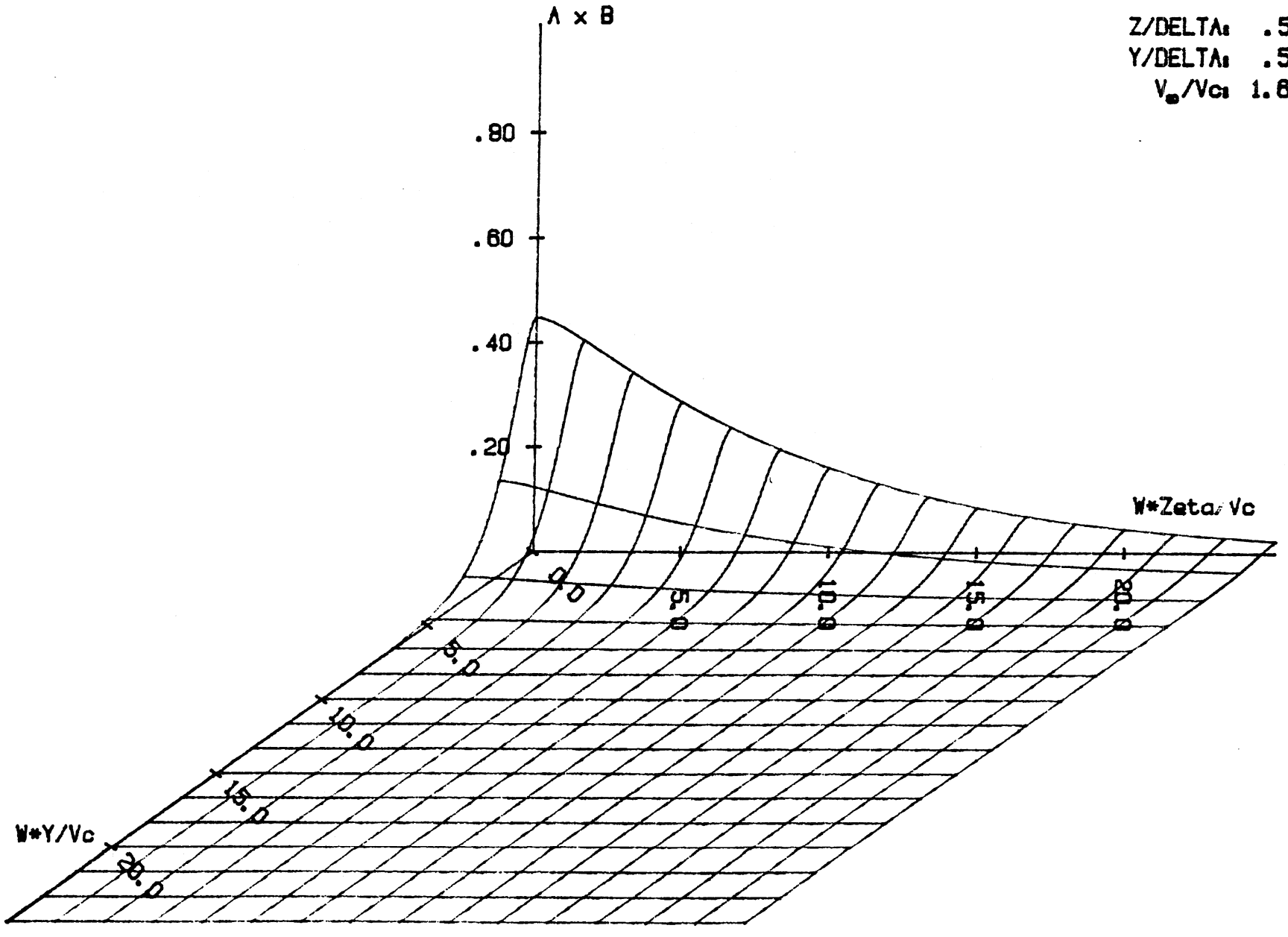
A x B
Z/DELTA: .500
Y/DELTA: .500
V∞/Vc: 1.667
.80
.60
.40
.20
W*Zeta/Vc
0.0
5.0
10.0
15.0
20.0
W*Y/Vc
5.0
10.0
15.0
20.0

Fig. 5

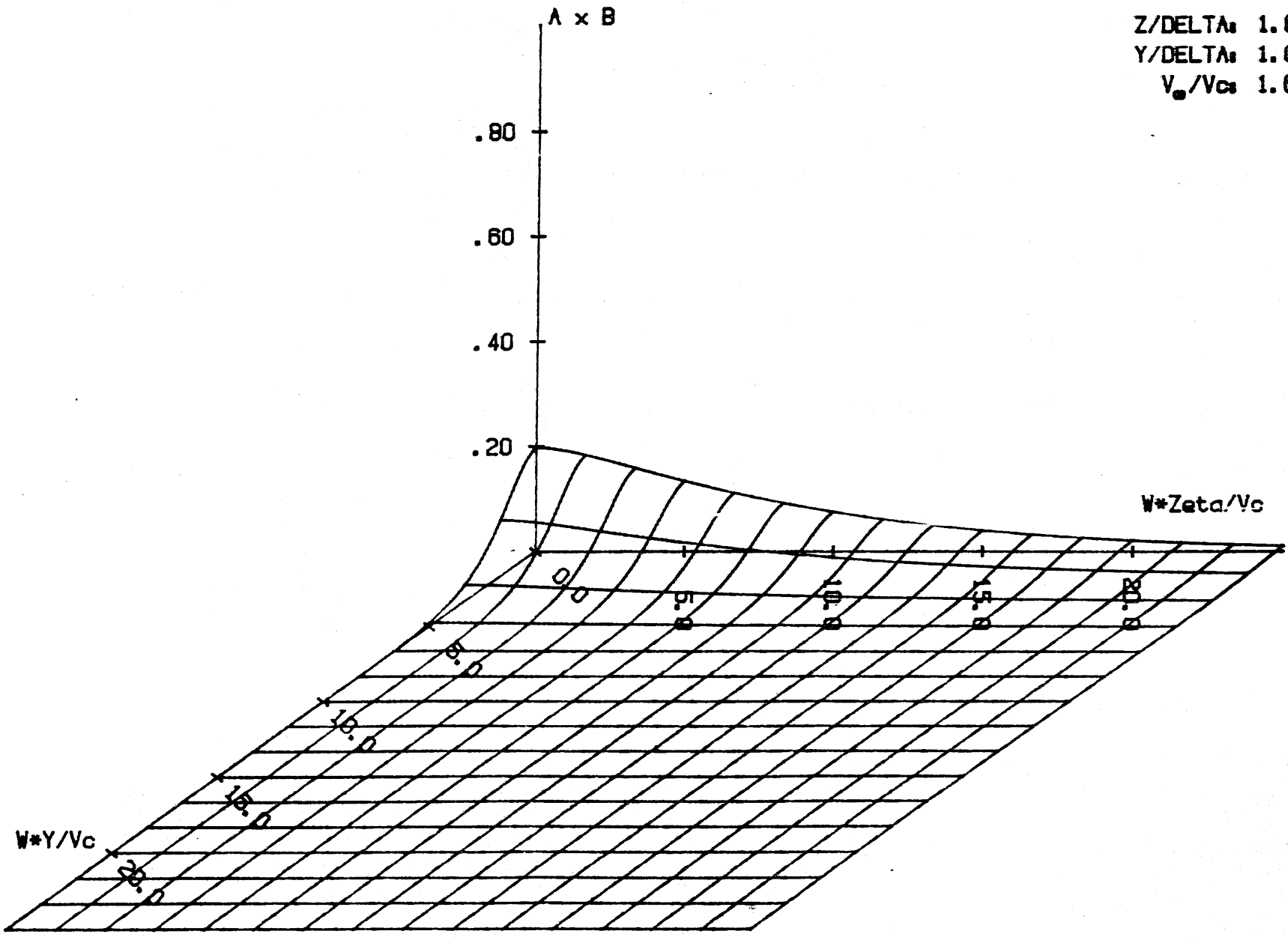
A x B
Z/DELTA: 1.000
Y/DELTA: 1.000
V∞/Vc: 1.667
.80
.60
.40
.20
W*Zeta/Vc
0.0
5.0
10.0
15.0
20.0
6.0
16.0
16.0
W*Y/Vc
26.0

Fig. 6

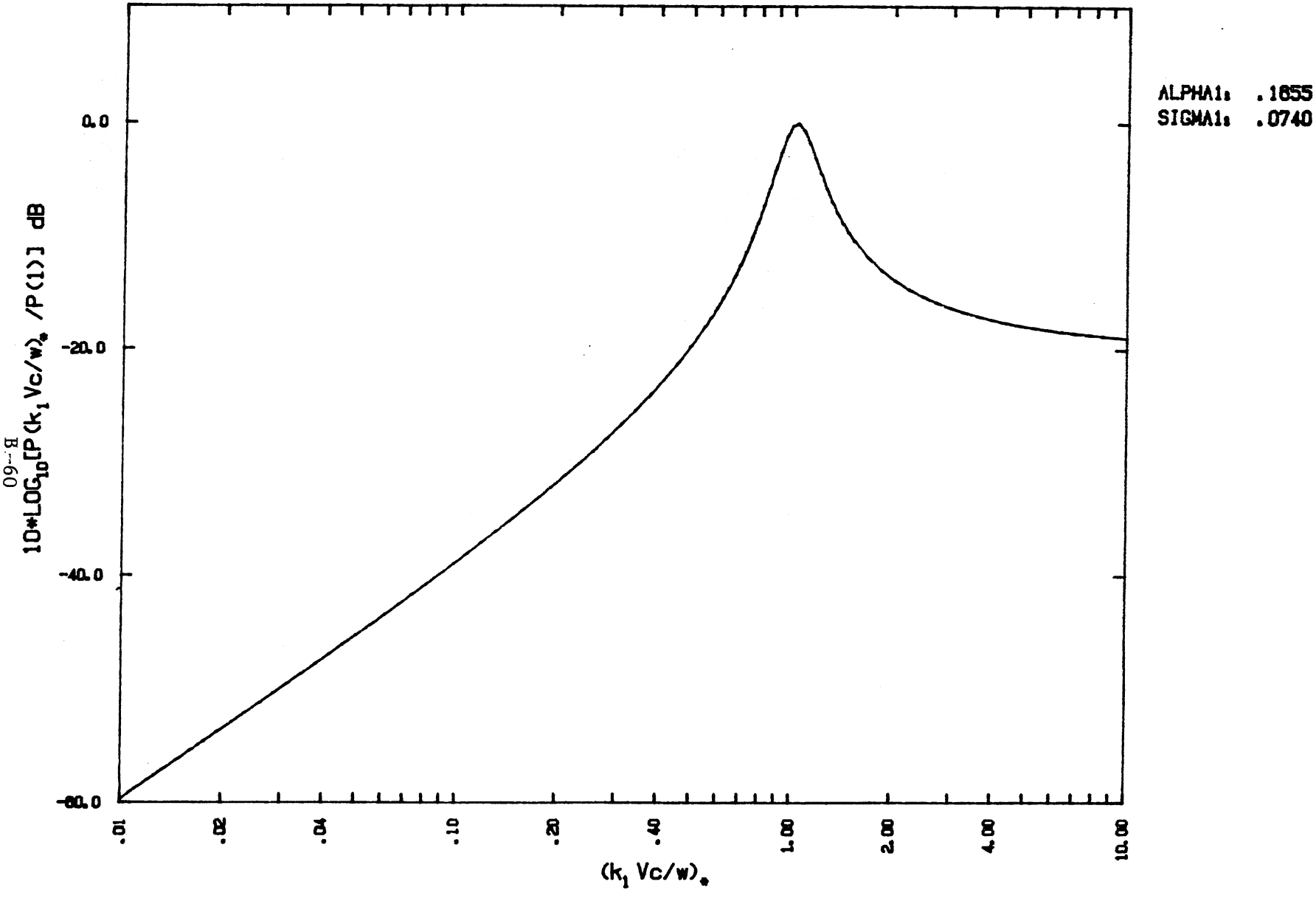
ALPHA1: .1655
SIGMA1: .0740
0.0
-20.0
-40.0
-60.0
10*LOG10[P(k1 Vc/w)* /P(1)] dB
.01
.02
.04
.10
.20
.40
1.00
2.00
4.00
10.00
(k1 Vc/w)*

Fig. 7

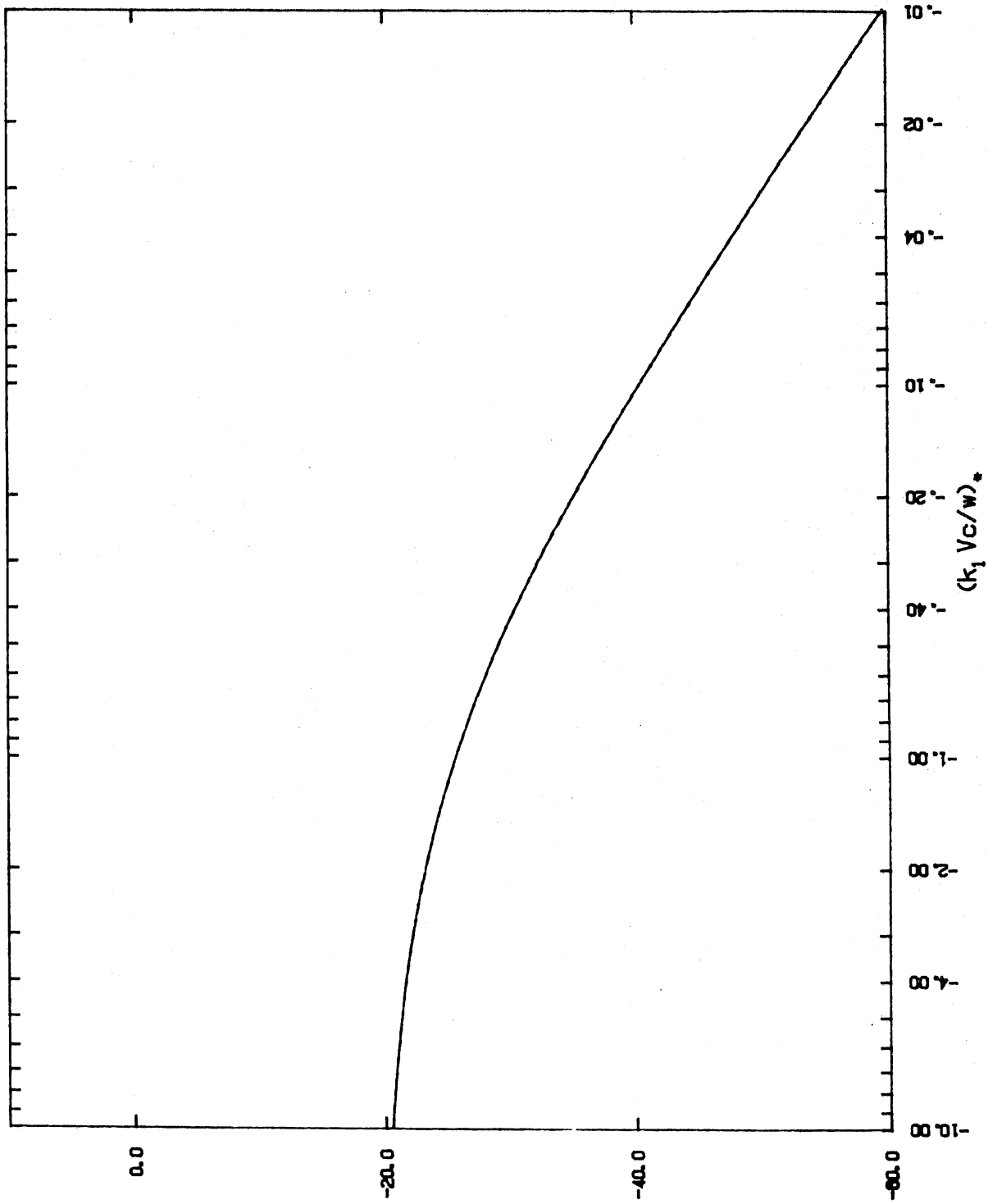
ALPHA1: .1665
SIGMA1: .0740
10*LOG10[P(k1Vc/w)* /P(1)] dB
0.0
-20.0
-40.0
-60.0
-10.00
-4.00
-2.00
-1.00
-.40
-.20
-.10
-.04
-.02
-.01
(k1 Vc/w)*

Fig. 8

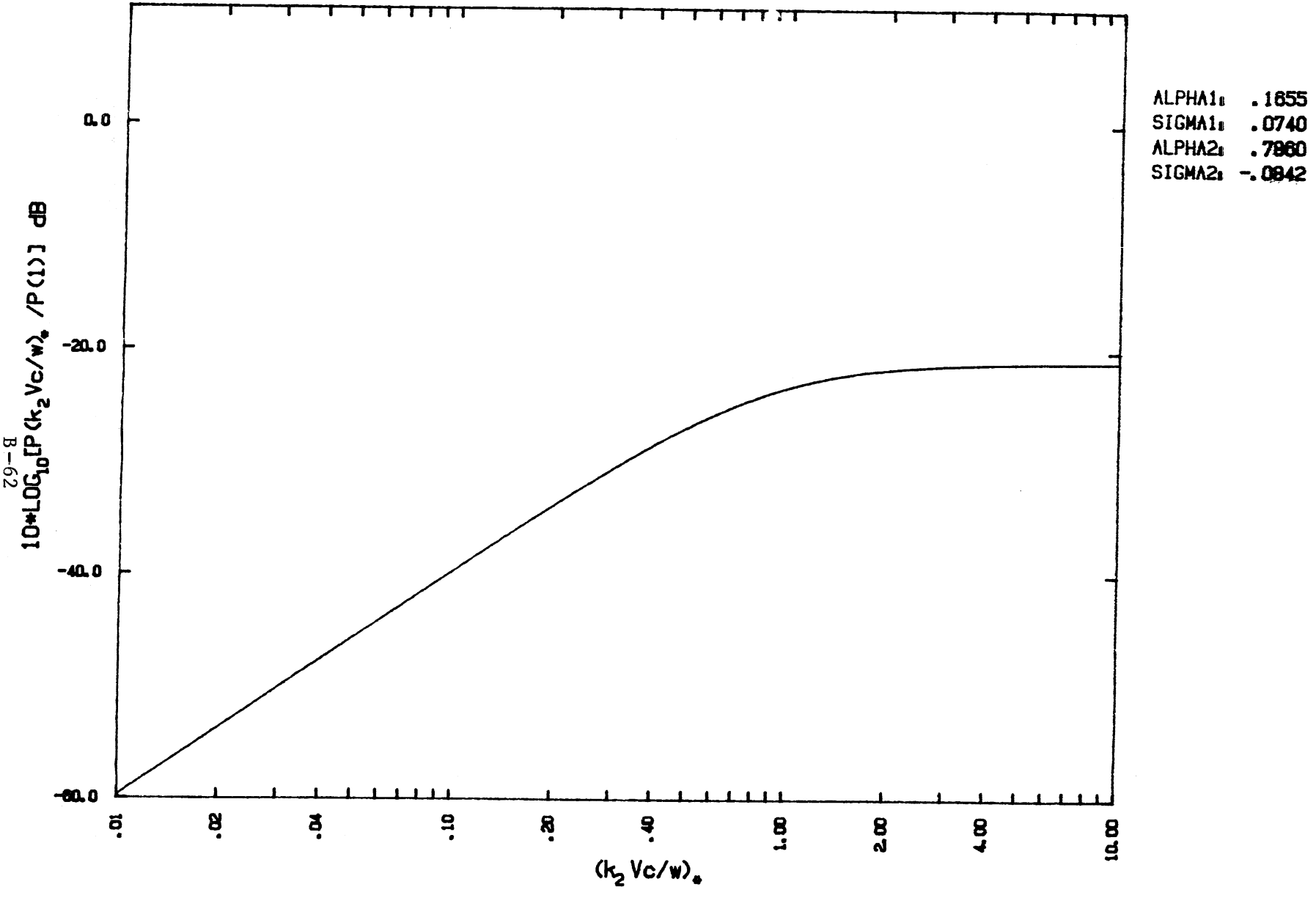
ALPHA1= .1655
SIGMA1= .0740
ALPHA2= .7860
SIGMA2= -.0842
0.0
-20.0
-40.0
-60.0
10*LOG10[P(k2 Vc/w)* /P(1)] dB
.01
.02
.04
.10
.20
.40
1.00
2.00
4.00
10.00
(k2 Vc/w)*

Fig. 9

Appendix B-Suggested Experiment

It was pointed out in tracts VI and VII that the convective waveguide model of boundary layer pressure fluctuations predicted a frequency dispersion not found in the Chase model.

The wave guide model predicts that $P(k_1, o, \omega)$ will exhibit a peak at the wavenumber value k_p given by

$$k_p = (\frac{\omega}{V_c})* = \sqrt{(\frac{\omega}{V_c})^2 + (\frac{V_\infty}{V_c})^2 \frac{1}{\delta^2}} \qquad (B\text{-}1)$$

whereas the Chase model predicts a peak at ω/V_c. If at the frequency in question, $\omega >> \omega_o = V_\infty/\delta$, then the two predictions are about the same.

However, at low frequencies, i.e. $\omega << \omega_o$, a significant difference is expected and this suggests that we try to verify this prediction by experiment.

Note that

$$\frac{\omega}{V_c} = \frac{1}{\delta^*} (\frac{V_\infty}{V_c})(\frac{\omega\delta^*}{V_\infty}) \qquad (B\text{-}2)$$

and

$$(\frac{\omega}{V_c})* = \frac{1}{\delta} (\frac{V_\infty}{V_c}) \sqrt{1+ (\frac{\delta}{\delta^*})^2 (\frac{\omega\delta^*}{V_\infty})^2} \qquad (B\text{-}3)$$

Thus, in the convective waveguide model the peak in $P(k_1, o, \omega)$ should occur at

$$k_p\delta = (\frac{V_\infty}{V_c}) \sqrt{1+ (\frac{\delta}{\delta^*})^2 (\frac{\omega\delta^*}{V_\infty})^2} \qquad (B\text{-}4)$$

The ratio V_∞/V_c is not constant but should vary with frequency according to the empirical relation

$$\frac{V_\infty}{V_c} \simeq \frac{1.67}{1+0.67e^{-(\omega\delta^*/V_\infty)}} \qquad (B\text{-}5)$$

which predicts that $V_c = V_\infty$ at $\omega\delta^*/V_\infty = 0$ and $V_c \to 0.60\ V_\infty$ as $\omega\delta^*/V_\infty \to \infty$ in good agreement with results from wind tunnel studies.

On this basis one can predict how k_p will behave with frequency if δ^*/δ is known. That prediction is shown on the attached figure for $\delta=8\delta^*$. The upper curve is a plot of Eqs. 4B and 5B for the range of $\omega\delta^*/V_\infty$ of greatest interest. The lower curve is a plot of $\omega\delta/V_c$. The two curves merge for $\omega\delta^*/V_\infty>0.4$ but do diverge significantly for $\omega\delta^*/V_\infty<0.1$. This should be well within the frequency range of the bouyant body facility if $\delta^*\simeq.001$m.

One of the initial experiments with the bouyant body facility should be to estimate the location of the peaks in $P(k_1, o, \omega)$ as a function of frequency. The spectral estimators should work very well in that region of k.

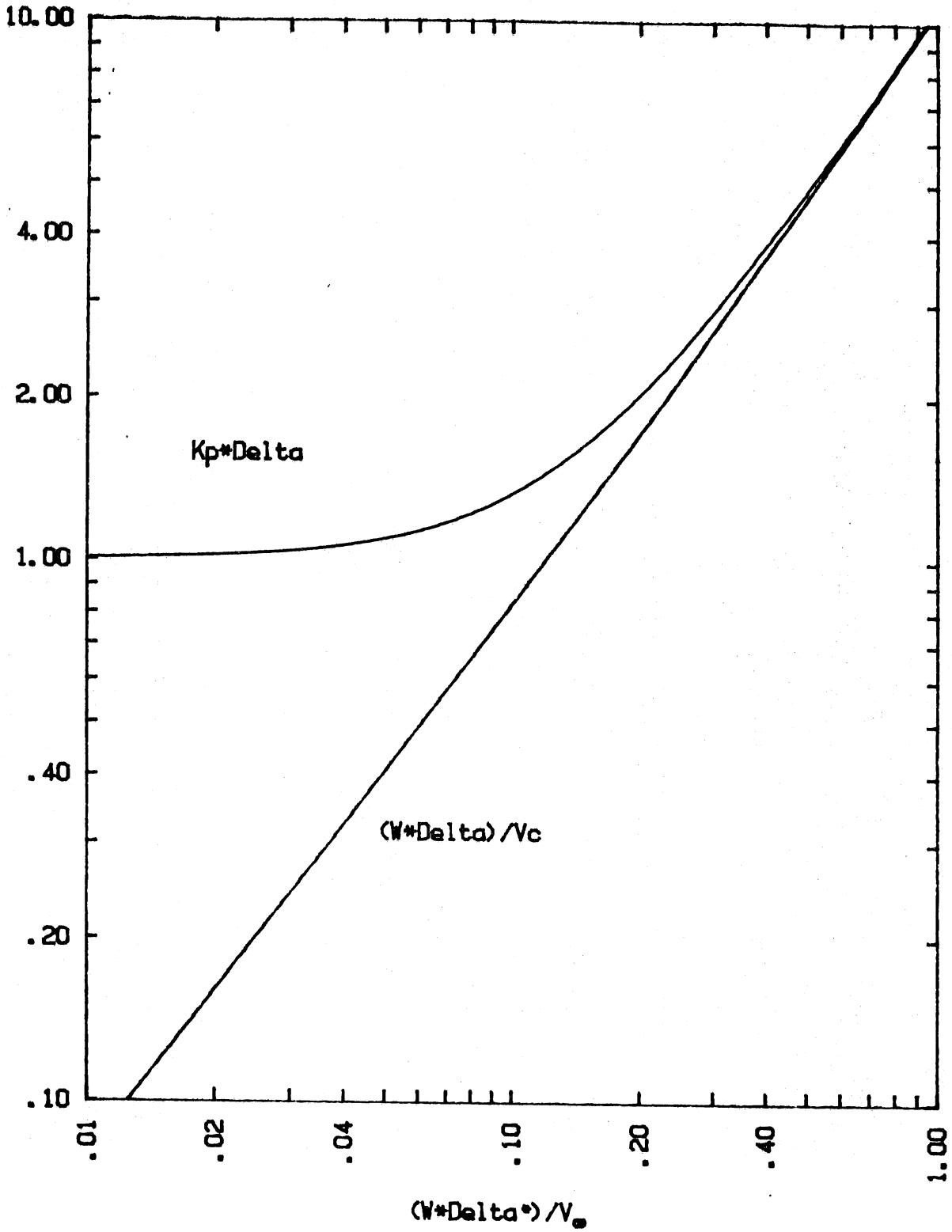
10.00
4.00
2.00
1.00
.40
.20
.10
Kp*Delta
(W*Delta)/Vc
.01
.02
.04
.10
.20
.40
1.00
(W*Delta*)/V

Fig. 10

IX. Pressure Phase Convection Speed Characteristics

Wall Pressure Fluctuations

by

Robert F. Lambert

Introduction

The purpose of this tract is to focus attention on convection speed characteristics and make some predictions based on the convective waveguide model. In particular, there is great interest in the behavior of the convection speeds with frequency and how to interpret convection speeds based on phase measurements. In my judgement they may have been misinterpreted in the past.

Analysis

The relative phase between two points a distance ξ apart in the streamwise direction based on the convective waveguide method is

$$\phi* = k_*\xi = \sqrt{(\frac{\omega\xi}{V_c})^2 + \frac{\xi^2}{\Delta^2}} = \left[\frac{\sqrt{\omega^2+\omega_o^2}}{V_c}\right] \xi \qquad (1)$$

where $k*$ is a streamwise wave number, ω is the frequency in question, V_c is the boundary layer convection speed, Δ is the half width of the flow channel, and the cut-on frequency

$$\omega_o \equiv \frac{V_c}{\Delta} \qquad (2)$$

In general V_c and hence ω_o will be frequency dependent. As will be pointed out V_c cannot be determined directly from phase measurements and must be inferred from other data.

For convenience I will interpret the boundary layer thickness δ to be identical with Δ.

Eq. 1 can be rewritten in terms of normalized parameters and expressed in

the dimensionless form

$$k_*\delta^* = \left(\frac{V_\infty}{V_c}\right)\Big/\sqrt{\tilde{\omega}^2+\left(\frac{V_c}{V_\infty}\right)^2\left(\frac{\delta^*}{\delta}\right)^2} \tag{3}$$

where V_∞ is the free stream or center-line flow speed, δ^* is the displacement boundary layer thickness, and $\tilde{\omega} \equiv \omega\delta^*/V_\infty$.

To interpret phase measurement we now define a wall pressure phase convection speed as

$$Vp \equiv \frac{\omega}{k_*} \tag{4}$$

which is a parameter that can be determined from relative pressure phase ϕ_* (or time delay T_d) measurement made by point transducers spaced a known distance ξ apart via the relations $\omega T_d=\phi_*$ or $V_p=\xi/T_d=\omega\xi/\phi_*$.

Eq. 4 yields a pressure convection phase speed ratio

$$\frac{V_p}{V_\infty} = \left(\frac{V_c}{V_\infty}\right)\frac{\omega}{\sqrt{\omega^2+\omega_o{}^2}} \qquad \text{a)}$$

or (5)

$$\frac{V_p}{V_\infty} = \left(\frac{V_c}{V_\infty}\right)\frac{\tilde{\omega}}{\sqrt{\tilde{\omega}^2+\left(\frac{V_c}{V_\infty}\right)^2\left(\frac{\delta^*}{\delta}\right)^2}} \qquad \text{b)}$$

It is evident from Eq. 5 that

$$V_c \simeq V_p \tag{6}$$

provided $\tilde{\omega}^2 >> \left(\frac{V_c}{V_\infty}\right)^2\left(\frac{\delta^*}{\delta}\right)^2$ at all frequencies of interest. Hence, phase measurements at high frequencies will yield good values for V_c. However, at lower frequencies where $\tilde{\omega}^2 < \left(\frac{V_c}{V_\infty}\right)^2\left(\frac{\delta^*}{\delta}\right)^2$ this is no longer the case and in the limit as $\tilde{\omega}$ approaches zero

$$\frac{V_p}{V_\infty} \xrightarrow[\tilde{\omega}\to 0]{} \tilde{\omega}\left(\frac{\delta}{\delta^*}\right) = \frac{\omega\delta}{V_\infty}. \tag{7}$$

Thus, we expect V_p/V_∞ to vanish at zero frequency and the slope of the characteristic will be δ/δ^* there.

We further expect the value of V_c/V_∞ in Eq. 5 to be well behaved in terms of frequency so the above conclusions should be valid.

However, to make numerical predictions of V_p/V_∞ based on Eq. 5 I have decided to approximate V_c/V_∞ by the semi-empirical relation

$$\frac{V_c}{V_\infty} = \frac{1+0.67e^{-\tilde{\omega}}}{1.67} \tag{8}$$

which predicts that $V_c \to 0.6V_\infty$ as $\tilde{\omega}\to\infty$. This characteristic satisfies my intuition about the drift velocity of large low frequency eddies* and satisfies experimental observations at high frequencies where $V_c \simeq V_p$, Eq. 6. It is essentially the same assumption made by Chase in his numerical predictions of V_p/V_∞.(1)

Numerical Predictions.

I will assume for prediction purposes that $\delta^*/\delta=0.125$ which is a fairly nominal value for this ratio. Employing Eq. 8 for V_c/V_∞ the predicted value for V_p/V_∞ is shown in Fig. 1. Note, it falls to zero rapidly as $\tilde{\omega}\to 0$ and peaks to a value of about 0.84 at $\tilde{\omega}\simeq 0.30$. For higher values of $\tilde{\omega}$ the characteristic levels off at the values required by the V_c/V_∞ characteristic. This prediction is in remarkable agreement with pressure phase speed values measured by Blake (2). However, his measured values do depend somewhat on the relative spacing ξ/δ^* used in the measurements. But, like all phase (or time delay) measurements employing random signals and finite size transducers there are some errors to be expected. Also, I believe that the observed behavior of V_p/V_∞ with ξ/δ^*,

* $V_c \to V_\infty$ as $\tilde{\omega} \to 0$.

including measurements reported by Aupperle and Lambert (3), has as much to do with the finite size of the transducers at close spacings as with the physics of the flow field. Such measurements are not highly repeatable and have never made good sense to me. The results predicted by Eq. 5 are independent of spacing.

So, in practice we actually measure V_p and the value of V_c must be inferred from Eq. 5 taking into account the expected frequency dispersion at low frequencies. A simple manipulation yields

$$\frac{V_c}{V_\infty} = \frac{V_p}{V_\infty} \frac{\tilde{\omega}}{\sqrt{\tilde{\omega}^2 - (\frac{V_p}{V_\infty})^2 (\frac{\delta^*}{\delta})^2}} \tag{9}$$

as an algorithm for computing V_c/V_∞ from measured values of V_p/V_∞ for known values of $\tilde{\omega}$ and δ^*/δ.

Finally, a few remarks about the fluctuating pressure group velocity V_g, which usually is defined as

$$V_g \equiv \frac{\partial \omega}{\partial k^*} . \tag{10}$$

In most dispersive media (where energy losses can be neglected) V_g is a measure of the speed at which the energy associated with the pressure fluctuations at the wall propagates. It also is frequency dependent.

The convective waveguide model predicts that

$$V_g = V_c \frac{\sqrt{\omega^2 + \omega_o^2}}{\omega} \qquad \text{a)}$$

or (11)

$$\frac{V_g}{V_\infty} = (\frac{V_c}{V_\infty}) \frac{\sqrt{\tilde{\omega}^2 + (\frac{V_c}{V_\infty})^2 (\frac{\delta^*}{\delta})^2}}{\tilde{\omega}} \qquad \text{b)}$$

The values of V_g/V_∞ predicted by Eq. 11 will be greater than the value V_c/V_∞

at all frequencies. In particular, the group velocity can exceed the speed of sound c below some frequency $\tilde{\omega}_s$ at all mach numbers. I expect $\tilde{\omega}_s$ to be fairly low at low mach numbers and hence approximate V_c by V_∞ for prediction purposes. The resulting expression for $\tilde{\omega}_s$ then becomes

$$\tilde{\omega}_s \simeq \frac{M_\infty}{\sqrt{1-M_\infty^2}} \left(\frac{\delta^*}{\delta}\right) \qquad \text{a)}$$

or (12)

$$\omega_s \simeq \frac{M_\infty}{\sqrt{1-M_\infty^2}} \left(\frac{V_\infty}{\delta}\right) \qquad \text{b)}$$

where $M_\infty = V_\infty/c << 1$.

The value of ω_s predicted by Eq. 12 should mark the lower edge of the convective energy regime assuming incompressible fluid flow since $V_g < c$ for $\tilde{\omega} > \tilde{\omega}_s$ and $V_g > c$ for $\tilde{\omega} < \tilde{\omega}_s$.

In conclusion, I recommend in the future that all speed and spectral measurements also be interpreted in the light of the convective waveguide model of boundary layer pressure fluctuations. Of special note are low frequencies i.e. $\tilde{\omega}^2 < (\frac{V_p}{V_\infty})^2 (\frac{\delta^*}{\delta})^2$, where dispersion is likely to be most pronounced. The characteristic shown in Fig. 1 is a direct result of such dispersion and the assumed innocuous behavior of V_c/V_∞. I find the high frequency model of Corcos and even the more elaborate one due to Chase somewhat misleading and inconsistent with certain experiments. Fortunately, Chase's model has a large number of adjustable parameters so that many experimental characteristics can be fit by judicious choices of these parameters. Of course, if our spectral measurement at low frequencies do not follow the predicted dispersion requirements of the convective waveguide model I will modify (or abandon) it quickly.

References

1) D. M. Chase, Jour. Sound and Vibration 70, 29-27 (1980).

2) W. K. Blake, Jour. of Fluid Mech. 44 637-660 (1970).

3) F. A. Aupperle and R. F. Lambert, Jour. Acoust. Soc. Am. 47 359-370 (1970).

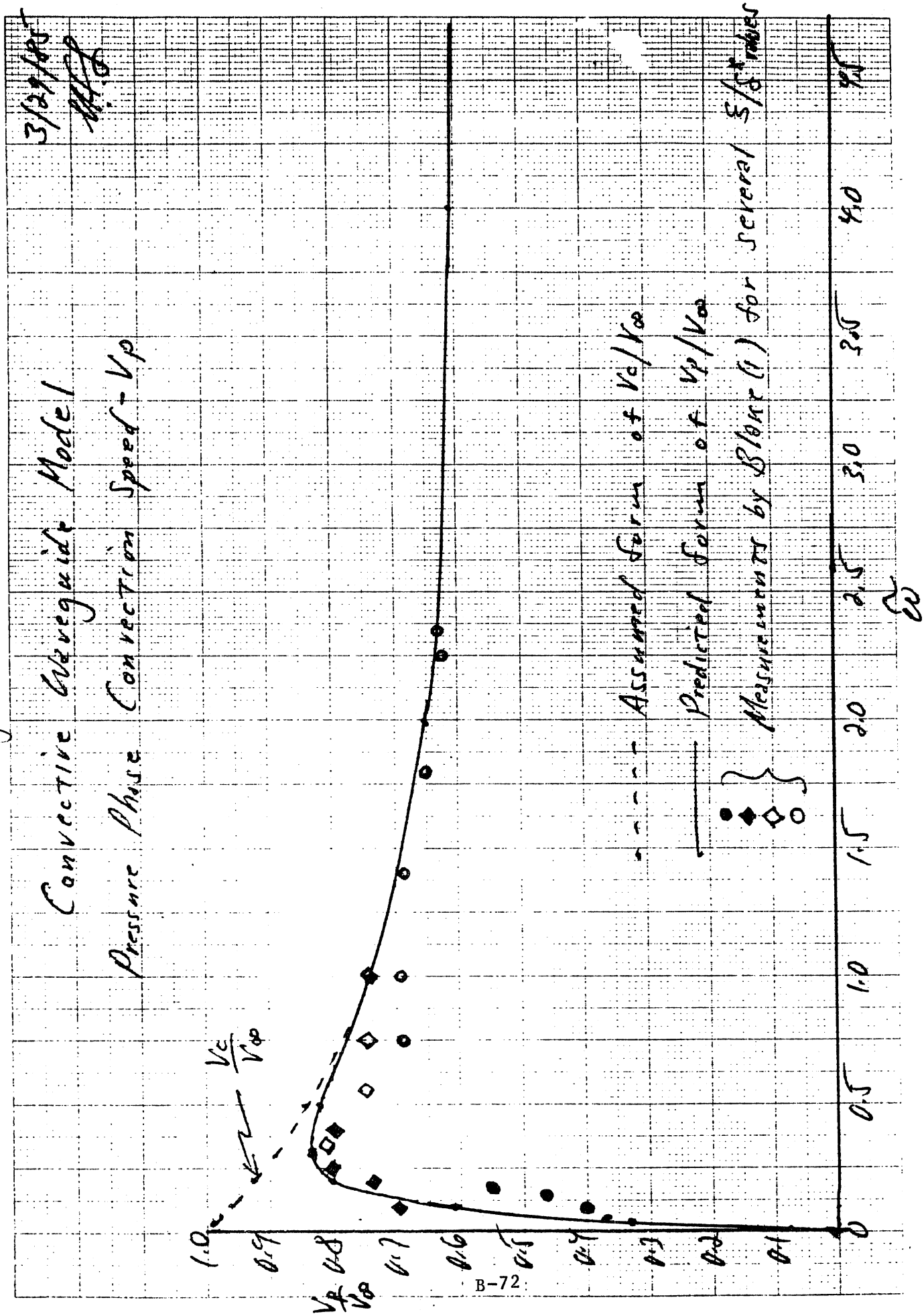

Fig. 1